Development of Dynamic *in vivo* carbon-13 Magnetic Resonance Spectroscopy for Rat Brain Imaging at 7-Tesla

Chathura Kumaragamage

Department of Biomedical Engineering
McGill University
Montreal, Canada

June 2018

A thesis submitted to McGill University in partial fulfillment of the requirements for the degree of Doctor of Philosophy

Abstract

The overarching objective of this thesis is to develop novel methods for dynamic *in vivo* carbon-13 (^{13}C) Magnetic Resonance Spectroscopy (MRS) for rodent brain imaging. Dynamic ^{13}C MRS is a powerful technique that provides non-invasive means to quantify neurotransmitter cycling rates and cell-specific neuroenergetics in the brain, following the infusion of a ^{13}C labeled substrate. Proton observed carbon edited (POCE) MRS is a popularly used indirect ^{13}C MRS technique, typically implemented with a surface coil transceiver on the proton channel to benefit from surface coil sensitivity gains. POCE MRS implementations for a surface coil transceiver benefit from the use of relatively long and power intensive adiabatic radiofrequency (RF) pulses to minimize nutation angle errors, signal losses, and artifacts due to the spatially varying magnetic field (B_1^+). The first goal of this work was thus to develop an RF coil platform with homogeneous B_1^+, in addition to providing receive sensitivity gains of a surface coil. This was achieved by combining a proton volumetric resonator, and detunable surface coil for proton signal reception, in addition to a surface coil on the ^{13}C channel. A point resolved spectroscopy (PRESS) localized POCE MRS sequence with a 12.6-ms echo time (TE) was implemented with short conventional pulses, enabling uniform nutation, two-shot edited POCE MRS, combined with a short TE; a feat that cannot be achieved with all-surface coil based approaches described in the literature.

An extension to the above goal was to improve the PRESS-POCE sequence by reducing the sequence TE and minimize T_2 and homonuclear J-evolution related losses. To that end, a novel PRESS localized POCE sequence that utilizes simultaneous editing and localization pulses (SEAL-PRESS) allowing the TE to be reduced to a theoretically optimal value of 8.1-ms was implemented. The SEAL-PRESS sequence was validated in phantom and in an *in vivo* rat preparation. Carbon editing efficiency of the SEAL-PRESS sequence was >95%, and provided a >17% improvement of ^{13}C labeled metabolites relative to the previously described PRESS-POCE sequence.

The final goal of this thesis was to investigate the feasibility of sequentially acquiring indirect and direct ^{13}C MRS during a dynamic *in vivo* ^{13}C MRS session, to harvest the benefits of indirect and direct ^{13}C methods, with the ultimate goal of improving metabolic modeling. Modifications to the RF chain were necessary to extend the developed coil platform to be capable of both direct and indirect ^{13}C MRS. A PRESS-localized semi-adiabatic distortionless enhancement by polarization transfer (DEPT) sequence was designed and evaluated in phantom, and the SEAL-PRESS sequence was used for indirect ^{13}C MRS. Phantom data showed that measurements made with the two sequences were in reasonable agreement. Finally a dynamic *in vivo* ^{13}C MRS study in rat brain was conducted while sequentially acquiring data with both sequences. Time-resolved indirect ^{13}C spectra were obtained as expected, however due to much poorer sensitivity of direct ^{13}C signal acquisition; no meaningful time-resolved spectra were recorded. Avenues for SNR degradation along the RF chain were investigated, and considerations for the next iteration coil setup are discussed.

Abrégé

L'objectif global de cette thèse est de développer de nouvelles méthodes dynamiques de spectroscopie par résonance magnétique (SRM) du carbone-13 (^{13}C) pour l'imagerie du cerveau des rongeurs in vivo. La SRM-^{13}C est une technique puissante qui fournit des moyens non-invasifs pour quantifier les taux de cyclage de neurotransmetteurs et de neuroénergétiques spécifiques aux cellules du cerveau, suite à la perfusion d'un substrat marqué au ^{13}C. La SRM par l'observation du proton, édité par le carbone (Proton Observed Carbon Edited - POCE), est une technique de SRM-^{13}C indirecte communément utilisée avec une antenne de surface émetteur-récepteur pour protons puisque c'est une construction relativement facile, et bénéficie de gains de sensibilité typiques aux antennes de surfaces. Les implémentations SRM-POCE pour une antenne de surface émetteur-récepteur bénéficient d'autant plus d'impulsions de radiofréquences (RF) adiabatiques relativement longues et puissantes pour minimiser les erreurs d'angle de nutation, les pertes de signaux et les artefacts dûs aux variations spatiales du champ magnétique (B_1^+). Le premier objectif de ce travail était donc de développer une antenne de RF avec un B_1^+ homogène, en plus de fournir des gains de sensibilité avec l'utilisation d'une antenne de surface. Ceci a été réalisé en combinant un résonateur volumétrique pour des impulsions de transmission de protons, une antenne de surface pour la réception de signaux de protons, en plus d'une antenne de transmission de surface pour le ^{13}C. Une séquence SRM-POCE localisée par spectroscopie résolu ponctuelle (Point Resolved SpectroScopy - PRESS) avec un temps d'écho de 12,6 ms (TE) a été implémentée avec de courtes impulsions conventionnelles permettant une nutation uniforme, une SMR-POCE édité en deux coups, et un TE court; une prouesse qui ne peut être atteinte avec des approches à base d'antennes de surface décrites dans la littérature.

Une extension à l'objectif ci-dessus était d'étudier les améliorations apportées à la séquence PRESS-POCE en réduisant le TE et donc minimisant les pertes liées à l'évolution de T_2 et des couplages-J homonucléaires. A cette fin, une nouvelle séquence POCE localisée PRESS utilisant des impulsions d'édition et de localisation simultanées (Simultaneous Editing And Localization, SEAL-PRESS) permettant de réduire le TE à une valeur théoriquement optimale de 8,1 ms a été mise en œuvre. La séquence SEAL-PRESS a été validée avec un fantôme et in vivo chez le rat. L'efficacité d'édition du carbone de la séquence SEAL-PRESS était >95% avec une amélioration de >17% des métabolites marqués au ^{13}C par rapport à la séquence PRESS-POCE précédente.

Le but final de cette thèse était d'étudier la faisabilité d'acquisition séquentielle de SRM-^{13}C indirects et directs au cours d'une seule session, in vivo, afin de récolter les bénéfices des méthodes indirectes et directes du ^{13}C dans le but ultime d'améliorer la modélisation métabolique. Des modifications de la chaîne radiofréquence ont été nécessaires pour effectuer une SRM-^{13}C directe. Une séquence localisé PRESS semi-adiabatique d'augmentation par transfert de polarisation sans distortions (Distortionless Enhancement by Polarization Transfer, DEPT) a été conçue et évaluée avec un fantôme, et la séquence SEAL-PRESS a été utilisée pour le SRM-^{13}C indirect. Les données obtenues avec le fantôme ont démontré que les mesures faites avec ces deux séquences étaient raisonnablement en accord. Finalement, une étude dynamique SRM-^{13}C dans le cerveau de rats in vivo a été menée en acquérant séquentiellement des données avec ces deux dites séquences. Les spectres indirects ^{13}C résolus dans le temps ont été obtenus comme prévu, cependant en raison d'une sensibilité beaucoup plus faible de l'acquisition directe du signal ^{13}C, aucun spectre significatif résolu dans le temps n'a été enregistré. Les avenues pour

la dégradation du ratio signal:bruit le long de la chaîne RF ont été étudiées, et des considérations pour une nouvelle itération de l’antenne y sont discutées.

Acknowledgements

This work would not have been possible without the support and guidance of many, which includes those who I closely associate with, and those who have indirectly supported me. First, I thank my parents for all their support and guidance throughout my career. My mother in particular has been, and continues to be my inspiration, and was a significant influence in me choosing to go down the academic pathway.

To my supervisor, Jamie Near, as his first PhD student I have nothing but the best to say to you; you gave me the most exhilarating project to run with, gave me independence to challenge myself and solve problems, while guiding me, you stood up for me when I needed your support, and you have been a constant pillar of support during this whole time. Furthermore, your enthusiasm made this period a thoroughly enjoyable one for me. I must also extend my acknowledgements to Jamie's family; his wife Sarah, and his kids Murray, Lydia, and Sam, for their understanding and letting Jamie be at work off-hours, often long hours during weekdays beyond midnight or weekends to run animal scans, when the MRI was fully utilized. If it wasn't for you guys, this work would not have happened by now. You guys are the best!

To Axel Mathieu, and Dan Madularu- my colleagues at work and buddies outside work; thank you for the multifaceted support you have given me during this time, and for making life in Montreal an enjoyable one.

To Dr. Rothman, Dr. de Graaf and Dr. De Feyter from Yale University; thank you for all your insights and support with ^{13}C MRS development.

To Tayna and Sophie our administrators at the Douglas institute during my time there; thank you for all your help with getting things out of my reach, done swiftly.

To members of my PhD advisory board, Dr, Hoge, Dr Baillet, Dr Cohen-Adad, Dr Narayanan, Dr Tabrizian, than you all for the guidance and feedback during this time.

To all students and staff at the CIC, and our lab, especially Caitlin, Steven, Charana, Sivaniya, Derek, and my coffee buddies at the CobraLab; thank you all for your support and friendship.

Finally, to my loving wife Piyumi; you were the glue that kept me together, thank you for your patience, encouragement, support and love.

Preface and Contribution of Authors

In accordance with the McGill Thesis Preparation guidelines, I have taken the option of writing the experiment section of this thesis as a compilation of original papers appropriate for publication.

Table of Contents

List of Figures

List of Tables

List of Abbreviations

AFP	Adiabatic full passage
Ace	Acetate
Asp	Aspartate
B_1^+	Transmit RF field on the proton channel
B_1^-	Receive RF field on the proton channel
B_2^+	Transmit RF field on the carbon (^{13}C) channel
B_2^-	Receive RF field on the carbon (^{13}C) channel
BISEP	B_1 insensitive spectral editing pulse
^{12}C	The carbon-12 isotope
^{13}C	The carbon-13 isotope
CPSE	Carr-Purcell spin echo
CRLB	Cramer Rao lower bound
CV	Coefficient of variation
DEPT	Distortionless enhancement by polarization transfer
Glc	Glucose
Gln	Glutamine
Glu	Glutamate
Glx	Glutamate + Glutamine
^1H	Protons
J_{HC}	Heteronuclear scalar coupling constant between ^1H-^{13}C
INEPT	Insensitive nuclear enhancement by polarization transfer
ISIS	Image selected in vivo spectroscopy
Lac	Lactate
LASER	Localization by adiabatic selective refocusing
MM	Macromolecules
MRI	Magnetic Resonance Imaging
MRS	Magnetic Resonance Spectroscopy
[n-^{13}C]-YYY	The nth carbon of metabolite YYY contains a ^{13}C atom

NMR	Nuclear Magnetic Resonance
OVS	Outer volume suppression
POCE	Proton observed carbon edited
ppm	parts per million
PRESS	Point resolved spectroscopy
Pyr	Pyruvate
SEAL	Simultaneous editing and localization
SPECIAL	Spin echo full intensity acquired localized
SNR	Signal-to-noise ratio
TCA	Tricarboxylic acid
TE	Echo time
TR	Repetition time
VAPOR	Variable pulse power and optimized relaxation delays

Chapter 1

General Introduction

1.1 Motivation for this Work

Magnetic resonance spectroscopy (MRS) is a powerful technique that provides a non-invasive means to study neurochemistry, metabolism, and neurotransmitter function in the brain. Specifically, dynamic *in vivo* Carbon-13 (^{13}C) MRS, following the infusion of a ^{13}C labeled substrate, is capable of detecting ^{13}C labeled metabolites, and obtaining quantitative measurements of neurotransmitter cycling rates and cell-specific neuroenergetics *in vivo* (1). The role of neuroenergetics and neurotransmitter cycling rates is increasingly being recognized in the pathogenesis of brain diseases (2). Though proton-MRS has been used to measure changes in neurotransmitter concentrations in a range of diseases such as psychiatric illnesses, epilepsy, and neurodegenerative disorders, changes in concentrations measured are not specific to the alterations underling metabolic fluxes. Dynamic ^{13}C MRS allows the measurement of metabolic fluxes in humans, and can be used in the study and treatment of brain disease (1). One recent example showed ^{13}C MRS to be sensitive to very early changes in an AD mouse model, when no significant static neurochemical changes were detected with proton-MRS (3). As a result ^{13}C

MRS may potentially provide insights into pathogenesis and effectiveness of treatments for AD. Despite its potential, applications of ^{13}C MRS in the clinical setting to-date has been limited due to the technical challenges involved, such as the requirement for non-standard instrument modifications, and thus has been mostly limited to research environments. The wide use of ^{13}C MRS is further hampered by practical difficulties, such as low sensitivity (relative to proton-MRS), and difficulties associated with metabolite quantification at low field strengths (<=3Tesla) with both direct and indirect ^{13}C MRS methods. Despite challenges associated with the method, many early studies have identified dynamic ^{13}C MRS as an important tool to study brain disease *in vivo*.

The overarching objective of this thesis is to develop novel methods for dynamic *in vivo* carbon-13 (^{13}C) Magnetic Resonance Spectroscopy (MRS) for rodent brain imaging, which can be broken down into the following specific objectives: 1) To develop a novel RF coil platform for ^{13}C MRS in the rat brain that provides optimal sensitivity, and B_1^+ field homogeneity for short echo-time, point resolved spectroscopy (PRESS; 4) localization based proton observed carbon edited (POCE 5,6) MRS; 2) To investigate novel methods for performing indirect ^{13}C MRS with the intention of shortening the echo time of single-shot localization ^{13}C MRS sequences, thus further minimizing signal losses due to T_2 relaxation and homonuclear J-evolution related losses; and finally 3) To investigate the possibility of improving the metabolic modeling process by acquiring direct and indirect ^{13}C MRS during the same session.

1.2 Thesis Outline

This thesis consists of 6 chapters. Chapter 2 provides an introduction to the material covered in the remainder of this thesis, with the goal of filling gaps in the concise introductory material provided in each of the manuscript based chapters. The fundamental concepts that govern magnetic resonance spectroscopy make up a significant portion of this chapter, which extends up to describing POCE (for material in chapter 3, 4, and 5), and polarization transfer experiments (for material in chapter 5). Next a brief section on radiofrequency probes is given (for material in chapter 3). Finally an overview of dynamic *in vivo* ^{13}C MRS is given, describing its capabilities, applications, and limitations. Chapter 3 describes a novel RF coil platform for POCE MRS utilized with a volumetric proton transmitter, which enables the use of PRESS localization with uniform nutation. As part of this work, a PRESS localized POCE sequence was also developed to validate the RF coil platform. Chapter 4 extends the work in chapter 3, where a novel proton observed carbon editing method is presented. The application of simultaneous editing and localization pulses (SEAL) on the PRESS module enables the sequence TE to be reduced to a theoretically optimal value of ~ $1/J_{CH}$. Chapter 5 describes a ^{13}C MRS setup capable of both direct and indirect ^{13}C MRS sequentially during the same scan session. To achieve this feat, the RF coil platform developed in chapter 3 was modified, and a localized direct ^{13}C MRS sequence was implemented.

1.3 Original Contributions

Original contributions that result from this work can be grouped into three parts as per contributions made in Chapter 3, Chapter 4 and Chapter 5 as detailed below:

Chapter 3:

- Design and implementation of a POCE ^{13}C MRS RF coil platform on a Bruker 7T MRI, compatible with heteronuclear decoupling that includes a volumetric ^{1}H transmitter to achieve a homogenous B_1^+ field. To-date, POCE-MRS platforms described in the literature use an all-surface coil approach for rodent imaging. The developed coil platform is the first of its kind for POCE-MRS, providing a homogenous B_1^+ field and highly sensitive receive capabilities due to the use of a Receive-only ^{1}H surface coil.

- A 12.6-ms PRESS localized POCE sequence was designed, implemented, and optimized for the developed coil platform on a Bruker 7T animal MRI. The implemented PRESS-POCE sequence, at the time of publication, had the lowest TE for a PRESS localized POCE sequence reported in the literature. The PRESS-localized POCE MRS sequence provides single-shot localization, and was realized with short conventional pulses, thus enabling uniform nutation combined with a short-TE; a feat that cannot be achieved with an all-surface coil based POCE-MRS coil platform.
- A high pass filter based on a 7th order Chebyshev filter design was designed and implemented. The developed filter provides >90dB of attenuation at 75 MHz (the ^{13}C frequency), and <-0.4dB attenuation at 300 MHz (the ^{1}H frequency). The novelty of the filter lies in its ability to absorb 75 MHz RF content; a classical highpass filters would reflect ^{13}C frequency RF content back to the ^{1}H Receive-only coil, which is minimized with this design. The design of absorptive RF filters is not novel; it is widely adopted and advertised by RF filter manufactures; however various manufactures claim their absorption filter technology to be proprietary and is not disclosed to the public. In this work we describe an approach to realizing an absorptive filter for a dual RF channel application (^{1}H and ^{13}C frequencies), and demonstrate that it works on the bench and in the magnet reliably (for the past 3 years and counting).

Chapter 4:

- A novel carbon editing method that employs Simultaneous Editing and Localization on both PRESS refocusing pulses (we named it SEAL-PRESS) was developed on a Bruker 7T animal MRI. The simultaneous use of editing and slice-selective refocusing pulses in both refocusing pulse directions made it possible to reduce the sequence TE to approach the theoretical minimum of $1/J_{HC}$ ms with full-intensity editing efficiency. The 8.1-ms TE SEAL-PRESS sequence reported in this work, achieves the shortest TE for within sequence edited POCE-MRS sequences reported in the literature with the additional benefit of single-shot localization.
- In simulation and in phantom experiments, inhibition of heteronuclear J-evolution was observed due to the use of non-selective RF pulses in the SEAL-PRESS sequence during the EDIT-ON scan. The theoretical framework for carbon editing (for SEAL-PRESS) was derived using the quantum mechanical density matrix formalism, and was extended to postulate the mechanism for the inhibition of heteronuclear J-evolution to manifest from double quantum coherence states that arise from anti-phase coherence terms during non-instantaneous rotations during non-selective RF pulses.

Chapter 5:

- As part of this work, a device that combines the Tx and Rx lines of a quadrature hybrid (termed the ‘quadrature hybrid combiner’) was designed in-house and implemented by Stark Industries for a Bruker 7T MRI. In the event that the output from the MRI system console is a single Tx/Rx port, and if a quadrature driven RF coil is to be used, the MRI and RF coil can be interfaced using the presented quadrature hybrid combiner.

- To the best of our knowledge, we report the first description of a PRESS-localized semi-adiabatic DEPT sequence. The development of PRESS-DEPT was previously reported (7), and the development of a ISIS localized semi-adiabatic DEPT sequence was previously reported (8). In this work PRESS localization provides single-shot localization, while the semi-adiabatic DEPT sequence utilizing a segmented BIR-4 pulse provides field insensitive rotations when surface coil transmitters are used on the ^{13}C channel. The PRESS-DEPT sequence was also implemented on a Bruker 7T MRI scanner.

1.4 Author Contributions

I am first author on all three manuscript based chapters (Chapter 3- 5) in this thesis, and I performed all the methodological developments, experimental design and analysis of all experiments. Contributions from all co-authors include: supervision, animal preparation and handling, 3D printing, and the review of manuscripts. Below, is a list summarizing co-author contributions for each chapter:

Chapter 3: *In vivo* proton observed carbon edited (POCE) 13C Magnetic Resonance Spectroscopy of the rat brain using a volumetric Transmitter and Receive-only surface coil on the proton channel (published- Kumaragamage C. et al, *MRM;* 79, pp 628-635, 2018)

Authors: C. Kumaragamage, D. Madularu, A. Mathieu, H. De Feyter, N. Rajah, J. Near

Guarantors of the study: All authors; study concepts and design: CK, JN; Radiofrequency coil and RF chain hardware design: CK; RF coil former and bed design: AM, CK; pulse sequence design: CK; pulse sequence optimization: CK, JN; Animal handling and animal preparation: CK, DM; Bruker console support: AM; Dynamic ^{13}C MRS experiment support: HDF; Data analysis and processing: CK, Funding support: NR, JN; manuscript preparation: CK; manuscript revision: CK, DM, AM, HDF, NR, JN; editing and final version approval: CK, DM, JN.

Chapter 4: Minimum echo time PRESS-based proton observed carbon edited (POCE) magnetic resonance spectroscopy in the rat brain using simultaneous editing and localization (published- Kumaragamage C. et al, *MRM;* 80 (4) pp 1279-1288, 2018)

Authors: C. Kumaragamage, D. Madularu, A. Mathieu, D. Lupinsky, R de Graaf, J. Near

Guarantors of the study: All authors; study concepts and design: CK, JN; Related density matrix simulation: CK; pulse sequence design and optimization: CK; Animal handling and animal preparation: CK, DM, DL; Bruker console support: AM; Heteronuclear decoupling scheme: RdG; Data analysis and processing: CK, Funding support: JN; manuscript preparation: CK; manuscript revision: CK, RdG, JN; editing and final version approval: CK, JN.

Chapter 5: Simultaneous direct and indirect ^{13}C MRS during dynamic *in vivo* rat brain imaging (unpublished at this time)

Authors: C. Kumaragamage, D. Madularu, A. Mathieu, J. Near

Guarantors of the study: All authors; study concepts and design: CK, JN; Radiofrequency chain modifications and testing: CK; pulse sequence design and optimization: CK; Animal handling and animal preparation: CK, DM; Bruker console support: AM; Data analysis and processing: CK, Funding support: JN; manuscript preparation: CK; manuscript revision: CK, JN.

1.5 References

1. Rothman DL, De Feyter HM, de Graaf RA, Mason GF, Behar KL. 13C MRS studies of neuroenergetics and neurotransmitter cycling in humans. NMR in biomedicine 2011;24(8):943-957.
2. de Graaf RA, Mason GF, Patel AB, Behar KL, Rothman DL. In vivo 1H-[13C]-NMR spectroscopy of cerebral metabolism. NMR in biomedicine 2003;16(6-7):339-357.
3. Tiwari V, Patel AB. Impaired glutamatergic and GABAergic function at early age in AbetaPPswe-PS1dE9 mice: implications for Alzheimer's disease. Journal of Alzheimer's disease : JAD 2012;28(4):765-769.
4. Bottomley PA. Spatial localization in NMR spectroscopy in vivo. Annals of the New York Academy of Sciences 1987;508:333-348.
5. Fitzpatrick SM, Hetherington HP, Behar KL, Shulman RG. The flux from glucose to glutamate in the rat brain in vivo as determined by 1H-observed, 13C-edited NMR spectroscopy. Journal of cerebral blood flow and metabolism : official journal of the International Society of Cerebral Blood Flow and Metabolism 1990;10(2):170-179.
6. Rothman DL, Howseman AM, Graham GD, Petroff OA, Lantos G, Fayad PB, Brass LM, Shulman GI, Shulman RG, Prichard JW. Localized proton NMR observation of [3-13C]lactate in stroke after [1-13C]glucose infusion. Magnetic resonance in medicine 1991;21(2):302-307.
7. Yahya A, Allen PS. Effect of strong homonuclear proton coupling on localized (13)C detection using PRESS. Magnetic resonance in medicine 2005;54(6):1340-1350.

8. Henry PG, Tkac I, Gruetter R. 1H-localized broadband 13C NMR spectroscopy of the rat brain in vivo at 9.4 T. Magnetic resonance in medicine 2003;50(4):684-692.

Chapter 2

Fundamentals of Magnetic Resonance Spectroscopy

2.1 The Nuclear Magnetic Resonance Phenomenon

The *nuclear magnetic resonance* (NMR) phenomenon is caused by the interaction of a particle with an external magnetic field, which was first described and discovered by Isidor Rabi in 1937 (1) who won the Nobel Prize in physics in 1944 for his pioneering work. In 1946, Bloch, Hansen, and Packard at Stanford University (2), and Purcell, Torrey, and Pound at MIT (3), simultaneously expanded on the technique for liquids and solids, which we now call NMR, for which Bloch and Purcell shared the Nobel Prize in physics in 1952. At this time, however NMR was purely an experimental apparatus to characterize nuclear magnetic moments of nuclei in a magnetic field. The phenomenon of *chemical shift*, or the difference in resonant frequencies of the same nuclear type in different chemical environments was a turning point in NMR, which was described by Proctor and Yu (4) and Dickinson (5) independently in 1950. These discoveries led to a barrage of applications in chemistry early on, and to the first reports of NMR spectroscopy experiments on intact living tissue in the early 1970s (6,7); however the first reports of ^{1}H NMR spectra were delayed by a further decade due to technical difficulties related to water suppression, lipid suppression and localization. In 1983 Behar et. al reported the first ^{1}H MR spectrum in rat brain (8), and in 1985 Bottomley (9) reported the first ^{1}H MR spectrum in human brain. Since its humble inception, MR Spectroscopy (MRS) has grown substantially, though for most of its life-time has been overshadowed by its celebrated younger sibling- MRI, and today MRS is a powerful tool that is used to study static and dynamic aspects of metabolism *in vivo* non-invasively.

2.2 The Classical Description of NMR

To-date, the quantum mechanical treatment provides the most accurate description of NMR. However, the classical description can provide a simpler and intuitive picture of the system in the macroscopic scale, with which we will begin this chapter.

2.2.1 The Magnetic Moment

Orbital angular momentum ($\boldsymbol{L}$) is given by the following relation $\boldsymbol{L} = \boldsymbol{r} \times \boldsymbol{p}$, where $\boldsymbol{p}$ is the linear angular momentum of an orbiting body, and $\boldsymbol{r}$ is the orbital radius. In contrast, the *intrinsic spin angular momentum* ($\boldsymbol{S}$) property of a particle, is not the same type as orbital angular momentum, yet it turns out to be a real form of angular momentum. A classical example can be used to partially understand the relationship between angular momentum of a charged particle, and its corresponding *magnetic moment* ($\boldsymbol{\mu}$).

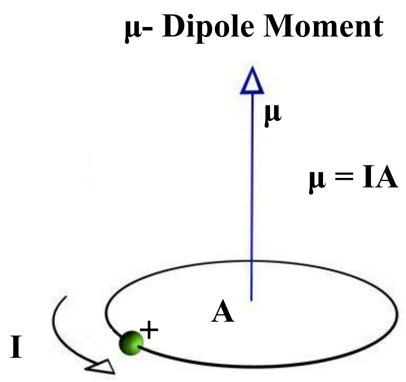

Figure 2-1 *Magnetic moment and orbital angular momentum.*

Consider a particle with charge q and mass m in circular motion with radius r, at speed v (see Figure 2.1); the magnetic moment μ of this charged particle is $\mu = IA$, where I is the current and A is the area of the circle with radius r. The relationship between the magnetic moment and angular momentum of the charged particle is as follows:

$$\mu = IA = \frac{q}{(2\pi r/v)}\pi r^2 = \frac{q}{2}rv = \frac{q}{2m}L \tag{2-1}$$

And since the orbital angular momentum and magnetic moment vectors are parallel/antiparallel based on the sign on charge q, Eq. 2-1 can be expressed in vector form

$$\boldsymbol{\mu} = \frac{q}{2m}\boldsymbol{L} \tag{2-2}$$

The relationship between the intrinsic spin angular momentum and observable magnetic moment of a particle is written as

$$\boldsymbol{\mu} = g\frac{q}{2m}\boldsymbol{S} = \gamma\boldsymbol{S} \tag{2-3}$$

where g is a constant (g-factor) with values $g = 5.6$ for a proton, $g = 2.0$ for an electron, and $g = -3.8$ for a neutron; and γ is the classical gyromagnetic ratio.

2.2.2 The Larmor Theorem

The Larmor theorem states that the motion of the magnet moment $\boldsymbol{\mu}$ in a magnetic field $\boldsymbol{B_0}$ (herein referred to as the static magnetic field of the MRI system) is a precession around the field. Based on several theorems in classical mechanics, the following can then be stated:

1) The energy of the magnetic moment in the $\boldsymbol{B_0}$ field is:

$$E = -\boldsymbol{\mu} \cdot \boldsymbol{B_0} \qquad \text{(2-4)}$$

Classically, Eq. 2-4 above can be written with the substitution $\mu_z = |\boldsymbol{\mu}| cos\theta$, where θ is the angle between magnetic moment $\boldsymbol{\mu}$ and z-axis (the magnetic field $\boldsymbol{B_0}$ in this context is by convention chosen to lie along the *z* direction). However, the scalar form above suggest that the energy (E) of a classical magnetic moment can take any continuous value corresponding to $0 \leq \theta \leq 180$ with energy varying from $+\mu \cdot B_0$ and $-\mu \cdot B_0$. It is at this point the classical description begins to break down, as demonstrated by the famous Stern-Gerlach experiment (10) demonstrating the revolutionary result that μ_z takes on only two values for spin ½ particles; we shall return to this topic in the quantum description of NMR section later.

2) The magnetic moment experiences a torque $\boldsymbol{C}$:

$$\boldsymbol{C} = \boldsymbol{\mu} \times \boldsymbol{B_0} \qquad \text{(2-5)}$$

3) And since the torque ($\boldsymbol{C}$) is equal to the time-derivative of the angular momentum ($\boldsymbol{L}$) the following can be deduced:

$$\boldsymbol{C} = \frac{d\boldsymbol{L}}{dt} = \frac{1}{\gamma}\frac{d\boldsymbol{\mu}}{dt} = \boldsymbol{\mu} \times \boldsymbol{B_0} \qquad \text{(2-6)}$$

Eq. 2.6 can then be rearranged to:

$$\frac{d\boldsymbol{\mu}}{dt} = \gamma \cdot (\boldsymbol{\mu} \times \boldsymbol{B_0}) \qquad (2\text{-}7)$$

Solving the first order differential equation in Eq. 2-7 describes the precession of $\boldsymbol{\mu}$ around $\boldsymbol{B_0}$ at a rate of $\gamma\boldsymbol{B_0}$; thus can be summarized by the famous Larmor equation:

$$\boldsymbol{\omega_0} = -\gamma\, \boldsymbol{B_0} \qquad (2\text{-}8)$$

where $\boldsymbol{\omega_0}$ is the so-called Larmor frequency; the rotational (precession) frequency of the magnetic moment $\boldsymbol{\mu}$ about $\boldsymbol{B_0}$.

Even though the classical description can be used to formulate the magnetic moment, angular momentum and Larmor relation, it cannot explain the fundamental resonance condition for spectroscopy $\Delta E = \hbar\omega$, which relates energy associated with the magnetic moment. Furthermore, when describing coupled spin systems, to some extent, a classical vector diagram picture can be used to visualize up to anti-phase coherence states (described later), however there is no classical analog that can be used to describe time-evolution of multiple quantum coherence states that arise in certain NMR pulse sequences (including some that will be described later in this thesis, such as the DEPT sequence). Therefore resorting to the quantum mechanical treatment is necessary, as it provides the most complete description of NMR to-date.

2.3 The Quantum Mechanical Description of NMR

In the previous subsection the discussion was abruptly terminated with the experimental results of the Stern-Garlach experiment, which showed that μ_z following Eq. 2-4 cannot take on a continuum of values; instead based on the fundamental postulates of quantum mechanics, μ_z is limited to a set of discrete values as the z component of the intrinsic angular momentum $\boldsymbol{S}$ can take on the values $m_z\hbar$ with $-I \leq m_z \leq I$, where $|\boldsymbol{S}| = \frac{h}{2\pi}\sqrt{I(I+1)}$. In this thesis, the quantum mechanical treatment is limited to spin ½ particles such as ^{1}H and ^{13}C nuclei, such that $I = 1/2$, and $m_z = 1/2$ (α-state) and $m_z = -1/2$ (β-state).

Eq. 2-3 then will be

$$\mu_z = \gamma S_z = \gamma m_z \hbar \tag{2-9}$$

In the presence of an external magnetic field $\boldsymbol{B_0}$, the discrete energy levels of a spin ½ particle from Eq. 2-4 becomes:

$$E_m = -(\gamma m_z \hbar) B_0 \tag{2-10}$$

Then $E_\alpha = -\frac{1}{2}(\gamma\hbar)B_0$, and $E_\beta = \frac{1}{2}(\gamma\hbar)B_0$

and since the energy levels are also quantized, the energy difference ΔE is given by:

$$\Delta E_{\alpha\rightarrow\beta} = E_\beta - E_\alpha = \gamma\hbar B_0 \tag{2-11}$$

This non-zero difference in energy between the two spin-states is known as the *Zeeman splitting* phenomenon as illustrated in Figure. 2-2 below.

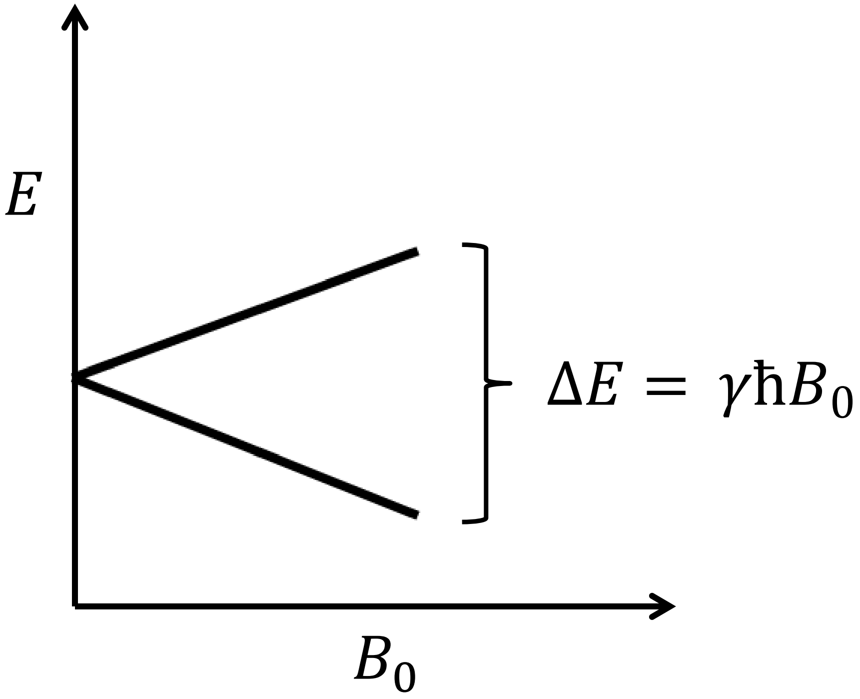

Figure 2-2 *Zeeman splitting of a spin ½ particle in the presence of a B_0 magnetic field.*

2.3.1 The Density Matrix, Boltzmann Distribution and Macroscopic Magnetization

Thus far we only described the spin states of individual spin ½ particles, which can be elegantly represented in the bra-ket form as described below:

$$|\Psi> = c_\alpha|\alpha> + c_\beta|\beta> \qquad (2\text{-}12)$$

where $|\Psi>$ is the wavefunction describing the ½ particle in a superposition of its two *Zeeman eigenstates* $|\alpha>$ (corresponding to the α state), and $|\beta>$ (corresponding to the β state) with probability amplitude values c_α and c_β, respectively, where$|c_\alpha|^2 + |c_\beta|^2 = 1$, and $|c_\alpha|^2$ corresponds to the probability of observing the $|\alpha>$ state, similarly and $|c_\beta|^2$ corresponds to the probability of observing the $|\beta>$ state.

Now let us consider an ensemble of spin ½ particles on the order of Avogadro's number ($\sim 10^{23}$), such as protons (^{1}H nuclei) in water. At a given moment in time each of the protons will have a different polarization state according to Eq. 2-12 with varying values of $c_\alpha$and c_β. The net nuclear magnetization will then be the summation of contribution from all spins. An elegant method called the *density operator* can be used to describe the quantum state of an ensemble of spins without referring to individual spin states; a central tool used for the description of NMR. The density operator $\hat{\rho}$ is defined as

$$\hat{\rho} = \overline{|\Psi><\Psi|} \qquad (2\text{-}13)$$

Where the overbar indicates taking the ensemble average, and $|\Psi>$ is as defined in Eq. 2-12. In this case now the complete density matrix representation for an ensemble of non-interacting spin ½ particles is given by:

$$\hat{\rho} = \begin{pmatrix} \rho_{\alpha\alpha} & \rho_{\alpha\beta} \\ \rho_{\beta\alpha} & \rho_{\beta\beta} \end{pmatrix} = \begin{pmatrix} \overline{c_\alpha c_\alpha^*} & \overline{c_\alpha c_\beta^*} \\ \overline{c_\beta c_\alpha^*} & \overline{c_\beta c_\beta^*} \end{pmatrix} \tag{2-14}$$

Here the *diagonal* elements of the density operator $\rho_{\alpha\alpha}$ and $\rho_{\beta\beta}$ are called *populations* of states $|\alpha >$ and $|\beta >$. The *off-diagonal* elements $\rho_{\alpha\beta}$ and $\rho_{\beta\alpha}$ are called *coherences* between $|\alpha >$ and $|\beta >$ states. Note that $\overline{c_\alpha c_\alpha^*}$ is the ensemble average of $c_\alpha c_\alpha^*$ contributions from all spins and then on measurement, $N\overline{c_\alpha c_\alpha^*}$ will be the number of spins in the $|\alpha >$ state, which shall be denoted n_α, and similarly $n_\beta = N\overline{c_\beta c_\beta^*}$.

The most convenient feature of the density operator is we can now compute the net magnetization of the ensemble of spins directly from the matrix form of the operator. For example, the *z*-magnetization is given by

$$M_z = \frac{1}{2}\gamma\hbar N(\rho_{11} - \rho_{22}) = \frac{1}{2}\gamma\hbar(n_\alpha - n_\beta) \tag{2-15}$$

Eq. 2-15 shows that the net *z*-magnetization is described by the population differences between the $|\alpha >$ and $|\beta >$ energy levels. At equilibrium, the populations n_α, and n_β are described by the *Boltzmann distribution* as follows:

$$n_{\alpha,eq} = \frac{1}{2}Nexp\left(-\frac{E_\alpha}{k_B T}\right), \quad n_{\beta,eq} = \frac{1}{2}Nexp\left(-\frac{E_\beta}{k_B T}\right) \tag{2-16}$$

where k_B is the Boltzmann's constant, T is the temperature in Kelvin, and N is the total number of spins. For spins with $\gamma > 0$, the $|\alpha >$ state has the lower energy, thus $n_{\alpha,eq} > n_{\beta,eq}$ and the sample will have a net magnetization in the *z*-direction. Since $\boldsymbol{M_0}$ is the net magnetization from the ensemble of spins:

$$\boldsymbol{M_0} = \sum_{i=1}^{N} \boldsymbol{\mu_i} \tag{2-17}$$

Then from Eqs. 2-15, 2-16, and 2-17 the amplitude of the net magnetization can be expressed to be:

$$M_0 = \frac{1}{2}\gamma\hbar\left(n_{\alpha,eq} - n_{\beta,eq}\right) = \frac{1}{4}\gamma N\hbar[exp\left(-\frac{E_\alpha}{k_B T}\right) - exp\left(-\frac{E_\beta}{k_B T}\right)] \qquad (2\text{-}18)$$

Recalling the energies $E_\alpha$and E_β from Eq. 2-10, and since $E_m \ll k_B T$ the exponential terms in Eq. 2-18 can be expressed as its truncated Taylor series as follows:

$$\Delta n = n_{\alpha,eq} - n_{\beta,eq} \cong \frac{N\gamma\hbar B_0}{2k_B T} \qquad (2\text{-}19)$$

Finally from Eq. 2-9, 2-18, and 2-19 the amplitude of the net magnetization $\boldsymbol{M_0}$ at thermal equilibrium is:

$$M_0 = \frac{1}{2}\gamma\hbar\left(n_{\alpha,eq} - n_{\beta,eq}\right) = \left(\gamma^2\hbar^2\right)\frac{NB_0}{4k_B T} \qquad (2\text{-}20)$$

Eq. 2-20 reveals a few aspects concerning the sensitivity of the NMR experiment, which is dependent on $\boldsymbol{M_0}$: 1) $\boldsymbol{M_0}$ has a quadratic dependence on the gyromagnetic ratio; proton spins (^{1}H) have the highest γ of all NMR observable nuclei and are the highest density nuclei encountered in tissue; thus conveniently provides the highest sensitivity. 2) $\boldsymbol{M_0}$ has a linear dependence with the static magnetic field strength $\boldsymbol{B_0}$, thus explains the drive towards higher $\boldsymbol{B_0}$ field strengths for research and ultimately the clinical setting. 3) $\boldsymbol{M_0}$ has a linear dependence with the number of nuclei (N) in the region imaged; this fact is intuitive- more protons equals more signal! 4) $\boldsymbol{M_0}$ is inversely dependent on the temperature of the sample; however for *in vivo* experiments, there is not much that can be done on this regard. Though the above statements stand true, the sensitivity during an actual experiment will be further governed by other factors such as $\boldsymbol{B_0}$ homogeneity, susceptibility effects, sample and systematic noise, relaxation properties of different tissue types, natural abundance of the nucleus studied, etc; some of these factors will be elaborated later in this chapter.

2.3.2 The Bloch Equations

The previous section described isolated spins, and was extended to an ensemble of isolated spins. These spins are embedded in a medium of condensed matter, historically termed the *lattice*, and are in constant interaction (coupling) with the medium or lattice. This interaction, termed *spin-lattice* coupling, tends to evolve the ensemble of spins and the lattice towards common thermal equilibrium. Starting with the case where the ensemble of spins is placed in a static magnetic field $\boldsymbol{B_0}$ and in thermal equilibrium; the time-varying net magnetization $\boldsymbol{M}(t) = \boldsymbol{M_0}$ will have acquired a longitudinal (*z*-direction) net magnetization M_z with non-zero value M_0 (as described in Eq. 2-20), and vanishing transverse magnetization (in the *x-y* plane). When $\boldsymbol{M_0}$ is perturbed (by the application of an RF pulse described later that elicits a rotation of $\boldsymbol{M_0}$) away from the longitudinal axis, evolution of the *z*-component of $\boldsymbol{M}(t)$ towards $\boldsymbol{M_0}$, alters the energy of the spin system, corresponding to an energy exchange with the lattice; in contrast, a decrease of transverse magnetization $M_{x,y}$ (where $M_{x,y} = M_x + iM_y$) does not produce such an energy exchange. The evolution of a perturbed spin system towards equilibrium is called *relaxation* with two different time constants: T_1 for relaxation in the longitudinal direction termed *spin-lattice* relaxation, and T_2 for relaxation of the transverse component termed *spin-spin* relaxation. These relaxation relationships with magnetization can be summarized as follows:

$$\frac{dM_z}{dt} = -\frac{(M_z - M_0)}{T_1} \tag{2-21}$$

$$\frac{dM_{x,y}}{dt} = -\frac{M_{x,y}}{T_2} \tag{2-22}$$

Eq. 2-7 can be extended for the net magnetization $\boldsymbol{M}$ from Eq. 2.17 to:

$$\frac{d\boldsymbol{M}}{dt} = \gamma \cdot \boldsymbol{M} \times \boldsymbol{B} \tag{2-23}$$

Combining the evolution term from the Larmor theorem in Eq. 2-23 to the relaxation terms above, produces the renowned Bloch equations:

$$\frac{d\boldsymbol{M}}{dt} = \gamma \boldsymbol{M} \times \boldsymbol{B} - \frac{M_x\vec{\imath} + M_y\vec{\jmath}}{T_2} - \frac{(M_z - M_0)\vec{k}}{T_1} \tag{2-24}$$

Where M_x, M_y, M_z are the x, y, and z magnitude components of $\boldsymbol{M}(t)$, respectively such that:

$$\boldsymbol{M} \triangleq M_x\vec{\imath} + M_y\vec{\jmath} + M_z\vec{k} \tag{2-25}$$

It is convenient to rewrite the Bloch equations in the rotating frame. But first, a few things need to be defined: a linearly polarized RF field along the *x*-axis will take the following form:

$$\boldsymbol{B_1}(t) = 2B_{1,max}\cos(\omega t + \varphi)\vec{\imath} \tag{2-26}$$

where ω and φ are the frequency and phase of the applied oscillating RF field superimposed on the longitudinal field $\boldsymbol{B_0}$ [such that $\boldsymbol{B}(t) = \boldsymbol{B_0} + \boldsymbol{B_1}(t)$]. For simplicity, we assume $\varphi = 0$. The linearly polarized field can be decomposed into two circularly polarized fields rotating in opposite directions ($\pm\,\boldsymbol{\omega}$) as follows (also illustrated in Figure. 2-3) starting from Eq. 2-26:

$$\boldsymbol{B_1}(t) = B_{1,max}\,[\cos(\omega t)\,\vec{\imath} + \sin(\omega t)\,\vec{\jmath}\,] + B_{1,max}\,[\cos(\omega t)\,\vec{\imath} - \sin(\omega t)\,\vec{\jmath}\,] \tag{2-27}$$

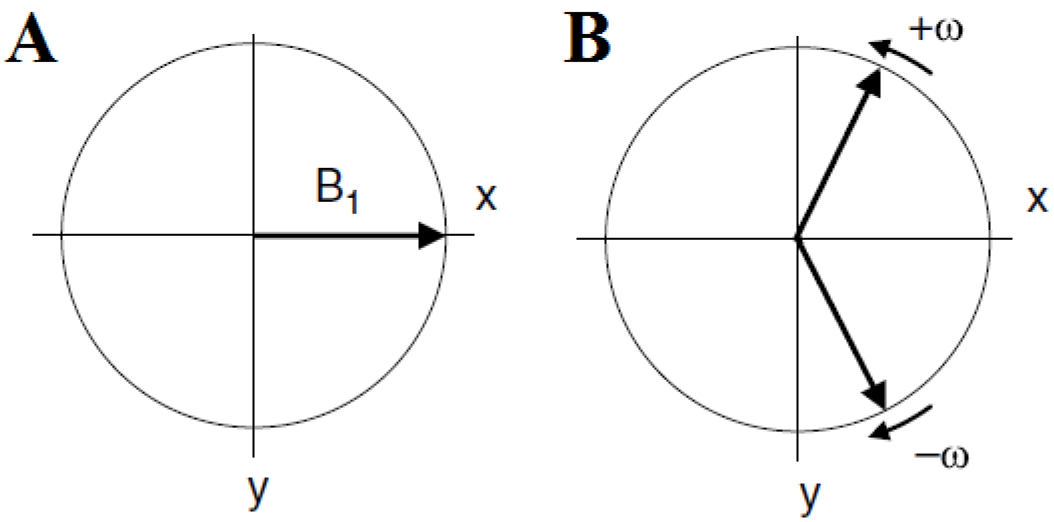

Figure 2-3 *(A) Linearly polarized RF field and (B) its decomposed polarized RF fields (the amplitude of the vectors are not to scale).*

When considering this decomposed circularly polarized RF fields, only the component rotating in the direction of the net magnetization $\boldsymbol{M}$ interacts, the second circularly polarized component is far off in resonance thus has negligible effects on $\boldsymbol{M}$ and can be ignored.

The relevant $\boldsymbol{B_1}$ field is then given by:

$$\boldsymbol{B_1}(t) = B_{1,max}\,[\cos(\omega t)\,\vec{\imath} - \sin(\omega t)\,\vec{\jmath}\,] \qquad (2\text{-}28)$$

Now consider a new coordinate system (*x', y', z'*) rotating about the static $\boldsymbol{B_0}$ field at frequency ω chosen to be the frequency of the oscillating RF field, where *z'* and *z* axes are collinear with $\boldsymbol{B_0}$. Next let us define the net magnetization in the rotating frame ($\boldsymbol{M}_{rot}$) following:

$$\boldsymbol{M}_{rot} \triangleq M_{x'}\vec{\imath}' + M_{y'}\vec{\jmath}' + M_{z'}\vec{k}' \qquad (2\text{-}29)$$

which can be related to $\boldsymbol{M}$ by the following rotation matrix form:

$$\begin{bmatrix} M_{x'} \\ M_{y'} \\ M_{z'} \end{bmatrix} = \begin{bmatrix} \cos(\omega t) & -\sin(\omega t) & 0 \\ \sin(\omega t) & \cos(\omega t) & 0 \\ 0 & 0 & 1 \end{bmatrix} \begin{bmatrix} M_x \\ M_y \\ M_z \end{bmatrix} \tag{2-30}$$

Differentiating both sides of Eq. 2-29 with respect to time yields the following:

$$\frac{d\boldsymbol{M}}{dt} = \frac{\partial \boldsymbol{M}_{rot}}{\partial t} + \boldsymbol{\omega} \times \boldsymbol{M}_{rot} \tag{2-31}$$

where $\frac{\partial \boldsymbol{M}_{rot}}{\partial t}$ is the rate of change of $\boldsymbol{M}$ as observed in the rotating frame. During an RF pulse, which typically has a duration much shorter than T_1 and T_2, the Bloch equation Eq. 2-24 then takes a simpler form $\frac{d\boldsymbol{M}}{dt} = \gamma \cdot \boldsymbol{M} \times \boldsymbol{B}$ which can be expressed in the rotating frame and substitution into Eq. 2-31:

$$\begin{aligned} \frac{\partial \boldsymbol{M}_{rot}}{\partial t} &= \gamma \cdot \boldsymbol{M}_{rot} \times \boldsymbol{B}_{rot} - \boldsymbol{\omega} \times \boldsymbol{M}_{rot} \\ &= \gamma \cdot \boldsymbol{M}_{rot} \times (\boldsymbol{B}_{rot} + \frac{\boldsymbol{\omega}}{\gamma}) \end{aligned} \tag{2-32}$$

Eq. 2-32 can now be rewritten as:

$$\frac{\partial \boldsymbol{M}_{rot}}{\partial t} = \gamma \cdot \boldsymbol{M}_{rot} \times (\boldsymbol{B}_{eff}) \tag{2-33}$$

where $\boldsymbol{B}_{eff} = \boldsymbol{B}_{rot} + \frac{\boldsymbol{\omega}}{\gamma}$ represents the effective magnetic field that interacts with the net magnetization $\boldsymbol{M}_{rot}$ in the rotating frame. The second term $\frac{\boldsymbol{\omega}}{\gamma}$ represents a fictitious field component. To visualize the behavior of the fictitious field, let $\boldsymbol{B} = B_0\vec{k}$, $\boldsymbol{\omega_0} = -\gamma B_0\vec{k}$.

$$\boldsymbol{B}_{eff} = \boldsymbol{B}_{rot} - \frac{\gamma B_0 \vec{k}}{\gamma} = \frac{\boldsymbol{\omega_0} - \boldsymbol{\omega}}{\gamma} \tag{2-34}$$

When $\boldsymbol{\omega} = -\gamma B_0 \vec{k}$, from Eq. 2-34 the apparent longitudinal magnetic field vanishes and from Eq. 2-33 $\boldsymbol{M}_{rot}$ appears to be stationary in the rotating frame as expected.

As defined before, if the rotating frame rotates with the frequency of the RF pulse, in this rotating frame $\boldsymbol{B}_1^e$ appears static along the *x'*-axis (see Eq. 2-28). The total effective magnetic field $\boldsymbol{B}_{eff}$ is computed in the presence of the $\boldsymbol{B}_1$ field will then be:

$$\boldsymbol{B}_{eff} = \boldsymbol{B}_1^e \vec{\imath'} + \frac{(\omega_0 - \omega)}{\gamma} \vec{k'} \tag{2-35}$$

and the magnitude of $\boldsymbol{B}_{eff}$ is given by:

$$B_{eff} = |\boldsymbol{B}_{eff}| = \sqrt{\boldsymbol{B}_1{}^2 + \left[\frac{\omega_0 - \omega}{\gamma}\right]^2} \tag{2-36}$$

When the on-resonance condition is satisfied (the applied RF frequency equals the Larmor frequency ω_0), Eq. 2-36 reduces to $\boldsymbol{B}_{eff} = \boldsymbol{B}_1$. A visual description of the on-resonance condition is summarized in Figure. 2-4: the first illustration traces the evolution of the net magnetization $\boldsymbol{M}$ in the laboratory frame of reference during a RF pulse $\boldsymbol{B}_1(t)$, and the second illustration demonstrates the evolution of $\boldsymbol{M}$ in the same scenario in the rotating frame of reference. Here the on-resonance condition is assumed, where $\boldsymbol{B}_{eff} = \boldsymbol{B}_1$, which is stationary along the *x'*-axis, and since $\boldsymbol{\omega}_0 - \boldsymbol{\omega} = \boldsymbol{0}$, the longitudinal component vanishes as per Eq. 2-35. From Eq. 2-23 it is apparent that $\boldsymbol{M}$ precesses about the *x'*-axis, with angular velocity $\boldsymbol{\omega}_1$ as show in in Figure 2-4, where

$$\boldsymbol{\omega}_1 = -\gamma \boldsymbol{B}_1 \tag{2-37}$$

In a situation where the on-resonance condition is not met $(\boldsymbol{\omega_0} - \boldsymbol{\omega} \neq \mathbf{0})$, from Eq. 2-35 we see that $\boldsymbol{B_{eff}}$ is no longer collinear with $\boldsymbol{B_1^e}$ and rotation of the magnetization vector around $\boldsymbol{B_{eff}}$ follows a more complex trajectory; an important aspect related to broadband RF pulse design.

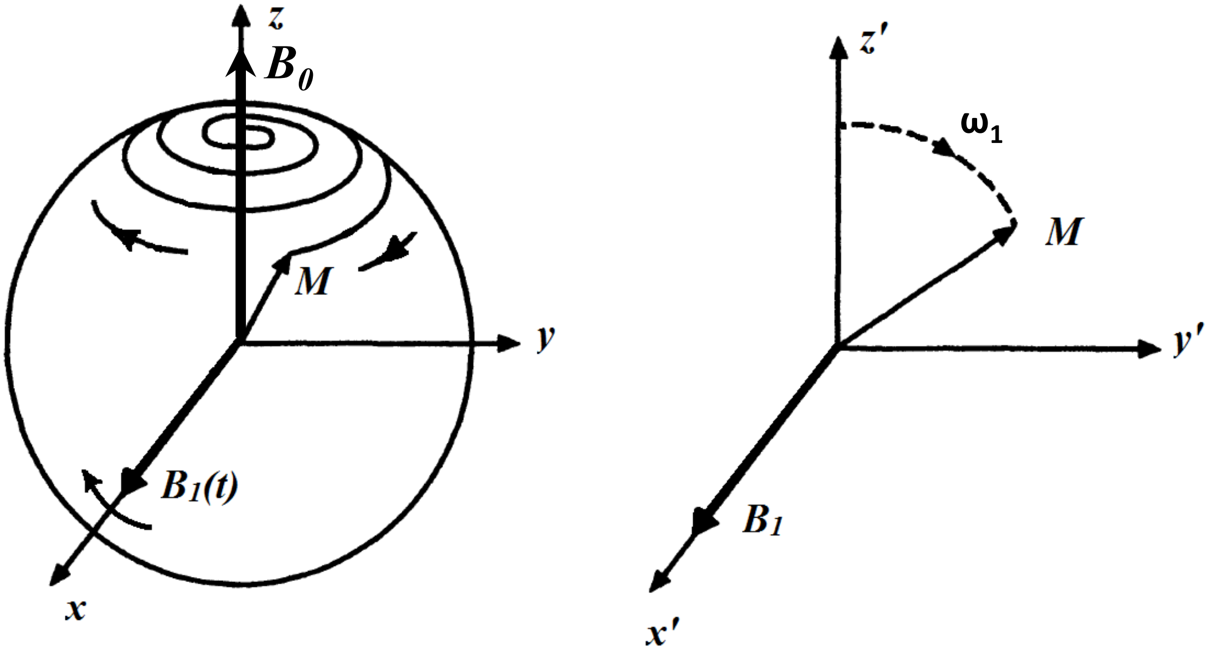

Figure 2-4 *Motion of the net magnetization in the presence of a RF field in the laboratory frame (left), and rotating frame of reference (right).*

2.3.3 Free Precession, Relaxation and Signal Detection

The previous section described the motion of the net magnetization due to an applied RF $\boldsymbol{B_1}$ field in the presence of a static $\boldsymbol{B_0}$ field along the longitudinal axis. After the equilibrium magnetization $\boldsymbol{M_0}$ is perturbed away from the longitudinal axis, it will return back to thermal equilibrium via a process called relaxation as we briefly described before. This process is characterized by the precession of $\boldsymbol{M}$ about the static $\boldsymbol{B_0}$ field termed *free precession*. The two relaxation processes, longitudinal and transverse, can be described by a first-order process; in the rotating frame of reference Eq. 2-21 and Eq. 2-22 can be written as follows:

$$\frac{dM_{z\prime}}{dt} = -\frac{(M_{z\prime} - M_0)}{T_1} \tag{2-38}$$

$$\frac{dM_{x\prime,y\prime}}{dt} = -\frac{M_{x,\prime y\prime}}{T_2} \tag{2-39}$$

Solving Eq. 2-38 and 2-39 provides the time evolution for the transverse and longitudinal components of the magnetization as follows:

$$M_{z'}(t) = M_0\left[1 - \exp\left(-\frac{t}{T_1}\right)\right] + M_{z'}(0_+)\exp\left(-\frac{t}{T_1}\right) \tag{2-40}$$

$$M_{x',y'}(t) = M_{x',y'}(0_+)\ \exp\left(-\frac{t}{T_2}\right) \tag{2-41}$$

Where 0_+ refers to the time point just after the RF pulse was applied in the cases for transverse and longitudinal magnetization, and both types of relaxation follow an exponential function. The above exponential decay functions are described in the rotating frame of reference, which can be expressed in the laboratory frame by combining free precession and relaxation components:

$$M_z(t) = M_0\left[1 - \exp\left(-\frac{t}{T_1}\right)\right] + M_z(0_+)\exp\left(-\frac{t}{T_1}\right) \tag{2-42}$$

$$M_{x,y}(t) = M_{x,y}(0_+)\ \exp\left(-\frac{t}{T_2}\right)\exp(-i\omega_0 t) \tag{2-43}$$

where $M_{x',y'}(t) = M_{x,y}(t)\exp(i\omega t)$ is substituted into Eq. 2-43.

From the above description, placing a sample containing an ensemble of spin ½ particles in an magnetic field $\boldsymbol{B_0}$ and exciting the system with a transient oscillating magnetic field $\boldsymbol{B_1}(t)$, a macroscopic rotating magnetization vector $M_{x,y}(t)$ can be generated. If a conductive loop is now placed in the vicinity of the sample, this $M_{x,y}(t)$ magnetization leads to an NMR signal corresponding to the resonant frequency detected via an electromotive force (voltage) induced in a loop; corresponding to the well-known NMR phenomenon. To understand the fundamental principles underlying signal detection, the well-known Faraday's law of induction must be invoked. Faraday's law of induction states that the time-varying magnetic flux (ϕ) through a conductive loop induces an electromotive force (emf) or voltage in the loop, with an oscillating frequency corresponding to the rate of change of the magnetic flux.

$$emf = -\frac{d\phi}{dt} \tag{2-44}$$

The total magnetic flux through the conductive loop by the precessing net magnetization $\boldsymbol{M}(r,t)$ is given by:

$$\phi(t) = \int_{sample} \boldsymbol{B}_1^-(r) \cdot \boldsymbol{M}(r,t)dr \tag{2-45}$$

where $r = (x, y, z)$, and $\boldsymbol{B}_1^-(r)$ is the receptive field sensitivity of the conductive loop.

Then according to Eq. 2-44, the voltage $V(t)$ or emf induced in the loop (11) is:

$$V(t) = emf = -\frac{d\phi}{dt} = -\int_{sample} \frac{\partial}{\partial t} \boldsymbol{B}_1^-(r) \cdot \boldsymbol{M}(r,t)dr \tag{2-46}$$

The received signal in modern NMR systems falls in the radio frequency (RF) range and for a typical NMR experiment, a conductive loop sensitive to the precession frequency is placed proximal to the sample under test for excitation and signal detection.

2.3.4 Chemical Shift

Up to this point in our discussion, it was assumed that the ensemble of spins contains only a single type of nucleus, thus resonating at a single frequency $\boldsymbol{\omega_0}$ (as determined by the gyromagnetic ratio γ and static magnetic field strength $\boldsymbol{B_0}$ as per Eq. 2-8). If all protons in nature resonate at $\boldsymbol{\omega_0}$ NMR spectroscopy would not be particularly interesting. Fortunately however, it turns out that proton nuclei in various chemical environments experience a slightly altered magnetic field, thus as per Eq. 2-8, resonate at slightly different precession frequencies. This phenomenon is called *chemical shift*, and is caused by an opposing magnetic field induced by the electron cloud surrounding the nucleus, in the presence of an external magnetic field. The effective magnetic field then experienced by the nucleus can be compactly expressed as follows:

$$\boldsymbol{B} = \boldsymbol{B_0}(1 - \sigma) \tag{2-47}$$

where σ, a dimensionless quantity, is the shielding constant, The magnetic field experienced by the nucleus $\boldsymbol{B}$ can be expressed as shown in Eq. 2-47 since the chemical shift (as measured in frequency units) scales linearly with the applied magnetic field $\boldsymbol{B}_0$. Now combining Eq. 2-8 and 2-47 provides the expression to calculate the resonance frequency $\boldsymbol{\omega}$ of a given spin in a particular environment.

$$\boldsymbol{\omega} = \gamma \boldsymbol{B}_0(1 - \sigma) \tag{2-48}$$

It is customary to express the chemical shift in terms of parts per million (ppm), where the chemical shift δ is defined as:

$$\delta = \frac{\boldsymbol{\omega} - \boldsymbol{\omega_{ref}}}{\boldsymbol{\omega_{ref}}} \times 10^6 \tag{2-49}$$

where $\boldsymbol{\omega}$ is the resonant frequency of spins in a particular chemical environment as in Eq. 2-48, and $\boldsymbol{\omega_{ref}}$ is the resonant frequency of a known reference compound to which $\boldsymbol{\omega}$ is referenced to. A widely accepted reference standard for proton and ^{13}C NMR is tetramethylsilane (TMS), to which $\delta = 0$ is assigned by convention. For *in vivo* proton MRS, typically the water peak is used as a reference, which then relative to TMS is $\delta = 4.65$ ppm.

2.3.5 Product Operator Formalism, and Coupled Spin Systems

2.3.5.1 Hamiltonian and Hamiltonians for Coupled Spin Systems

For conciseness, this section contains a brief introduction to selected elementary concepts in quantum mechanics, which are required to develop the framework for the product operator formulism, and is limited to AX type spin systems (described later).

We start by introducing the operator associated with the energy of the system called the *Hamiltonian*, where the Hamiltonian eigenstates are called *energy eigenstates*, and Hamiltonian eigenvalues are called *energy levels.*

$$\hat{H}|n> = E_n|n> \qquad (2\text{-}50)$$

The quantum state of the ensemble of particles can be fully described by a wavefunction $|\Psi_{full}>$ which encompasses information such as position (r), velocities and spin states of nuclei and electrons, and obeys the time-dependent Schrödinger Equation:

$$\hat{H}_{full}|\Psi_{full}(r,t)> = \boldsymbol{i}\hbar\frac{\boldsymbol{\partial}}{\boldsymbol{\partial t}}|\Psi_{full}(r,t)> \qquad (2\text{-}51)$$

where the Hamiltonian $\hat{H}_{full}$ contains all interactions in the system. However, for the purposes of NMR, Eq. 2-51 can be made simpler by accounting for only the nuclear spin component as follows:

$$\hat{H}_{spin}|\Psi_{spin}(t)> = \boldsymbol{i}\hbar\frac{\boldsymbol{\partial}}{\boldsymbol{\partial t}}|\Psi_{spin}(t)> \qquad (2\text{-}52)$$

In Eq. 2-52 $\hat{H}_{spin}$ is the *nuclear spin Hamiltonian,* $|\Psi_{spin}>$ is the spin state of the nuclei, and Eq. 2-52 describes the time-evolution of the wavefunction $|\Psi_{spin}(t)>$. Here on, since we deal with only nuclear spin Hamiltonians, the term $\hat{H}$ will be used instead of $\hat{H}_{spin}$; and we will define a Hamiltonian in natural units as $\hat{\mathcal{H}} = \hat{H}/\hbar$**.** Now the Schrödinger Equation reads as:

$$\widehat{\mathcal{H}}|\Psi(t)> = i\frac{\partial}{\partial t}|\Psi(t)> \tag{2-53}$$

and $\widehat{\mathcal{H}}$ has the same eigenfunctions, as in Eq. 2-50

$$\widehat{\mathcal{H}}|n> = \omega_n|n> \tag{2-54}$$

where the eigenvalues of $\widehat{\mathcal{H}}$ are denoted ω_n and are conveniently given by $\omega_n = \hbar^{-1}E_n$.

If the Hamiltonian $\widehat{\mathcal{H}}$ is time-independent, the solution to Eq. 2-53 is a first-order differential equation given by:

$$|\Psi(t)> = \exp\{-i\widehat{\mathcal{H}}\}|\Psi(0)> \tag{2-55}$$

where $|\Psi(0)>$ is the system state at $t = 0$, and Eq.2-55 describes time-evolution of the initial spin system under the Hamiltonian.

Now for a spin ½ particle, we also state three other operators $\hat{I}_x$, $\hat{I}_y$, $\hat{I}_z$ which are *x*, *y* and *z* components of angular momentum, respectively. For a spin ½ particle these angular momentum operators are as follows: $\hat{I}_z = \frac{1}{2}\begin{pmatrix} 1 & 0 \\ 0 & -1 \end{pmatrix}, \hat{I}_x = \frac{1}{2}\begin{pmatrix} 0 & 1 \\ 1 & 0 \end{pmatrix}, \hat{I}_y = \frac{1}{2}\begin{pmatrix} 0 & -i \\ i & 0 \end{pmatrix}$. These operators will be extensively described and used later in this chapter and in subsequent chapters of this thesis. In addition, the complex exponentials of angular momentum operators are called *rotation operators*, and take the following form:

$$\hat{R}_x(\beta) = \exp\{-i\beta\hat{I}_x\} \tag{2-56}$$
$$\hat{R}_y(\beta) = \exp\{-i\beta\hat{I}_y\}$$
$$\hat{R}_z(\beta) = \exp\{-i\beta\hat{I}_z\}$$

A rotation sandwich on angular momentum operators can be used to clarify its use as in Eq. 2-57 below (which stems from a lengthy derivation which will be skipped): and a pictorial description is shown in Figure. 2-5:

$$\hat{R}_x(\beta)\hat{I}_y\hat{R}_x(-\beta) = \hat{I}_y\cos(\beta) + \hat{I}_z\sin(\beta) \tag{2-57}$$

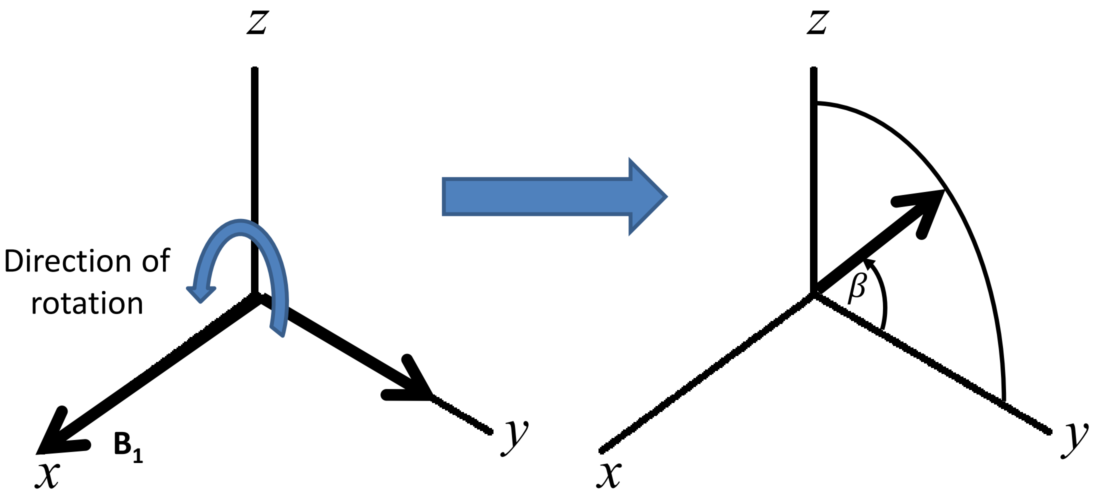

Figure 2-5 *Rotation of the angular momentum operator during an RF pulse applied along the x-axis with angle β.*

where the angular momentum operator $\hat{I}_y$ is rotated about the x-axis through an arbitrary angle β (by an applied RF pulse). For example, in this case for $\beta = 0$, or $\beta = \frac{\pi}{2}$ the expression in Eq. 2-57 simplifies to $\hat{I}_y$ and $\hat{I}_z$, respectively as expected.

The interaction of a magnetic dipole moment with the external magnetic field was described earlier, where in operator form Eq. 2-3 can be written as:

$$\hat{\boldsymbol{\mu}}_s = \gamma_s \hat{\boldsymbol{I}}_s \tag{2-58}$$

or more explicitly:

$$\hat{\boldsymbol{\mu}}_s = \gamma_s(\hat{I}_{sx}\vec{\imath} + \hat{I}_{sy}\vec{\jmath} + \hat{I}_{sz}\vec{k}) \tag{2-58}$$

where, the subscript S represents spin S and its associated gyromagnetic ratio, and $\hat{I}_{sx}$, $\hat{I}_{sy}$, $\hat{I}_{sz}$ are its angular momentum operators. The nuclear magnetic energy associated with spin S, in the presence of a magnetic field $\boldsymbol{B} = B_x\vec{\imath} + B_y\vec{\jmath} + B_z\vec{k}$ is:

$$E_s = -\gamma_s \hat{\boldsymbol{I}}_s \cdot \boldsymbol{B} \tag{2-59}$$

Thus the Hamiltonian for the nuclear magnetic energy between spin S and the magnetic field is:

$$\hat{\mathcal{H}}_s^{mag} = -\hat{\boldsymbol{\mu}}_s \cdot \boldsymbol{B} \tag{2-60}$$

And can be expanded to give:

$$\hat{\mathcal{H}}_s^{mag} = -\gamma_s(B_x\hat{I}_{sx} + B_y\hat{I}_{sy} + B_z\hat{I}_{sz}) \tag{2-61}$$

In the presence of a $\boldsymbol{B_0}$ magnetic field as previously defined to lie along the *z* direction Eq. 2-61 can be simplified to be:

$$\hat{\mathcal{H}}_s^{mag} = -\gamma_s B_0 \hat{I}_{sz} = \omega_0 \hat{I}_{sz} \tag{2-62}$$

Called the *nuclear Zeeman interaction*, where the $-\gamma_s B_0$ term can be recalled to be the Larmor frequency (ω_0) of spin I_s (after including the chemical shift as described in the previous section). Now, considering an arbitrary spin (let us drop the subscript *S*), Eq. 2-55 substituting Eq. 2-56 can be written as:

$$\left|\Psi(t) > = exp\left\{-i\omega_0 t\hat{I}_z\right\}\right|\Psi(0) > = \hat{R}_z(\omega_0 t)|\Psi(0) > \tag{2-63}$$

where Eq.2-63 describes a rotation of the $|\Psi(0) >$ spin state around the *z*-axis with Larmor frequency ω_0 in the presence of the static magnetic field $\boldsymbol{B_0}$ as was previously described in the classical sense.

In the presence of an RF field, it is convenient to denote the Schrödinger equation in the rotating frame; as such the symbol "$\sim$" will be used to denote a state as viewed from the rotating frame as follows by introducing a counter-rotation around the *z*-axis:

$$|\tilde{\Psi} > = \hat{R}_z(-\emptyset)|\Psi > \tag{2-64}$$

Then the *rotating-frame Schrödinger equation* can be written out to be:

$$\hat{\tilde{\mathcal{H}}}|\tilde{\Psi}(t) > = i\frac{\partial}{\partial t}|\tilde{\Psi}(t) > \tag{2-65}$$

where the expression for the rotating frame Hamiltonian $\hat{\tilde{\mathcal{H}}}$ is given by:

$$\hat{\tilde{\mathcal{H}}} = \hat{R}_z(-\emptyset)\hat{\mathcal{H}}\hat{R}_z(\emptyset) - \omega\hat{I}_z \tag{2-66}$$

Now to describe the precession of a spin in the presence of the static magnetic field $\boldsymbol{B_0}$ as seen in the rotating frame, the rotating frame Hamiltonian is:

$$\widehat{\tilde{\hat{\mathcal{H}}}} = \hat{R}_z(-\emptyset)\omega_0\hat{I}_z\hat{R}_z(\emptyset) - \omega_{ref}\hat{I}_z = (\omega_0 - \omega)\hat{I}_z \tag{2-67}$$

which appears in the expected familiar form. The frequency $\Omega^0 = (\omega_0 - \omega)$ is the difference between the Larmor frequency of the spin and the rotating frame.

The rotating frame spin Hamiltonian in the presence of an RF pulse, can then be expressed as follows:

$$\widehat{\tilde{\hat{\mathcal{H}}}} = (\Omega^0)\hat{I}_z + \hat{\mathcal{H}}_{RF}(t) \tag{2-68}$$

and if a rectangular RF pulse (time-independent amplitude function) is applied along the *x*-axis, Eq. 2-68 the rotating frame Hamiltonian becomes:

$$\widehat{\tilde{\hat{\mathcal{H}}}} = (\omega_0 - \omega)\hat{I}_z + \omega_1\hat{I}_x \tag{2-69}$$

which can be seen to be in the familiar from as in Eq. 2-35. If $\omega_0 = \omega$, the rotating frame spin Hamiltonian reduces to just the $\omega_1\hat{I}_x$ term due to the RF pulse, inducing a rotation around the x-axis with angular velocity ω_1 as illustrated in Figure 2-4. The above description can also be expanded to describe dynamics during off-resonance ($\Omega^0 \neq 0$).

We will now return back to the density matrix, of an ensemble spin ½ system $\hat{\rho}$ which can be represented by its product operator basis $\hat{I}_x$, $\hat{I}_y$, $\hat{I}_z$, and $\hat{\mathbb{1}}$, where $\hat{\mathbb{1}}$ is an identity operator, as follows:

$$\hat{\rho} = \sum_k b_k\hat{B}_k \tag{2-70}$$

where $\hat{B}_k$ represents the product operator basis, and b_k is the associated coefficient with product operator $\hat{B}_k$. By representing $\hat{\rho}$ in the product operator basis, it is possible to easily identify the important/significant observables of the system following a pulse-sequence played out.

Now that we have introduced the Hamiltonian for a spin system, and density matrix, the time dependence of the density matrix can be expressed according to the solution of the Liouville-von Neumann equation for a time-independent Hamiltonian as follows:

$$\hat{\rho}(t) = \exp\{-i\hat{\mathcal{H}}t\}\,\hat{\rho}(0)\exp\{i\hat{\mathcal{H}}t\} \qquad (2\text{-}71)$$

where $\hat{\rho}(0)$ is the initial density matrix.

To extract the expectation value for an operator $\hat{Q}$ in $\hat{\rho}$, which as described in Eq. 2-70 may contain an ensemble of spin states, the following operation can be performed:

$$\langle\hat{Q}\rangle = Tr\{\,\hat{\rho}\hat{Q}\} \qquad (2\text{-}72)$$

where $Tr\{\,\}$ is the trace operation.

Based on the expression derived for the net magnetization $\boldsymbol{M_0}$ at thermal equilibrium in Eq. 2-20, it is convenient to define the *Boltzmann factor* $\mathbb{B}$ to be:

$$\mathbb{B} = \frac{\hbar\gamma B_0}{k_B T} \qquad (2\text{-}73)$$

The density matrix $\hat{\rho}$ at thermal equilibrium in Eq. 2-14, 2-15 can now be expressed as follows:

$$\hat{\rho} = \frac{1}{2}\hat{\mathbb{1}} + \frac{1}{2}\,\mathbb{B}\hat{I}_z \qquad (2\text{-}74)$$

where $\mathbb{1}$ corresponds to equal $|\alpha >$ and $|\beta >$ character across the ensemble, which dominates the $\mathbb{B}$ component corresponding to the net magnetization.

We now look at a rudimentary *pulse sequence*, starting with the spin-system at thermal equilibrium, and apply an instantaneous 90° RF pulse along the *y*-axis [denoted by the short hand notation: $\left(\frac{\pi}{2}\right)_y$] then let the system evolve during time τ as illustrated in Figure. 2-6.

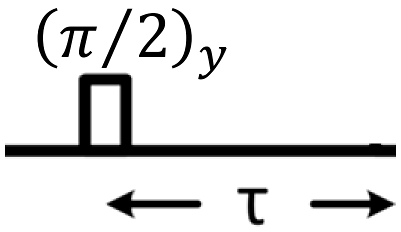

Figure 2-6 *Simple pulse sequence involving a 90 degree pulse and τ time evolution.*

The above described sequence of events can be described in product operator form as follows:

$$\hat{\rho}_{eq} = \frac{1}{2}\hat{\mathbb{1}} + \frac{1}{2}\,\mathbb{B}\hat{I}_z \xrightarrow{\left(\frac{\pi}{2}\right)_y} \frac{1}{2}\hat{\mathbb{1}} + \frac{1}{2}\,\mathbb{B}\hat{I}_x \xrightarrow{\hat{\mathcal{H}}(\tau)} \tag{2-75}$$

$$\frac{1}{2}\hat{\mathbb{1}} + \frac{1}{2}\,\mathbb{B}(\hat{I}_x\cos\Omega^0\mathrm{t} + \hat{I}_y\sin\Omega^0\mathrm{t})$$

where the τ time period represents evolution under the rotating frame Zeeman Hamiltonian as in Eq. 2-67. It is seen that the $\hat{\mathbb{1}}$ terms in Eq. 2-75 provide no useful information; hence going forward this term will be omitted and only product operator terms associated with the net magnetization will be considered for clarity.

Thus far the discussion was limited to isolated spins, with the addition of chemical shift. In reality however, a sample of interest will likely consist of complex molecules with more than one spin leading to multiple chemical shifts and spin-spin couplings resulting in complex resonances. If we start by considering an ensemble of spin ½ pairs, the behavior of the pair will additionally consist of *dipole-dipole* coupling and *J-coupling* compared to the isolated spin system treatment above. The Hamiltonian for a coupled spin system (consisting of spins $\hat{I}_1$ and $\hat{I}_2$) can be written as follows:

$$\hat{\mathcal{H}} = \omega_1^0\hat{I}_{1z} + \omega_2^0\hat{I}_{2z} + 2\pi J_{12}\hat{\boldsymbol{I}}_1\cdot\hat{\boldsymbol{I}}_2 + d_{12}f(\hat{\boldsymbol{I}}_1,\hat{\boldsymbol{I}}_2) \tag{2-76}$$

where $\omega_n^0 = -\gamma B_0(1 + \delta_n)$ represent chemical shifts for each spin, the third term corresponds to the J-coupling term (described next), and the dipole-dipole interaction term. Note that the $\hat{\boldsymbol{I}}_1 \cdot \hat{\boldsymbol{I}}_2$ operator is constructed by taking the direct product between the first (spin 1) and second operator (spin 2). In an isotropic liquid, the dipole-dipole interaction to a good approximation, can be ignored, thus will not be considered in the remainder of this thesis. The third term in Eq. 2-76 is the J-coupling term, also known as *indirect spin-spin coupling.* The J-coupling term $2\pi J_{12}\hat{\boldsymbol{I}}_1 \cdot \hat{\boldsymbol{I}}_2$ arises from the influence of the bonding electrons on the magnetic fields experienced by the pair of nuclei. In other words, it is termed 'indirect-coupling' since the presence of the neighboring nucleus is "felt" by the other nucleus through the shared electron cloud. Note that J-coupling is exclusively an intramolecular component. The J-coupling term in Eq. 2-76 can be expanded as follows into its orthogonal angular momentum operators:

$$\hat{\boldsymbol{I}}_1 \cdot \hat{\boldsymbol{I}}_2 = \hat{I}_{1x}\hat{I}_{2x} + \hat{I}_{1y}\hat{I}_{2y} + \hat{I}_{1z}\hat{I}_{2z} \tag{2-77}$$

The behavior of a coupled spin ½ pair depends on the difference between their chemical shifts compared to the spin-spin coupling. If the difference in chemical shift is much larger than the spin-spin coupling, such that:

$$|\omega_1^0 - \omega_2^0| \gg \pi J_{12} \tag{2-78}$$

the interaction is termed *weakly coupled* (also called an AX spin system), and as per the *secular approximation*, the complete spin Hamiltonian can be simplified to be:

$$\widehat{\mathcal{H}} = \omega_1^0\hat{I}_{1z} + \omega_2^0\hat{I}_{2z} + 2\pi J_{12}\hat{I}_{1z}\hat{I}_{2z} \tag{2-79}$$

where the $\hat{I}_{1x}\hat{I}_{2x}$, and $\hat{I}_{1y}\hat{I}_{2y}$ terms in Eq. 2-76 are ignored (12). For spin pairs with the difference in chemical shift between the two spin species roughly similar in magnitude to the spin-spin coupling, are termed *strongly coupled* (also called an AB spin system), and the approximation in Eq. 2-79 no longer holds. The interaction between the ^{13}C and ^{1}H nuclei pair satisfies the relation in Eq. 2-78 thus the Hamiltonian in Eq. 2-79 can be re-written as follows:

$$\hat{\mathcal{H}} = \omega_I^0 \hat{I}_z + \omega_S^0 S_z + 2\pi J_{HC} \hat{I}_z \hat{S}_z \tag{2-80}$$

where $\hat{I}$ and $\hat{S}$ represent ^{1}H spins and ^{13}C spins, respectively, and J_{HC} is the heteronuclear J-coupling constant for ^{1}H-^{13}C pairs. The Zeeman product states of the AX system ($|\alpha\alpha>, |\alpha\beta>, |\beta\alpha>, |\beta\beta>$) are eigenstates of the weakly coupled Hamiltonian in Eq. 2-80 and can be calculated as follows:

$$\begin{aligned}
\hat{\mathcal{H}}\ |\alpha\alpha> &= \left(\frac{1}{2}\omega_I^0 + \frac{1}{2}\omega_S^0 + \frac{1}{2}\pi J_{HC}\right)\ |\alpha\alpha> \\
\hat{\mathcal{H}}\ |\alpha\beta> &= \left(\frac{1}{2}\omega_I^0 - \frac{1}{2}\omega_S^0 - \frac{1}{2}\pi J_{HC}\right)\ |\alpha\beta> \\
\hat{\mathcal{H}}\ |\beta\alpha> &= \left(-\frac{1}{2}\omega_I^0 + \frac{1}{2}\omega_S^0 - \frac{1}{2}\pi J_{HC}\right)\ |\beta\alpha> \\
\hat{\mathcal{H}}\ |\beta\beta> &= \left(-\frac{1}{2}\omega_I^0 - \frac{1}{2}\omega_S^0 + \frac{1}{2}\pi J_{HC}\right)\ |\beta\beta>
\end{aligned} \tag{2-81}$$

From the four expressions in Eq. 2-81, and assuming $J_{HC} > 0$, and $\gamma > 0$, which is the case for ^{1}H-^{13}C pairs, the relationship between transitions and observed resonances is illustrated in Figure. 2-7. There are four separate resonances (spectral peaks), a doublet around the Larmor frequency of protons (ω_I^0), and a doublet around the Larmor frequency of carbon (ω_S^0) nuclei. In both cases the splitting of the doublet is given by J_{HC}. Furthermore, from the transitions in Figure 2-7, it is seen that the left side peak of both doublets are coupled to spins of the second species in the $|\beta>$ state, and the right side peak of both doublets are coupled to spins of the second species in the $|\alpha>$ state, as labeled on the spectral peaks in Figure 2-7 below.

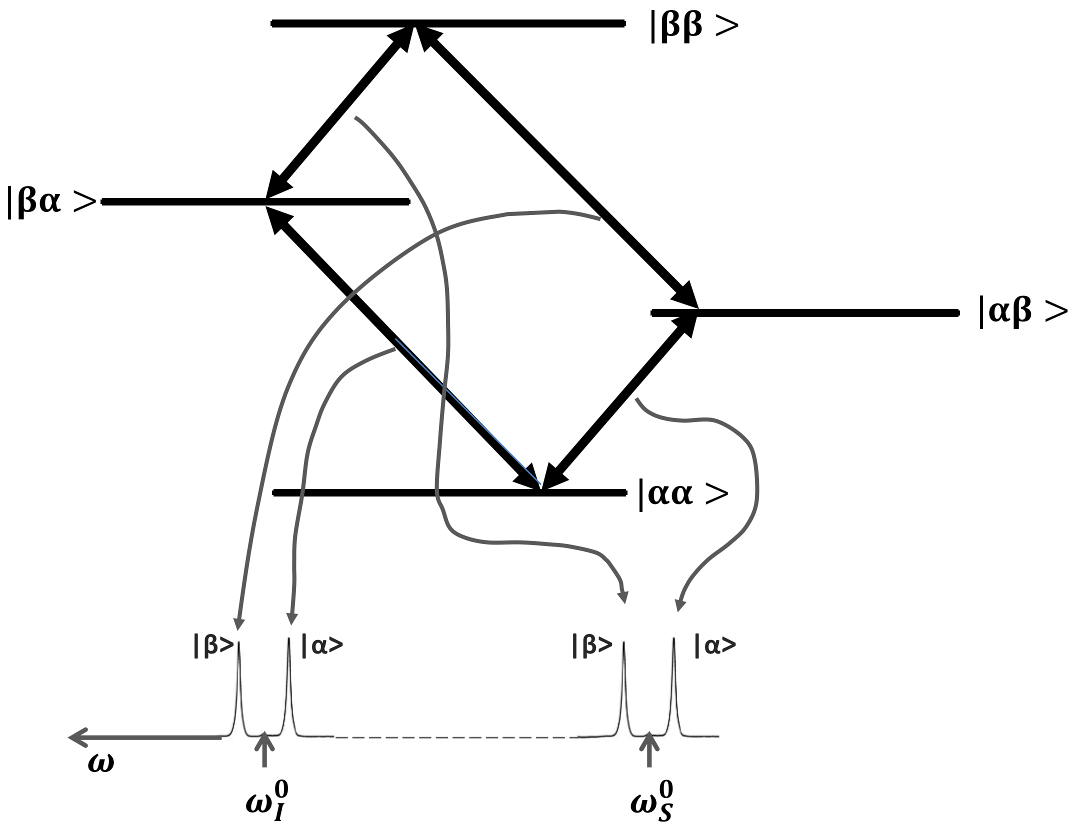

Figure 2-7 *Energy level diagram for a weakly coupled 2-spin system (IS) and its resonances.*

The density matrix $\hat{\rho}$ for an AX spin system can be constructed to be a 4 x 4 matrix, and consists of 16 product operators as described in Table 2-1 below: and interesting properties will be described later in this chapter.

Table 2-1 *Description of product operators for two-2pin system.*

Description	Operators
z-magnetization on spin *I*	$\hat{I}_z$
in phase *x*-magnetization, in phase *y*-magnetization on spin *I*	$\hat{I}_x, \hat{I}_y$
z-magnetization on spin *S*	$\hat{S}_z$
in phase *x*-magnetization, in phase *y*-magnetization on spin *S*	$\hat{S}_x, \hat{S}_y$
anti-phase *x*-magnetization, anti- phase *y*-magnetization on spin *I*	$2\hat{I}_x\hat{S}_z, 2\hat{I}_y\hat{S}_z$
anti-phase *x*-magnetization, anti- phase *y*-magnetization on spin *S*	$2\hat{I}_z\hat{S}_x, 2\hat{I}_z\hat{S}_y$
multiple-quantum coherence	$2\hat{I}_x\hat{S}_x, 2\hat{I}_x\hat{S}_y, 2\hat{I}_y\hat{S}_x, 2\hat{I}_y\hat{S}_y$
non-equilibrium population	$2\hat{I}_z\hat{S}_z$

2.3.5.2 J-modulation, Spin-Echoes and Multiple-Quantum Coherence

Let us attempt at differentiating between anti-phase and in-phase magnetization, which turns out to be a result of J-evolution or *scalar coupling*. Rewriting the weakly coupled spin Hamiltonian in Eq. 2-80 in the rotating frame gives:

$$\hat{\tilde{\mathcal{H}}} = \Omega_I^0 \hat{I}_z + \Omega_S^0 S_z + 2\pi J_{HC} \hat{I}_z \hat{S}_z \tag{2-82}$$

Here $\Omega_I^0 = (\omega_I^0 - \omega_I)$ and $\Omega_S^0 = (\omega_S^0 - \omega_S)$ are the differences between the chemical shift included Larmor frequencies and reference frequencies for *I* and *S* spins, respectively.

For simplicity let $\Omega_I^0 = \Omega_S^0 = 0$, and apply an instantaneous 90° rotation around the *y*-axis selectively on the *I* spin, denoted by $\left(\frac{\pi}{2}\right)_y^I$, starting at equilibrium magnetization, and let the system evolve for a time period τ. The above set of instructions can be described in a flow diagram form as illustrated in Eq. 2-83 and 2-87 below:

$$\hat{I}_z \xrightarrow{\left(\frac{\pi}{2}\right)_y^I} \hat{I}_x \xrightarrow{\hat{\tilde{\mathcal{H}}}(\tau)} \rho(\tau) = \exp\{-i\tau\pi J_{HC} \hat{I}_z \hat{S}_z\}\, \hat{I}_x \exp\{i\tau\pi J_{HC} \hat{I}_z \hat{S}_z\} \tag{2-83}$$

In Eq. 2-83 only the third component of the Hamiltonian in Eq. 2-82 is at play since we set $\Omega_I^0 = \Omega_S^0 = 0$. By matrix multiplication it can be shown that Eq. 2-83 simplifies to:

$$\hat{I}_x \xrightarrow{\hat{\tilde{\mathcal{H}}}(\tau)} \rho(\tau) = \hat{I}_x \cos(\pi J_{HC}\tau) + 2\hat{I}_y \hat{S}_z \sin(\pi J_{HC}\tau) \tag{2-84}$$

Eq.2-84 describes evolution of the $\hat{I}_x$ spin state under the weak coupling Hamiltonian, resulting in a purely anti-phase coherence state on spin *I*, if $\tau = \frac{1}{2J_{HC}}$. Further evolution of the system untill $\tau = \frac{1}{J_{HC}}$ brings the system back to a purely in-phase coherence state $-\hat{I}_x$. Evolution of the $\hat{I}_x$ spin state and $\hat{S}_y$ spin system (in isolation) during a chain of $\tau = \frac{1}{J_{HC}}$ time intervals is summarized below:

$$\hat{I}_x \xrightarrow{\hat{\mathcal{H}}\left(\frac{1}{2J_{HC}}\right)} 2\hat{I}_y\hat{S}_z \xrightarrow{\hat{\mathcal{H}}\left(\frac{1}{J_{HC}}\right)} -\hat{I}_x \xrightarrow{\hat{\mathcal{H}}\left(\frac{3}{2J_{HC}}\right)} -2\hat{I}_y\hat{S}_z \xrightarrow{\hat{\mathcal{H}}\left(\frac{2}{J_{HC}}\right)} \hat{I}_x \qquad (2\text{-}85)$$

$$\hat{S}_y \xrightarrow{\hat{\mathcal{H}}\left(\frac{1}{2J_{HC}}\right)} -2\hat{I}_z\hat{S}_x \xrightarrow{\hat{\mathcal{H}}\left(\frac{1}{J_{HC}}\right)} -\hat{S}_y \xrightarrow{\hat{\mathcal{H}}\left(\frac{3}{2J_{HC}}\right)} 2\hat{I}_z\hat{S}_x \xrightarrow{\hat{\mathcal{H}}\left(\frac{2}{J_{HC}}\right)} \hat{S}_y$$

Figure. 2-8 below illustrates the spectral representation (real part) of the first three spin states in Eq. 2-85, and a pictorial representation of the coupled spin system in the rotating frame. Note that the $|\alpha>$ and $|\beta>$ labels in the vector diagram represent the spin states the observed spins are coupled to.

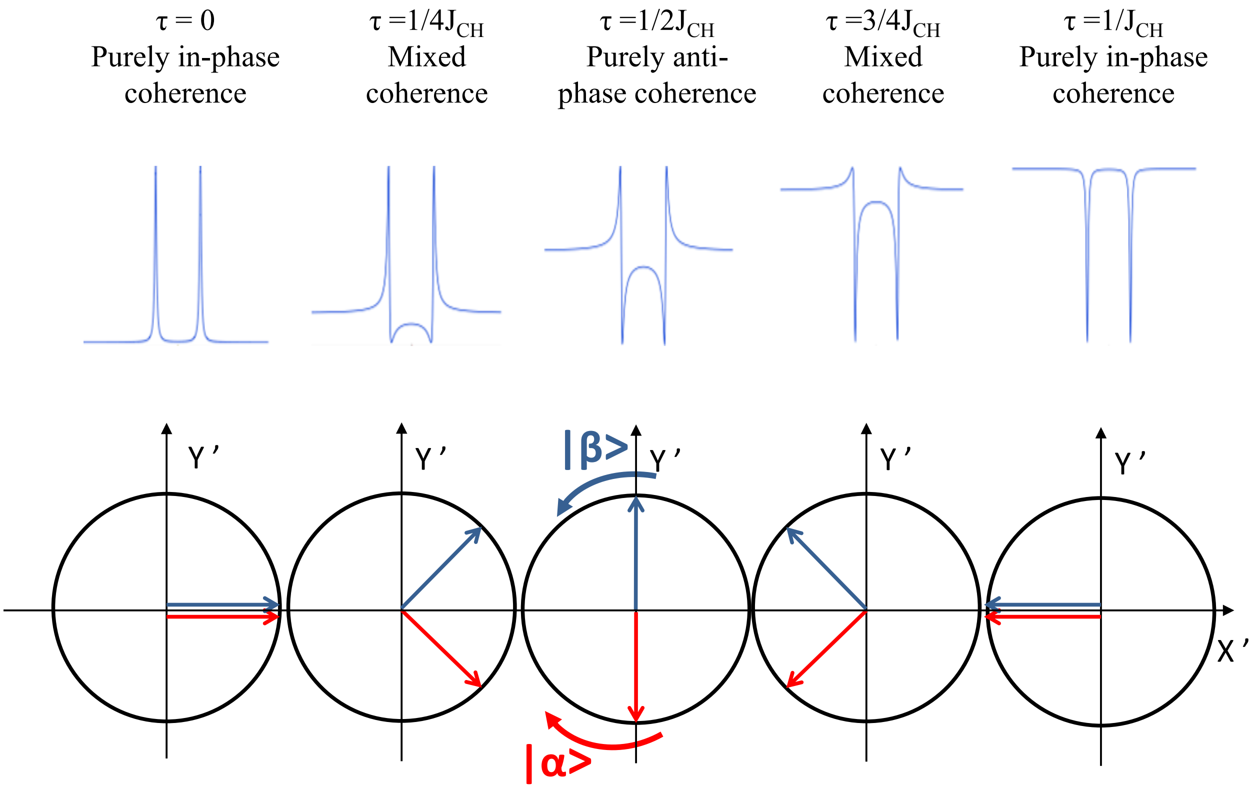

Figure 2-8 *Spectral representation of the five states described in Eq. 2-83, and their equivalent vector diagram illustration.*

For a two- spin AX system, evolution of the density matrix during a spin-echo sequence can be described as illustrated in Figure. 2-9 below which consists of an instantaneous 90° pulse along the *y*-axis on the proton channel and a second 180° pulse along the *x*-axis [denoted $\hat{R}_x^I(\pi)$ in Eq. 2-86] affecting all protons symmetrically placed around $\tau/2$ delays.

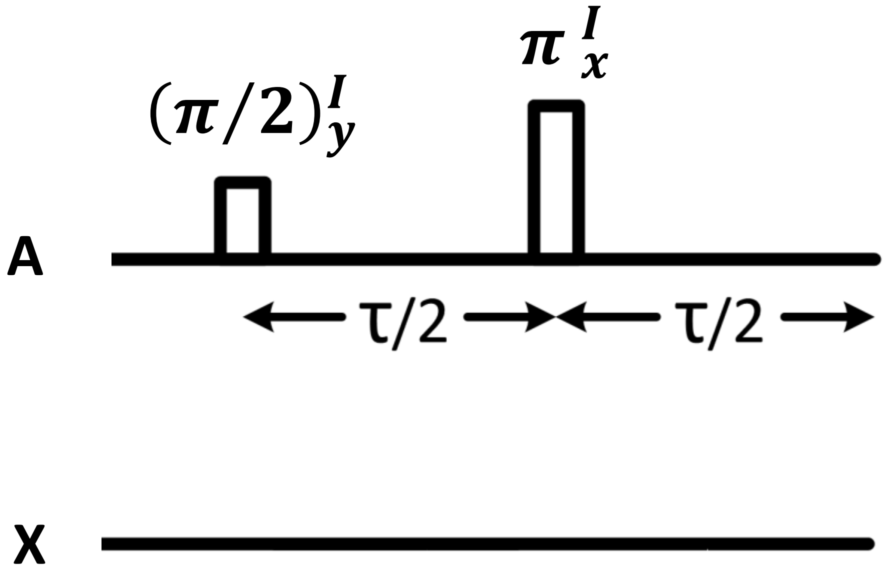

Figure 2-9 *Pulse sequence for a selective spin-echo.*

First we consider evolution of a heteronuclear AX spin system (such as a ^{1}H-^{13}C system) following a selective spin echo (refocusing pulse on only the observed nucleus) which can be described as follows:

$$\hat{I}_z \xrightarrow{\left(\frac{\pi}{2}\right)_y^I} \hat{I}_x \xrightarrow{\hat{\hat{\mathcal{H}}}\left(\frac{\tau}{2}\right)} exp\left\{-\frac{i\hat{\hat{\mathcal{H}}}\tau}{2}\right\}\hat{I}_x\; exp\left\{\frac{i\hat{\hat{\mathcal{H}}}\tau}{2}\right\} \qquad (2\text{-}86)$$

$$\xrightarrow{\pi_x^I} \hat{R}_x^I(\pi) exp\left\{-\frac{i\hat{\hat{\mathcal{H}}}\tau}{2}\right\}\hat{I}_x\; exp\left\{\frac{i\hat{\hat{\mathcal{H}}}\tau}{2}\right\}\hat{R}_x^I(-\pi)$$

$$\xrightarrow{\hat{\hat{\mathcal{H}}}\left(\frac{\tau}{2}\right)} \rho(\tau)$$

$$= exp\left\{-\frac{i\hat{\hat{\mathcal{H}}}\tau}{2}\right\}\hat{R}_x^I(\pi) exp\left\{-\frac{i\hat{\hat{\mathcal{H}}}\tau}{2}\right\}\hat{I}_x\; exp\left\{\frac{i\hat{\hat{\mathcal{H}}}\tau}{2}\right\}\hat{R}_x^I(-\pi) exp\left\{\frac{i\hat{\hat{\mathcal{H}}}\tau}{2}\right\}$$

where $\hat{\hat{\mathcal{H}}}$ is as defined in Eq. 2-82 for a weakly coupled spin system, however, where the S_z population state is ignored, as it is not observed in this experiment. It can be seen that the following rotation sandwich $\hat{R}_x^I(-\pi)exp\left\{-\frac{i\hat{\hat{\mathcal{H}}}\tau}{2}\right\}\hat{R}_x^I(\pi) = exp\left\{\frac{i\hat{\hat{\mathcal{H}}}\tau}{2}\right\}$, thus inserting a $\hat{R}_x^I(\pi)\ \hat{R}_x^I(-\pi)$ terms on the left and right side of the final expression in Eq. 2-83 simplifies to:

$$\rho(\tau) = \hat{R}_x^I(\pi)\hat{I}_x\hat{R}_x^I(-\pi) = \hat{I}_x \qquad (2\text{-}87)$$

since $exp\left\{\frac{i\hat{\hat{\mathcal{H}}}\tau}{2}\right\}exp\left\{-\frac{i\hat{\hat{\mathcal{H}}}\tau}{2}\right\} = \hat{\mathbb{1}}$. Eq-2-87 simplifies to the expected observation where all chemical shifts and heteronuclear J-evolution is refocused. Next we consider evolution of a homonuclear AX spin system following a non-selective spin echo (refocusing pulse on both nuclei) which can be described as in Eq. 2-86, with the exception that all protons will be affected by the 90° and 180° pulses. To evaluate evolution of one spin species (say $\hat{I}$), without loss of generality, we can separately evaluate the following spin-echo sequence in Figure. 2-10:

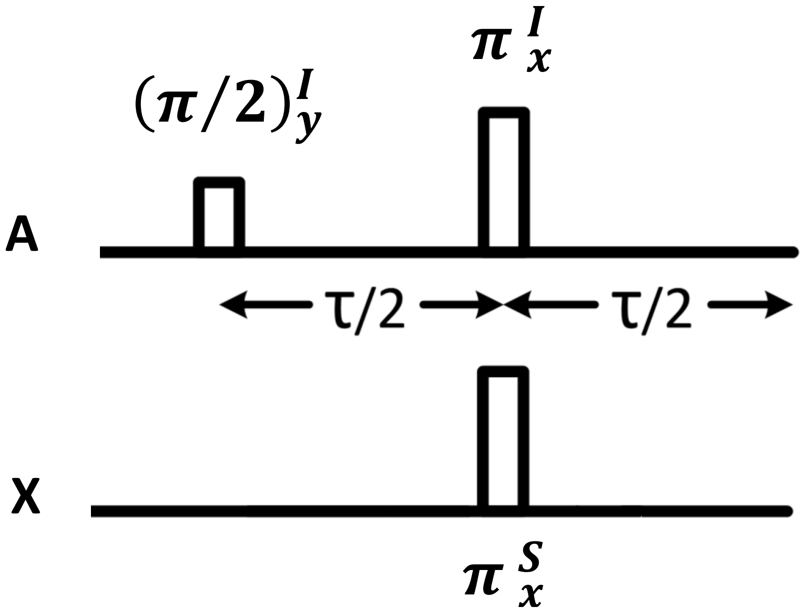

Figure 2-10 *Pulse sequence for a non-selective spin echo.*

The final expression in Eq. 2-86 can be re written for the above case as follows:

$$\rho(\tau) = exp\left\{-\frac{i\hat{\hat{\mathcal{H}}}\tau}{2}\right\}\hat{R}_x^{I,S}(\pi)exp\left\{-\frac{i\hat{\hat{\mathcal{H}}}\tau}{2}\right\}\hat{I}_x\, exp\left\{\frac{i\hat{\hat{\mathcal{H}}}\tau}{2}\right\}\hat{R}_x^{I,S}(-\pi)exp\left\{\frac{i\hat{\hat{\mathcal{H}}}\tau}{2}\right\} \tag{2-88}$$

where 180° pulses on both *I* and *S* spins is denoted by $\hat{R}_x^{I,S}(\pi)$. Here spins *I* and *S* are both protons. In this case however, the rotation sandwich on the Hamiltonian does not result in an inverted version of itself. Rather, we see that only some components of the Hamiltonian are inverted as follows:

$$\hat{R}_x^{I,S}(-\pi)exp\left\{-\frac{i\hat{\hat{\mathcal{H}}}\tau}{2}\right\}\hat{R}_x^{I,S}(\pi) = \hat{R}_x^{I,S}(-\pi)exp\left\{-\frac{i\Omega_I^0\hat{I}_z\tau}{2}\right\}exp\left\{-\frac{i\Omega_S^0 S_z\tau}{2}\right\}exp\left\{-\frac{i\pi J_{HC}2\hat{I}_z\hat{S}_z\tau}{2}\right\}\hat{R}_x^{I,S}(\pi) \tag{2-89}$$

By inserting the identity operator $\hat{\mathbb{1}} = \hat{R}_x^{I,S}(\pi)\hat{R}_x^{I,S}(-\pi)$ on both sides of the second exponential term in the expanded expression in Eq. 2-89, we arrive at the following:

$$\hat{R}_x^{I,S}(-\pi)exp\left\{-\frac{i\hat{\hat{\mathcal{H}}}\tau}{2}\right\}\hat{R}_x^{I,S}(\pi) = \hat{R}_x^{I,S}(-\pi)exp\left\{\frac{i\Omega_I^0\hat{I}_z\tau}{2}\right\}exp\left\{\frac{i\Omega_S^0 S_z\tau}{2}\right\}exp\left\{-\frac{i\pi J_{HC}2\hat{I}_z\hat{S}_z\tau}{2}\right\}\hat{R}_x^{I,S}(\pi) \tag{2-90}$$

where the chemical shift terms get inverted, while the J-evolution term is not. Then similar to the simplified expression obtained in Eq. 2-87, the overall expression in Eq. 2-88 simplifies to the following:

$$\rho(\tau) = \hat{R}_x^{I,S}(-\pi)exp\left\{-\frac{i\pi J_{HC}2\hat{I}_z\hat{S}_z\tau}{2}\right\}\hat{I}_x exp\left\{\frac{i\pi J_{HC}2\hat{I}_z\hat{S}_z\tau}{2}\right\}\hat{R}_x^{I,S}(\pi) \tag{2-91}$$

where chemical shifts are seen to be refocused, but homonuclear J-evolution is not. This is an important phenomenon which affects localized proton spectroscopy, and also be used to great advantage in edited MRS, where global refocusing pulses used [such as in the PRESS (13) sequence] do not refocus homonuclear J-evolution. In this case, this J- modulation leads to signal losses for longer echo time (TE) sequences.

We now briefly return back to describing multiple-quantum (MQ) coherence described in Table. 2-1. Demonstrated below is one way to achieve a (MQ) coherence state, by the following set of instantaneous RF pulses and delays:

$$\hat{I}_z \xrightarrow{\left(\frac{\pi}{2}\right)_y^I} \hat{I}_x \xrightarrow{\hat{\hat{\mathcal{H}}}\left(\frac{1}{2J_{HC}}\right)} 2\hat{I}_y\hat{S}_z \xrightarrow{\left(\frac{\pi}{2}\right)_x^S} -2\hat{I}_y\hat{S}_y \tag{2-92}$$

All operations in Eq. 2-92 were previously described except the last $\left(\frac{\pi}{2}\right)_x^S$ rotation, which is an instantaneous 90° rotation around the *x*-axis selectively on the *S* spin. It can be shown that the commutator relation $[2\hat{I}_y\hat{S}_y,\ 2\hat{I}_z\hat{S}_z] = 0$ for all MQ states, thus they do not evolve under weak scalar coupling. We will return back to MQ coherence states when describing polarization transfer (PT) experiments later.

2.3.5.3 Coherence Transfer

Coherence transfer is a key component of multi-pulse NMR experiments, and a building block of polarization transfer (PT) experiments. Before describing coherence transfer, we start with the equilibrium density matrix for a heteronuclear AX spin system by extending the density matrix for an ensemble of isolated spin ½ particles in Eq. 2-74:

$$\hat{\rho}_{eq} = \frac{1}{4}\hat{\mathbb{1}} + \frac{1}{4}\,\mathbb{B}_I\hat{I}_z + \frac{1}{4}\,\mathbb{B}_S\hat{S}_z \tag{2-93}$$

where $\mathbb{B}_I$ and $\mathbb{B}_S$ are Boltzmann factors for the two spin species as follows:

$$\mathbb{B}_I = \frac{\hbar\gamma_I B_0}{k_B T} \qquad \mathbb{B}_S = \frac{\hbar\gamma_S B_0}{k_B T} \tag{2-94}$$

In this work we are interested in ^{1}H and ^{13}C nuclear species, corresponding to I and S, respectively, where $\frac{\gamma_I}{\gamma_S} \cong 4$.

Now returning back to Coherence transfer; the concept involves generating anti-phase magnetization on one spin (as previously described): then executing a set of pulses to transfer magnetization of one spin species to the second spin species. One such process is described below in Eq. 2-95 (the $\hat{S}_z$ equilibrium magnetization will be ignored for now).

(2-95)

$$\begin{tikzcd}
\hat{\rho} = \frac{1}{4}\hat{\mathbb{1}} + \frac{1}{4}\,\mathbb{B}_I\hat{I}_z \arrow[d, "\left(\frac{\pi}{2}\right)_y^I"] \\
\hat{\rho} = \frac{1}{4}\hat{\mathbb{1}} + \frac{1}{4}\,\mathbb{B}_I\hat{I}_x \arrow[d, "\hat{\bar{\mathcal{H}}}(1/2J_{HC})"] \\
\hat{\rho} = \frac{1}{4}\hat{\mathbb{1}} + \frac{1}{4}\,\mathbb{B}_I 2\hat{I}_y\hat{S}_z \arrow[d, "\left(\frac{\pi}{2}\right)_x^I"] \\
\hat{\rho} = \frac{1}{4}\hat{\mathbb{1}} + \frac{1}{4}\,\mathbb{B}_I 2\hat{I}_z\hat{S}_z \arrow[d, "\left(\frac{\pi}{2}\right)_x^S"] \\
\hat{\rho} = \frac{1}{4}\hat{\mathbb{1}} - \frac{1}{4}\,\mathbb{B}_I 2\hat{I}_z\hat{S}_y
\end{tikzcd}$$

The key feature here is that the anti-phase coherence term on spin *I* ($2\hat{I}_y\hat{S}_z$) is transferred to be an anti-phase coherence term on spin *S* ($2\hat{I}_z\hat{S}_y$) following two 90° pulses: this process is called *coherence transfer*. Also note that the net polarization (magnetization) of spin *I* has been transferred to spin *S*. The importance of coherence transfer will be evident in the next section on polarization transfer.

2.3.5.4 Polarization Transfer Experiments (INEPT/DEPT)

The INEPT (14) sequence (insensitive nuclear enhancement by polarization transfer) is a relatively straightforward example to describe how coherence transfer can be used to increase sensitivity of an insensitive nucleus (spin *S*) by transferring polarization from a higher sensitivity nucleus (spin *I*). Figure. 2-11 below illustrates the classical INEPT sequence, and the spin states that result are shown at each step in the process in Eq. 2-96.

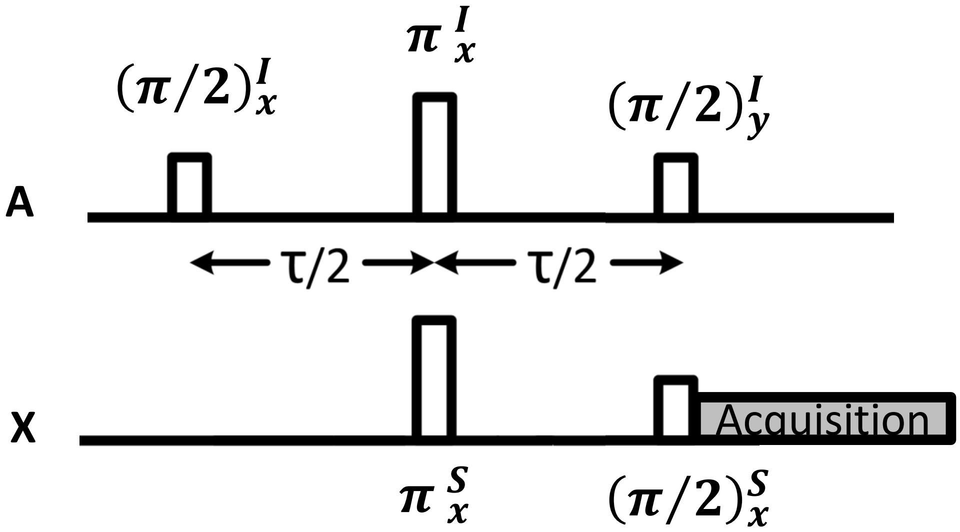

Figure 2-11 *The INEPT sequence.*

The sequence starts with the equilibrium density matrix described in Eq. 2-93. To simplify the resulting expressions for the INPET sequence,

let: $\hat{Q} = exp\left\{-\frac{i\hat{\mathcal{H}}\tau}{2}\right\} = exp\left\{\frac{i\Omega_I^0 \hat{I}_z\tau}{2}\right\} exp\left\{\frac{i\Omega_S^0 \hat{S}_z\tau}{2}\right\} exp\left\{-\frac{i\pi J_{HC}2\hat{I}_z\hat{S}_z\tau}{2}\right\}$. Following the first 90° rotation on the I spin, the equilibrium $\hat{I}_z$ magnetization will be rotated to $-\hat{I}_y$. The $\tau/2$ time evolution followed by the two 180° rotations on both I and S spins, and last $\tau/2$ time evolution, just before the final pair of 90° rotations $[\rho(\tau^-)]$ can be represented by the following expression:

$$\rho(\tau^-) = -\hat{Q}\hat{R}_x^{I,S}(\pi)\hat{Q}\hat{I}_y\hat{Q}^{-1}\hat{R}_x^{I,S}(-\pi)\hat{Q}^{-1} \tag{2-96}$$

When $\tau = 1/2J_{HC}$ the expression in Eq. 2-96 simplifies to:

$$\rho(\tau^-) = 2\hat{I}_x\hat{S}_z \tag{2-97}$$

The final pair of 90° rotations comprises of the coherence transfer component as described in the last two steps of Eq. 2-95. However, the entire density matrix prior to the final pair of 90° rotations will be as follows:

$$\hat{\rho}(\tau^-) = \frac{1}{4}\hat{\mathbb{1}} + \frac{1}{4}\,\mathbb{B}_I 2\hat{I}_x\hat{S}_z - \frac{1}{4}\,\mathbb{B}_S\hat{S}_z \tag{2-98}$$

$$\Big\downarrow \left(\frac{\pi}{2}\right)_y^I$$

$$\hat{\rho} = \frac{1}{4}\hat{\mathbb{1}} - \frac{1}{4}\,\mathbb{B}_I 2\hat{I}_z\hat{S}_z - \frac{1}{4}\,\mathbb{B}_S\hat{S}_z$$

$$\Big\downarrow \left(\frac{\pi}{2}\right)_x^S$$

$$\hat{\rho} = \frac{1}{4}\hat{\mathbb{1}} + \frac{1}{4}\,\mathbb{B}_I 2\hat{I}_z\hat{S}_y + \frac{1}{4}\,\mathbb{B}_S\hat{S}_y$$

At the start of Eq. 2-98 the $\hat{S}_z$ magnetization starts inverted due to the 180° rotation on the S spin. The second term $\frac{1}{4}\,\mathbb{B}_I 2\hat{I}_z\hat{S}_y$ is now anti-phase coherence on the S spin which has polarization of spin I (hence is the polarization transferred component); the last term $\frac{1}{4}\,\mathbb{B}_S\hat{S}_y$ is the non-transferred direct component from the S spin as illustrated in Figure. 2-12 below:

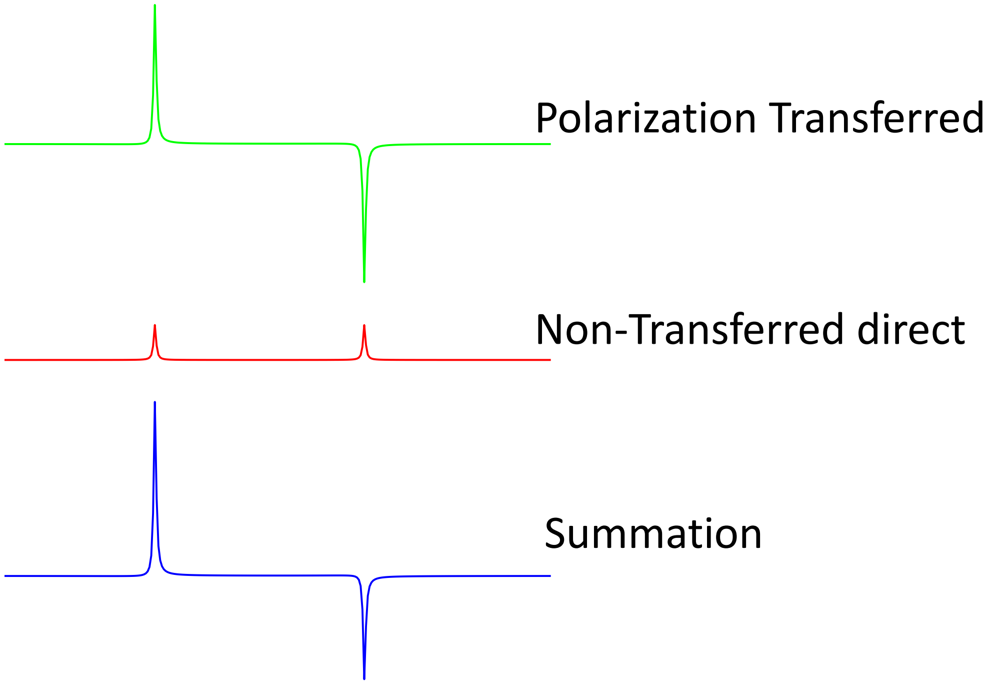

Figure 2-12 *Components of the INEPT spectrum as seen in Eq. 2-96.*

Figure. 2-12 illustrates the signal enhancement seen for the PT component since it benefits from a ~4 fold improvement in signal intensity due to $\frac{\mathbb{B}_I}{\mathbb{B}_S}\sim 4$ when the coupled system is ^{1}H-^{13}C. However, it is beneficial to have the polarization transferred component to be purely in-phase before acquisition, which can be achieved with a modified INEPT sequence with two refocusing pulses (hence termed Refocused INEPT) which is not discussed here.

The DEPT (15) sequence (distortionless enhanced polarization transfer) is another popularly used sequence for heteronuclear NMR spectroscopy. A benefit of DEPT is it allows determining ^{1}H connectivity with ^{13}C atoms (CH_3, CH_2, and CH) groups based on the flip angle of the last rotation on the I spin as illustrated in the pulse sequence in Figure. 2-13 below:

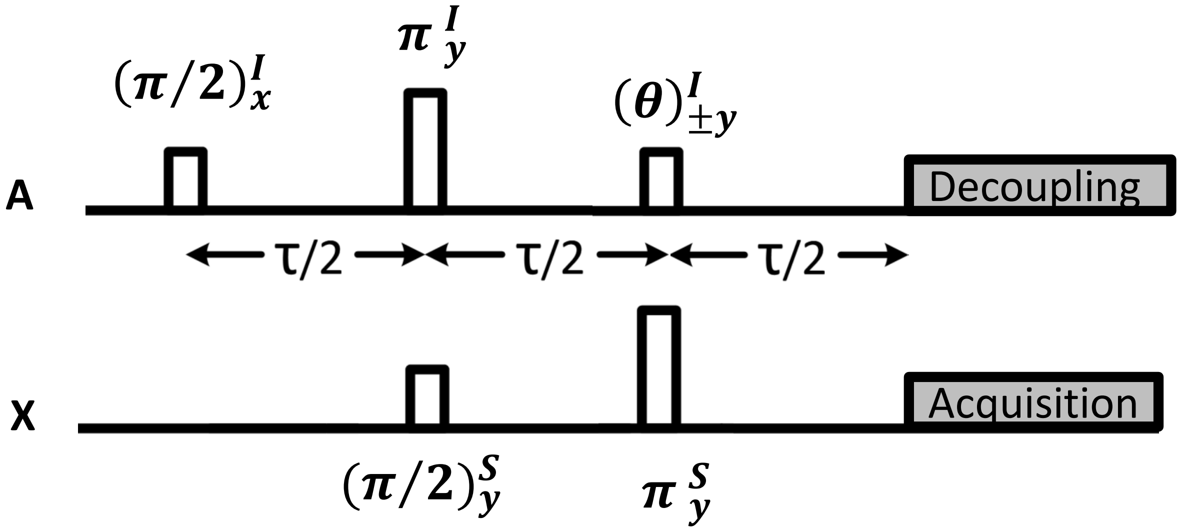

Figure 2-13 *DEPT sequence.*

For *in vivo* ^{13}C MRS, the flip angle θ on the last *I* spin rotation is typically set to $\theta = 45°$ which results in peaks from CH, CH$_2$, and CH$_3$ groups to be positive (there are specific values for θ to optimize sensitivity towards each group), and $\frac{\tau}{2} = 1/2J_{HC}$. The use of the alternating last rotation around $\pm y$ in harmony with the acquisition phase cycle ($\pm 180°$) eliminates the non-transferred direct component when a pair of acquisitions is added. Furthermore, during acquisition, continuous irradiation on the *I* spin is employed (labeled “Decoupling”), which will be described later in this chapter. A flow diagram (similar to Eq. 2-98) is used to describe the DEPT sequence in Eq. 2-100, and to provide visual understanding of in-phase coherence with polarization transfer on the *S* spin. The flow diagram starts with a modification to the equilibrium density matrix in in Eq. 2-93 as follows. The identity matrix $\frac{1}{4}\hat{\mathbb{1}}$ is ignored as it is a dead weight; and the magnetization of $\hat{S}_z$ is normalized to 1 as follows:

$$\hat{\rho}_{eq} = \left(\frac{\mathbb{B}_I}{\mathbb{B}_S}\right) \hat{I}_z + \hat{S}_z \qquad (2\text{-}99)$$

$$\begin{tikzcd}
\hat{\rho}_{eq} = \left(\frac{\mathbb{B}_I}{\mathbb{B}_S}\right) \hat{I}_z + \hat{S}_z \arrow[d, "\left(\frac{\pi}{2}\right)_x^I"] \\
\hat{\rho} = -\left(\frac{\mathbb{B}_I}{\mathbb{B}_S}\right) \hat{I}_y + \hat{S}_z \arrow[d, "\hat{\hat{\mathcal{H}}}(1/2J_{HC})"] \\
\hat{\rho} = \left(\frac{\mathbb{B}_I}{\mathbb{B}_S}\right) 2\hat{I}_x\hat{S}_z + \hat{S}_z \arrow[d, "\left(\frac{\pi}{2}\right)_y^S"] \\
\hat{\rho} = \left(\frac{\mathbb{B}_I}{\mathbb{B}_S}\right) 2\hat{I}_x\hat{S}_x + \hat{S}_x \arrow[d, "(\pi)_y^I"] \\
\hat{\rho} = -\left(\frac{\mathbb{B}_I}{\mathbb{B}_S}\right) 2\hat{I}_x\hat{S}_x + \hat{S}_x \arrow[d, "\hat{\hat{\mathcal{H}}}(1/2J_{HC})\ \text{–DQ state}"] \\
\hat{\rho} = -\left(\frac{\mathbb{B}_I}{\mathbb{B}_S}\right) 2\hat{I}_x\hat{S}_x + 2\hat{I}_z\hat{S}_y \arrow[d, "(\pi)_y^S"] \\
\hat{\rho} = \left(\frac{\mathbb{B}_I}{\mathbb{B}_S}\right) 2\hat{I}_x\hat{S}_x + 2\hat{I}_z\hat{S}_y \arrow[d, "(\pm\theta)_y^I"] \\
\hat{\rho} = \left(\frac{\mathbb{B}_I}{\mathbb{B}_S}\right)\left(2\hat{I}_x\hat{S}_x cos\theta \mp 2\hat{I}_z\hat{S}_x \sin\theta\right) + \left(2\hat{I}_z\hat{S}_y cos\theta \pm\ 2\hat{I}_x\hat{S}_y sin\theta\right) \arrow[d, "\hat{\hat{\mathcal{H}}}(1/2J_{HC})"] \\
\hat{\rho} = \left(\frac{\mathbb{B}_I}{\mathbb{B}_S}\right)\left(2\hat{I}_x\hat{S}_x cos\theta \mp \hat{S}_y \sin\theta\right) -\left(\hat{S}_x cos\theta \mp\ 2\hat{I}_x\hat{S}_y sin\theta\right)
\end{tikzcd} \tag{2-100}$$

A few points to note from the DEPT sequences diagram are as follows:

We can see that after the second set of rotations, the spin system of interest $\left(\frac{\mathbb{B}_I}{\mathbb{B}_S}\right) 2\hat{I}_x\hat{S}_x$ is in a double quantum coherence state, which does not evolve under heteronuclear scalar coupling (during the second $\frac{\tau}{2}$ time period). In addition, the equilibrium S spin magnetization also gets rotated onto the transverse plane (non-transferred component). Alternating the $(\pm\theta)_y^I$ rotation phase between acquisitions can be seen to alter the phase of the polarization transferred spin state $\left(\frac{\mathbb{B}_I}{\mathbb{B}_S}\right)\left(\mp\hat{S}_y\sin\theta\right)$ in concert; while simultaneously the observable non-transferred component $(-\hat{S}_x cos\theta)$ is unaffected by this alternating $(\pm\theta)_y^I$ rotation. Note that the non-transferred $\mp 2\hat{I}_x\hat{S}_y sin\theta$ component alters phase in concert with the last pulse phase, however it is never observable. As a result, the subtraction of two acquisitions will produce signal from the purely coherence transferred spin state, and summation will produce signal purely from the non-transferred spin state. The $2\hat{I}_x\hat{S}_x cos\theta$ component never becomes observable.

As illustrated above, polarization transfer methods provide enhanced signal detection from S-spins (^{13}C nuclei) directly attached to one or more protons. The main challenges associated with direct excitation of ^{13}C NMR however are: limited sensitivity due to the low gyromagnetic ratio of ^{13}C nuclei, and complexity in spatial localization due to large chemical shift dispersion associated with ^{13}C nuclei (in the realm of 100ppm). Chemical shift effects can be minimized by using highest possible gradient fields (16). However, with large gradient fields, large bandwidth RF pulses are also required, resulting also in high RF power deposition (17). Since both the INEPT and DEPT sequences start with an excitation pulse (90° rotation) on the I spin (or proton channel in ^{13}C MRS), it provides a mechanism to perform localized ^{13}C MRS on the proton channel. We will describe a proton localized DEPT sequence for rat brain imaging in Chapter 5.

2.3.5.5 *Indirect ^{13}C MRS*

Detecting protons has a $\left(\frac{\gamma_I}{\gamma_S}\right)^3 \sim 64$ advantage in signal intensity, and a $\left(\frac{\gamma_I}{\gamma_S}\right)^2 \sim 16$ advantage in SNR (in this thesis, SNR and sensitivity mean the same thing and are used interchangeably), relative to direct detection. Relative to polarization transferred ^{13}C MRS, SNR can be increased by a factor ~4 with indirect ^{13}C MRS methods (also depicted symbolically as ^{1}H-[^{13}C] MRS), where like the nomenclature suggests, signal is detected from protons directly attached to ^{13}C nuclei. Indirect ^{13}C MRS can be categorized into 2 main parts (17); single-shot multiple quantum coherence (MQC) based methods (18), and J-difference based (19) methods. MQC based methods selectively de-phase signal from all protons not attached to ^{13}C nuclei in a single scan; hence, can achieve single-shot water suppression, with the main drawback of losing information to calculate fractional enrichment of ^{13}C metabolites.

Proton observed carbon edited (POCE) ^{1}H-[^{13}C] MRS is a J-difference method (20,21) which involves obtaining two sets of data; 1) a scan that includes a selective spin echo (180° rotations on the ^{1}H channel only as illustrated in Figure. 2-9 called the EDIT OFF scan). 2) a scan that includes a non-selective spin echo (180° rotations on both ^{1}H and ^{13}C channels, a non-selective RF pulse as described in Figure. 2-10 called the EDIT ON scan) which refocuses all phenomena in the previous case except heteronuclear scalar coupling. However, for POCE, the $\frac{\tau}{2}$ time needs to be set such that $\tau = 1/J_{HC}$.We now re-write the spin evolution expressions for the two cases; since the simplified density matrix expression [$\rho_{OFF}(\tau)$] for the EDIT OFF scan (Eq. 2-87) is independent of the evolution time it stands as:

$$\rho_{OFF}(\tau) = \hat{R}_x^I(\pi)\hat{I}_x\hat{R}_x^I(-\pi) = \hat{I}_x \qquad (2\text{-}101)$$

The density matrix expression [$\rho_{ON}(\tau)$] for the EDIT ON scan follows from Eq. 2-91 simplifies when $\tau = 1/J_{HC}$ to:

$$\rho_{ON}(\tau) = \hat{R}_x^{I,S}(-\pi) exp\left\{-\frac{i\pi J_{HC}2\hat{I}_z\hat{S}_z\tau}{2}\right\}\hat{I}_x exp\left\{\frac{i\pi J_{HC}2\hat{I}_z\hat{S}_z\tau}{2}\right\}\hat{R}_x^{I,S}(\pi) \qquad (2\text{-}102)$$

$$\rho_{ON}(\tau) = \hat{R}_x^{I,S}(-\pi)\left\{\hat{I}_x\cos\left[\frac{\pi J_{HC}\tau}{2}\right] + 2\hat{I}_y\hat{S}_z\sin\left[\frac{\pi J_{HC}\tau}{2}\right]\right\}\hat{R}_x^{I,S}(\pi)$$

$$\rho_{ON}(\tau) = \hat{R}_x^{I,S}(-\pi)\{-\hat{I}_x\}\hat{R}_x^{I,S}(\pi) = -\hat{I}_x$$

The evolution of the heteronuclear scalar coupled spins are cosinusoidal with respect to time τ for the EDIT ON case hence for $\tau = 1/J_{HC}$ the scalar coupled protons are inverted to $-\hat{I}_x$. As a result, when the two experiments are separately acquired and subtracted, signal from all ^{1}H nuclei directly bound to ^{13}C nuclei remains, and when added, signal from all ^{1}H bound to ^{12}C is retained. This way POCE provides means to obtain fractional enrichment of ^{13}C nuclei.

Many methods have been developed to perform localized POCE MRS; a commonly employed technique is to perform a localized spectroscopy sequence such as image selected *in vivo* spectroscopy (ISIS; 22), localization by adiabatic spin-echo refocusing (LASER;23), or PRESS first, with typically the final echo time (TE) of the sequence set to be $TE > 1/J_{HC}$ ms (where $1/J_{HC}$ is in the 7-8ms range for *in vivo* ^{13}C studies), and placing an inversion pulse on the ^{13}C channel $1/2J_{HC}$ ms before the acquisition (for the EDIT ON scan). An example PRESS localized POCE MRS sequence (24) is illustrated in Figure 2-14.

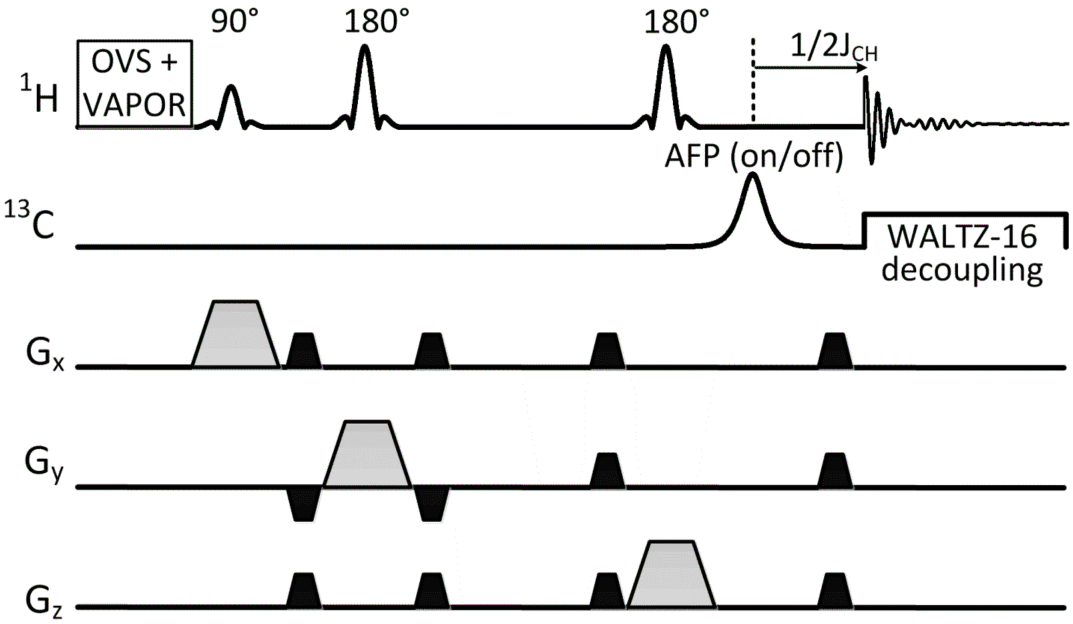

Figure 2-14 *A pulse sequence for the PRESS localized POCE sequence.*

At the time point $1/\,2J_{HC}$ ms before the acquisition (illustrated by the vector diagram in Figure. 2-15), protons coupled to ^{13}C nuclei will be in a purely anti-phase coherence state.

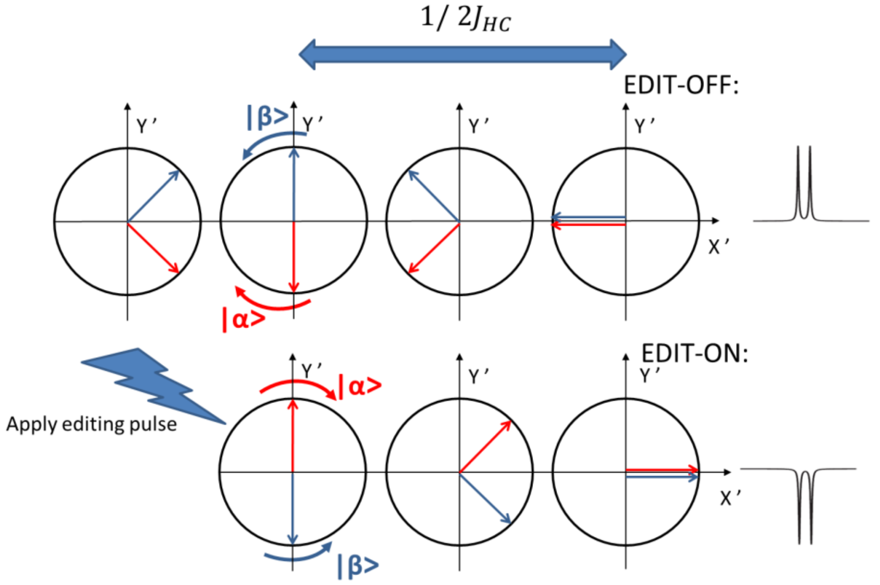

Figure 2-15 *Vector diagram illustrating EDIT OFF and EDIT ON conditions.*

At this anti-phase coherence state, playing out an inversion pulse (EDIT ON) can be seen to invert the sense of rotation in Figure. 2-15 relative to the case where no editing pulse was used (EDIT OFF), resulting in $\hat{I}_x$ and $-\hat{I}_x$ spin states at the end for the two scans.

2.3.5.6 *Heteronuclear Decoupling*

Heteronuclear decoupling involves the application of a train of inversion pulses on the non-observing nucleus to remove effects of heteronuclear scalar coupling which causes peak splitting (see Figure. 2-7). As a result of decoupling, signal intensity can be enhanced due to collapsing of the doublet, and reduces spectral crowding. In principle, heteronuclear decoupling is similar to J-difference editing described for POCE MRS above. By applying an inversion pulse, we saw that the sense of rotation was flipped in Figure. 2-15. Now imagine a case, where such inversion pulses are played out repeatedly as illustrated in Figure. 2-16A. The resulting evolution of the coupled spin system during the first two inversion pulses will be as illustrated in Figure 2-16B as a result, where the sense of rotation has been inverted twice. It then becomes clear that by applying such a train of pulses during the entire acquisition, we have achieved a spin-lock like situation where the coupled spin system appears frozen along the *x*-axis. Figure. 2-16C illustrates an undecoupled spectrum of ^{13}C labeled Acetate (left sub figure in red), and the effect of heteronuclear decoupling on the methyl group of the Acetate doublet, which has collapsed to a singlet (right) with doubled amplitude. Note that the spectral footprint in blue is from Choline with no ^{13}C labeling, hence is unaffected by decoupling. However, applying continuous inversion pulses on the ^{13}C channel while acquiring signal on the ^{1}H channel (as illustrated in Figure. 2-16A), is a cause for hardware complications, that will be described later in this chapter, and in chapter 3.

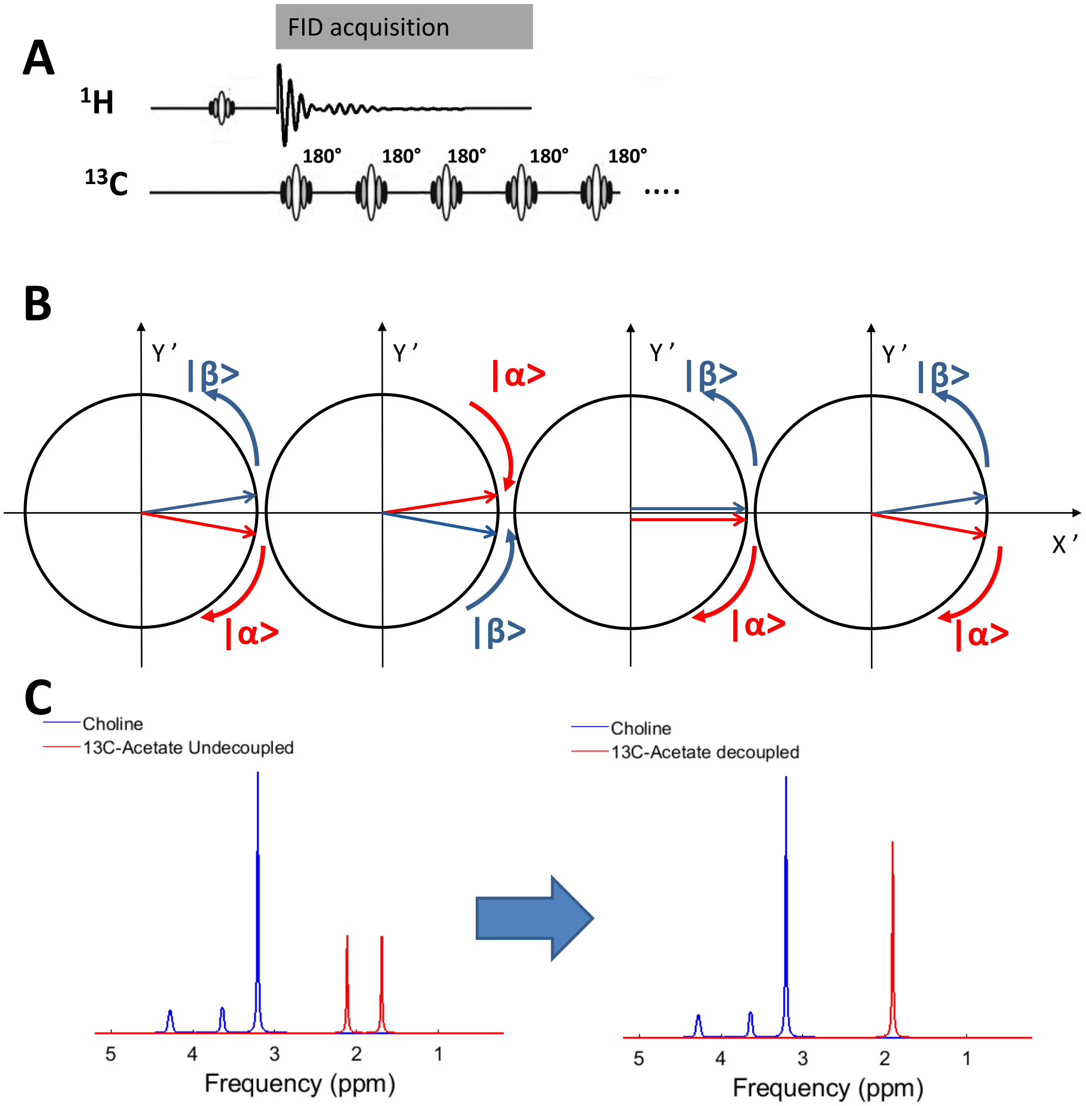

Figure 2-16 *(A) Principle of heteronuclear decoupling,(B) Vector diagram of heteronuclear spin evolution during decoupling, (C) Spectra of* ^{13}*C labeled Acetate without decoupling (left), and with decoupling (right).*

Now we can combine editing, and heteronuclear decoupling to illustrate POCE MRS at work. Figure. 2-17A illustrates an EDIT OFF POCE spectrum with decoupling on, where ^{13}C labeled and unlabeled metabolites are all in the $\hat{I}_x$ state; Figure. 2-17B illustrates an EDIT ON POCE spectrum, also with decoupling on, however due to the inversion pulse, ^{13}C coupled protons are inverted (-$\hat{I}_x$ state) relative to Choline, which is unaffected by the inversion pulse.

Next, subtracting these two scans produces a spectrum exclusively of protons coupled to ^{13}C nuclei, which is the proton observed carbon edited spectrum.

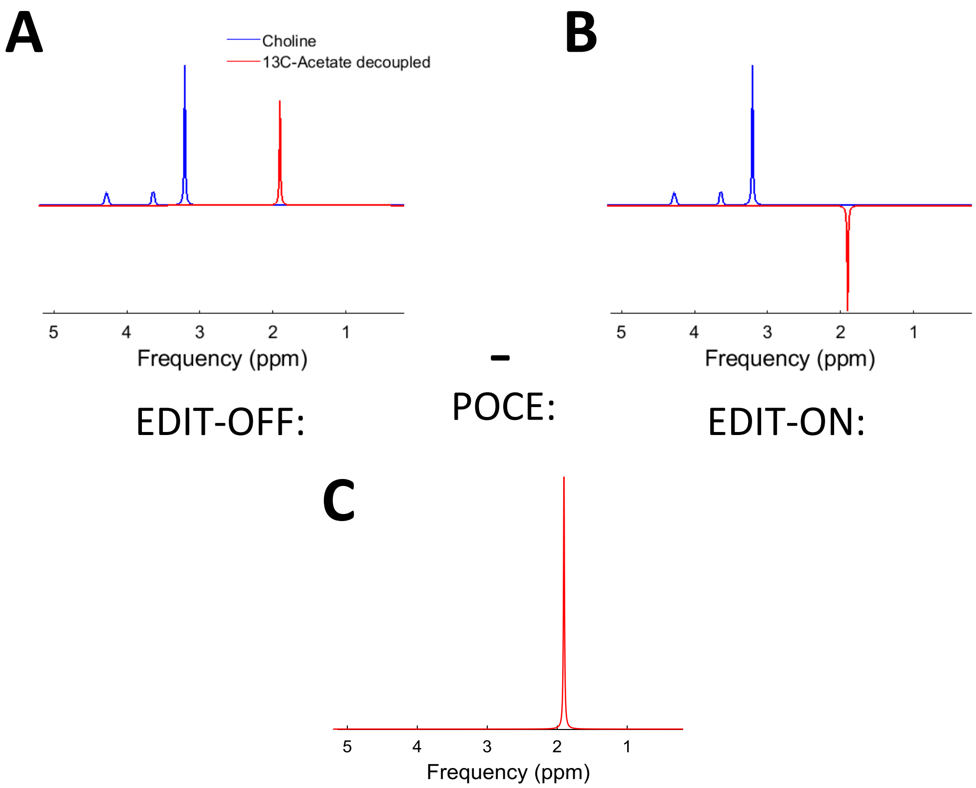

Figure 2-17 *(left) undecoupled spectra where the Acetate signal is seen to be a doublet. (right) if acquired during decoupling, the double collapses into a singlet with doubled intensity.*

2.4 MRI Hardware

An MRI scanner (human or animal) in its entirety is a complex apparatus that can be decomposed to six essential components: 1) The main superconducting electromagnet used to generate the main magnetic field $\mathbf{B_0}$. 2) A gradient coil system that can generate linearly varying magnetic fields in the *x*, *y*, and *z* directions and be superimposed to generate time varying magnetic field gradients for spatial localization in MRS, and spatial encoding in MRI. 3) A shim coil system to induce minute spatially varying magnetic fields to adjust the magnetic field inhomogeneities caused by susceptibility artifacts. 4) A radiofrequency (RF) coil system to generate the RF field ($\mathbf{B}_1$) described earlier, and to detect the NMR signal. 5) A receiver system consisting of low-noise small signal amplifiers, filtering and analog to digital conversion (ADC) to digitize and store the data. 6) A central computer system that communicates and synchronizes all the hardware to work in synergy during an MRI experiment.

For brevity, this section focuses on RF coil design and RF hardware considerations for heteronuclear ^{1}H/^{13}C MRS experiments for dynamic *in vivo* rat brain imaging.

2.4.1 Radio Frequency Coils

2.4.1.1 Resonant Circuits

The starting point of a sensitive RF probe involves the development of a *resonant* circuit tuned to the frequency of interest. Many practical day-to-day analogs can be used to describe the mechanism in which the sensitivity of a system is maximized; when it is at resonance (or its natural frequency). For instance, if two neighboring strings on a guitar were far apart in pitch, suspend a small piece of paper on top of one string while strumming the second string, you will notice that the piece of paper starts to vibrate violently at one point when the tension of this string is adjusted; at this point long behold, you will realize that the pitch (resonant frequency) of the two strings are similar. The message to learn is that transmission and reception of energy from the first string to second string is most efficient when they share the same resonant frequency. The same principle applies for electrical resonators, where the sensitivity of a RF probe will be maximized if it was designed to be resonant at the Larmor frequency (ω_0) of the spin species of interest. The simplest lossless resonant circuit can be constructed by connecting a capacitor and inductor together; in reality however, there would be some form of resistance in the circuit, hence let us consider a Resistor (R), inductor (L), capacitor (C) circuit (RLC in short) as illustrated in Figure. 2-18.

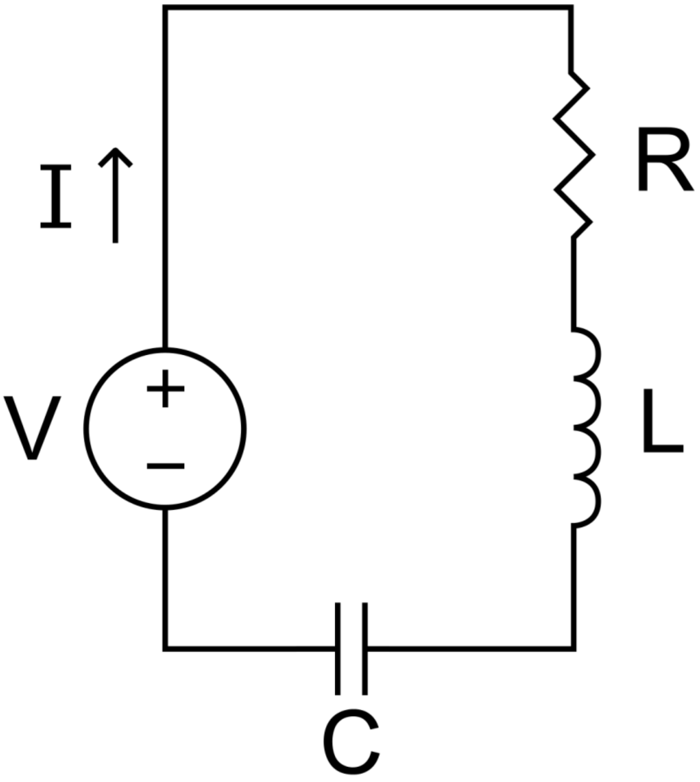

Figure 2-18 *A series RLC circuit diagram.*

We can start circuit analysis by writing Kirchoff's voltage law, which give:

$$V = V_R + V_L + V_C \tag{2-103}$$

In frequency domain we can apply Ohm's law using complex impedances to get:

$$V(i\omega) = I(i\omega)\left(R + i\omega L + \frac{1}{i\omega L}\right) \tag{2-104}$$

From Rearranging the above:

$$I(i\omega) = \frac{1}{\left(R + i\omega L - \frac{i}{\omega C}\right)} V(i\omega) \tag{2-105}$$

When $\left(i\omega L - \frac{i}{\omega C}\right) = 0$ we can see that the maximum current condition is achieved; this is also where the reactances are cancelled out leaving only the real part of resistance R. Rearranging this expression gives:

$$\omega_0 = \frac{1}{\sqrt{LC}} \tag{2-106}$$

This expression turns out to be the resonant condition for the circuit described above. In the case for an RF probe, which can also be represented by an RLC circuit, L and C are chosen such that the expression in Eq. 2-106 equals the Larmor frequency ω_0.

2.4.1.2 Impedance Matching

All loads and sources within the RF hardware chain have input and output impedances. Thus when components are connected, impedances at the interfaces (between the source and load) need to be matched for efficient power transfer where the reflection coefficient (Γ) is minimized. Γ is given by:

$$\Gamma = \frac{Z_L - Z_S}{Z_L + Z_S} \tag{2-107}$$

where Z_L and Z_S are load and source impedances, respectively. From Eq. 2-107 it is immediately apparent that Γ is minimized when load and source impedances are matched. In practice all load and source impedances are set to be 50Ω, which happens to be due to the 50Ω standard characteristic impedance of transmission lines used to interface RF components in MRI hardware.

Returning back to the resonant RLC circuit described, we now see that the probe impedance needs to be matched to the source for efficient power transfer. In general, a matching network would be placed immediately after the probe as illustrated in Figure. 2-19, which would transform the probe impedance Z_L to Z_{In}, and desired to be equal to the source impedance Z_S. The topology of the matching network can vary based on the probe impedance and desired characteristics, but a rudimentary network can be realized with a series or parallel capacitor.

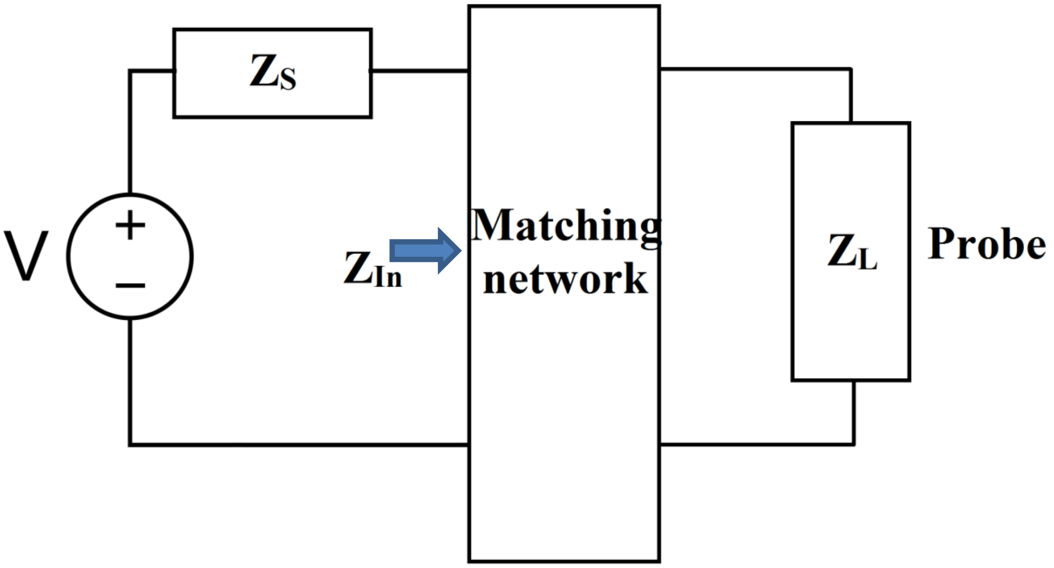

Figure 2-19 *Impedance matching of an RF probe with a matching network.*

2.4.1.3 Coil Losses

Ideal capacitors and inductors have no internal resistances, thus reactive energy stored in a LC circuit would not dissipate through circuital elements. In reality however all conductors (such as wire wound inductors) have some form of resistance, and capacitors have a certain level of leakage as characterized by the *loss tangent*. The *quality factor* (Q) is a metric used to gauge the coil performance (the higher the better) which is defined as the ratio between the maximum stored energy, to the total energy dissipated per cycle, and for an RF coil can be given by:

$$Q = \frac{\omega L}{R} \tag{2-108}$$

here, R is the resistive component of the coil.

All forms of energy losses in the RF probe can be treated as effective resistances that introduce thermal noise as given by the Nyquist-Johnson (25) equation given by:

$$\sigma = \sqrt{4Rk_BT\,\Delta f} \tag{2-109}$$

where R is the effective resistance, k_B is the Boltzmann constant, T is the temperature in Kelvin, and Δf is the bandwidth of the operating frequency. Apart from coil losses, other dominant sources of noise encountered in an RF probe include: load/sample related losses, and radiation losses, which we will discuss next.

Coil losses as described above originate from resistances of electrical components used to construct the RF probe. Resistive losses through conductors will be larger than its static resistance (DC) due to the skin effect that restricts current flow along the conductor surface at RF frequencies.

Load or sample related losses are caused by induced currents in the conducting sample at the frequency of operation, and increases with the square of the magnetic field strength (26). Sample related losses can be reduced by minimizing electric fields within the sample produced by the probe; as such the two components of the electric field generated that lead to sample losses must be noted: 1) the non-conservative electric field, also known as the rotational component and 2) the conserved electric field, also known as the irrotational component. The non-conservative electric field is caused by the time-varying magnetic field in the sample, which cannot be reduced, since the $\mathbf{B}_1$ field is required to perform imaging. The conserved electric field arises from voltage differences in the probe, which can be reduced by distributing capacitors along the inductive loop, and by balancing the probe.

Radiation losses occur when the RF probe behaves like an antenna; a phenomenon that becomes significant at higher field strengths due to the operating wavelength approaching the RF probe dimensions. Radiation related losses can be minimized by shielding, and by balancing the RF probe.

2.4.1.4 RF Coil Design Considerations for Heteronuclear $^{13}C/^{1}H$ MRS

When comparing a proton based MRI sequence or MR spectroscopy pulse sequence with a heteronuclear MRS experiment such as the POCE sequence illustrated in Figure 2-14, or the DEPT sequence in Figure 2-13 a few contrasting differences can be noticed from a RF coil design perspective; first, RF pulses are employed on two different nuclear species, thus the apparatus needs to be sensitive to two separate frequency bands. Secondly, heteronuclear decoupling is employed with high power (>200W_{pk}) RF irradiation on one nuclear species while acquiring NMR signals from the second nuclear species to improve sensitivity and reduce spectral crowding. Throughout the hardware developments as part of this work, I have not come across a more daunting challenge than working towards attenuating decoupling noise from affecting the received signal!

The requirement for the RF apparatus to be operational at two different frequency bands calls for either the use of dual tuned RF probes (a single probe with two resonant frequencies); however such a probe will be a challenging build for POCE MRS since RF irradiation and signal reception must happen simultaneously. Alternatively, two separate probes, tuned to each respective Larmor frequency can be utilized. In this case however, proper isolation between probes (typically via geometric decoupling) is used to attain some level of attenuation of decoupling noise related artifacts. A popular coil topology for heteronuclear MRS is the design described by Adriany and Gruetter (27) utilized for direct ^{13}C detection, in which one RF probe is split into two geometrically isolated (with overlap) surface loops driven in quadrature, and a second separate RF probe is placed geometrically centered between the quadrature pair is used for the second channel (further detailed in chapter 3). Besides the RF power advantage of quadrature drive, it also provides better RF field homogeneity and improves isolation between the two channels. Despite this favorable design for reduced coil-coil interactions, further isolation of decoupling noise is still required. Placement of a low insertion loss (< -0.5dB) RF filters immediately before the preamplifier is necessary, in addition strategic placement of high power handling (~1kW) low insertion loss RF filters will need to be strategically placed to minimize spurious noise due to non-linearities of the power amplifier and RF switching circuits from leaking into the acquired signal of interest (17). A more in-depth description of the successful RF apparatus we developed is presented in chapter 3.

2.5 Dynamic *in vivo* Carbon-13 Magnetic Resonance Spectroscopy

Carbon-13 MRS presently remains to be the only method capable of providing measurements of neuroenergetics and neurotransmitter cycling in the brain, non-invasively, *in vivo* (28). In this section we provide an overview surrounding this powerful method, its capabilities, and limitations; and describe the motivations for this work and the gaps attempted to be filled.

2.5.1 General Introduction

The ability to probe into the relationship between neuronal activity and cerebral energy metabolism is essential to understand brain function (17). Under normal conditions, it is well known that the primary mode of cerebral energy production occurs from glucose oxidation. Positron emission tomography (PET) and other radiolabel based techniques are commonly used to assess local glucose uptake in the brain (29) following the infusion of a radioactive glucose analog (such as 2-fluoro-2-deoxy-D-glucose, known as FDG). However, information provided by local glucose uptake with such radioactive tracers is limited, as it may not accurately reflect glucose metabolism through metabolic pathways such as glycolysis, and cannot provide related flux information, since different metabolic pools cannot be distinguished. In contrast, NMR detectable tracer studies performed with stable isotopes can be followed non-invasively with NMR techniques since different chemical groups of metabolites (as a result of metabolism) provide a unique spectral footprint due to chemical shift.

Carbon-12 is the most abundant isotope of carbon in nature (accounting for 98.89% of all carbon), and has no net nuclear spin– thus is unobservable with NMR. The second most abundant isotope of carbon is carbon-13 (^{13}C), which is a stable isotope with natural abundance of 1.11% and is an NMR visible spin ½ particle. Due to the relatively low natural abundance, *in vivo* ^{13}C MRS has an intrinsically very low sensitivity. However, following the infusion of a carbon-13 enriched substrate, such as glucose, ^{13}C MRS provides a means to detect metabolites labeled with ^{13}C (with concentrations sufficient for NMR detection) due to metabolism of the infused ^{13}C labeled glucose. With ^{13}C NMR, the additional neutron to carbon-12 (in carbon-13) has negligible effects on the biochemical properties of ^{13}C labeled substrates, thus is metabolized in the brain as if it was carbon-12 based. In comparison, FDG used in PET requires modifications to correct for differences between glucose and the glucose analog transport through membranes (30).

Two of the most abundant and rapidly labeled metabolites following a ^{13}C labeled glucose infusion are: [4-^{13}C]-Glutamate (Glu) and [4-^{13}C]-Glutamine (Gln) in the mammalian brain (31), which at the bare minimum, are easily detected with ^{13}C MRS (provided [4-^{13}C]-Glu and [4-^{13}C]-Gln are resolved at the operating magnetic field). A detailed description of Glu and Gln detection with direct and indirect ^{13}C MRS is detailed in chapter 5. Labeling of Glu and Gln is recognized as a mechanism to study brain metabolic compartmentation (detailed later), making ^{13}C MRS a powerful technique to study neuroenergetics *in vivo*.

2.5.2 The 2-Compartment Model and Metabolic Modeling

Excitatory glutamatergic neurons have been recognized to account for over 80% of neurons, and synapses in the cerebral cortex (32). The released neurotransmitter glutamate, during neurotransmission, however cannot be re-up taken by neurons, and is known to be mostly shuttled into astroglia (33). Glutamate entering astroglia may enter the astroglial TCA cycle, or be converted to glutamine (34), where glutamine synthesis via metabolism of glutamate is one of the primary metabolic pathways in astroglia (16). Glutamine is then shuttled back into the neuron from the astroglia for the synthesis of glutamate via glutaminase lost during neurotransmission. This cycle of Glutamate released from the neuron during neurotransmission, converted to glutamine in astrocytes and shuttled back to the neuron for the re-synthesis of glutamate is called the *glutamate-glutamine cycle*, as illustrated by the two-compartment model in Figure 2-20.

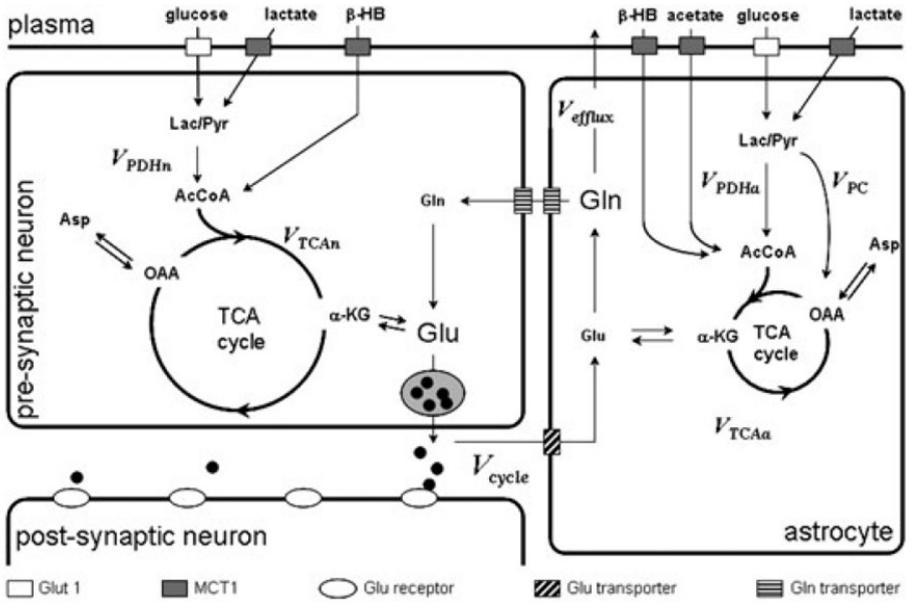

Figure 2-20 *A diagram illustrating the glutamate glutamine cycle [adopted from (28) with permissions A.1]. The diagram illustrates a two-compartment model consisting of a pre-synaptic glutamatergic neuron, and surrounding astroglia. The blood brain barrier is illustrated by the solid horizontal line separating the two compartments and plasma. In the case of a* ^{13}*C labelled glucose infusion, glucose enters the brain and astrocyte with the aid of a glucose transporter in the blood brain barrier and is metabolized producing* ^{13}*C labeled metabolites as illustrated.*

Now let us backtrack to glutamate synthesis in the glutamatergic neuron from [1-^{13}C] glucose (glc) in plasma. As illustrated in Figure 2-20, [1-^{13}C]-glc flows through glycolytic intermediates (with negligible concentrations) and labels pyruvate at the third position (3-^{13}C-Pyr), which gets rapidly converted to 3-^{13}C-Lactate (Lac) (with 0.5-1.5mm/kg concentrations, and thus is NMR visible). [3-^{13}C]-Pyr is then converted to Acetyl-CoA, which is directly incorporated into the neuronal tricarboxylic acid (TCA) cycle, where the small pool of [4-^{13}C]-2-oxoglutarate is labeled, followed by its transfer of mitochondrial [4-^{13}C]-2-oxoglutarate to the larger [4-^{13}C]-Glu pool (16). Accumulation of [4-^{13}C]-Glu is then considered to be indicative of the neuronal TCA cycling rate, and subsequent labeling of [4-^{13}C]-Gln to be indicative of the Glutamate-Glutamine neurotransmitter cycling rate. Our discussion will be primarily limited to glucose metabolism and the labeling of glutamate and glutamine. The interested reader is referred to the following review articles for a more in-depth discussion (16,17,28,35) on *in vivo* ^{13}C MRS.

Figure 2-21 illustrates an example of time-resolved localized ^{13}C MR spectra obtained on rat brain following an infusion of ^{13}C labeled glucose (such as [1-^{13}C]-Glc or [1,6-$^{13}C_2$]-Glc). Here, early labeling of [4-^{13}C]-Glu, and subsequent labeling of [4-^{13}C]-Gln can be observed.

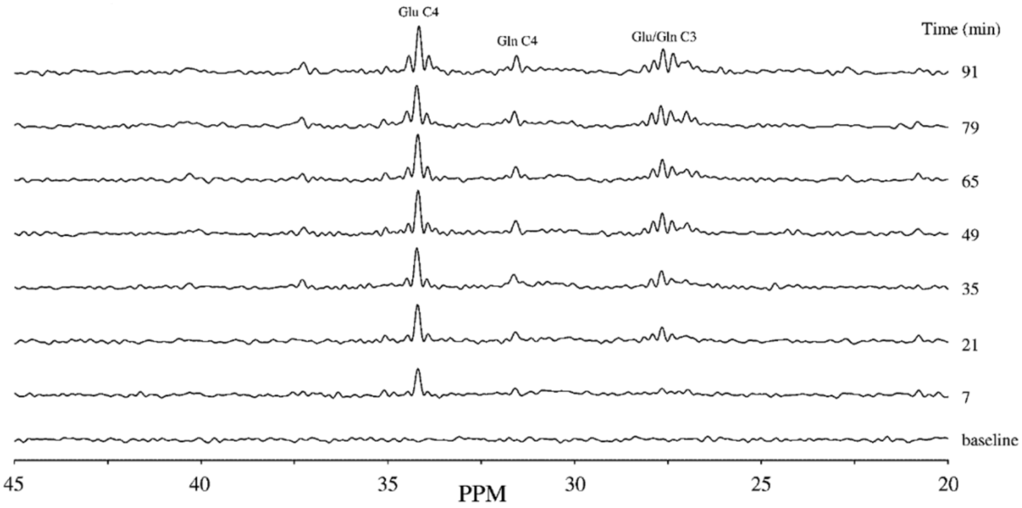

Figure 2-21 *Time-resolved ^{13}C MR spectra from rat brain [adopted from (4) with permissions A2]. The time-resolved direct ^{13}C spectra are from a 300µl voxel in rat brain at 7T following a [1,6-$^{13}C_2$]-glc infusion.*

Towards the end of a [1-^{13}C]-glc infusion experiment, typically ~15 different ^{13}C labeled metabolite groups will be detected, and by using a spectral estimation tool such as LCModel (36), time-resolved concentrations of each labeled metabolite group (especially [4-^{13}C]-Glu, and [4-^{13}C]-Gln) can be obtained. LCModel is a software package for automatic quantification of *in vivo* proton MR spectroscopy data. Based on basis-sets generated for the sequence and TE used, the software package computes a linear combination of the basis-set that minimizes the error relative to the actual data. In order to obtain quantitative metabolic fluxes (such as the neuronal TCA cycling rate, Glu-Gln cycling rate, etc) from the metabolite concentrations, the experimental data is fitted to a quantitative mathematical model devised based on mass-balance equations for the various metabolic pools. For example, illustrated in Figure 2-22 is the total concentration of a metabolite M, where $V_{in}[k]$ corresponds to influx rates, and $V_{out}[n]$ corresponds to efflux rates that would individually be linked with other metabolic pools.

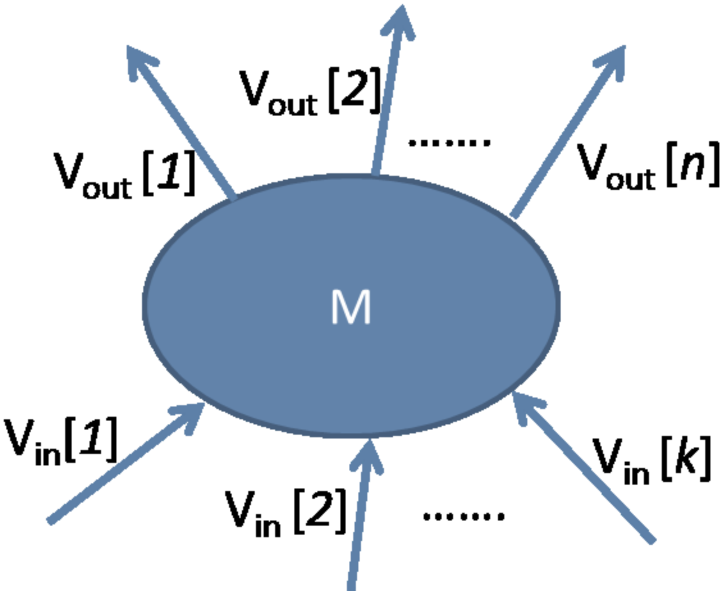

Figure 2-22 *Fluxes of a metabolic pool for quantitative metabolic modeling.*

The flux rates and concentration of metabolite M can then be described according to the following equations:

$$\frac{dM(t)}{dt} = \sum_{k=1}^{K} V_{in}[k] - \sum_{n=1}^{N} V_{out}[n] \tag{2-110}$$

$$\frac{dM^*(t)}{dt} = \sum_{k=1}^{K} \left(\frac{S_k^*(t)}{S_k}\right) V_{in}[k] - \left(\frac{M^*(t)}{M}\right) \sum_{n=1}^{N} V_{out}[n] \tag{2-111}$$

where M is the total (^{12}C +^{13}C) metabolite concentration, and M^* is the ^{13}C concentration of metabolite M, K and N represent the number of influx and efflux pathways associated with metabolite M, respectively; and the fraction $\left(\frac{S_k^*(t)}{S_k}\right)$ corresponds to the fractional ^{13}C labeling of each substrate S_k.

The differential equations for metabolite M in Eq. 2-110 and 2-111 can be written out for all metabolite pools observed. The metabolic flux rates can then be estimated numerically by minimizing the least-squares difference between the measured concentrations (as per metabolite quantification described above) and calculated concentrations.

2.5.3 Typical Experimental Set-Up

From the aforementioned description of dynamic *in vivo* ^{13}C MRS experiments, it can be seen that the set-up requires non-standard hardware upgrades, in addition to animal/human subject preparation. In this section, we describe the typical experimental setup for rat brain imaging which is the relevant component for this thesis.

The experimental set-up can broadly be broken down into three sub-sections: 1) Animal preparation, 2) type of substrate used, and 3) direct vs indirect ^{13}C detection:

Animal preparation: Commonly animal preparation for a dynamic *in vivo* ^{13}C MRS experiment involves the infusion of the ^{13}C labeled substrate (such as glucose in saline) intravenously. In addition, a necessary input for metabolic modeling is the fractional content of the ^{13}C enriched substrate in plasma, which requires periodic arterial blood sampling. As such following general anaesthesia, typically two small lines are placed on the femoral vein (for infusion), and the femoral artery (for blood collection). Since the cannulation happens approximately half an hour before the study begins, the cannulae are flushed with ~1/20 ratio of heparin in saline, to avoid coagulation. If the study involves a ^{13}C labeled glucose infusion, the rat is typically fasted overnight to reach a state of hypoglycemia (~4mM) and achieve stable hyperglycemic levels (~10mM) within a couple of minutes into the experiment, after the infusion onset following an exponentially decaying infusion protocol (17). The overall infusion typically lasts for 90-150 mins.

Type of substrate used: The vast majority of *in vivo* ^{13}C MRS studies use [1-^{13}C]-Glc or [1,6-$^{13}C_2$]-Glc as the labeled substrate. [1-^{13}C]-Glc is the most common of the two (specially in human populations) as it is economically more favorable compared to [1,6-$^{13}C_2$]-Glc. The labeling pattern of [1,6-$^{13}C_2$]-Glc is nearly identical to that of [1-^{13}C]-Glc with the benefit of doubling the fractional enrichment of Pyruvate. Extending our previous discussion on glucose metabolism, the glucose molecule is broken down into two Pyruvate molecules; in the case of [1-^{13}C]-Glc, only one of the two Pyruvate molecules becomes [3-^{13}C]-Pyr; on the other hand, if [1,6-$^{13}C_2$]-Glc is used, both pyruvate molecules become [3-^{13}C]-Pyr; hence doubling the [3-^{13}C]-Pyr pool and subsequent metabolites that get labeled. The doubling of metabolite fractional enrichment directly relates to ~2 times SNR of ^{13}C labeled metabolites, and for animal experiments the extra cost of [1,6-$^{13}C_2$]-Glc is a minor consideration given the SNR benefits attainable.

[2-^{13}C]-Acetate is an interesting substrate that is almost exclusively transported and metabolized by astroglia (see Figure 2-20). In comparison, glucose is transported and metabolized in both astroglia and neurons (see Figure 2-20), where extensive mixing of glucose occurs, and the TCA cycle fluxes of both compartments are convolved. The labeling of [4-^{13}C]-Glu is then heavily weighted by the neuronal TCA cycle, thus making the glucose experiment relatively insensitive to changes of the smaller astroglial TCA cycling fluxes. Acetate, that is selectively transported into the astrocyte, is converted to [2-^{13}C]-acetylCoA, which then labels intermediates of the astroglial TCA cycle and subsequently labels the astroglial glutamate pool, thus can be used to exclusively study cellular energetics of astrocytes.

In addition to the three substrates described above ([1-^{13}C]-Glc, [1,6-$^{13}C_2$]-Glc, and [2-^{13}C]-Acetate), there are other variants of glucose, such as [2-^{13}C]-Glc and other substrates such as β-hydroxybutyrate and lactate, that can be used to study specific aspects of the 2-compartment model under different conditions.

Direct vs indirect ^{13}C detection - As described in section 2.3.5, ^{13}C labeled substrates can be detected directly or alternatively via protons attached to carbons indirectly. Each detection mechanism has its own set of advantages and disadvantages. In essence, direct detection provides superior spectral dispersion and thus a higher amount of spectral information over indirect detection (such as ^{13}C-^{13}C isotopomer information, that cannot be obtained with *in vivo* indirect ^{13}C MRS), however at the cost of reduced SNR relative to indirect ^{13}C MRS. When considering direct detection via polarization transfer (PT), a sensitivity gain of ~4x is achieved, which is still a factor ~4 lower than sensitivity gains achievable with indirect ^{13}C MRS (considering an AX spin system). Time-resolved spectra following the ^{13}C substrate infusion, typically is averaged in the range of 4-10 mins, which is dictated by the attainable SNR and ability to detect dynamic changes in the spectrum. SNR can be improved by increasing the size of the localized region imaged, or by acquiring more averages per time point. On the other hand accuracy of the metabolic modeling process is improved with improved time resolution, and region specificity is compromised when large voxels are used. Furthermore, the disparity between attainable sensitivity with direct and indirect detection requires the study to be designed accordingly. For example ^{13}C MRS studies on rat brain conducted on 7-9.4T field strengths report: the use of ~100μl voxel sizes for indirect ^{13}C MRS with time resolution of 5-8mins

(37,38), and the use of >300µl voxels for direct ^{13}C MRS with PT with similar time resolution (16,39). As can be noted, the ~3 times increase in volume size provides a proportionately improved SNR and thus PT based direct detection can be acquired with similar time resolution as indirect ^{13}C detection at the cost of spatial specificity.

Given the attainable SNR with both detection techniques, the method to use is further complicated by other aspects such as the magnetic field strength. Moving towards higher fields >7T, the increased spectral dispersion of proton spectroscopy improves quantification of overlapping metabolites (this aspect will be further detailed in chapter 5), thus the benefits of indirect detection partially outweigh its limitations. Below 4T, the partial overlap of GluH4 and GlnH4 makes quantification difficult with indirect ^{13}C MRS, thus the use of direct detection becomes an easier decision.

Following a ^{13}C MRS experiment, metabolite concentration information needs to be converted to absolute and fractional enrichment (FE) concentrations for metabolic modeling. With indirect ^{13}C MRS such as POCE, the calculation FE values is straightforward since EDIT-OFF and EDIT-ON scans contain the required information, and absolute quantification of metabolites is obtained with reference to the concentration of total creatine, an internal reference known to be stable with age or a variety of diseases (30). With direct ^{13}C MRS, absolute quantification and obtaining FE curves is not as straightforward. The absolute concentrations is typically obtained indirectly with a known or assumed reference, such as the natural abundance (1.11%) NAA signals, or from an assumed concentration for a specific metabolite pool (30), as further detailed in Chapter 5.

2.5.4 Applications

The application of ^{13}C MRS in the clinical setting to-date has been limited due to non-standard instrument modifications required, and the need for staff to perform infusions and data analysis; thus has been mostly limited to research environments. The wide use of ^{13}C MRS is further hampered by technical difficulties, such as magnetic field shimming and the relatively low sensitivity that restricts the method to larger volume resolution attainable relative to proton-MRS. Despite challenges associated with the method, metabolic information that can be interrogated non-invasively make dynamic ^{13}C MRS an important tool to study brain disease *in vivo*.

The role of neuroenergetics and glutamate/GABA neurotransmitter (primary excitatory and inhibitory neurotransmitters in the brain, respectively) cycling rates is increasingly being recognized in the pathogenesis of brain diseases. Though proton-MRS has been used to measure changes in neurotransmitter concentrations in a range of diseases such as psychiatric illnesses, epilepsy, and neurodegenerative disorders, changes in concentrations measured are not specific to the alterations underling metabolic fluxes. Dynamic ^{13}C MRS allows the measurement of metabolic fluxes in humans, and can be used in the study and treatment of brain disease (28).

One of the most significant findings obtained with dynamic *in vivo* ^{13}C MRS is that the glutamate-glutamine cycling rate is linearly related to the TCA cycling rate (40) over a broad spectrum of cerebral activity. In essence what this means is, for every glutamate molecule that is labeled via the Glutamate-glutamine cycle once, a glucose molecule is oxidized in the TCA cycle. Furthermore, dysfunction in glutamate and GABA neurotransmitters has been associated with many neurological (41) and psychiatric disorders (42), which, if the previous statement is true, can be probed with *in vivo* ^{13}C MRS by investigating oxidative glucose metabolism. In a review article Rothman et al. (28) summarizes a range of initial applications of dynamic ^{13}C MRS in humans to study neurological disorders including in stroke, tumors, Alzheimer's disease, and epilepsy. We will now briefly describe previous applications of ^{13}C MRS in Alzheimer's disease.

Applications of ^{13}C MRS to study Alzheimer's disease: Alzheimer's disease (AD) is a chronic neurodegenerative disease that typically manifests slowly and progressively worsens overtime. Proton-MRS studies have shown neurochemical changes (43), such as increased myo-inositol and decreased N-acetyl aspartate [a marker of viable neurons, axons, and dendrites (44)] in AD patients (45). A ^{13}C MRS study by Lin et al. (46) in AD patients found reductions in [4-^{13}C]-Glu labeling, consistent with a compromised TCA cycle, and reduced glutamate neurotransmission. Furthermore, this study showed reduced glucose oxidation and glutamate neurotransmission which were significantly correlated with proton-MRS findings (reduced N-acetyl aspartate, and myo-inositol).

A ^{13}C MRS study was recently conducted by Tiwari et al. (47) on an AD mouse model (AβPP-PS1) with reported pathology and neurochemical profile closely matched to human AD. At an early stage (5-6 months) these mice are reported to present with occasional amyloid plaques however, without significant memory impairment or neuronal loss. Their study included acquiring ^{13}C-MRS at two time points, 10 mins after the infusion, and 90 after the infusion. Findings show that glutamatergic and GABAergic functions were significantly reduced in the early stage AβPP-PS1 mouse model compared to wild type mice, indicating reductions in TCA cycling fluxes associated with GABAergic and glutamatergic neurons. The study also reports hypo-metabolism of glucose at this early stage, which is in agreement with findings reported for AD patients. Interestingly, differences in steady state ^{13}C labeling (at the 90 min time point) were reported to be not significant, and changes in neurochemical profiles obtained with proton-MRS were also reported to be not significant between groups. This mouse model is reported to have an unaltered neurochemical profile till ~12 months of age, thus demonstrating that ^{13}C MRS to be sensitive to early stages of AD relative to proton-MRS. Furthermore ^{13}C MRS may provide insights into pathogenesis and effectiveness of treatments for AD, as current treatment is mostly ineffective at mid-late stages of the disease.

2.6 Summary and Moving Forward

This chapter consists of an overall introduction to the fundamentals of magnetic resonance spectroscopy, with the intension of filling the voids in introductory content of latter chapters (chapters 3-5), which are concise due to the manuscript based thesis format used. In the last subsection we described dynamic *in vivo* ^{13}C MRS, its capabilities and limitations. As described above, low sensitivity currently limits the use of ^{13}C MRS to large voxel regions (~100μl in rat brain with indirect detection), and time resolution in the order of 4-10 minutes. Improvements to SNR can be used towards further reducing voxel sizes-thus improved region specificity, or improved time resolution and improve the accuracy of metabolic modeling.

In the case of indirect ^{13}C detection, the MRS sequence must provide both localization and editing in the presence of an inhomogeneous RF (B_1) field, as typically employed in previous studies using surface coils (37,38,48-51), thus the method benefits from localization based on B_1field insensitive adiabatic RF pulses. Image selected *in vivo* spectroscopy (ISIS; 22) and localization by adiabatic selective refocusing (LASER;23), are two classes of localized MRS sequences that mitigate such B_1^+ inhomogeneities. ISIS however suffers from outer volume signal contamination for metabolites with relatively long T_1 relaxation times due to T_1 smearing

(52,53), and requires 16 transients to construct each POCE time point, and thus is sensitive to movement and relies on good stability over the full cycle of acquisitions. LASER based POCE on the other hand provides single-shot localization, however TE of reported sequences are >22 ms, thus suffers from T_2 losses relative to shorter TE POCE MRS implementations, and homonuclear J-evolution related losses for weakly coupled spin systems such as Lactate. Therefore, current state-of-the-art techniques either are prone to subtraction errors due to multi-shot localization (ISIS), or require longer than optimal TE thus compromising attainable SNR (LASER).

In chapter 3 we describe a RF coil platform that provides a spatially uniform B_1^+ field, thus mitigating the requirement for ISIS or LASER based POCE implementations, and in Chapter 4 we describe a novel PRESS localized POCE sequence utilizing simultaneous editing and localization (SEAL-PRESS) that provides single-shot localization, short TE (8.1-ms) combined with uniform nutation, optimal sensitivity and editing efficiency.

Direct and indirect ^{13}C detection methods have their own advantages and disadvantages as described above. Direct ^{13}C MRS provides a wealth of information unavailable with indirect ^{13}C detection however suffers from sensitivity benefits relative to indirect detection, and means to obtain absolute concentrations and FE curves is not straightforward compared to indirect detection. Chapter 5 describes our attempt at acquiring both direct and indirect ^{13}C time-course spectra during a dynamic *in vivo* ^{13}C session, with the goal of improving quantitative metabolic modeling.

2.7 References

1. Rabi II. Space Quantization in a Gyrating Magnetic Field. Physical Review 1937;51(8):652-654.
2. Bloch F. Nuclear Induction. Physical Review 1946;70(7-8):460-474.
3. Purcell EM, Torrey HC, Pound RV. Resonance Absorption by Nuclear Magnetic Moments in a Solid. Physical Review 1946;69(1-2):37-38.
4. Proctor WG, Yu FC. The Dependence of a Nuclear Magnetic Resonance Frequency upon Chemical Compound. Physical Review 1950;77(5):717-717.
5. Dickinson WC. Dependence of the F19 Nuclear Resonance Position on Chemical Compound. Physical Review 1950;77(5):736-737.
6. Moon RB, Richards JH. Determination of intracellular pH by 31P magnetic resonance. The Journal of biological chemistry 1973;248(20):7276-7278.
7. Hoult DI, Busby SJ, Gadian DG, Radda GK, Richards RE, Seeley PJ. Observation of tissue metabolites using 31P nuclear magnetic resonance. Nature 1974;252(5481):285-287.
8. Behar KL, den Hollander JA, Stromski ME, Ogino T, Shulman RG, Petroff OA, Prichard JW. High-resolution 1H nuclear magnetic resonance study of cerebral hypoxia in vivo. Proceedings of the National Academy of Sciences of the United States of America 1983;80(16):4945-4948.
9. Bottomley PA, Edelstein WA, Foster TH, Adams WA. In vivo solvent-suppressed localized hydrogen nuclear magnetic resonance spectroscopy: a window to metabolism?

Proceedings of the National Academy of Sciences of the United States of America 1985;82(7):2148-2152.

10. Gerlach W, Stern O. Der experimentelle Nachweis der Richtungsquantelung im Magnetfeld. Zeitschrift für Physik 1922;9(1):349-352.
11. Hoult DI. The Principle of Reciprocity. Journal of Magnetic Resonance 2011;213(2):344-346.
12. Goldman M, Webb GA. M. Goldman. Quantum description of high-resolution NMR in liquids. Oxford University Press, 1988. £35.00. Magnetic Resonance in Chemistry 1989;27(5):507-507.
13. Bottomley PA. Spatial localization in NMR spectroscopy in vivo. Annals of the New York Academy of Sciences 1987;508:333-348.
14. Morris GA, Freeman R. Enhancement of nuclear magnetic resonance signals by polarization transfer. Journal of the American Chemical Society 1979;101(3):760-762.
15. Doddrell DM, Pegg DT, Bendall MR. Distortionless enhancement of NMR signals by polarization transfer. Journal of Magnetic Resonance (1969) 1982;48(2):323-327.
16. de Graaf RA, Mason GF, Patel AB, Behar KL, Rothman DL. In vivo 1H-[13C]-NMR spectroscopy of cerebral metabolism. NMR in biomedicine 2003;16(6-7):339-357.
17. de Graaf RA, Rothman DL, Behar KL. State of the art direct 13C and indirect 1H-[13C] NMR spectroscopy in vivo. A practical guide. NMR in biomedicine 2011;24(8):958-972.
18. Hurd RE, Freeman D. Proton editing and imaging of lactate. NMR in biomedicine 1991;4(2):73-80.
19. Rothman DL, Behar KL, Hetherington HP, den Hollander JA, Bendall MR, Petroff OA, Shulman RG. 1H-Observe/13C-decouple spectroscopic measurements of lactate and

glutamate in the rat brain in vivo. Proceedings of the National Academy of Sciences of the United States of America 1985;82(6):1633-1637.

20. Fitzpatrick SM, Hetherington HP, Behar KL, Shulman RG. The flux from glucose to glutamate in the rat brain in vivo as determined by 1H-observed, 13C-edited NMR spectroscopy. Journal of cerebral blood flow and metabolism : official journal of the International Society of Cerebral Blood Flow and Metabolism 1990;10(2):170-179.

21. Rothman DL, Howseman AM, Graham GD, Petroff OA, Lantos G, Fayad PB, Brass LM, Shulman GI, Shulman RG, Prichard JW. Localized proton NMR observation of [3-13C]lactate in stroke after [1-13C]glucose infusion. Magnetic resonance in medicine 1991;21(2):302-307.

22. Ordidge RJ, Connelly A, Lohman JAB. Image-selected in Vivo spectroscopy (ISIS). A new technique for spatially selective nmr spectroscopy. Journal of Magnetic Resonance (1969) 1986;66(2):283-294.

23. Slotboom J, Mehlkopf AF, Bovée WMMJ. A single-shot localization pulse sequence suited for coils with inhomogeneous RF fields using adiabatic slice-selective RF pulses. Journal of Magnetic Resonance (1969) 1991;95(2):396-404.

24. Kumaragamage C, Madularu D, Mathieu AP, De Feyter H, Rajah MN, Near J. In vivo proton observed carbon edited (POCE) (13) C magnetic resonance spectroscopy of the rat brain using a volumetric transmitter and receive-only surface coil on the proton channel. Magnetic resonance in medicine 2018;79(2):628-635.

25. Johnson JB. Thermal Agitation of Electricity in Conductors. Physical Review 1928;32(1):97-109.

26. Hoult DI, Lauterbur PC. The sensitivity of the zeugmatographic experiment involving human samples. Journal of Magnetic Resonance (1969) 1979;34(2):425-433.

27. Adriany G, Gruetter R. A half-volume coil for efficient proton decoupling in humans at 4 tesla. Journal of magnetic resonance 1997;125(1):178-184.

28. Rothman DL, De Feyter HM, de Graaf RA, Mason GF, Behar KL. 13C MRS studies of neuroenergetics and neurotransmitter cycling in humans. NMR in biomedicine 2011;24(8):943-957.

29. Reivich M, Kuhl D, Wolf A, Greenberg J, Phelps M, Ido T, Casella V, Fowler J, Gallagher B, Hoffman E, Alavi A, Sokoloff L. Measurement of local cerebral glucose metabolism in man with 18F-2-fluoro-2-deoxy-d-glucose. Acta neurologica Scandinavica Supplementum 1977;64:190-191.

30. De Graaf RA. In vivo NMR spectroscopy: Wiley; 2007.

31. Cruz F, Cerdan S. Quantitative 13C NMR studies of metabolic compartmentation in the adult mammalian brain. NMR in biomedicine 1999;12(7):451-462.

32. Shephard Gm. The synaptic organization of the brain: Oxford University Press; 1994.

33. Rothstein JD, Dykes-Hoberg M, Pardo CA, Bristol LA, Jin L, Kuncl RW, Kanai Y, Hediger MA, Wang Y, Schielke JP, Welty DF. Knockout of glutamate transporters reveals a major role for astroglial transport in excitotoxicity and clearance of glutamate. Neuron 1996;16(3):675-686.

34. Hertz L, Peng L, Dienel GA. Energy metabolism in astrocytes: high rate of oxidative metabolism and spatiotemporal dependence on glycolysis/glycogenolysis. Journal of cerebral blood flow and metabolism : official journal of the International Society of Cerebral Blood Flow and Metabolism 2007;27(2):219-249.

35. Gruetter R, Adriany G, Choi IY, Henry PG, Lei H, Oz G. Localized in vivo 13C NMR spectroscopy of the brain. NMR in biomedicine 2003;16(6-7):313-338.

36. Provencher SW. Automatic quantitation of localized in vivo 1H spectra with LCModel. NMR in biomedicine 2001;14(4):260-264.

37. Pfeuffer J, Tkac I, Choi IY, Merkle H, Ugurbil K, Garwood M, Gruetter R. Localized in vivo 1H NMR detection of neurotransmitter labeling in rat brain during infusion of [1-13C] D-glucose. Magnetic resonance in medicine 1999;41(6):1077-1083.

38. de Graaf RA, Brown PB, Mason GF, Rothman DL, Behar KL. Detection of [1,6-13C2]-glucose metabolism in rat brain by in vivo 1H-[13C]-NMR spectroscopy. Magnetic resonance in medicine 2003;49(1):37-46.

39. Henry PG, Tkac I, Gruetter R. 1H-localized broadband 13C NMR spectroscopy of the rat brain in vivo at 9.4 T. Magnetic resonance in medicine 2003;50(4):684-692.

40. Sibson NR, Dhankhar A, Mason GF, Behar KL, Rothman DL, Shulman RG. In vivo 13C NMR measurements of cerebral glutamine synthesis as evidence for glutamate-glutamine cycling. Proceedings of the National Academy of Sciences of the United States of America 1997;94(6):2699-2704.

41. Pearl PL, Gibson KM. Clinical aspects of the disorders of GABA metabolism in children. Current opinion in neurology 2004;17(2):107-113.

42. Sanacora G, Rothman DL, Mason G, Krystal JH. Clinical studies implementing glutamate neurotransmission in mood disorders. Annals of the New York Academy of Sciences 2003;1003:292-308.

43. Chen SQ, Wang PJ, Ten GJ, Zhan W, Li MH, Zang FC. Role of myo-inositol by magnetic resonance spectroscopy in early diagnosis of Alzheimer's disease in APP/PS1 transgenic mice. Dementia and geriatric cognitive disorders 2009;28(6):558-566.

44. Moffett JR, Namboodiri MA, Neale JH. Enhanced carbodiimide fixation for immunohistochemistry: application to the comparative distributions of N-acetylaspartylglutamate and N-acetylaspartate immunoreactivities in rat brain. The journal of histochemistry and cytochemistry : official journal of the Histochemistry Society 1993;41(4):559-570.

45. Kantarci K, Jack CR, Jr., Xu YC, Campeau NG, O'Brien PC, Smith GE, Ivnik RJ, Boeve BF, Kokmen E, Tangalos EG, Petersen RC. Regional metabolic patterns in mild cognitive impairment and Alzheimer's disease: A 1H MRS study. Neurology 2000;55(2):210-217.

46. Lin AP, Shic F, Enriquez C, Ross BD. Reduced glutamate neurotransmission in patients with Alzheimer's disease -- an in vivo (13)C magnetic resonance spectroscopy study. Magma 2003;16(1):29-42.

47. Tiwari V, Patel AB. Impaired glutamatergic and GABAergic function at early age in AbetaPPswe-PS1dE9 mice: implications for Alzheimer's disease. Journal of Alzheimer's disease : JAD 2012;28(4):765-769.

48. Chen W, Adriany G, Zhu XH, Gruetter R, Ugurbil K. Detecting natural abundance carbon signal of NAA metabolite within 12-cm3 localized volume of human brain using 1H-[13C] NMR spectroscopy. Magnetic resonance in medicine 1998;40(2):180-184.

49. Yang J, Li CQ, Shen J. In vivo detection of cortical GABA turnover from intravenously infused [1-13C]D-glucose. Magnetic resonance in medicine 2005;53(6):1258-1267.

50. Xin L, Mlynarik V, Lanz B, Frenkel H, Gruetter R. 1H-[13C] NMR spectroscopy of the rat brain during infusion of [2-13C] acetate at 14.1 T. Magnetic resonance in medicine 2010;64(2):334-340.

51. Meeus I, Brown MJ, De Graaf DC, Smagghe G. Effects of invasive parasites on bumble bee declines. Conservation biology : the journal of the Society for Conservation Biology 2011;25(4):662-671.

52. Lawry TJ, Karczmar GS, Weiner MW, Matson GB. Computer simulation of MRS localization techniques: an analysis of ISIS. Magnetic resonance in medicine 1989;9(3):299-314.

53. Ljungberg M, Starck G, Vikhoff-Baaz B, Alpsten M, Ekholm S, Forssell-Aronsson E. Extended ISIS sequences insensitive to T(1) smearing. Magnetic resonance in medicine 2000;44(4):546-555.

Chapter 3

Proton Volumetric Resonator Based POCE MRS

Dynamic *in vivo* ^{13}C MRS for rat brain imaging is popularly performed with an all-surface coil based approach. With such coil platforms, the use of adiabatic RF pulses is beneficial to minimize nutation angle errors, signal losses and artefacts due to a spatially varying radiofrequency (B_1^+) field. Image selected *in vivo* spectroscopy (ISIS) and LASER, are two classes of localized MRS sequences that have been used to mitigate such B_1^+ inhomogeneities, however with limitations associated with each method. Single-shot localized POCE-MRS techniques mitigate subtraction artefacts associated with ISIS based implementations, and sensitivity of POCE-MRS can be enhanced through the use of short TE sequences due to minimized T_2 and homonuclear J-evolution related losses. To that end, this chapter describes the development of a RF coil platform that provides homogeneous B_1^+ by utilizing a volumetric resonator on the proton channel, which is paired with a ^{1}H-[^{13}C] surface coil. The content of this chapter has been published in *Magnetic Resonance in Medicine*.

In vivo proton observed carbon edited (POCE) ^{13}C Magnetic Resonance Spectroscopy of the rat brain using a volumetric transmitter and receive-only surface coil on the proton channel

Chathura Kumaragamage [1,4], Dan Madularu [2,4], Axel P. Mathieu [2,4], Henk De Feyter [5], M. Natasha Rajah [2-4], and Jamie Near [1,2,4]

[1] Department of Biomedical Engineering, McGill University, Montreal, QC, Canada.
[2] Department of Psychiatry, Faculty of Medicine, McGill University, Montreal, QC, Canada.
[3] Department of Psychology, Faculty of Arts, McGill University, Montreal, QC, Canada.
[4] Brain Imaging Centre, Douglas Mental Health University Institute, McGill University, Montreal, QC, Canada.
[5] Radiology and Biomedical Imaging, Yale University, New Haven, CT, USA

Magnetic Resonance in Medicine. 2018; 79: 628-635.

3.1 Abstract

Purpose: *In vivo* carbon-13 (^{13}C) magnetic resonance spectroscopy (MRS) is capable of measuring energy metabolism and neuroenergetics, non-invasively in the brain. Indirect (^{1}H-[^{13}C]) MRS provides sensitivity benefits compared with direct ^{13}C methods, and normally includes a ^{1}H surface coil for both localization and signal reception. The aim was to develop a coil platform with homogenous B_1^+ and utilize short conventional pulses for short echo time POCE-MRS.

Methods: A ^{1}H-[^{13}C] MRS coil platform was designed with a volumetric resonator for ^{1}H transmit, and surface coils for ^{1}H reception and ^{13}C transmission. The Rx-only ^{1}H surface coil nullifies the requirement for a T/R switch before the ^{1}H preamplifier; the highpass filter and preamplifier can be placed proximal to the coil, thus minimizing sensitivity losses inherent with POCE-MRS systems described in the literature. The coil platform was evaluated with a PRESS-POCE sequence (TE = 12.6 ms) on a rat model.

Results: The coil provided excellent localization, uniform spin nutation, and sensitivity. ^{13}C labeling of Glu-H4 and Glx-H3 peaks, and the Glx-H2 peaks were observed approximately 13 and 21 min following the infusion of 1-^{13}C glucose, respectively.

Conclusion: A convenient and sensitive platform to study energy metabolism and neurotransmitter cycling is presented.

3.2 Introduction

^{13}C Magnetic resonance spectroscopy (MRS) remains to be the only noninvasive method capable of measuring neuroenergetics and neurotransmitter cycling in the brain *in vivo* (1). Indirect detection of ^{13}C nuclei with proton (^{1}H-[^{13}C]) MRS is gaining popularity for *in vivo* human and animal imaging due to signal-to-noise-ratio (SNR) gains achievable relative to direct ^{13}C MRS methods. Proton observed carbon edited (POCE) MRS (2,3) is one such indirect ^{13}C MRS method where heteronuclear J-difference editing is used to detect protons coupled to ^{13}C nuclei.

A few variants of POCE-MRS with heteronuclear decoupling have been reported (4-8), in which surface coils are used for proton (^{1}H) transmission/reception, and carbon (^{13}C) transmission. With such coil platforms, the use of adiabatic RF pulses (9) is beneficial to minimize nutation angle errors, signal losses and artefacts due to a spatially varying radiofrequency (B_1^+) field (10). De Graaf et al. (5) describe a 9.4 ms echo time (TE) POCE sequence with 3D localization achieved using both outer volume suppression (OVS) and image-selected *in vivo* spectroscopy (ISIS; 11) with adiabatic pulses. However, ISIS suffers from outer volume signal contamination for metabolites with relatively long T_1 relaxation times due to T_1 smearing (12,13). Furthermore, ISIS based POCE-MRS requires 16 transients to construct each time point, and thus is sensitive to movement and relies on good stability over the full cycle of acquisitions. Ultra-short TE (2.8 ms), SPECIAL localized (14) POCE MRS was introduced by Xin et al. (8), in which ^{13}C spectral editing was applied prior to localization (15). In this implementation, B_1^+ heterogeneity was partially mitigated with adiabatic inversion for the first slice selective pulse in the plane orthogonal to the coil plane; the direction in which B_1^+ inhomogeneity is highest for surface coils. However, the subsequent slice selective spin-echo is based on purely amplitude-modulated pulses (herein referred to as conventional pulses), which affects localization performance and sensitivity (16) due to B_1^+ inhomogeneity (17). Furthermore, 1D-ISIS based SPECIAL-POCE requires four transients for each POCE-MRS time point, thus also relies on good stability and minimal subtraction artifacts (18).

POCE-MRS methods based on single-shot localization techniques (hence two transients to construct each difference spectrum) mitigate subtraction artefacts associated with ISIS based localization. POCE based on Point resolved spectroscopy (PRESS; 19) (4,20) localization, is one such method reported with TE > 15.8 ms. In these studies, however, conventional pulses were used in combination with surface coil transmitters for excitation and refocusing; once again likely resulting in spatially non-uniform spin nutation. Furthermore, it is beneficial to shorten the sequence TE to minimize T_2 and homonuclear J-evolution related losses in POCE-MRS. For example, integrated peak area for both glutamate (Glu)-H4 and glutamine (Gln)-H4 multiplets are reduced by >50% (neglecting T_2 losses) when TE is increased from 15 ms to 30 ms purely due to homonuclear J-evolution (density matrix formalism (21) simulations for a PRESS sequence utilizing Hermite pulses). The LASER sequence (22) is another single-shot localized sequence commonly used for POCE-MRS (6,10,23), which mitigates many shortcomings associated with PRESS as follows: 1) robust and excellent localization even with surface coils since pairs of adiabatic full passage (AFP) pulses (24) are used for each slice direction, 2) homonuclear J-evolution is inhibited (25), provided the Carr-Purcell Spin-Echo (CPSE; 26) condition (27) is met ($\sqrt{\omega_{AB}^2 + J_{AB}^2} \cdot \tau_{cp} \ll 1$, where ω_{AB} and J_{AB} are the chemical shift and scalar coupling constant of the coupled homonuclear system, respectively, and τ_{cp} is the echo spacing of a Carr-Purcell spin-echo pulse train), and 3) high bandwidth AFP pulses minimize chemical shift displacement errors associated with relatively low bandwidth conventional pulses. The TE of reported LASER-POCE sequences, however are >22 ms, primarily due to the requirement for pairs of ~1 ms AFP pulses and the 1/$J_{H\text{-}C}$ ms final echo requirement, and thus suffers from T_2 losses relative to shorter TE POCE MRS implementations described above. Furthermore, for practical values of τ_{cp}, the sensitivity of LASER is reduced in large ω_{AB} spin systems (e.g. lactate) as the CPSE condition begins to break down (25).

In this study a ^{1}H-[^{13}C] surface coil is paired with an 86 mm volumetric resonator for homogeneous B_1^+ (herein collectively referred to as the ^{1}H-[^{13}C] coil setup). The ^{1}H-[^{13}C] surface coil consists of a ^{1}H receive (Rx)-only surface coil and a quadrature driven ^{13}C surface coil (for heteronuclear decoupling and editing pulses). The ^{1}H Rx-only surface coil provides sensitivity gains compared to a volume coil approach; the requirement for a T/R switch (and related losses) before the ^{1}H preamplifier is avoided. Furthermore, a highpass filter and preamplifier can be placed proximal to the coil, further minimizing SNR losses inherent with POCE-MRS systems described in the literature. Using the ^{1}H-[^{13}C] coil setup described above, we implemented a PRESS-localized POCE MRS sequence with short conventional pulses: thus enabling uniform nutation, two-shot edited POCE MRS, combined with a short-TE; a feat that cannot be achieved with an all-surface coil based approach.

3.3 Methods

3.3.1 Coil Design

POCE-MRS requires RF excitation on both ^{1}H, and ^{13}C frequencies (corresponding to 300.3 MHz, and 75.5 MHz respectively, on a Bruker 7T magnet), and signal reception on the ^{1}H frequency. However, the requirement for heteronuclear decoupling (10) on the ^{13}C frequency during signal acquisition can result in leakage of unwanted "decoupling noise" in the acquisition.

This issue is mitigated with often site-specific modifications to the coils and RF chain (10,28). A conservative approach is to start with a coil topology that provides favorable isolation (~ -30 dB at the decoupling frequency) between ^{1}H and ^{13}C surface coils. The overlapped quadrature driven surface coil for the decoupling frequency, and centered smaller surface coil for the observed frequency, described by Adriany et al. (29), is a popular solution for heteronuclear MRS due to the excellent geometric isolation achievable between coils, and improved B_2^+ homogeneity relative to a single loop design. The use of a volumetric coil on the irradiating channel (^{1}H) with a surface coil for the observed channel (^{13}C) has also been previously described for direct ^{13}C MRS experiments with heteronuclear decoupling (30,31). In this work, a circular 20 mm Rx-only coil for ^{1}H observation is geometrically centered between two partially overlapped 30 mm square ^{13}C loops driven in quadrature (Figure 3-1). Both ^{13}C loops include passive trap circuits tuned to the ^{1}H frequency to minimize interactions with the ^{1}H volumetric resonator. The ^{1}H Rx-only loop is fitted with an active detuning circuit for isolation from the ^{1}H volumetric resonator during transmission, as previously described in proton imaging studies (32,33).

Passive trap circuits on each ^{13}C loop were adjusted in isolation with a weakly coupled (< -80 dB) double probe; similarly, > 50 dB of active decoupling was achieved for the ^{1}H Rx-only loop. Overlap between the two ^{13}C loops was adjusted to gain ~ 30 dB (at 75.5 MHz) of geometric decoupling; and ~ -30 dB of coupling between the ^{13}C coil (quadrature driven) and ^{1}H Rx-only loop at 75.5 MHz.

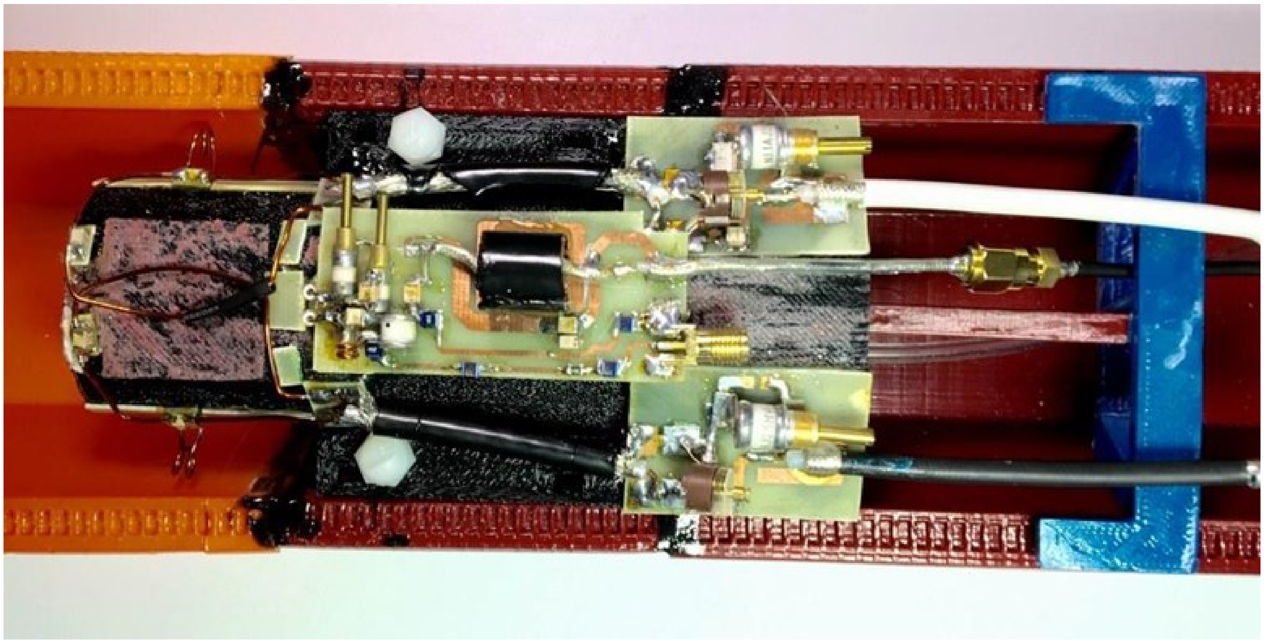

***Figure 3-1** The developed ^{1}H-[^{13}C] surface coil*

The dual quadrature driven ^{13}C loops are visible on the left, placed with partial overlap. Both loops are segmented with capacitors to minimize electrical losses, and each ^{13}C loop has a tank circuit tuned to 300.3 MHz to minimize interactions with the proton volumetric resonator. A 20mm diameter ^{1}H Rx-only loop is symmetrically placed under the dual ^{13}C coil on the underside of the 3D printed former, closer to the rat brain. The Rx-only loop has an active detuning circuit activated by a PIN diode populated on the PCB illustrated in the center of the figure.

3.3.2 ^{13}C Filter and Overall Coil Setup

A highpass filter with adequate attenuation of ^{13}C frequency signals (> 60 dB) and low insertion loss (IL) for ^{1}H frequency signals (-0.5 dB or better) is key for a sensitive POCE-MRS setup (10). Coil systems designed for heteronuclear decoupling experiments (10,29) often employ a high power handling, highpass/lowpass or bandpass filter between the coil and preamplifier on the observed channel (28). However, such filters are bulky and typically would not fit inside a small bore preclinical MRI.

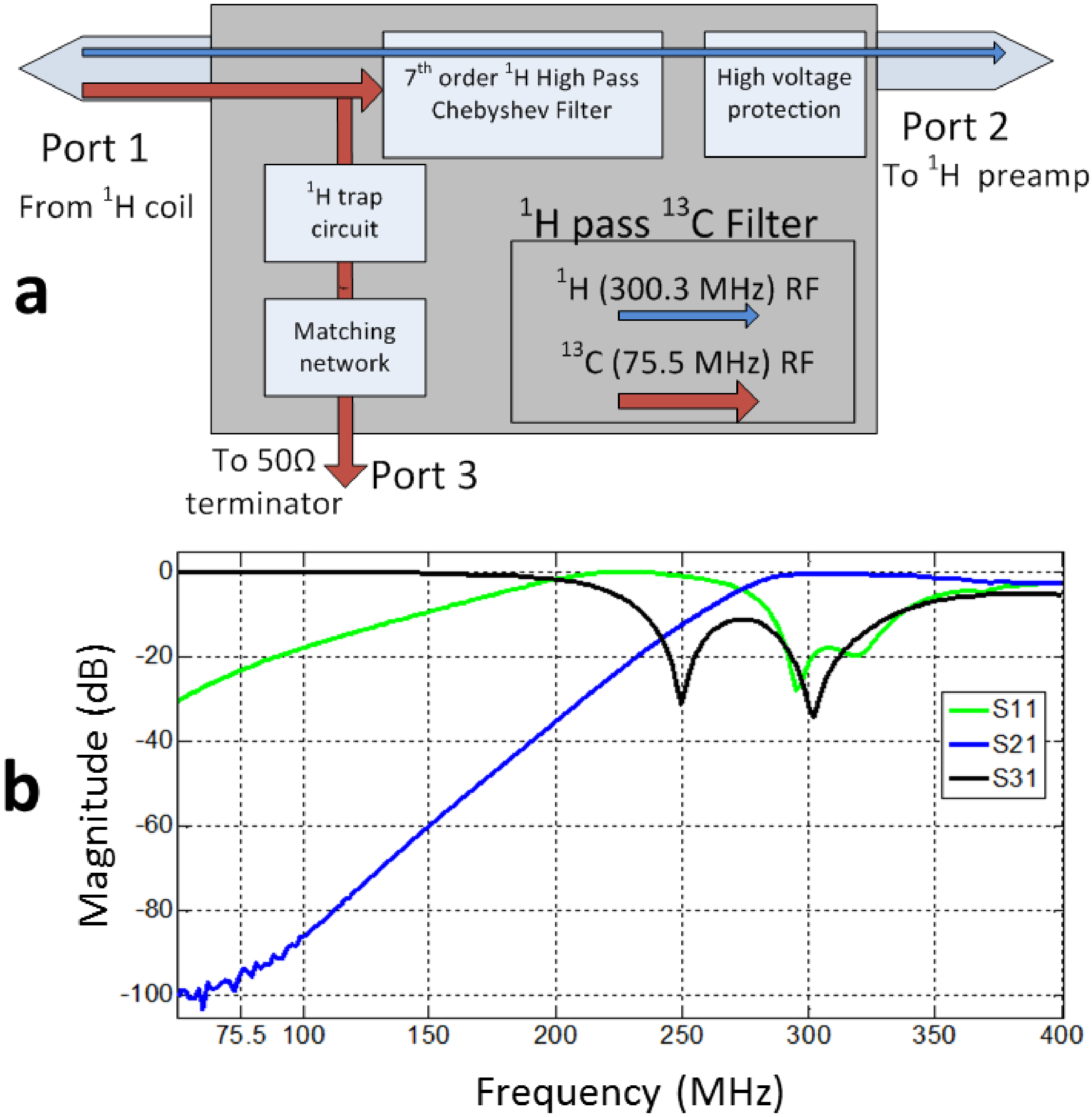

Figure 3-2 Block diagram and frequency response of the highpass filter designed for POCE experiments (a) A block diagram of the absorptive highpass filter designed for POCE ^{13}C experiments. The filter is placed between the 1H-Rx-only coil and preamplifier. High power decoupling noise at the ^{13}C frequency entering via port 1 is diverted out of port 3, into a 50 Ω terminator. In some instances, a matching network before the output of port 3 may be necessary to obtain a low loss pathway for 75.5MHz content. A pair of RF clamping diodes is placed before the output of port 2 as secondary protection for the preamplifier. (b) Frequency response of the 3 port highpass absorption filter used at the 1H Rx-only coil. The through response (S21) of the filter shows high attenuation at 75MHz (>95dB) and low insertion losses at 300.3MHz (- 0.38dB). Furthermore, > -20dB of reflection at port 1 for RF content below 75MHz ensures absorption of the primary harmonic of decoupling noise. The tank circuit before the output to port 3 ensures at least -35dB of isolation for 300.3MHz (S31), and port 3 provides a low loss pathway (-0.08dB) for 75.5MHz content.

As part of the coil design, a small footprint (5.5 x 3.5 cm^2) highpass filter, capable of handling heteronuclear decoupling tailored for ^{1}H-[^{13}C] MRS at 7T was implemented (Figure 3-2a). The filter was based on a 0.1 dB passband ripple 7th order Chebyshev HP filter with a -3 dB cut off at 275 MHz and ~100 dB attenuation at 75.5 MHz in simulation.

Additionally, the filter was designed to divert 75.5 MHz RF content (from heteronuclear decoupling, and editing pulses) into a 50 Ω terminator (Figure 3-2a), thus minimizing RF power reflecting back to the ^{1}H-Rx-only coil. In contrast, a classical highpass filter presents a high reflection coefficient for low frequency content (<< cut off frequency).

The filter was designed with 500V rated ATC non-magnetic capacitors (ATC corp. 100B series, Huntington Station NY, USA) to withstand at least 100 Watts of peak RF power. A 25 W 50 Ω terminator (Bourns, Riverside, CA, USA) was attached to the housing of the filter enclosure, to which port 3 was connected as illustrated in Figure 3-2a. Port 2 of the filter connects to a 50-Ω low noise (0.4 dB noise figure) preamplifier with 26 dB gain @ 300 MHz (Wantcom, Chanhassen, MN, USA); placed proximal to the ^{1}H-[^{13}C] coil setup inside the magnet bore (Figure 3-3).

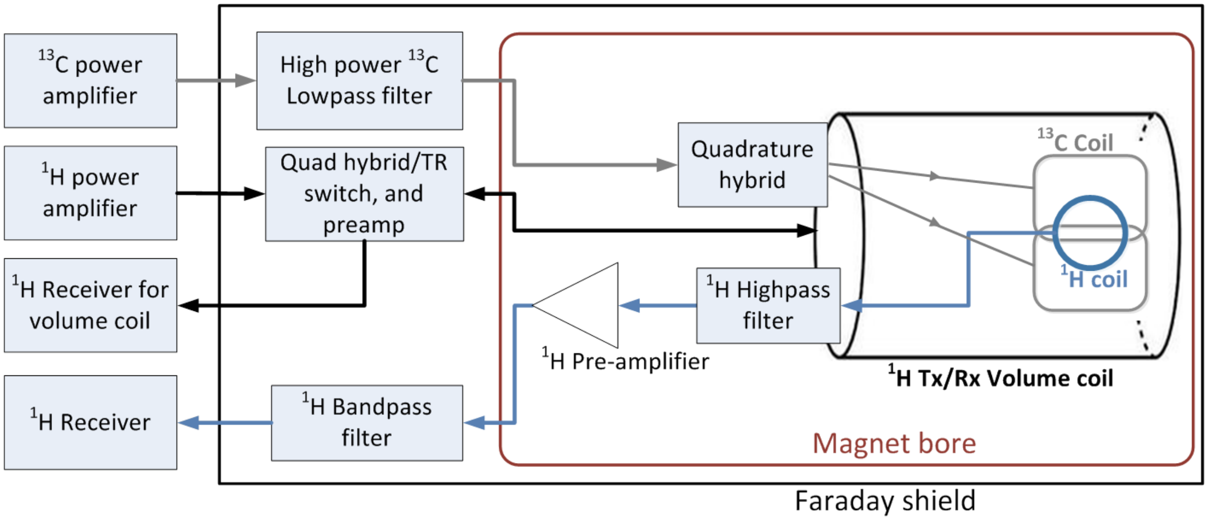

Figure 3-3 *A block diagram of the ^{1}H-[^{13}C] coil setup with major components used for POCE ^{13}C MRS*
The ^{1}H-[^{13}C] surface coil is placed in the ^{1}H volumetric resonator; the ^{1}H highpass filter, quadrature hybrid and preamplifier are in the magnet bore proximal to the ^{1}H-[^{13}C] surface coil. A second bandpass filter on the ^{1}H line is placed before the 2nd amplifier stage to further attenuate coupled spurious RF.

Non-linearities associated with the ^{13}C power amplifier and associated RF chain generates observable higher order harmonics. Higher order harmonics (such as the third harmonic of 75.5 MHz, ~225 MHz at 7T) readily get coupled from the ^{13}C coil to ^{1}H surface coil (due to insufficient attenuation of the highpass filter at ~225 MHz) causing spurious signals to appear on the acquired signal. Furthermore, the unfortunate coincidence of $\gamma_H/\gamma_C \sim 4$ results in the 4th harmonic of 75.5 MHz to be ~300 MHz, which if coupled, is impossible to isolate. A few modifications, such as notch filtering 225 MHz, were investigated as part of the filter design with minimal success due to the broadband nature of these harmonics. Utilization of a high power handling 80 MHz lowpass filter (Reactel Inc., Gaithersburg, MD, USA) at the output of the ^{13}C high power amplifier (IL= -0.3 dB @75 MHz, and >80 dB of attenuation beyond 150 MHz) was the most effective and robust solution. A small package 300 MHz bandpass filter (20 MHz bandwidth, IL= -3.5 dB; Reactel Inc,. Gaithersburg, MD, USA) was placed after the ^{1}H preamplifier, outside the magnet bore to further attenuate coupled spurious RF content. All major components and their placement are illustrated in Figure 3-3.

3.3.3 Phantom and *in vivo* NMR Spectroscopy

All experiments were performed on a Bruker (Billerica, MA, USA) Biospec 70/30 horizontal bore preclinical scanner with an actively shielded gradient insert (120 mm inner diameter, 650 mT/m in 150 µs). A gradient echo based multi-slice localizer was used to plan the remainder of the experiments. FASTMAP (34) was used for B_0 shimming, resulting in water line widths of ~4-6 Hz in a 216 µl (6 x 6 x 6 mm^3) voxel in phantoms, and ~10-13 Hz in a 100 µl (5 x 4 x 5 mm^3) voxel in rat brain. VAPOR (35) was used for water suppression utilizing Gaussian pulses (length = 27 ms and 17.1 ms, bandwidth = 200 Hz), and outer volume suppression (OVS) was used with hyperbolic secant (sech) pulses (length = 2.0 ms, bandwidth = 10,125 Hz). A PRESS-POCE sequence (TR = 4000 ms, TE = 12.6 ms, TE_1 = 2.6 ms, TE_2 = 10 ms, SW = 6009 Hz, 3605 points) was implemented, and followed after OVS and VAPOR as illustrated in Figure 3-4. Excitation and refocusing on the ^{1}H channel were performed with conventional pulses: excitation using a 5-lobe sine-modulated sinc pulse (length = 0.7 ms, bandwidth = 13,500 Hz), and both refocusing pulses were Hermite (length = 0.8 ms, bandwidth = 4,250 Hz, $B_{1,\,max}$ ~ 3.6 kHz).

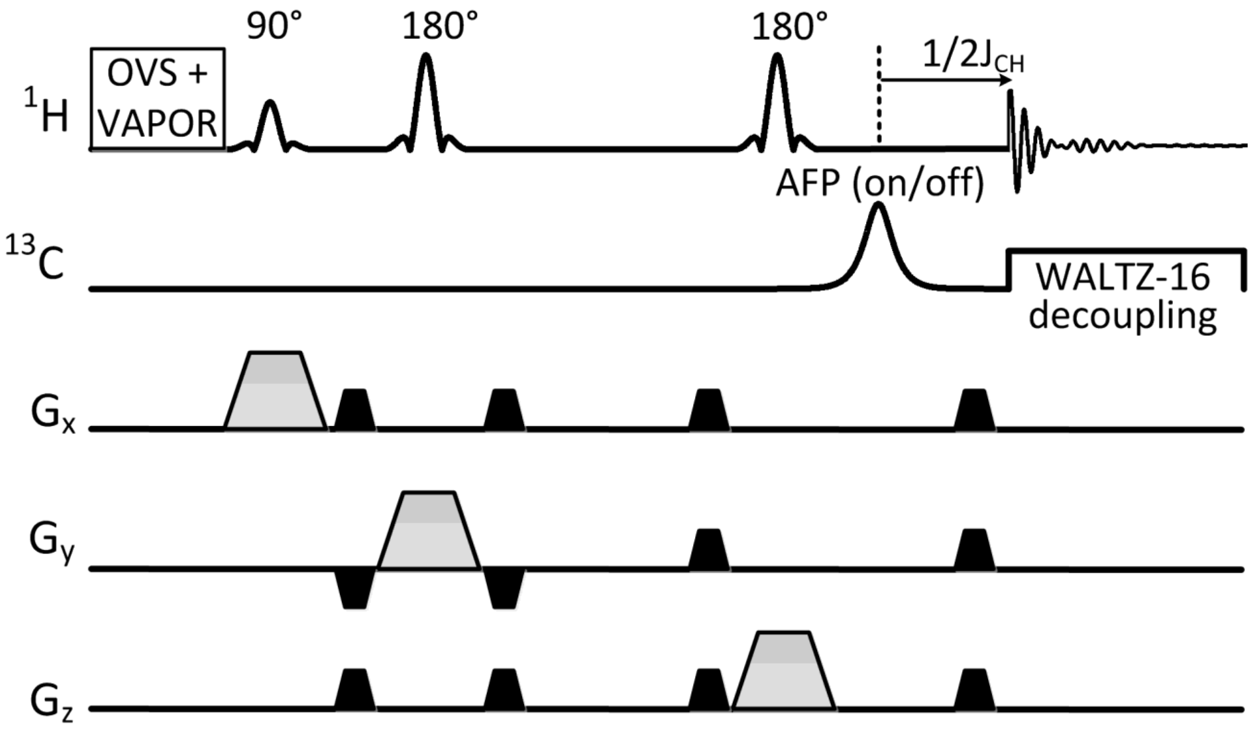

Figure 3-4 *Schematic representation of the PRESS localized POCE sequence (TR=4s, TE=12.6ms)*
OVS and VAPOR are executed prior to localization as illustrated in Figure 3-4. A 5-lobe sine-modulated sinc pulse is used for excitation, and two identical Hermite pulses are used for refocusing. A 1.5ms AFP hyperbolic secant inversion pulse is used for editing on the ^{13}*C channel timed 1/2jCH before the final echo. WALTZ-16 heteronuclear decoupling is applied on the* ^{13}*C channel during signal acquisition.*

Manipulation of protons (I) scalar coupled to ^{13}C nuclei (S) was achieved by applying an editing pulse on the ^{13}C channel $1/2J_{HC}$ (3.7 ms) before the final echo in edit-ON scans. $1/2J_{HC}$ ms before the final echo, the coupled spin system will be in the I_yS_z state in edit-OFF scans, and $-I_yS_z$ state in edit-ON scans. Evolution of these two states under the coupled spin Hamiltonian ($\widetilde{\mathcal{H}} = 2\pi J_{HC}I_zS_z$) produces $+I_x$ and $-I_x$ states at the final echo for edit-OFF and edit-ON scans, respectively. Subtraction of the two scans then results in a ^{1}H-[^{13}C] MRS spectrum. ^{13}C Editing was realized with an AFP sech inversion pulse (length = 1.5 ms, bandwidth = 11,700 Hz, $B_{2,\ max}$ ~ 5 kHz).

WALTZ-16 (36) was used for heteronuclear decoupling during the first 200 ms of the acquisition. The WALTZ composite pulse segment was empirically determined in phantoms to be 0.7 ms in length to provide >70% decoupling efficiency in the 20 - 60 ppm ^{13}C spectral bandwidth on a 6 x 6 x 6 mm^3 voxel. A 32-step phase cycle was used to cancel out residual contributions from unwanted coherence pathways. All transients were stored separately, zero padded by a factor of four to a total of 14420 data points, and field drift was corrected. Edit-ON and edit-OFF scans were then separately averaged, and aligned prior to subtraction. Spectral preprocessing was performed in MATLAB (Natick, MA, USA) using the FID-A toolkit (18).

B_1^+ field inhomogeneity can occur proximal to the ^{1}H-[^{13}C] surface coil elements due to interactions with the ^{1}H volumetric resonator, which was evaluated using flip angle maps generated using a double angle spin-echo sequence (37). However, no such distortions were visible, a maximum of ±4° variations in flip angle were observed in the region of interest (results not shown).

Sensitivity of the ^{1}H Rx-only element of the ^{1}H-[^{13}C] coil setup was evaluated using SNR maps (38), with all components in place (as illustrated in Figure 3-3). A FLASH sequence (TR/TE = 350/5.4 ms, repetitions = 3, flip angle = 40°, slices = 23, slice thickness = 1.2 mm, spatial resolution = 0.15 mm x 0.15 mm, matrix size = 256 by 256, acquisition time = 3m 21s) was used. ^{1}H signal sensitivity of the coil was compared against two commercially available coils: 1) an equivalent geometry Bruker-20 mm Rx-only surface coil with integrated preamplifier (T115534; Bruker, Billerica, MA, USA) using the same volumetric resonator for transmit, 2) a rat brain optimized 45 mm birdcage volumetric coil for transmit/receive. Three coronal slices spanning 6 mm in the anterior-posterior (A-P) direction were used to represent A-P coverage of the spectroscopy voxel.

Two male Long Evans (Charles River Laboratories, Montreal, QC, Canada) rats weighing 260-300 g were used for this study, one for coil SNR evaluations and one for dynamic ^{13}C MRS. Following an overnight fast of 14 hours, the tail vein on one animal was cannulated for the infusion of 1-^{13}C glucose, under free-breathing of 2% isoflurane anesthesia. The animal was maintained under anesthesia and placed in the MRI scanner with the ^{1}H-[^{13}C] coil setup. Animal preparation and procedures were previously approved by McGill University's animal research committee and are in accordance with guidelines set by the Council on Animal Care.

A bolus of 1.1M 1-^{13}C glucose (99% enriched Cambridge Isotope Laboratories Inc., Andover, MA, USA) in saline was prepared and delivered intravenously via tail vein 8.5 minutes after the start of the PRESS-POCE sequence (each 8.5 min block with 128 averages, TR = 4 s). A 350 µl volume was infused over the first 15 seconds (5400 µl/kg/min), and the infusion rate was tapered off exponentially every 30 seconds to rapidly raise and maintain plasma glucose levels at ~10 mM as previously described (10). Eight minutes and 15 seconds into the experiment, the infusion rate was reduced to 17.8 µl/min, and maintained till the end of the experiment. Each 8.5min block of transients was repeated 12 times to cover 94 mins of acquisition after the infusion. A total of 2.3 ml of glucose solution (or ~ 460 mg of 1-^{13}C enriched glucose) was infused. Following data acquisition, spectral fitting of POCE difference spectra was performed in LCModel (39) using a simulated basis set that was generated using the FID-A simulation toolkit (18).

3.4 Results

3.4.1 Coil Bench Tests

Frequency response plots of the designed highpass filter are illustrated in Figure 3-2b. Reflection coefficient (S_{11}) values < -20 dB below 75.5 MHz and at 300.3 MHz, indicating negligible reflections at ^{13}C and ^{1}H frequencies. The transfer function (S_{21}) plot shows < -95 dB attenuation at 75.5 MHz, and insertion loss (IL) of -0.38 dB at the ^{1}H frequency of 300.3 MHz (including protection diode losses) before the preamplifier input. The tank circuit between ports 1 and 3 provides -36 dB of isolation at 300.3 MHz, which assists in minimizing S_{21} losses at the ^{1}H frequency. Low insertion losses (-0.08 dB at 75.5 MHz) on the S_{31} plot provides a low-loss path for decoupling RF content out of port 3 into a 50 Ω terminator. The maximum power handling capabilities of the filter have not been laboriously tested; however, it has been extensively used during POCE scans with 50 W CW for 600 ms, and 1 kW for 2 ms pulses spanning ~ 2 hours (TR = 4 s), with no apparent adverse effects.

3.4.2 *In vivo* and *in vitro* Measurements ^{1}H NMR

Figure 3-5 summarizes sensitivity comparisons between the ^{1}H-[^{13}C] coil setup, Bruker-20 mm surface coil, and volume coil optimized for rat. The ^{1}H-[^{13}C] coil setup shows comparable sensitivity profiles to those obtained from the Bruker-20 mm surface coil, even though a ~ -0.4 dB IL highpass filter is in-line between the coil and preamp, and a ^{13}C coil is in close proximity.

Both surface coils show superior SNR up to depths of ~8 mm relative to the 45 mm volumetric coil.

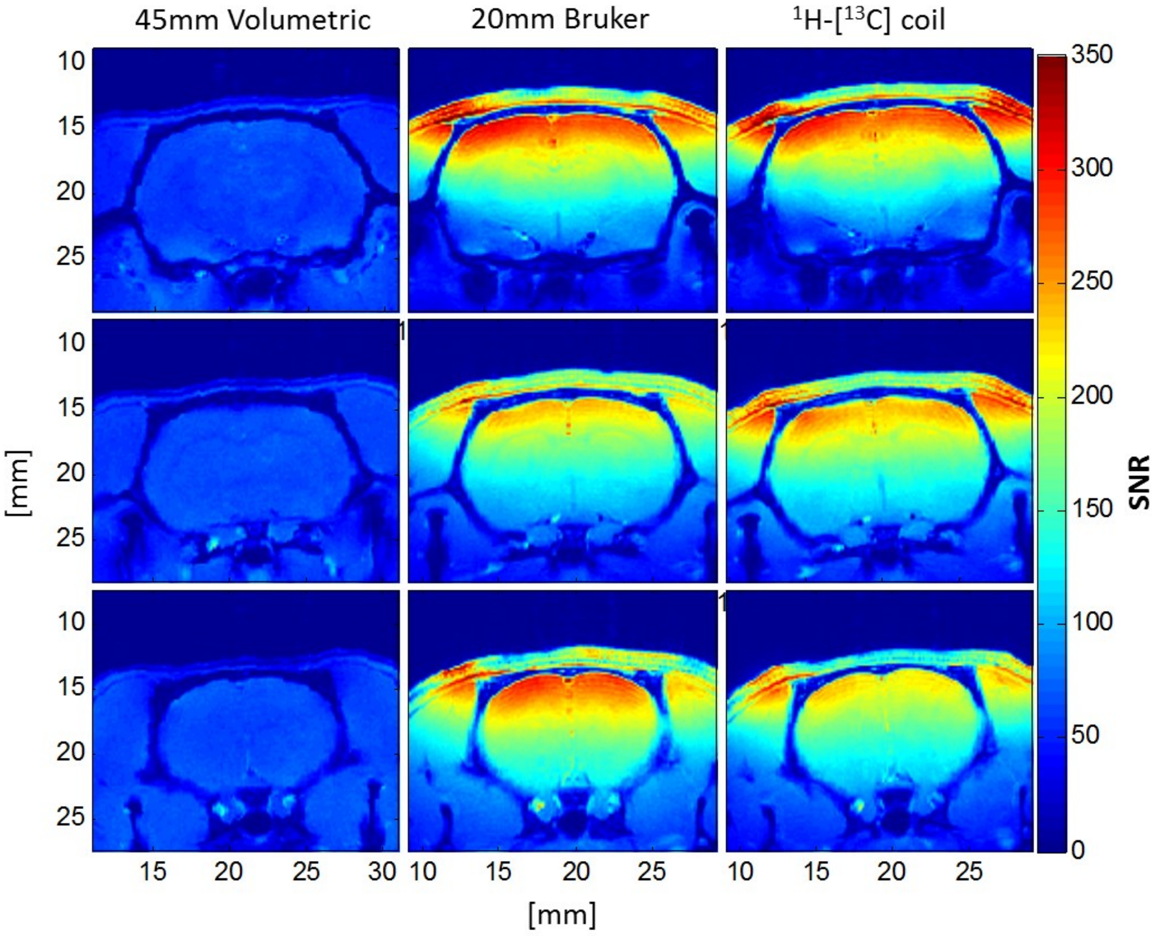

Figure 3-5 *Sensitivity maps of the* ^{1}*H*-^{13}*C coil setup*

Sensitivity maps of the ^{1}*H*-[^{13}*C] coil setup compared against a 20mm Bruker surface coil with integrated preamplifier, and a rat brain optimized 45mm birdcage coil. The figure Illustrates 3 slices, 6mm apart in the anterior-posterior direction in which the spectroscopy voxel was placed. Both surface coils show similar receive sensitivity profiles in terms of depth coverage; however more regions with slightly increased SNR are seen for the Bruker-20 mm coil. Marginally worse sensitivity from the* ^{1}*H*-[^{13}*C] coil setup was expected due to the presence of a -0.38 dB filter before the preamplifier. It is difficult to make direct sensitivity comparisons between the two surface coils as coil placement (anterior-posterior direction and distance from the rat head) significantly affect spatial SNR.*

3.4.3 *In vitro* and Dynamic *in vivo* Measurements ^{1}H-[^{13}C] NMR Spectroscopy

Localization and outer signal suppression performance of the POCE sequence was evaluated on a 6 x 6 x 6 mm^3 voxel as illustrated in Figure 3-6. The profiles show excellent localization and spin nutation in the three dimensions with a mean < 0.3% outer volume signal content for all directions.

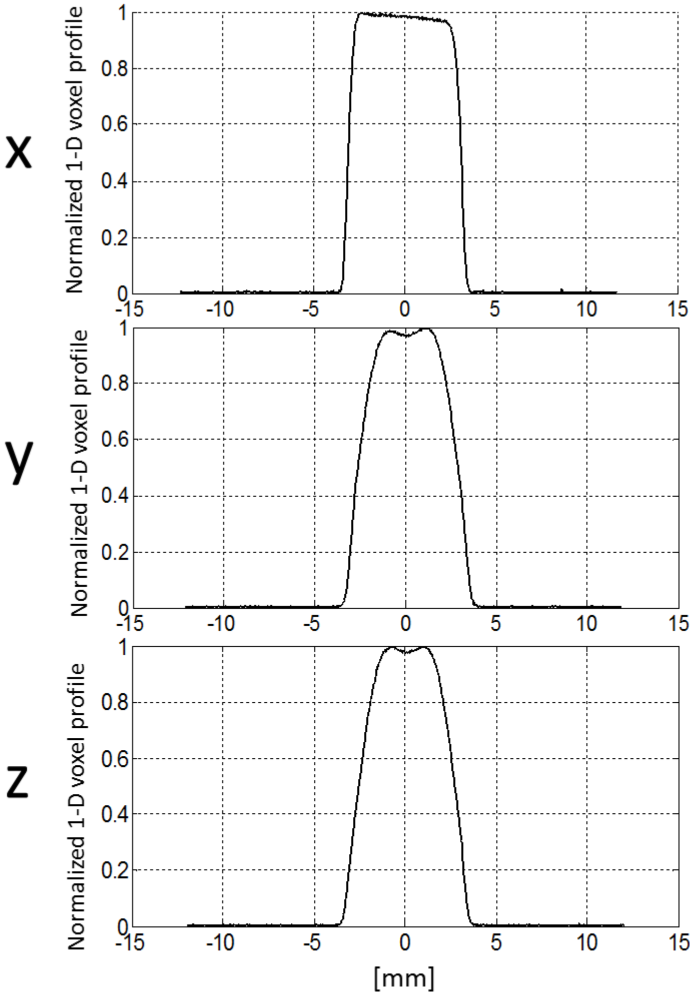

Figure 3-6 *Evaluation of spatial localization of the realized POCE sequence with 12.6 ms TE*
One dimensional spatial profiles in X, Y, and Z directions based on a 6 x 6 x 6 mm3 volumetric voxel created for spectroscopy is shown. The profiles show excellent localization in all three dimensions with minimal outer volume signal content (mean signal value < 0.3% for all directions outside the selected region).

Figure 3-7 summarizes ^{1}H and ^{1}H-[^{13}C] spectra obtained from a 100 µl voxel primarily encompassing the anterior cerebral cortex, and LCmodel (39) fitted spectra.

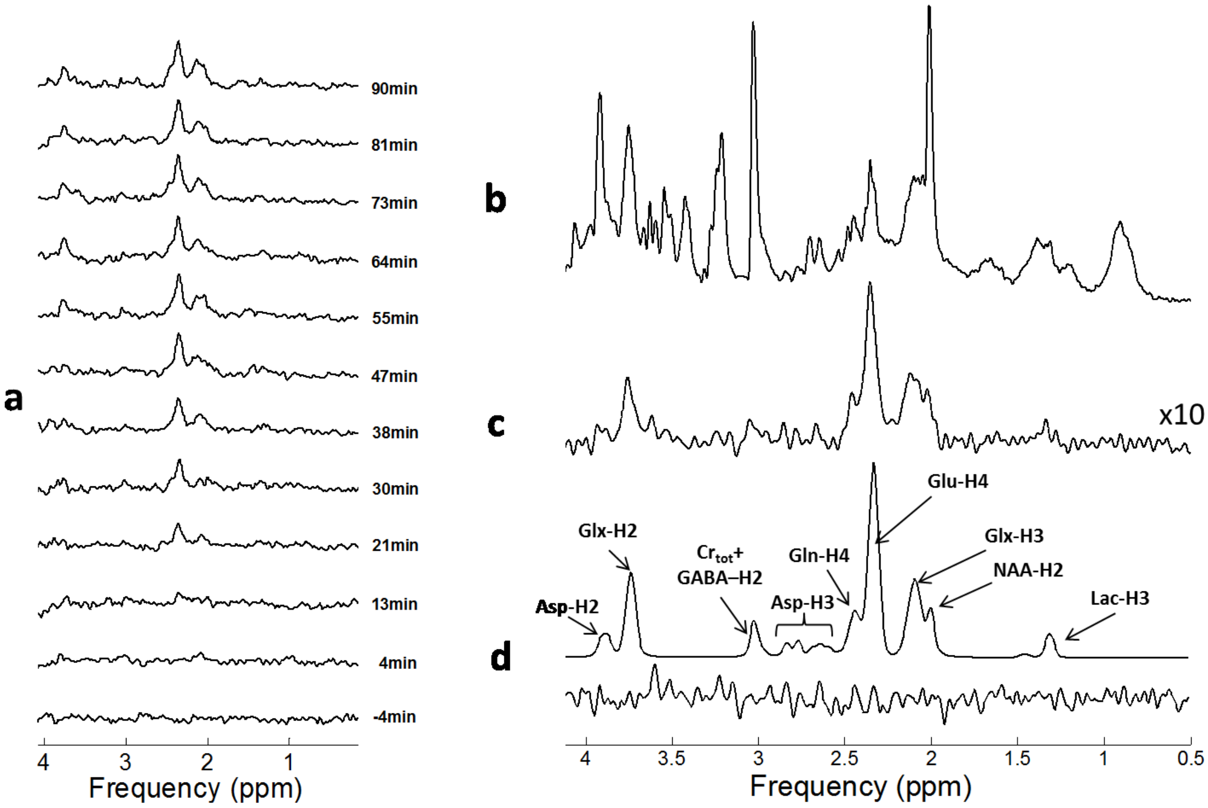

Figure 3-7 *Overall outcome of a dynamic in vivo ^{13}C MRS study following the infusion of 1-^{13}C glucose (a) Time resolved measurement of ^{13}C metabolite labeling in the rat brain in vivo during the infusion of 1-^{13}C glucose. Spectra were obtained with the PRESS-POCE sequence (TE = 12.6 ms, TR = 4000 ms) in a 100 µl volume. Each spectral time point is generated by averaging 128 transients, and apodized with a 1.7 Hz Guassian filter. The time points indicate temporal mid points of each acquisition block relative to the start of the 1-^{13}C glucose infusion. (b) ^{1}H spectrum from averaging edit-OFF scans only (apodized with a 5 Hz Lorentz-Gaussian filter) during the last 256 transients (77-94 mins). (c) Average of the edited ^{1}H-[^{13}C] spectrum (apodized with a 15 Hz Lorentz-Gaussian filter) during the last 384 transients (68-94 mins). Baseline corrections were not performed on any spectra. (d) An LCmodel fit of the ^{1}H-[^{13}C] spectrum in (c) is shown above, and the fit residual is shown below.*

Figure 3-7a illustrates a time series of ^{1}H-[^{13}C] spectra, with each individual spectrum arising from an 8.5 min acquisition (128 repetitions, TR=4 s), repeated for 94 mins, initiated 8.5 mins before the 1-^{13}C glucose infusion. The Glu-H4, Glx-H3 peaks and the Glx-H2 peak are visible approximately 13 min and 21min following the infusion, respectively. The edit-OFF spectrum in Figure 3-7b demonstrate excellent spectral resolution comparable to spectra at 7T reported elsewhere (5) for identical voxel size. The averaged ^{1}H-[^{13}C] spectrum towards the end of the experiment in Figure 3-7c show labeling of Glu-H4, Gn-H4, Glx-H3, Glx-H2, as well as low concentrations of Lactate-H3. Figure 3-7d shows the LCmodel fitted spectrum (top), and the fit residual (bottom).

3.5 Discussion

The PRESS sequence is readily available with most MRI scanners, thus the implementation of a short TE PRESS-POCE sequence is relatively straightforward (compared to a LASER, ISIS, or SPECIAL based implementation) provided a compatible ^{1}H-[^{13}C] coil is used. The feasibility of performing dynamic *in vivo* ^{13}C MRS using the presented coil was validated with a PRESS-POCE sequence during an infusion of 1-^{13}C glucose in a rat. The POCE spectrum in Figure 3-7c illustrate that the prominent metabolites (Glu-C4, Gln-C4, Lac-C3, Glx-C2, NAA-H2, Glx-H2, Glc-C6) are satisfactorily decoupled, and spectral quality and time resolution are comparable to previous studies (5,7) in rats. It is difficult to make quantitative comparisons of sensitivity between the presented method and previous studies, though a few variations can be noted: the study by de Graaf et al. (5) was conducted using a 1,6-^{13}C Glucose infusion, where a factor-of-two gain in SNR is obtained relative to 1-^{13}C glucose for similar fractional enrichment (a 7T magnet, 100 μl voxel, 128 transients per time point); the study by Pfeuffer et al. (7) was conducted on a 9.4T magnet, with a 137 μl voxel, 192 transients per time point, and injection of ~ 1100 mg of 1-^{13}C glucose 90 mins into the experiment (> 2 times the amount of 1-^{13}C glucose used in our study for similar weight rats). The Pfeuffer study also used ACED-STEAM localization, which inherently suffers from a 50% reduction in SNR compared to ISIS, PRESS, SPECIAL, or LASER-based implementations.

Utilization of a ^{1}H volumetric resonator accommodates the realization of a PRESS-localized POCE sequence with highly uniform spin nutation with conventional pulses. With little or no modifications, the proposed ^{1}H-[^{13}C] coil platform is expected to provide excellent localization and uniform nutation when paired with POCE sequences utilizing conventional pulse such as: PRESS-POCE (described here and elsewhere; 4,20), ACED-STEAM based POCE (7), and SPECIAL based POCE (8). Furthermore, the coil platform is compatible with spin-echo and gradient-echo based imaging sequences utilizing conventional pulses (due to the B_1^+ field homogeneity relative to an all-surface coil ^{1}H-^{13}C MRS coil approach), thus providing the convenience of using optimized and established functional imaging sequences during ^{1}H-^{13}C MRS studies.

A limitation of the described coil system is its peak B_1^+ capabilities relative to surface coil transmitters which limit the use of short, high bandwidth pulses, thus increase chemical shift displacement errors (CSDE). CSDE for the PRESS-POCE sequence was $< 25\%$ (for voxel shift between water and fat) with vendor-supplied Hermite refocusing pulses. However, ^{13}C labeled metabolites observed in dynamic ^{1}H-^{13}C MRS studies reside in a spectral window of ~2.6 ppm (1.3 - 3.9 ppm), hence CSDE is reduced to $< 20\%$. If CSDE is a limitation at higher field strengths, a few modifications to the platform can be exploited: 1) employ peak-B_1^+ constrained optimal control high bandwidth refocusing pulses (40,41); 2) replace the volumetric ^{1}H resonator with a smaller (head-only) detunable volumetric resonator to achieve higher peak B_1^+; or 3) at ultra-high field strengths when the FOV dimensions approach the RF wavelength (~ $\lambda/2$), a detunable transmit array coil can be used in combination with parallel transmit or rf shimming approaches to improve B_1^+ (42,43).

In addition to the use of RF filters, further attenuation of heteronuclear decoupling signals from coupling to the ^{1}H channel was achieved with double shielded coax cables, and strategically placing ^{13}C baluns on all RF carrying cables. In practice it can be difficult to completely filter out decoupling noise due to finite attenuation characteristics of filters and parasitic RF coupling between cables; thus phase cycled decoupling assists to further minimize decoupling noise with signal averaging.

The presented POCE-MRS method utilizes WALTZ-16 decoupling, which inherently has limited decoupling efficiency at large bandwidths required on the ^{13}C channel in the presence of an inhomogeneous B_2^+ field (44). By utilizing a calibrated adiabatic decoupling scheme with similar bandwidth, (S) spins of interest can be inverted with > 99% efficiency in a varying B_2^+ field (5,44), thus improving SNR of ^{1}H-[^{13}C] spectra.

3.6 Conclusions

A ^{1}H-[^{13}C] coil setup consisting of a ^{1}H volumetric resonator, a ^{1}H receive-only surface coil, and a quadrature driven ^{13}C coil is presented. The developed platform provides homogenous B_1^+ in the region imaged, and SNR performance comparable to an equivalent geometry, commercially available Rx-only surface coil with integrated preamplifier. A short TE (12.6 ms), PRESS-localized POCE sequence with excellent voxel localization and sensitivity was realized utilizing the presented coil setup. The overall setup provides a convenient and sensitive platform from which to study energy metabolism and glutamate neurotransmission in the rat brain *in vivo*.

3.7 Acknowledgements

This research was funded by NSERC (Grant No. RGPIN-2014-07072) awarded to JN, FRSQ Subvention pour projet de développement stratégique innovants 2012-2016 (Grant No. 26679) awarded to MR and QBIN travel grant awarded to CK. The authors thank Dr. Doug Rothman and Dr. Robin de Graaf for stimulating scientific discussions on ^{13}C experiments and invitation to visit Yale University. The authors thank Pier Larochelle for her assistance with animal preparations. The authors thank Saaussan Madi for Bruker related support, Helmut Stark, and Steven Toddes for their insights on related RF Engineering. Finally the authors thank the Robarts Institute of Western University for hosting and inviting CK for a high-Field MRI winter school workshop (2015), and the McKnight Brain Institute at University of Florida for hosting an RF coil workshop (2016).

3.8 References

1. Rothman DL, De Feyter HM, de Graaf RA, Mason GF, Behar KL. 13C MRS studies of neuroenergetics and neurotransmitter cycling in humans. NMR in biomedicine 2011;24(8):943-957.
2. Fitzpatrick SM, Hetherington HP, Behar KL, Shulman RG. The flux from glucose to glutamate in the rat brain in vivo as determined by 1H-observed, 13C-edited NMR spectroscopy. Journal of cerebral blood flow and metabolism : official journal of the International Society of Cerebral Blood Flow and Metabolism 1990;10(2):170-179.
3. Rothman DL, Howseman AM, Graham GD, Petroff OA, Lantos G, Fayad PB, Brass LM, Shulman GI, Shulman RG, Prichard JW. Localized proton NMR observation of [3-13C]lactate in stroke after [1-13C]glucose infusion. Magnetic resonance in medicine 1991;21(2):302-307.
4. Chen W, Adriany G, Zhu XH, Gruetter R, Ugurbil K. Detecting natural abundance carbon signal of NAA metabolite within 12-cm3 localized volume of human brain using 1H-[13C] NMR spectroscopy. Magnetic resonance in medicine 1998;40(2):180-184.
5. de Graaf RA, Brown PB, Mason GF, Rothman DL, Behar KL. Detection of [1,6-13C2]-glucose metabolism in rat brain by in vivo 1H-[13C]-NMR spectroscopy. Magnetic resonance in medicine 2003;49(1):37-46.
6. Yang J, Li CQ, Shen J. In vivo detection of cortical GABA turnover from intravenously infused [1-13C]D-glucose. Magnetic resonance in medicine 2005;53(6):1258-1267.
7. Pfeuffer J, Tkac I, Choi IY, Merkle H, Ugurbil K, Garwood M, Gruetter R. Localized in vivo 1H NMR detection of neurotransmitter labeling in rat brain during infusion of [1-13C] D-glucose. Magnetic resonance in medicine 1999;41(6):1077-1083.

8. Xin L, Mlynarik V, Lanz B, Frenkel H, Gruetter R. 1H-[13C] NMR spectroscopy of the rat brain during infusion of [2-13C] acetate at 14.1 T. Magnetic resonance in medicine 2010;64(2):334-340.

9. Tannus A, Garwood M. Adiabatic pulses. NMR in biomedicine 1997;10(8):423-434.

10. de Graaf RA, Rothman DL, Behar KL. State of the art direct 13C and indirect 1H-[13C] NMR spectroscopy in vivo. A practical guide. NMR in biomedicine 2011;24(8):958-972.

11. Ordidge RJ, Connelly A, Lohman JAB. Image-selected in Vivo spectroscopy (ISIS). A new technique for spatially selective nmr spectroscopy. Journal of Magnetic Resonance (1969) 1986;66(2):283-294.

12. Lawry TJ, Karczmar GS, Weiner MW, Matson GB. Computer simulation of MRS localization techniques: an analysis of ISIS. Magnetic resonance in medicine 1989;9(3):299-314.

13. Ljungberg M, Starck G, Vikhoff-Baaz B, Alpsten M, Ekholm S, Forssell-Aronsson E. Extended ISIS sequences insensitive to T(1) smearing. Magnetic resonance in medicine 2000;44(4):546-555.

14. Mlynarik V, Gambarota G, Frenkel H, Gruetter R. Localized short-echo-time proton MR spectroscopy with full signal-intensity acquisition. Magnetic resonance in medicine 2006;56(5):965-970.

15. Garwood M, Merkle H. Heteronuclear spectral editing with adiabatic pulses. Journal of Magnetic Resonance (1969) 1991;94(1):180-185.

16. Wang J, Yang QX, Zhang X, Collins CM, Smith MB, Zhu XH, Adriany G, Ugurbil K, Chen W. Polarization of the RF field in a human head at high field: a study with a quadrature surface coil at 7.0 T. Magnetic resonance in medicine 2002;48(2):362-369.

17. Fuchs A, Luttje M, Boesiger P, Henning A. SPECIAL semi-LASER with lipid artifact compensation for 1H MRS at 7 T. Magnetic resonance in medicine 2013;69(3):603-612.

18. Simpson R, Devenyi GA, Jezzard P, Hennessy TJ, Near J. Advanced processing and simulation of MRS data using the FID appliance (FID-A)-An open source, MATLAB-based toolkit. Magnetic resonance in medicine 2015.

19. Bottomley PA. Spatial localization in NMR spectroscopy in vivo. Annals of the New York Academy of Sciences 1987;508:333-348.

20. Doan BT, Autret G, Mispelter J, Meric P, Meme W, Montecot-Dubourg C, Correze JL, Szeremeta F, Gillet B, Beloeil JC. Simultaneous two-voxel localized (1)H-observed (13)C-edited spectroscopy for in vivo MRS on rat brain at 9.4T: Application to the investigation of excitotoxic lesions. Journal of magnetic resonance 2009;198(1):94-104.

21. Sørensen OW, Eich GW, Levitt MH, Bodenhausen G, Ernst RR. Product operator formalism for the description of NMR pulse experiments. Progress in Nuclear Magnetic Resonance Spectroscopy 1984;16:163-192.

22. Slotboom J, Mehlkopf AF, Bovée WMMJ. A single-shot localization pulse sequence suited for coils with inhomogeneous RF fields using adiabatic slice-selective RF pulses. Journal of Magnetic Resonance (1969) 1991;95(2):396-404.

23. Jonkers RA, Geraedts TR, van Loon LJ, Nicolay K, Prompers JJ. Multitissue assessment of in vivo postprandial intracellular lipid partitioning in rats using localized 1H-[13C] magnetic resonance spectroscopy. Magnetic resonance in medicine 2012;68(4):997-1006.

24. Garwood M, DelaBarre L. The return of the frequency sweep: designing adiabatic pulses for contemporary NMR. Journal of magnetic resonance 2001;153(2):155-177.

25. de Graaf RA. Single Volume Localization and Water Suppression. In Vivo NMR Spectroscopy: John Wiley & Sons, Ltd; 2007. p 297-348.

26. Carr HY, Purcell EM. Effects of Diffusion on Free Precession in Nuclear Magnetic Resonance Experiments. Physical Review 1954;94(3):630-638.

27. Allerhand A. Analysis of Carr—Purcell Spin-Echo NMR Experiments on Multiple-Spin Systems. I. The Effect of Homonuclear Coupling. The Journal of Chemical Physics 1966;44(1):1-9.

28. Gruetter R, Adriany G, Choi IY, Henry PG, Lei H, Oz G. Localized in vivo 13C NMR spectroscopy of the brain. NMR in biomedicine 2003;16(6-7):313-338.

29. Adriany G, Gruetter R. A half-volume coil for efficient proton decoupling in humans at 4 tesla. Journal of magnetic resonance 1997;125(1):178-184.

30. Klomp DW, Renema WK, van der Graaf M, de Galan BE, Kentgens AP, Heerschap A. Sensitivity-enhanced 13C MR spectroscopy of the human brain at 3 Tesla. Magnetic resonance in medicine 2006;55(2):271-278.

31. Li S, Zhang Y, Wang S, Araneta MF, Johnson CS, Xiang Y, Innis RB, Shen J. 13C MRS of occipital and frontal lobes at 3 T using a volume coil for stochastic proton decoupling. NMR in biomedicine 2010;23(8):977-985.

32. Barberi EA, Gati JS, Rutt BK, Menon RS. A transmit-only/receive-only (TORO) RF system for high-field MRI/MRS applications. Magnetic resonance in medicine 2000;43(2):284-289.

33. Avdievich NI, Hetherington HP. 4 T actively detunable transmit/receive transverse electromagnetic coil and 4-channel receive-only phased array for (1)H human brain studies. Magnetic resonance in medicine 2004;52(6):1459-1464.

34. Gruetter R. Automatic, localized in vivo adjustment of all first- and second-order shim coils. Magnetic resonance in medicine 1993;29(6):804-811.

35. Tkáč I, Starčuk Z, Choi IY, Gruetter R. In vivo 1H NMR spectroscopy of rat brain at 1 ms echo time. Magnetic resonance in medicine 1999;41(4):649-656.

36. Shaka AJ, Keeler J, Freeman R. Evaluation of a new broadband decoupling sequence: WALTZ-16. Journal of Magnetic Resonance (1969) 1983;53(2):313-340.

37. Stefan O. Schönberg OD, Maximilian F Reiser Parallel Imaging in Clinical MR Applications: Springer; 2007. 564 p.

38. Insko EKB, L. Mapping of the Radiofrequency Field. Journal of Magnetic Resonance, Series A 1993;103(1):82-85.

39. Provencher SW. Estimation of metabolite concentrations from localized in vivo proton NMR spectra. Magnetic resonance in medicine 1993;30(6):672-679.

40. Soher BJS, P; Todd, S; Steinberg, J; Young, K. VeSPA: integrated applications for RF pulse design, spectral simulation and MRS data analysis. Proc Intl Soc Magn Reson Med 2011;19:1410.

41. Matson GB, Young K, Kaiser LG. RF pulses for in vivo spectroscopy at high field designed under conditions of limited power using optimal control. Journal of magnetic resonance 2009;199(1):30-40.

42. Zhao W, Cohen-Adad J, Polimeni JR, Keil B, Guerin B, Setsompop K, Serano P, Mareyam A, Hoecht P, Wald LL. Nineteen-channel receive array and four-channel transmit array coil for cervical spinal cord imaging at 7T. Magnetic resonance in medicine 2014;72(1):291-300.

43. Gilbert KM, Gati JS, Barker K, Everling S, Menon RS. Optimized parallel transmit and receive radiofrequency coil for ultrahigh-field MRI of monkeys. NeuroImage 2016;125:153-161.

44. de Graaf RA. Theoretical and experimental evaluation of broadband decoupling techniques for in vivo nuclear magnetic resonance spectroscopy. Magnetic resonance in medicine 2005;53(6):1297-1306.

Chapter 4

POCE MRS Utilizing Simultaneous Editing And Localization Pulses (SEAL)

Chapter 3 described the development of a volumetric resonator base ^{13}C MRS coil platform to realize single-shot PRESS localized POCE MRS, in which a 12.6ms TE PRESS-POCE sequence was presented. However, due to instrument limitations (peak B_1 and spoiler gradient strength and stabilization time), conventional methods used for editing and localization would not provide both $<$ 10ms TE and single-shot localization. In this chapter, we describe a novel single-shot PRESS-localized POCE-MRS sequence that involves the application of simultaneous editing and localization pulses (SEAL-PRESS), allowing the TE to be reduced to a theoretically optimal value of ~ $1/J_{HC}$ (8.1-ms) for within-sequence edited ^{1}H-[^{13}C] spectroscopy. The content of this chapter has been published in *Magnetic Resonance in Medicine*.

Minimum echo time PRESS-based proton observed carbon edited (POCE) magnetic resonance spectroscopy in rat brain using simultaneous editing and localization pulses.

Chathura Kumaragamage [1,3], Dan Madularu [2,3,4], Axel P. Mathieu [2,3], Derek Lupinsky[2,3], Robin A. de Graaf [5], and Jamie Near [1,2,3]

[1] Department of Biomedical Engineering, McGill University, Montreal, QC, Canada.
[2] Department of Psychiatry, Faculty of Medicine, McGill University, Montreal, QC, Canada.
[3] Brain Imaging Centre, Douglas Mental Health University Institute, McGill University, Montreal, QC, Canada.
[4] Center for Translational NeuroImaging, Northeastern University, Boston, MA, USA.
[5] Radiology and Biomedical Imaging, Yale University, New Haven, CT, USA.

Magnetic Resonance in Medicine. 2018;[Early view], DOI: 10.1002/mrm/27119.

4.1 Abstract

Purpose: Indirect ^{13}C magnetic resonance spectroscopy (MRS) by proton observed carbon editing (POCE) is a powerful method to study brain metabolism. The sensitivity of POCE-MRS can be enhanced through the use of short echo-times (TE), which primarily minimizes homonuclear J-evolution and T_2 related losses; previous POCE-MRS implementations use longer than optimal echo times due to sequence limitations, or short TE image selected *in vivo* spectroscopy (ISIS) based multi-shot acquisitions for 3D localization. To that end, this paper presents a novel single-shot PRESS-localized POCE-MRS sequence that involves the application of Simultaneous Editing And Localization pulses (SEAL-PRESS), allowing the TE to be reduced to a theoretically optimal value of ~ $1/J_{HC}$.

Methods: The optimized SEAL-PRESS sequence was first evaluated in simulation and in phantom; next the sequence was validated with dynamic *in vivo* POCE-MRS performed in a rat preparation during a 1,6-$^{13}C_2$-Glc infusion, and on a microwave fixed rat brain following a 2-hour long [1,6-$^{13}C_2$]-Glc infusion. POCE spectra from the SEAL-PRESS sequence were compared against a previously described 12.6-ms PRESS-POCE sequence utilizing a classical carbon editing scheme.

Results: The SEAL-PRESS sequence provides >95% editing efficiency, optimal sensitivity and localization for POCE MRS with an overall sequence TE of 8.1-ms. Signal amplitude of ^{13}C labeled metabolites GluH4, Gln-H4, Glx-H3, GlcH6+Glx-H2, and Asp-H2 were shown to be improved by >17% relative to a 12.6-ms PRESS-POCE sequence *in vivo*.

Conclusion: We report for the first time, a single-shot PRESS-localized and edited 8.1-ms TE POCE-MRS sequence with optimal sensitivity, editing efficiency, and localization.

4.2 Introduction

Dynamic *in vivo* ^{13}C magnetic resonance spectroscopy (MRS) following the infusion of ^{13}C enriched substrates allows for the non-invasive investigation of neuroenergetics and neurotransmitter cycling in the brain (1). Spatially localized ^{13}C MRS techniques (2) further allow the study of metabolism in specific regions of interest. J-difference editing (3) for proton-observed carbon-edited (POCE) MRS (4,5) is an attractive alternative to direct ^{13}C MRS methods due to signal-to-noise-ratio (SNR) gains achievable (5,6), while enabling quantification of fractional enrichment (6). However, indirect ^{13}C MRS is somewhat limited by poorer spectral dispersion compared to direct ^{13}C MRS, which is proportionately overcome at higher magnetic field strengths.

POCE-MRS can in theory be achieved with two spin-echo acquisitions, one with non-selective refocusing [180° pulses simultaneously on both ^{1}H (I), and ^{13}C (S) spins, herein referred to as a $\hat{R}^{I,S}(\pi)$ pulse], and another with selective refocusing [180° pulses on I spins only, herein referred to as a $\hat{R}^{I}(\pi)$ pulse]. For maximum editing efficiency, the sequence echo time (TE) should be $1/\mathrm{J_{HC}}$ ms, where $\mathrm{J_{HC}}$ is the heteronuclear scalar coupling constant. Then, in the $\hat{R}^{I,S}(\pi)$ spin-echo (also known as the EDIT-ON scan), all heteronuclear coupled ^{1}H spins are acquired with an inverted phase relative to uncoupled ^{1}H spins, while the $\hat{R}^{I}(\pi)$ spin-echo (the EDIT-OFF scan) refocuses all ^{1}H spins to be in-phase. Thus the difference between the two scans yields signal exclusively from ^{1}H nuclei directly attached to ^{13}C nuclei.

A few notable approaches to localized, J-difference edited POCE-MRS reported in the literature are as follows: **1**) employ a $\hat{R}^{S}(\pi)$ pulse on alternate scans centered $1/2\mathrm{J_{HC}}$ ms before the final echo: this type of editing is seen in Point REsolved SpectroScopy (PRESS; 7) localized POCE (8,9) and Localization by adiabatic spin-echo refocusing (LASER;10) POCE (6,11,12) sequences. However, POCE via this scheme typically necessitates the final echo to be >10 ms to accommodate two non-simultaneously employed $\hat{R}^{I}(\pi)$ and $\hat{R}^{S}(\pi)$ pulses and the $1/2\mathrm{J}_{\mathrm{HC}}$ ms delay. **2**) employ $\hat{R}^{I,S}(\pi)$ and $\hat{R}^{I}(\pi)$ refocusing pulses on alternate scans, centered $\sim 1/2\mathrm{J}_{\mathrm{HC}}$ ms before a $\sim 1/\mathrm{J}_{\mathrm{HC}}$ ms echo, reported for Image-Selected *In vivo* Spectroscopy (ISIS; 13), PRESS, and LASER implementations (14-16); this approach can reduce the sequence TE relative to method 1) due to the simultaneous use of editing and refocusing, **3**) employ ^{13}C editing with the global B_1 Insensitive Spectral Editing Pulse (BISEP; 17) prior to localization. The BISEP block prepares spins in the z-axis (uncoupled ^{1}H spins and heteronuclear coupled spins will be aligned in anti-parallel directions on alternate scans), thus can be followed by an ultra-short TE spin-echo localization sequence of interest with full intensity editing (neglecting T_1 relaxation) as reported by Xin and colleagues (18) using SPECIAL (19).

Due to the lower SNR of POCE-MRS relative to its unedited water suppressed counterparts, POCE-MRS is highly susceptible to subtraction and instrument instability related artifacts. Hence, POCE methods based on single-shot localization such as PRESS or LASER (two transients for each POCE-MRS spectrum) is beneficial relative to ISIS based implementations. Furthermore, it is beneficial to shorten the sequence TE to minimize homonuclear J-evolution and T_2 related losses. LASER-POCE sequences reported have TE >22 ms, primarily due to the requirement for three pairs of ~1 ms adiabatic full passage (AFP) pulses (20), and an ~10 ms final echo; however, the effects of homonuclear J-evolution (21) and diffusion (22,23) are minimized for LASER-POCE due to the Carr-Purcell spin-echo (CPSE; 22) character of the sequence, and chemical shift displacements are minimal due to the high bandwidth AFP pulses (relative to purely amplitude modulated pulses) used. PRESS-POCE sequences have been implemented with TE <16 ms (9,14), which is an attractive alternative to

LASER and multi-shot ISIS based implementations, provided a spatially homogenous B_1^+ field is present.

In this study we report a PRESS-POCE sequence that employs Simultaneous Editing And Localization on both PRESS refocusing pulses (herein referred to as SEAL-PRESS) with a total sequence TE of $\sim 1/J_{HC}$ (8.1 ms, optimized for the [2-^{13}C]-Ace spin system); the sequence approaches the theoretical minimum TE for within-sequence edited POCE-MRS. The simultaneous application of editing and slice-selective pulses adds an additional consideration into the sequence design; namely, the normally broadband frequency selective carbon-editing pulses now become slice-selective. The sequence was validated in phantom and a rat preparation at 7T. Reducing the TE from 12.6-ms (TE of a PRESS-POCE sequence presented in an earlier study 9) to 8.1-ms increased signal intensity of ^{13}C labeled metabolites by >17.0% for GluH4, Gln-H4, Glx-H3, GlcH6 + Glx-H2, and Asp-H2 systems *in vivo*, primarily due to reduced homonuclear J-evolution related losses of strongly coupled metabolite systems.

4.3 Theory

4.3.1 Simultaneous Editing And Localization with PRESS

The SEAL-PRESS sequence is presented in Figure 4-1. The EDIT-OFF scan consists of two $\hat{R}^{I}(\pi)$ refocusing pulses similar to a PRESS sequence with $TE_1 = TE_2$, and two $\hat{R}^{I,S}(\pi)$ refocusing pulses for the EDIT-ON scan. The use of $\hat{R}^{I}(\pi)$ and $\hat{R}^{I,S}(\pi)$ refocusing simultaneously provides single-shot localization and two-shot carbon editing.

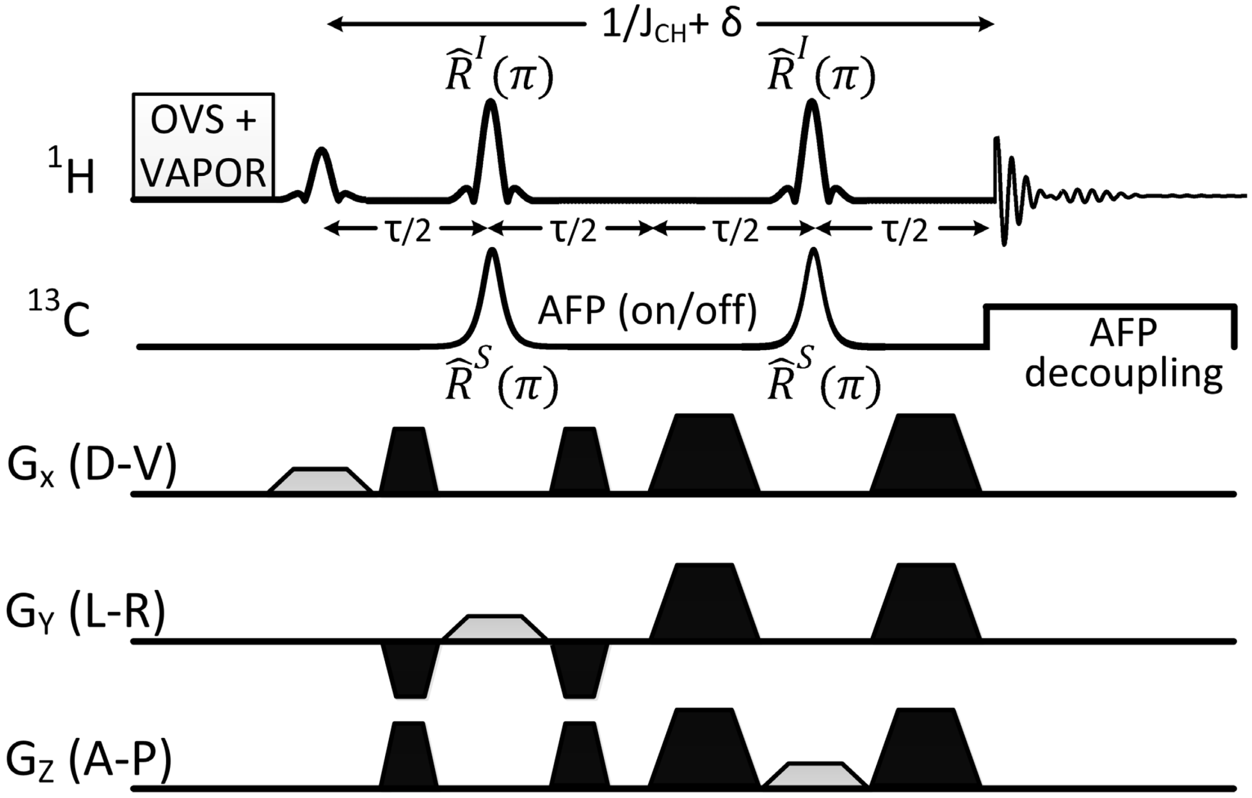

Figure 4-1 *The SEAL-PRESS sequence.*

A schematic representation of the TE = 8.1 ms (TE$_1$ = TE$_2$ = τ = 4.05 ms) ^{1}H-[^{13}C] SEAL-PRESS sequence. The sequence TE needs to be extended by a δ amount to obtain maximal editing efficiency, which varies based on the modulation functions and lengths of the shaped $\hat{R}_x^{I,S}(\pi)$ pulses used. In the present work δ = 0.2 ms, to account for retardation of heteronuclear J-evolution (described in text). An AFP decoupling scheme is used during 200-ms of the acquisition; the sequence is preceded by OVS and VAPOR modules as illustrated.

Evolution of the *IS* spin system for EDIT-OFF and EDIT-ON scans during the first spin-echo (TE$_1$) is presented below according to the solution of the Liouville-von Neumann equation for a time-independent Hamiltonian: $\hat{\rho}(t) = \exp\{-i\hat{\mathcal{H}}t\}\hat{\rho}(0)\exp\{+i\hat{\mathcal{H}}t\}$: where $\hat{\rho}(0)$ is the initial density matrix.

EDIT-OFF: $\hat{I}_z \xrightarrow{(\pi/2)_y^I} \hat{I}_x \xrightarrow{\hat{\mathcal{H}}(\tau/2)} \hat{Q}\hat{I}_x\hat{Q}^{-1} \xrightarrow{\pi_x^I} \hat{R}_x^I(\pi)\hat{Q}\hat{I}_x\hat{Q}^{-1}\hat{R}_x^I(-\pi)$

$$\xrightarrow{\hat{\mathcal{H}}(\tau/2)} \hat{Q}\hat{R}_x^I(\pi)\hat{Q}\hat{I}_x\hat{Q}^{-1}\hat{R}_x^I(-\pi)\hat{Q}^{-1} = \hat{I}_x \qquad (4\text{-}1)$$

EDIT-ON: $\hat{I}_z \xrightarrow{(\pi/2)_y^I} \hat{I}_x \xrightarrow{\hat{\mathcal{H}}(\tau/2)} \hat{Q}\hat{I}_x\hat{Q}^{-1} \xrightarrow{\pi_x^{I,S}} \hat{R}_x^{I,S}(\pi)\hat{Q}\hat{I}_x\hat{Q}^{-1}\hat{R}_x^{I,S}(-\pi)$

$$\xrightarrow{\hat{\mathcal{H}}(\tau/2)} \hat{Q}\hat{R}_x^{I,S}(\pi)\hat{Q}\hat{I}_x\hat{Q}^{-1}\hat{R}_x^{I,S}(-\pi)\hat{Q}^{-1} =$$

$$\hat{R}_x^{I,S}(\pi)\exp\{-i\pi J_{HC}2\hat{I}_z\hat{S}_z\tau\}\,\hat{I}_x\exp\{+i\pi J_{HC}2\hat{I}_z\hat{S}_z\tau\}\,\hat{R}_x^{I,S}(-\pi) = 2\hat{I}_y\hat{S}_z\,\{when\,\tau = 1/(2\,J_{HC})\} \tag{4-2}$$

where

$$\hat{Q} = \exp\{-i\hat{\mathcal{H}}\,\tau/2\},\hat{\mathcal{H}} = \Omega_I\hat{I}_z + \Omega_S\hat{S}_z + \pi J_{HC}2\hat{I}_z\hat{S}_z \tag{4-3}$$

During the EDIT-OFF scan, heteronuclear J-evolution and chemical shifts (Ω_I) are refocused at the first echo, and results in the $\hat{I}_x$ spin state as expected (Eq. 4-1). Since the second spin-echo (TE_2) is identical to TE_1, $\hat{I}_x$ will be subjected to the same set of operations in Eq. 4-2, and evolve back to $\hat{I}_x$. For EDIT-ON scans during TE_1, chemical shifts are refocused at the first echo (Eq. 4-3); while evolution under the weak heteronuclear coupling Hamiltonian is unaffected. As a result, the system evolves to a purely anti-phase coherence state $2\hat{I}_y\hat{S}_z$, and evolution during TE_2 is:

$$\hat{R}_x^{I,S}(\pi)\exp\{-i\pi J_{HC}2\hat{I}_z\hat{S}_z\tau\}\,2\hat{I}_y\hat{S}_z\exp\{+i\pi J_{HC}2\hat{I}_z\hat{S}_z\tau\}\,\hat{R}_x^{I,S}(\pi) = -\hat{I}_x\,\{when\,\tau = 1/(2\,J_{HC})\} \tag{4-4}$$

Thus, subtraction of EDIT-OFF and EDIT-ON scans result exclusively in a full intensity ^{1}H-[^{13}C] MRS spectrum. It is not necessary for $TE_1 = TE_2 = 1/(2\,J_{HC})$ ms for full-intensity editing with the SEAL-PRESS sequence; the above editing condition is met as long as $TE_1 + TE_2 = 1/(J_{HC})$ ms. However, homonuclear J-evolution related losses will be minimal when $TE_1 = TE_2$ due to the shortest inter-pulse spacing as per the CPSE condition (21,22).

The above product operator analysis however assumes instantaneous rotations. Shaped refocusing and AFP inversion pulses with a well-defined frequency profile would typically be in the order of a millisecond on a pre-clinical MRI scanner, thus instantaneous non-selective $\hat{R}_x^{I,S}(\pi)$ pulses are an oversimplification that do not account for partial inhibition of heteronuclear J-evolution. For example instead of a non-selective $\hat{R}_x^{I,S}(\pi)$ rotation, consider the following hypothetical segment where $\hat{R}_x^{S}(\pi)$ is split into two $\hat{R}_x^{S}(\pi/2)$ rotations symmetrically placed around a $\hat{R}_x^{I}(\pi)$ rotation with small δ time delays, starting from the $\hat{\rho}(0) = 2\hat{I}_y\hat{S}_z$ spin state as follows:

$$2\hat{I}_y\hat{S}_z \xrightarrow{\hat{R}_x^S(\pi/2)} \xrightarrow{\hat{\mathcal{H}}(\delta)} \xrightarrow{\hat{R}_x^I(\pi)} \xrightarrow{\hat{\mathcal{H}}(\delta)} \xrightarrow{\hat{R}_x^S(\pi/2)} \hat{\rho}(2\delta) \tag{4-5}$$

Computation of the above simplifies to:

$$\hat{\rho}(2\delta) = \hat{R}_x^S(\pi)\hat{R}_x^I(\pi)2\hat{I}_y\hat{S}_z\,\hat{R}_x^I(-\pi)\hat{R}_x^S(-\pi) = 2\hat{I}_y\hat{S}_z, \tag{4-6}$$

where the heteronuclear J-evolution operator is absent during the 2δ period in Eq. 4-4. The above situation can be easily visualized since the heteronuclear spin system will be in a multiple quantum coherence state $(2\hat{I}_y\hat{S}_y)$ following the first $\hat{R}_x^{S}(\pi/2)$ pulse, which does not evolve under heteronuclear scalar coupling during the entire 2δ period. The above observation is valid for an arbitrary IS spin-state $\hat{\rho}(0)$, as evident by the simplified form in Eq. 4-6. Thus, in practice inhibition of heteronuclear J-evolution can be thought to manifest from heteronuclear multiple quantum coherence states that arise from heteronuclear anti-phase coherence terms during non-instantaneous $\hat{R}_x^{I,S}(\pi)$ pulses.

4.4 Methods

4.4.1 Animal Preparation

Experiments were performed on two adult male Long Evans rats (Charles River Laboratories, Montreal, QC, Canada) weighing 260-280 g. One rat was used for ^{1}H-[^{13}C] coil and sequence calibration, the second rat was used for dynamic *in vivo* ^{13}C MRS. The tail vein of the second rat was cannulated for the [1,6-$^{13}C_2$]-Glc infusion, after which the animal was placed in the MRI scanner with a ^{1}H-[^{13}C] coil setup consisting of a volumetric ^{1}H transmitter, a ^{1}H Rx-only surface coil, and a quadrature ^{13}C transmit surface coil as previously described (9), under anesthesia (1-1.5% isoflurane, free breathing at ~ 45 resp/min). After a 2.5-hr dynamic *in vivo* ^{13}C MRS session, the rat head was microwave-fixed (1.4s at 8.5-kW, 10-kW Muromachi Microwave Fixation System), to inhibit enzyme modulated metabolic changes (24), and placed back in the coil system for further scanning. Animal preparation and procedures were previously approved by McGill University's animal research ethics committee and are in accordance with guidelines set by the council on animal care.

All scans were performed on a 7T Bruker Biospec 70/30 horizontal bore preclinical scanner (Billerica, MA, USA) with a 12-cm-diameter actively shielded gradient insert (650-mT/m in 150-µs). Data processing and simulations were performed in MATLAB (Natick, MA, USA) using the simulation module within the FID-A toolkit (25) modified to account for weakly coupled *IS* spin systems. A gradient-echo based multi-slice localizer was used to plan the remainder of experiments. FASTMAP (26) was used for first and second order B_0 shims, resulting in water line widths of ~10 Hz (*in vivo*) and ~18 Hz (*ex vivo*) in a 100 µl (5 x 5 x 4 mm^3) voxel in rat brain. Water suppression was achieved with an optimized vendor supplied

VAPOR (27) sequence utilizing Hermite pulses with 200Hz bandwidth (excitation pulse length = 27 ms, and inversion pulse length = 17.1-ms), and outer volume suppression (OVS) was achieved with AFP hyperbolic secant (HS pulses 28) pulses (length = 2.0 ms, bandwidth = 10,125 Hz).

4.4.2 Pulse Sequence

Retardation of heteronuclear J-evolution due to non-instantaneous $\hat{R}_x^{I,S}(\pi)$ pulses for the SEAL-PRESS sequence can be determined by evaluating the TE at which maximal editing efficiency for the heteronuclear spin system is obtained, relative to the expected TE of $1/\mathrm{J}_{\mathrm{HC}}$ ms. The SEAL-PRESS sequence was simulated using FID-A, with Mao (29) pulses for $\hat{R}_x^{I}(\pi)$ and HS pulses for $\hat{R}_x^{S}(\pi)$ used on the MRI scanner, in an effort to approximate the retardation of heteronuclear J-evolution for the [2-^{13}C]-Acetate (Ace) spin system, and compared against experimental results with a [2-^{13}C]-Ace phantom. Evolution of the spin system during the shaped $\hat{R}_x^{I,S}(\pi)$ pulse was simulated by treating the time-dependent Hamiltonian to be piece-wise constant (by segmenting $\hat{R}_x^{I,S}(\pi)$ into 128 components), and each component of $\hat{R}_x^{I,S}(\pi)$ to be a constant rotation. The time evolution at the end of the $\hat{R}_x^{I,S}(\pi)$ pulse was then calculated (30) as:

$$\hat{\rho}(t_1 + t_2 + \cdots + t_n) =$$

$$\exp\{-i\widehat{\mathcal{H}}_n t_n\} \ldots \exp\{-i\widehat{\mathcal{H}}_2 t_2\} \exp\{-i\widehat{\mathcal{H}}_1 t_1\}\, \hat{\rho}(0) \exp\{i\widehat{\mathcal{H}}_1 t_1\} \exp\{i\widehat{\mathcal{H}}_2 t_2\} \ldots \exp\{i\widehat{\mathcal{H}}_n t_n\}.$$

The SEAL-PRESS sequence was implemented with the following parameters (TR = 4000 ms, TE = 8.1 ms, TE$_1$ = 4.05ms, TE$_2$ = 4.05 ms, SW = 6.0 kHz, 1502 points, 250-ms acquisition). Excitation on the ^{1}H channel was performed using a 5-lobe sine-modulated sinc pulse (length = 0.6 ms, bandwidth = 15.7 kHz), and both $\hat{R}_x^{I}(\pi)$ pulses were Mao (length = 1.3

ms, bandwidth = 4.8 kHz, $B_{1,\ \max}$ ~ 4.1 kHz). Both $\hat{R}_x^S(\pi)$ were HS pulses [length = 1.3 ms, bandwidth (99% inversion efficiency) = 8.2 kHz, $B_{2,\ \max}$ ~ 5 kHz].

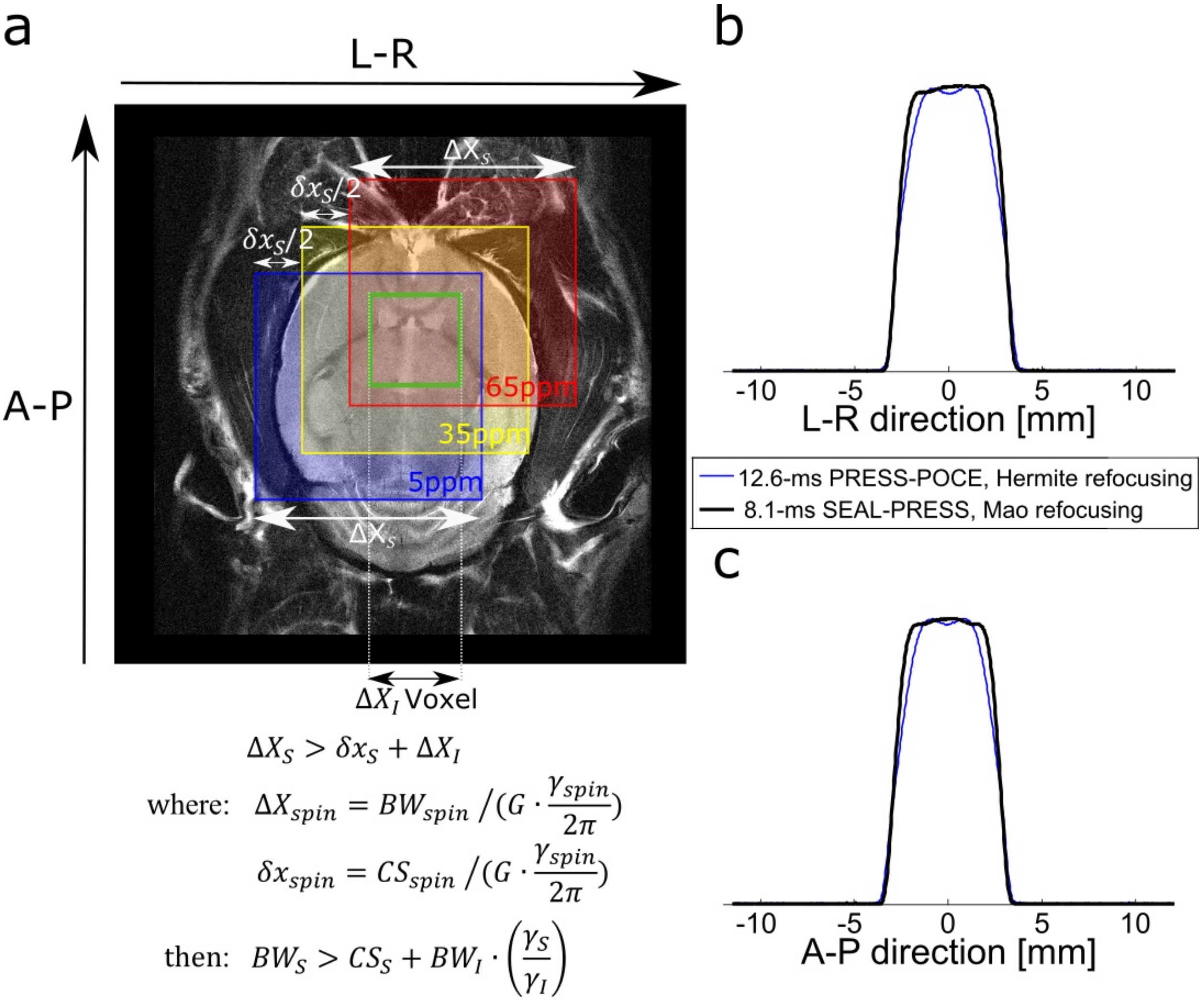

Figure 4-2 *Chemical shift displacement on the ^{13}C channel, and 1D voxel profiles on the ^{1}H channel. (a) The required bandwidth of the $\hat{R}_x^S(\pi)$ pulse (BW_S) is graphically illustrated as it is applied during a slice-selective gradient (G) for a ΔX_I x ΔX_I mm^2 footprint voxel (illustrated in green). A chemical shift of 5 - 65 ppm (~ 4.5 kHz at 7T) centered at ~35 ppm is desired to be covered for ^{13}C nuclei (CS_S) within the green voxel. Spatially, the regions that invert 5ppm, 35ppm, and 65ppm spins by a hypothetical $\hat{R}_x^S(\pi)$ pulse (with ΔX_S profile) are represented by the blue, yellow, and red squares respectively, shifted by the chemical shift displacement of $\delta x_S/2$ (corresponding to 30ppm) in the A-P and L-R directions. (b) 1-D voxel profiles along the refocusing A-P and L-R (c) directions obtained with the 12.6-ms PRESS-POCE and SEAL-PRESS sequences.*

The $\hat{R}_x^S(\pi)$ pulse bandwidth (BW$_S$) needs to be sufficient to cover the ^{13}C chemical shift range (5-65 ppm, centered at 35 ppm, the [4-^{13}C]-Glu resonance) and within-voxel frequency shift, since $\hat{R}_x^S(\pi)$ is applied during a slice selective gradient (see Figure 4-1). The Mao $\hat{R}_x^I(\pi)$ pulse bandwidth (BW$_I$) used in the current implementation necessitates the gradients (G_{L-R} and G_{A-P}) to be ~22mT/m for a 5 x 5 mm^2 slice-selection in L-R and A-P directions as illustrated in Figure 4-2a. Thus the minimum required BW$_S$ of the $\hat{R}_x^S(\pi)$ pulse is calculated to be 5.7 kHz from the derivation shown in Figure 4-2a.

Performance of the SEAL-PRESS sequence was compared against a previously described (9) PRESS-POCE sequence (TR = 4000 ms, TE = 12.6 ms, TE$_1$ = 2.6 ms, TE$_2$ = 10 ms, SW = 6.0 kHz, 1502 points) where $\hat{R}_x^S(\pi)$ was also a HS pulse [length = 1.4 ms, bandwidth (99% inversion efficiency) = 7.7 kHz] applied $1/2\mathrm{J}_{\mathrm{HC}}$ ms before the final echo, hereafter referred to as the 12.6-ms PRESS-POCE sequence. Comparisons between the two sequences were made primarily to evaluate and validate carbon editing in phantom and *in vivo*, for the proposed SEAL scheme relative to a classical carbon-editing scheme used on the 12.6-ms PRESS-POCE sequence.

An adiabatic decoupling scheme consisting of a WURST20 (31) AFP pulse [length = 1.8 ms, bandwidth (99% inversion efficiency) = 4.3 kHz, $B_{2,\ \mathrm{max}}$ ~ 1.8 kHz, $B_{2,\ \mathrm{RMS}}$ ~ 1.4 kHz] centered at [4-^{13}C]-Glu was used for both sequences. A five-step phase cycle nested within a MLEV-4 cycle was utilized to improve the decoupling performance (32,33) and applied during the first 200-ms of the acquisition. Both sequences utilized identical OVS and VAPOR modules as described above, and both sequences had a 32-step phase cycle to cancel out contributions from unwanted coherence pathways. All transients were stored separately, and zero-padded to a total of 16,384 points. Frequency and phase drift were corrected using spectral registration (34), and Edit-ON and edit-OFF scans were separately averaged prior to subtraction.

4.4.3 Phantom Experiments and Dynamic *in vivo* ^{1}H-[^{13}C] MRS in the Rat Brain

A spherical phantom with 0.14M [2-^{13}C]-Ace (2-^{13}C 99% enriched Cambridge Isotope Laboratories Inc., Andover, MA, USA) and 0.05M Choline in solution, were used to calibrate and evaluate sequences. A 0.85 M [1,6-$^{13}C_2$]-Glc (1-^{13}C 99%, 6-^{13}C 97% enriched Cambridge Isotope Laboratories Inc.) solution was prepared in saline and delivered to the rat intravenously via tail vein 8.5-mins after the start of the SEAL-PRESS sequence acquisitions (each 8.5-min block with 128 averages). An initial 58-mg bolus of [1,6-$^{13}C_2$]-Glc was infused over the first 15-seconds, and the rate was tapered off exponentially every 30-seconds to rapidly raise and maintain plasma glucose levels at ~10 mM as described previously (6). The infusion rate was reduced to 2.9-mg/min and maintained 8.25-mins after the infusion onset until the end of the experiment; a total of 0.55-g of [1,6-$^{13}C_2$]-Glc was infused. Spectral fitting of POCE data was performed in LCModel (35) using basis sets simulated in FID-A according to the sequence TE.

4.5 Results

4.5.1 Phantom Experiments

Figure 4-2b-c illustrates 1-D spatial profiles for the refocusing pulse directions (L-R, and A-P) obtained with the SEAL-PRESS and 12.6-ms PRESS-POCE sequences, where sharper profiles were obtained for the SEAL-PRESS sequence due to the use of Mao pulses. Furthermore, near-uniform nutation in the region of interest is seen due to the homogenous B_1^+ field generated with the ^{1}H volumetric transmitter (9).

The editing efficiency of the SEAL-PRESS sequence was simulated for varying TE for the [2-^{13}C]-Ace spin system (Figure 4-3, blue plot), where $\mathrm{J_{HC}}$ for [2-^{13}C]-Ace used in simulation was experimentally found in phantom from an un-decoupled dataset to be $1/\mathrm{J_{HC}} = 7.89$ ms. If no retardation of heteronuclear J-evolution were present, editing efficiency is expected to be maximum at 7.89-ms. Editing efficiency was however experimentally seen to peak at ~8.1-ms ([2-^{13}C]-Ace phantom, on a 5 x 5 x 4 mm^3 voxel), and ~ 8.2-ms in simulation. Editing efficiency of the SEAL-PRESS was >95.5%, and >96.3% for the 12.6-ms PRESS-POCE sequence. The slightly decreased lower bound in editing efficiency for the SEAL-PRESS sequence can be attributed to consisting of two $\hat{R}_x^S(\pi)$ pulses with >99% inversion efficiency in the bandwidth of interest, compared to the single $\hat{R}_x^S(\pi)$ pulse utilized on the 12.6-ms PRESS-POCE sequence.

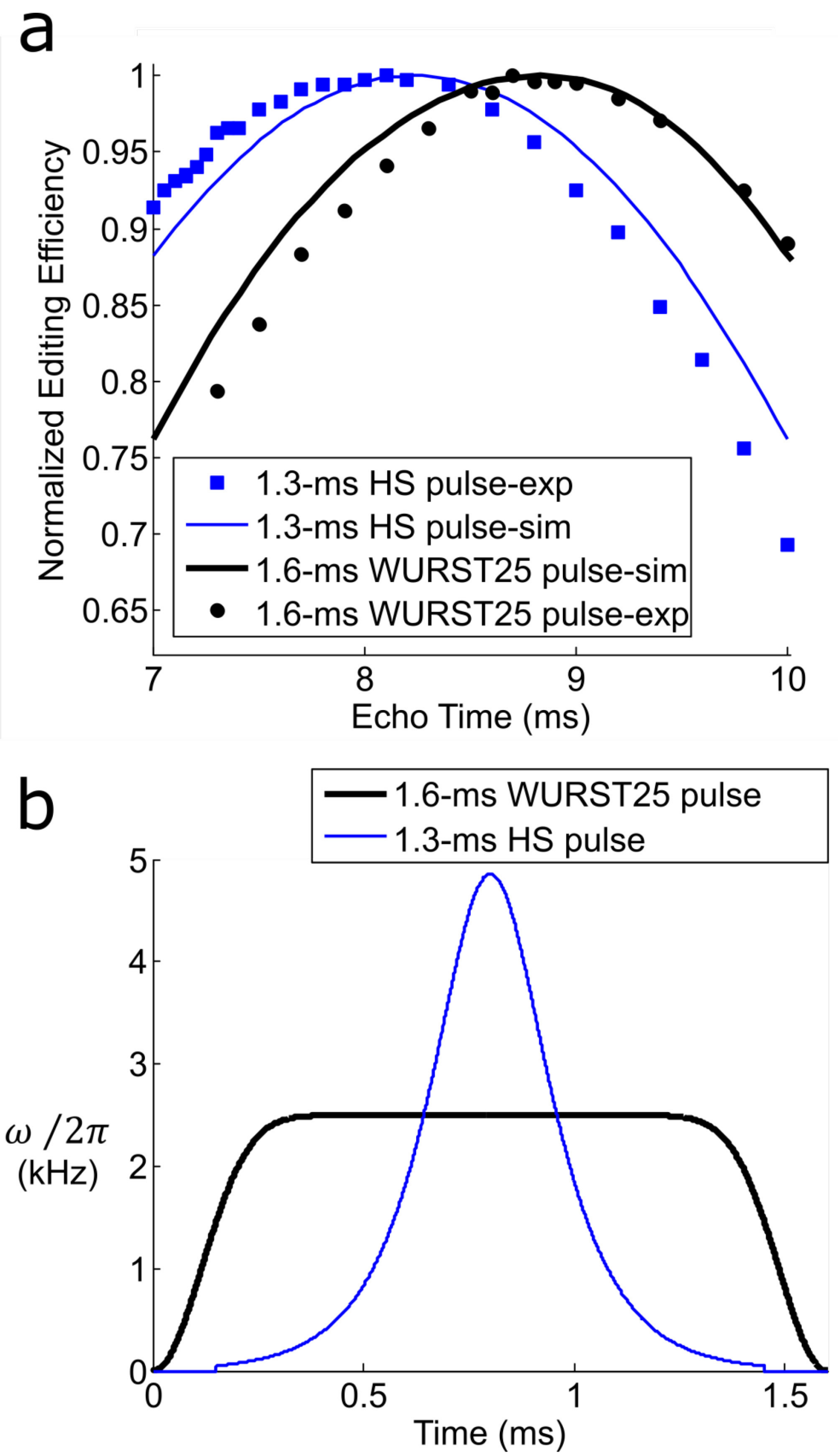

Figure 4-3 *Editing efficiency of SEAL-PRESS vs TE for two cases of inversion pulses.*

(a) Normalized editing efficiency of the SEAL-PRESS sequence vs TE in simulation and from experimental data for the [2-^{13}C]-Ace spin system with a modified SEAL-PRESS sequence with 1.6-ms Mao pulses (in blue), and WURST25 pulses (in black). (b) The modulation function and duration of AFP inversion pulses used in (a) are illustrated, where the HS and WURST25 pulses have envelope factors of ~0.3 and ~0.8, respectively.

The above comparison was extended for a scenario when the SEAL-PRESS sequence was modified (Figure 4-3, black plot) with a WURST25 pulse (length = 1.6 ms, bandwidth (99% inversion efficiency) = 5.9 kHz) for $\hat{R}_x^S(\pi)$, and a Mao pulse (length = 1.6 ms, bandwidth = 3.9 kHz) for $\hat{R}_x^I(\pi)$ to emphasize retardation of heteronuclear J-evolution when $\hat{R}_x^{I,S}(\pi)$ is longer and when the envelope factor (see Figure 4-3b) of the $\hat{R}_x^S(\pi)$ is higher (Figure 4-3a). In this case, a more pronounced effect on retardation of J-evolution is observed, with maximal editing efficiency delayed to ~8.7-ms experimentally and ~8.8-ms in simulation.

4.5.2 *In vivo* Dynamic ^{1}H-[^{13}C] MRS in the Rat Brain, and ^{1}H-[^{13}C] MRS in the Microwave-Fixated Rat Brain

Figure 4-4a illustrates time-resolved ^{1}H-[^{13}C] spectra obtained primarily encompassing the anterior cerebral cortex following the [1,6-$^{13}C_2$]-Glc infusion (100-µl voxel, 11-Hz water linewidth). Optimal sensitivity of spectra can be seen, with the last 8.5-min averaged acquisition (107-min time-point) showing low-concentration ^{13}C metabolites such as Lac-H2, Ala-H3, Asp-H3, and Asp-H2 in addition to the prominent Glu and Gln complexes. Unedited ^{1}H spectra averaged over the first 34-mins are illustrated in Figure 4-4b and demonstrate excellent spectral resolution. After 112-mins of time-resolved spectra, the [1,6-$^{13}C_2$]-Glc infusion was maintained to accommodate two 8.5-min *in vivo* scans each, with the SEAL-PRESS and 12.6-ms PRESS-POCE sequences for comparison (see Figure 4-4c) obtained in an interleaved fashion (A➔B➔B➔A). The averaged ^{1}H-[^{13}C] spectra summarized in Figure 4-4c show a 24.2 ± 5.0% increase in Glu-H4 signal for SEAL-PRESS relative to the 12.6-ms PRESS-POCE sequence; and similar or better improvements for Gln-H4, Glx-H3, GlcH6 + Glx-H2, and Asp-H2 complexes (see *in vivo* comparisons in Table 4-1).

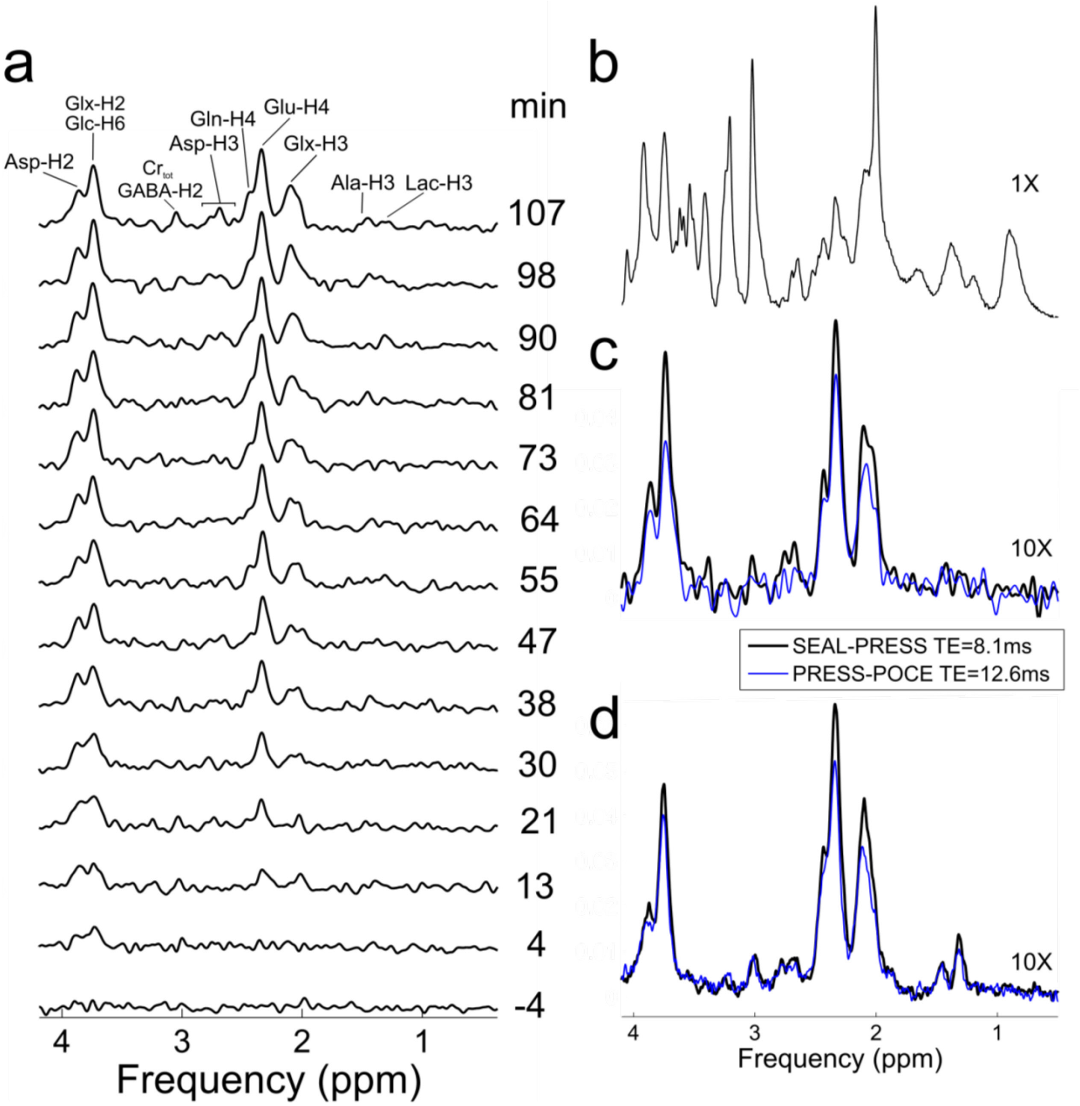

Figure 4-4 *Spectra following a dynamic in vivo* ^{13}*C MRS experiment with SEAL-PRESS MRS.*
(a) Time-resolved ^{1}*H-[*^{13}*C] spectra obtained with the SEAL-PRESS sequence from a 100µl (5 x 5 x 4 mm*^{3}*) voxel. Each averaged 8.5-min block of transients (128 repetitions, TR=4s, apodized with a 5Hz Lorentz-Gaussian filter) was repeated 13 times to cover 110-mins of time resolved* ^{13}*C metabolite labelling, initiated 8.5 mins before the [1,6-*$^{13}C_2$*]-Glc infusion. The marked time stamps correspond to the temporal mid-point of each summed spectrum. (b) The average of EDIT-OFF scans during the first 34-mins of the time series demonstrates excellent sensitivity and spectral resolution. An Eddy current correction was performed using a water-unsuppressed dataset (c) The average of two 8.5 min scans (apodized with a 10 Hz Lorentz-Gaussian filter), obtained with the SEAL-PRESS and PRESS-POCE sequences between 112 – 145 mins after the [1,6-*$^{13}C_2$*]-Glc infusion are compared; spectra for the two sequences were acquired in an interleaved fashion. (d) Average of eight 8.5-min scans obtained using each of the two sequences (apodized with a 6 Hz Lorentz-Gaussian filter) from the microwave-fixated rat brain. A 100 µl voxel was used, and placed similar to in vivo scans (also acquired in an interleaved fashion). Baseline corrections were not performed on any spectra.*

Following microwave-fixing the rat brain, eight scans (8.5-mins per scan) were obtained using each sequence in an interleaved fashion. The averaged spectra are illustrated in Figure 4d, and summarized in Table 4-1. Spectral resolution, however suffered (17-Hz water linewidth) likely a result of: **1)** micro-susceptibility effects as a result of low oxygenation (hypercapnia), or **2)** due to magnetic field inhomogeneities caused by microwave-induced air bubbles (24), though no signs of edema were present on high-resolution (50-µm in plane, see Figure 4-2a) T_2-weighted images (Effective TE = 73 ms). Signal amplitude improvements with the SEAL-PRESS sequence for Glx-H4, Glx-H3, and Asp-H2 complexes for the microwave-fixated rat brain were in agreement with *in vivo* data in Table 4-1, with the addition of 30.9 ± 9.1% signal improvement for Lac-H3 (see ex vivo comparisons in Table 4-1).

Table 4-1 *Summary of signal improvements in ^{13}C labeled metabolites for SEAL-PRESS relative to the 12.6-ms PRESS-POCE sequence for in vivo and ex vivo spectra in Figure 4-4 c-d.*

Metabolite	*In vivo* improvement	Ex vivo improvement
GluH4	24.2 ± 5.0 %	24.1 ± 1.9 %
GlnH4	28.5± 11.1 %	20.5 ± 3.6 %
GlxH3	28.0 ± 8.3 %	32.2 ± 2.9 %
AspH2	32.3 ± 12.5 %	25.0 ± 5.8 %
GlxH2 + GlcH6	56.6 ± 6.6 %	17.0 ± 2.5 %
LacH3	-	30.9 ± 9.1 %

Enzyme modulated metabolism inhibited in microwave-fixated rat brain (24) provides a static metabolic profile to conduct repeated comparisons between the 12.6-ms PRESS-POCE and SEAL-PRESS sequences. All these 8.5-mins spectra (sixteen in total) were analyzed in LCModel, and reproducibility of metabolite concentrations [quantified by Coefficient of Variation (CV)], and Cramer-Rao lower bound (CRLB) values were used to assess the two sequences. Resolvable ^{13}C labelled metabolites with a mean CRLB <15% for both sequences were used for comparisons (summarized in Table 4-2). CV for the SEAL-PRESS sequence were found to be smaller compared to those obtained with the 12.6-ms PRESS-POCE sequence for all tested metabolites, likely due to improved SNR. The CRLB values are also lower for all metabolites obtained with the SEAL-PRESS sequence.

Table 4-2 *Coefficient of variation (CV) and Cramer Rao lower bound (CRLB) values from LCModel. The summarized results are from eight 8.5-min spectra obtained with each of the two sequences tested, on the microwave-fixated rat brain.*

Metabolite	**CV for metabolite concentrations estimated by LCModel**		**Mean LCModel CRLB values**	
	12.6-ms PRESS-POCE	SEAL-PRESS	12.6-ms PRESS-POCE	SEAL-PRESS
GluH4	6.24%	4.83%	2.6 ± 0.5%	2.00 ± 0%
GlnH4	26.83%	4.48% *	7.8 ± 2.3%	4.1 ± 0.4%
LacH3	20.41%	17.77%	14.4 ± 3.5%	9.3 ± 1.9%
AspH2	34.51%	22.78%	14.0 ± 6.1%	11.4 ± 3.2%

*Difference in variance of the two datasets is statistically significant ($P < 0.0001$) based on a statistical F-test.

4.6 Discussion

This study describes a simultaneous PRESS localized and carbon edited POCE sequence (SEAL-PRESS) with an 8.1-ms TE. Despite the minor (<1%) reduction in editing efficiency for the SEAL-PRESS sequence compared to a 12.6-ms PRESS-POCE, the SEAL-PRESS sequence led to a >24% improvement in signal amplitude for ^{13}C labeled metabolites *in vivo*, which can be attributed to three main factors: reduced homonuclear J-evolution related losses, improved voxel localization with Mao relative to Hermite refocusing pulses, and a minor contribution from reduced T_2 losses. The contribution due to better defined voxel localization with Mao refocusing was found to contribute ~5.2% higher signal than Hermite refocusing; therefore signal improvement as a result of reducing TE from 12.6-ms to 8.1-ms for ^{13}C labeled metabolites can be attributed to be >17%. Phantom experiments conducted with ^{13}C labeled Glu-H4, Glu-H3 also showed similar signal improvements for SEAL-PRESS, relative to the 12.6-ms PRESS-POCE sequence (data not shown). Ideally the 12.6-ms PRESS-POCE sequence used for comparisons would have also utilized Mao refocusing pulses; however, the TE of the sequence would require to be extended to ~15 ms [due to higher R valued Mao pulses relative to Hermite pulses (6200 Vs 3400)] to accommodate the non-simultaneous $\hat{R}_x^S(\pi)$ and $\hat{R}_x^I(\pi)$ pulses. The 12.6-ms PRESS-POCE sequence in its current state provides good sensitivity and localization, as described in a previous study (9) for *in vivo* POCE-MRS; therefore, the SEAL-PRESS sequence was compared against this unmodified 12.6-ms PRESS-POCE sequence with the primary intention of validating editing efficiency of SEAL.

The TE of the SEAL-PRESS sequence was optimized for the [2-^{13}C]-Ace system, similar to previous reports (15,18). However, for optimal editing efficiency of ^{13}C Glu/Gln, the sequence TE should be calibrated to an average value of J_{HC} for [n-^{13}C]-Glx systems (n=2, 3, 4).

The bandwidth of $\hat{R}_x^S(\pi)$ inversion pulses used in the current implementation do not sufficiently edit [1-^{13}C]-Glc resonances; this can be achieved with 8.8 kHz bandwidth $\hat{R}_x^S(\pi)$ pulses (for the current voxel size) centered at ~ 50ppm.

Close inspection of the Glx-H2 + Glc-H6 resonances, around 4ppm in Figure 4-4c and Figure 4-4d, reveals some inconsistencies. Specifically, relative to the 12.6-ms PRESS-POCE sequence, the SEAL-PRESS sequence shows a larger improvement in signal intensity for resonances around 4ppm in the *in vivo* data relative to the ex vivo data. A few differences between the *in vivo* and ex vivo acquisitions may have contributed to the above: first, the water linewidth achieved for the ex vivo rat brain was poor (due to issues described above). This poor linewidth may have had an effect on the baseline signal around the water resonance on the 12.6-ms PRESS-POCE sequence due to less efficient gradient spoiling utilized, which had been optimized for typical *in vivo* rat brain water linewidths in a previous study (9); second, the voxel for the ex vivo rat was close but not identically placed compared to that of the *in vivo* session; finally, due to the likely possibility of small amounts of animal head movement during in-vivo scans may have changed the spectral quality and influence the results, given that these two sequences were acquired sequentially.

The chemical shift displacement for the SEAL-PRESS sequence was <22% (voxel shift between water and fat) with vendor-supplied Mao pulses. If chemical shift displacements becomes a limitation at higher field strengths, hardware and pulse design modifications (see discussion in 9) can be exploited.

Retardation of heteronuclear J-evolution during $\hat{R}_x^{I,S}(\pi)$ pulses was observed with the SEAL-PRESS implementation, and is ~0.2-ms with 1.3-ms $\hat{R}_x^{I,S}(\pi)$ pulses used, and extended to ~0.9-ms when broader envelope and 1.6-ms $\hat{R}_x^{I,S}(\pi)$ pulses were used. These observations are in agreement with previous reports by de Graaf et al. (15), where an ISIS localized POCE sequence TE was empirically extended by ~1.5-ms due to retardation of heteronuclear J-evolution with $\hat{R}^{I,S}(\pi)$ consisting of 2-ms and 4.0-ms RF pulses for $\hat{R}^{I}(\pi)$ and $\hat{R}^{S}(\pi)$, respectively.

Ultra-short TE MRS acquisitions are normally associated with a macromolecular (MM) baseline; however, POCE MRS is insensitive to MM resonances due to difference editing. The MM baseline associated with short-TE unedited ^{1}H spectra can be addressed with a reference MM acquisition before ^{13}C MRS, as reported for ultra-short 2.8-ms TE dynamic POCE MRS for rat brain imaging by Xin et al (18), to improve the measurement of isotopic enrichment.

Performance degradation of the sequence due to RF coil interactions, during simultaneous irradiation on ^{1}H and ^{13}C coils for $\hat{R}_x^{I,S}(\pi)$pulses, was indirectly evaluated. Artifact free ^{1}H-[^{13}C] spectra obtained with 24-min long SEAL-PRESS sequence acquisitions on a rat with no infusions validate stability of the sequence and that $\hat{R}_x^I(\pi)$ pulses are unaffected during simultaneous $\hat{R}_x^S(\pi)$ pulses for EDIT-ON scans. Secondly, editing efficiency of the SEAL-PRESS sequence was found to be >95% in phantom, demonstrating that $\hat{R}_x^S(\pi)$ pulses are also unaffected by simultaneous $\hat{R}_x^I(\pi)$ pulses.

Accurate metabolic modeling relies on early detection of ^{13}C labeled metabolites following the infusion. Considering SNR in the time-resolved spectra presented, we can speculate that a 10% reduction in volume (90µl voxel) would minimally affect detection of Glu-H4 and GlxH3 resonances seen at the 13-min time point (following the Glucose infusion) in Figure 4-4a; however, it must be noted that improved tissue specificity is gained at the cost of reduced sensitivity of time-resolved ^{1}H-[^{13}C] spectra.

Movement and scanner instabilities contribute to the slow degradation of the B_0 field homogeneity in the region of interest which affect long (> 2-hour) continuous scan sessions, thus will be beneficial to include a navigator based shim correction between MRS blocks to maintain SNR. Further improvements in SNR can be achieved through the use of alternate coil geometries optimized for the region of interest: an aspect for future exploration.

Simulation results were used throughout this work, which provided valuable a-priori knowledge regarding attainable benefits relative to the 12.6-ms PRESS-POCE sequence. Heteronuclear J-evolution retardation during $\hat{R}_x^{I,S}(\pi)$ pulses was predicted in simulation to within 0.1-ms accuracy relative to experimental results in two cases. Knowledge of retardation is valuable information since a difference of ~1.0-ms from optimal TE could cost >10% in editing efficiency (see Figure 4-3). Simulation results were in excellent agreement with phantom and rat brain MRS data, demonstrating the benefits of incorporating simulations in synergy with experimentation.

4.7 Conclusions

We present a single-shot PRESS-localized and two-shot edited POCE-MRS sequence with a TE of 8.1-ms. Minimizing the sequence TE from 12.6-ms to 8.1-ms for PRESS provides marked improvements in sensitivity for strongly coupled metabolites such as Glutamate and Glutamine; the primary metabolites observed in dynamic ^{13}C POCE-MRS experiments following a ^{13}C labeled glucose infusion. The sequence is straightforward to implement, immune to scanner instabilities and subtraction artifacts (relative to ISIS based implementations), while providing superior sensitivity.

4.8 Acknowledgements

This research was funded by NSERC (Grant No. RGPIN-2014-07072) awarded to JN.

4.9 References

1. Rothman DL, De Feyter HM, de Graaf RA, Mason GF, Behar KL. 13C MRS studies of neuroenergetics and neurotransmitter cycling in humans. NMR in biomedicine 2011;24(8):943-957.
2. Gruetter R, Adriany G, Choi IY, Henry PG, Lei H, Oz G. Localized in vivo 13C NMR spectroscopy of the brain. NMR in biomedicine 2003;16(6-7):313-338.
3. Rothman DL, Behar KL, Hetherington HP, den Hollander JA, Bendall MR, Petroff OA, Shulman RG. 1H-Observe/13C-decouple spectroscopic measurements of lactate and glutamate in the rat brain in vivo. Proceedings of the National Academy of Sciences of the United States of America 1985;82(6):1633-1637.
4. Fitzpatrick SM, Hetherington HP, Behar KL, Shulman RG. The flux from glucose to glutamate in the rat brain in vivo as determined by 1H-observed, 13C-edited NMR spectroscopy. Journal of cerebral blood flow and metabolism : official journal of the International Society of Cerebral Blood Flow and Metabolism 1990;10(2):170-179.
5. Rothman DL, Howseman AM, Graham GD, Petroff OA, Lantos G, Fayad PB, Brass LM, Shulman GI, Shulman RG, Prichard JW. Localized proton NMR observation of [3-13C]lactate in stroke after [1-13C]glucose infusion. Magnetic resonance in medicine 1991;21(2):302-307.
6. de Graaf RA, Rothman DL, Behar KL. State of the art direct 13C and indirect 1H-[13C] NMR spectroscopy in vivo. A practical guide. NMR in biomedicine 2011;24(8):958-972.
7. Bottomley PA. Spatial localization in NMR spectroscopy in vivo. Annals of the New York Academy of Sciences 1987;508:333-348.

8. Chen W, Adriany G, Zhu XH, Gruetter R, Ugurbil K. Detecting natural abundance carbon signal of NAA metabolite within 12-cm3 localized volume of human brain using 1H-[13C] NMR spectroscopy. Magnetic resonance in medicine 1998;40(2):180-184.
9. Kumaragamage C, Madularu D, Mathieu AP, De Feyter H, Rajah MN, Near J. In vivo proton observed carbon edited (POCE) 13 C magnetic resonance spectroscopy of the rat brain using a volumetric transmitter and receive-only surface coil on the proton channel. Magnetic resonance in medicine 2017.
10. Slotboom J, Mehlkopf AF, Bovée WMMJ. A single-shot localization pulse sequence suited for coils with inhomogeneous RF fields using adiabatic slice-selective RF pulses. Journal of Magnetic Resonance (1969) 1991;95(2):396-404.
11. Yang J, Li CQ, Shen J. In vivo detection of cortical GABA turnover from intravenously infused [1-13C]D-glucose. Magnetic resonance in medicine 2005;53(6):1258-1267.
12. Jonkers RA, Geraedts TR, van Loon LJ, Nicolay K, Prompers JJ. Multitissue assessment of in vivo postprandial intracellular lipid partitioning in rats using localized 1H-[13C] magnetic resonance spectroscopy. Magnetic resonance in medicine 2012;68(4):997-1006.
13. Ordidge RJ, Connelly A, Lohman JAB. Image-selected in Vivo spectroscopy (ISIS). A new technique for spatially selective nmr spectroscopy. Journal of Magnetic Resonance (1969) 1986;66(2):283-294.
14. Doan BT, Autret G, Mispelter J, Meric P, Meme W, Montecot-Dubourg C, Correze JL, Szeremeta F, Gillet B, Beloeil JC. Simultaneous two-voxel localized (1)H-observed (13)C-edited spectroscopy for in vivo MRS on rat brain at 9.4T: Application to the investigation of excitotoxic lesions. Journal of magnetic resonance 2009;198(1):94-104.

15. de Graaf RA, Brown PB, Mason GF, Rothman DL, Behar KL. Detection of [1,6-13C2]-glucose metabolism in rat brain by in vivo 1H-[13C]-NMR spectroscopy. Magnetic resonance in medicine 2003;49(1):37-46.

16. Marjanska MH, P; Gruetter, R.; Garwood, M.; Ugurbil, K. A new method for proton detected carbon edited spectroscopy using LASER. 2004; Proceedings of the 12th Annual Meeting of ISMRM, Kyoto. p 679.

17. Garwood M, Merkle H. Heteronuclear spectral editing with adiabatic pulses. Journal of Magnetic Resonance (1969) 1991;94(1):180-185.

18. Xin L, Mlynarik V, Lanz B, Frenkel H, Gruetter R. 1H-[13C] NMR spectroscopy of the rat brain during infusion of [2-13C] acetate at 14.1 T. Magnetic resonance in medicine 2010;64(2):334-340.

19. Mlynarik V, Gambarota G, Frenkel H, Gruetter R. Localized short-echo-time proton MR spectroscopy with full signal-intensity acquisition. Magnetic resonance in medicine 2006;56(5):965-970.

20. Garwood M, DelaBarre L. The return of the frequency sweep: designing adiabatic pulses for contemporary NMR. Journal of magnetic resonance 2001;153(2):155-177.

21. Allerhand A. Analysis of Carr—Purcell Spin-Echo NMR Experiments on Multiple-Spin Systems. I. The Effect of Homonuclear Coupling. The Journal of Chemical Physics 1966;44(1):1-9.

22. Carr HY, Purcell EM. Effects of Diffusion on Free Precession in Nuclear Magnetic Resonance Experiments. Physical Review 1954;94(3):630-638.

23. Michaeli S, Garwood M, Zhu XH, DelaBarre L, Andersen P, Adriany G, Merkle H, Ugurbil K, Chen W. Proton T2 relaxation study of water, N-acetylaspartate, and creatine

in human brain using Hahn and Carr-Purcell spin echoes at 4T and 7T. Magnetic resonance in medicine 2002;47(4):629-633.

24. de Graaf RA, Chowdhury GM, Brown PB, Rothman DL, Behar KL. In situ 3D magnetic resonance metabolic imaging of microwave-irradiated rodent brain: a new tool for metabolomics research. Journal of neurochemistry 2009;109(2):494-501.

25. Simpson R, Devenyi GA, Jezzard P, Hennessy TJ, Near J. Advanced processing and simulation of MRS data using the FID appliance (FID-A)-An open source, MATLAB-based toolkit. Magnetic resonance in medicine 2015.

26. Gruetter R. Automatic, localized in vivo adjustment of all first- and second-order shim coils. Magnetic resonance in medicine 1993;29(6):804-811.

27. Tkáč I, Starčuk Z, Choi IY, Gruetter R. In vivo 1H NMR spectroscopy of rat brain at 1 ms echo time. Magnetic resonance in medicine 1999;41(4):649-656.

28. Silver MS, Joseph RI, Chen CN, Sank VJ, Hoult DI. Selective population inversion in NMR. Nature 1984;310(5979):681-683.

29. Mao J, Mareci TH, Andrew ER. Experimental study of optimal selective 180° radiofrequency pulses. Journal of Magnetic Resonance (1969) 1988;79(1):1-10.

30. Duer MJ. The Basics of Solid-State NMR. Solid-State NMR Spectroscopy Principles and Applications: Blackwell Science Ltd; 2001. p 1-72.

31. Kupce E, Freeman R. Adiabatic Pulses for Wideband Inversion and Broadband Decoupling. Journal of Magnetic Resonance, Series A 1995;115(2):273-276.

32. Fujiwara T, Nagayama K. Composite inversion pulses with frequency switching and their application to broadband decoupling. Journal of Magnetic Resonance (1969) 1988;77(1):53-63.

33. de Graaf RA. Theoretical and experimental evaluation of broadband decoupling techniques for in vivo nuclear magnetic resonance spectroscopy. Magnetic resonance in medicine 2005;53(6):1297-1306.

34. Near J, Edden R, Evans CJ, Paquin R, Harris A, Jezzard P. Frequency and phase drift correction of magnetic resonance spectroscopy data by spectral registration in the time domain. Magnetic resonance in medicine 2015;73(1):44-50.

35. Provencher SW. Estimation of metabolite concentrations from localized in vivo proton NMR spectra. Magnetic resonance in medicine 1993;30(6):672-679.

Chapter 5

Simultaneous Direct and Indirect ^{13}C MRS

While direct ^{13}C MRS methods provide excellent spectral resolution, sensitivity is poorer due to the lower sensitivity and polarization of ^{13}C nuclei relative to protons. Indirect ^{13}C MRS on the other hand, provides sensitivity gains over direct ^{13}C methods. However indirect ^{13}C methods suffers from spectral crowding as most observable metabolites fall within the 1.2ppm-4ppm range. This renders reliable quantification of overlapping metabolites impossible (such as Glu-H3 and Gln-H3 which are unresolved at 7T *in vivo*). Furthermore, it is shown that the reliability of metabolic modeling on a two-compartment model to be improved when at least four time-resolved metabolite curves are used (such as Glu-H4, Gln-H4, Glu-H3, and Gln-H3). Acquisition of both indirect and direct ^{13}C MRS in an interleaved fashion is expected to provide sensitivity benefits and direct fractional enrichment curves from indirect ^{13}C MRS, and spectral dispersion benefits from direct ^{13}C MRS, and improve metabolic modeling of Glutamate-Glutamine cycling in the brain *in vivo*.

Simultaneous direct and indirect ^{13}C MRS during dynamic *in vivo* rat brain imaging

Chathura Kumaragamage [1,3], Dan Madularu [2,3,4], Axel P. Mathieu [2,3], and Jamie Near [1,2,3]

[1] Department of Biomedical Engineering, McGill University, Montreal, QC, Canada.
[2] Department of Psychiatry, Faculty of Medicine, McGill University, Montreal, QC, Canada.
[3] Brain Imaging Centre, Douglas Mental Health University Institute, McGill University, Montreal, QC, Canada.
[4] Center for Translational NeuroImaging, Northeastern University, Boston, MA, USA.

5.1 Abstract

Purpose: ^{13}C magnetic resonance spectroscopy (MRS) is a powerful technique capable of measuring metabolic fluxes non-invasively, *in vivo*. ^{13}C MRS can be performed using direct detection or indirect detection, with each method having inherent advantages and disadvantages. Proton observed carbon edited (POCE)-MRS is an indirect detection technique commonly used to study brain metabolism, which provides sensitivity gains relative to direct ^{13}C methods, and provides direct measurement of fractional enrichment (FE) time courses for resolvable metabolites. POCE-MRS however suffers from spectral crowding relative to direct detection, which hinders quantification of overlapping and thus unresolved metabolites such as Glu-H3 and Gln-H3 at 7T. Direct detection techniques suffer from lower sensitivity, however due to larger spectral dispersion, can resolve Glu-C3 and Gln-C3 at 7T (in addition to all other metabolites resolved with indirect ^{13}C methods), and provide ^{13}C-^{13}C coupled isotopomer information. This work presents the development of a ^{13}C MRS platform compatible with sequential direct and indirect ^{13}C MRS for dynamic *in vivo* rat brain imaging at 7T such that time-resolved FE curves for Glu-H4, Gln-H4, Glu-H3, and Gln-H3 can be directly achieved; a feat that cannot be achieved with either indirect, or direct ^{13}C detection alone at 7T.

Methods: A PRESS localized semi-adiabatic distortionless enhancement by polarization transfer (DEPT-PRESS) sequence was designed and evaluated in phantom for direct ^{13}C detection, and the optimized SEAL-PRESS sequence (TE = 8.1 ms) developed in our previous work was used for indirect detection. A quadrature-hybrid combiner was developed to drive a pair of ^{13}C loops in quadrature, and to combine Tx/Rx lines, which was required due to a limitation on the Bruker MRI scanner. Spectra were acquired sequentially using both methods on identical regions in phantom, and subsequently evaluated during a dynamic *in vivo* ^{13}C MRS session in a rat preparation.

Results: The DEPT-PRESS sequence was optimized and validated in water phantoms with ^{13}C enriched substrates. In addition, spectra were obtained using the DEPT-PRESS and PRESS-POCE sequences on water phantoms with varying ratios of ^{13}C labeled Glu-H3 and Gln-H3. Phantom data demonstrated that Glu and Gln ratios obtained with direct ^{13}C MRS were in reasonable agreement with indirect detection. Finally a dynamic *in vivo* ^{13}C MRS study was conducted in rat brain where spectra were obtained sequentially with DEPT-PRESS and PRESS-POCE, respectively, in a 660μl voxel (5 x 11 x 12 mm^3). Time-resolved indirect ^{13}C spectra were obtained as expected, however, due to poorer sensitivity of direct ^{13}C MRS, time courses could not be obtained to validate time-resolved FE quantification of Glu-H3 and Gln-H3 in rat brain *in vivo* at 7T. We propose that sensitivity limitations could be addressed by relatively simple modifications to the RF coil configuration.

Conclusion: We report a ^{13}C MRS platform for simultaneously acquiring direct and indirect ^{13}C MRS at 7T, but modifications to the RF coil configuration are needed in order to achieve sufficient sensitivity for direct detection *in vivo*.

5.2 Introduction

Carbon-13 magnetic resonance spectroscopy (MRS) following the infusion of a ^{13}C enriched substrate allows for the non-invasive measurement of metabolic fluxes used for the quantification of neuroenergetics and neurotransmitter cycling in the brain (1). In addition, localized ^{13}C MRS (2) allows the study of metabolism in specific regions of interest. Dynamic *in vivo* ^{13}C MRS can be performed with direct detection or indirect detection, with benefits and weaknesses associated with each technique. While direct ^{13}C MRS provides excellent spectral resolution, sensitivity is poorer by a factor ~16 compared to indirect ^{13}C due to the lower gyromagnetic ratio of ^{13}C nuclei. This can be partially overcome with a polarization transfer sequence such as insensitive nuclear enhancement by polarization transfer (INEPT) (3) or distortionless enhancement by polarization transfer (DEPT) (4) which provides up to a ~4 times improvement in SNR relative to direct detection. J-difference editing (5) for proton-observed carbon-edited (POCE) or ^{1}H-[^{13}C] MRS (6,7) is an attractive alternative to direct ^{13}C MRS methods due to signal-to-noise-ratio (SNR) gains achievable (7,8), and ability to directly quantify fractional enrichment (8). Calculation of fractional enrichment (FE) time courses for metabolites is straightforward with POCE-MRS since unedited and edited spectra provide total (^{12}C +^{13}C) and ^{13}C fractions of detected metabolite pools, respectively. However POCE-MRS suffers from spectral crowding as most observable metabolites fall within the 1.2ppm-4ppm range, thus rendering quantification of certain overlapping metabolites impossible.

Following an infusion of ^{13}C labeled glucose (such as 1-^{13}C-Glc or 1,6-^{13}C$_2$-Glc), early labeling of 4-^{13}C Glu can be observed. Accumulation of 4-^{13}C-Glu is considered to be indicative of the neuronal TCA cycling rate, and subsequent labeling of 4-^{13}C-Gln to be indicative of the Glutamate-Glutamine neurotransmitter cycling rate (9). Coincidently, 4-^{13}C-Glu and 4-^{13}C-Gln pools happen to be the most rapidly and abundantly labeled metabolites, and produce resolvable resonances with both indirect and direct ^{13}C MRS techniques at 7T. Illustrated in Figure 5-1 is a POCE spectra obtained in rat brain (100µl) at 7T during the infusion of 1,6-$^{13}C_2$-Glc, where Glu/Gln-H4 peaks are resolved, however Glu/Gln-H3 (Glx-H3) and Glu/Gln-H2 (Glx-H2) multiplets are overlapping (see Figure 5-1) with *in vivo* MRS, and cannot be resolved for inclusion in metabolic modeling.

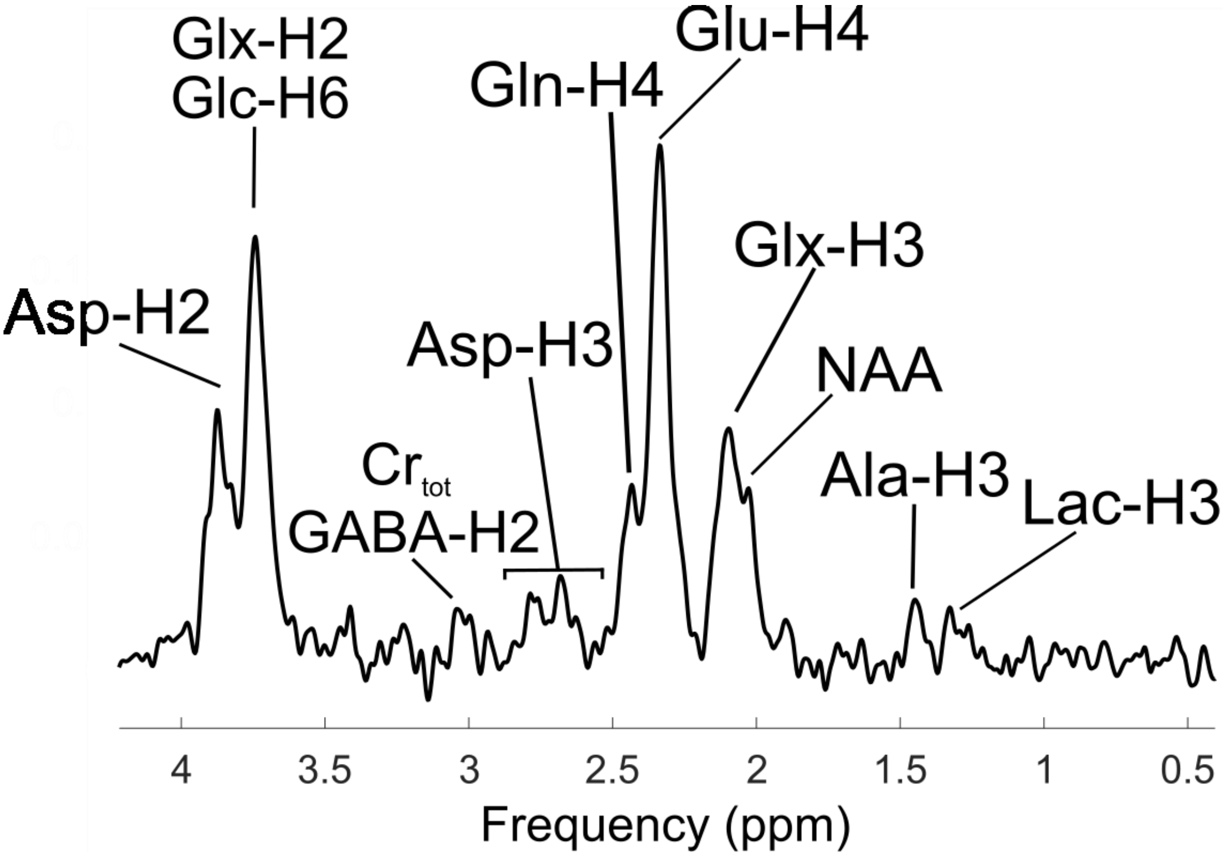

Figure 5-1 *POCE MRS at 7T on a 100µl voxel in rat brain.*

The above observation can be further clarified with simulated spectra of Glu and Gln at 7T illustrated in Figure 5-2, where10Hz line-broadening was used. The top sub-figure in Figure 5-2 illustrates the individual spectral footprints of Glu and Gln in the span of 1-4ppm, and the bottom sub-figure illustrates the summation of Glu and Gln. In the summed spectrum it is clearly seen that the Glu/Gln-H2 multiplets as well as the Glu/Gln-H3 multiplets are strongly overlapping, while the Glu/Gln-H4 multiplets are resolved enough for quantification purposes. The measurement of Glu/Gln-H3 time courses provides a measure of the exchange rate between 2-oxyglutarate and glutamate (10), and simulation studies show that the reliability of two-compartment metabolic modeling is improved when at least four time resolved metabolite curves (Glu-H4, Glu-H3, Gln-H4, and Gln-H3) are used relative to the use of three time resolved curves (Glu-H4, Gln-H4 and Glx-H3) (11).

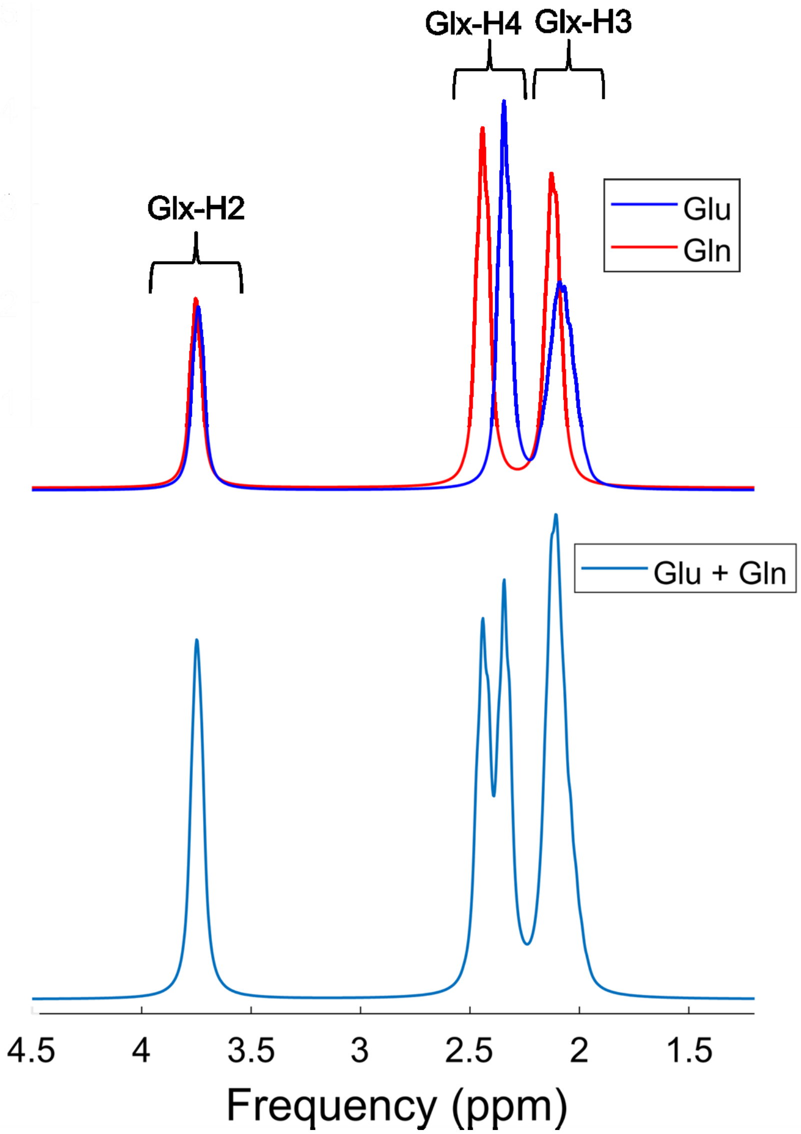

Figure 5-2 *Simulated Glu/Gln spectra at 7T with line broadening of 10Hz.*

The smaller spectral dispersion of indirect ^{13}C MRS compared to direct ^{13}C MRS is however proportionately overcome at higher magnetic fields. At 14T, an indirect ^{13}C MRS study by Xin et al (12) showed that in addition to Glu/Gln-H4, Glu/Gln-H3 was also resolved, thus providing the capability to produce FE curves for all four resonances.

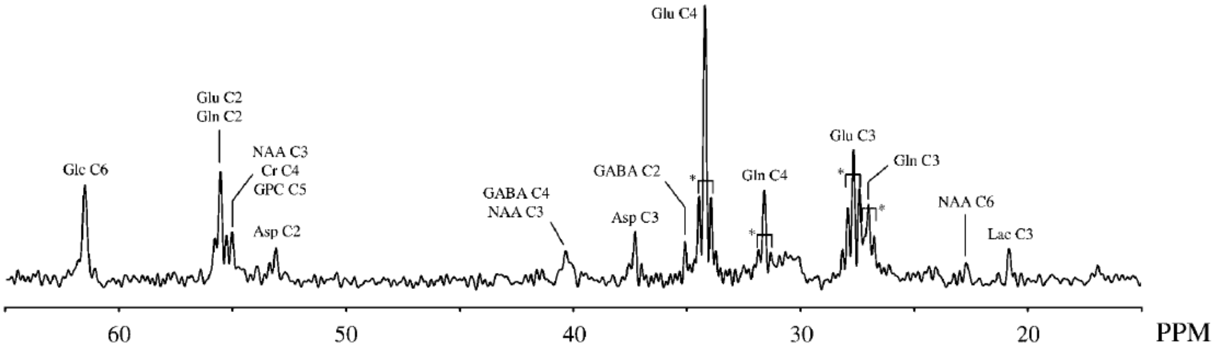

Figure 5-3 *Direct ^{13}C spectra in rat brain at 7T [adopted from (9) with permission [A.2]].*

In comparison, direct ^{13}C MRS at 7T is capable of resolving Glu-C3 and Gln-C3 in rat brain [Figure 5-3, obtained using the INEPT sequence by de Graaf et. al.(9)] in addition to resolving Glu-C4 and Gln-C4. Another benefit of direct ^{13}C MRS is its ability to detect ^{13}C-^{13}C isotopomers, which occurs, for example, when Glu-C4 labeled in the first round of the TCA cycle is labeled again at its C3 position (creating 3,4-^{13}C$_2$-Glu doublets, and subsequently 3,4-^{13}C$_2$-Gln doublets at both C3 and C4 positions) in the second turn of the TCA cycle (9). At the start of the experiment, the occurrences of 3, 4-^{13}C$_2$-Glu labeling is sparse, however becomes increasingly more probable, thus complicating spectra of Glx-C4 and Glx-C3 as can be seen in Figure 5-3 averaged towards the end of the 120 min experiment. Towards the end of the experiment there will also be contributions from 2, 3, 4-^{13}C$_3$-Glu, and 2, 3, 4-^{13}C$_3$-Glu triplets at the C3 position and can be accounted for by including these basis sets illustrated in Figure 5-4 (13). ^{13}C-^{13}C isotopomer information extractable with direct ^{13}C MRS can then be used to improve metabolic modeling, which is unavailable with indirect ^{13}C MRS methods.

Metabolite concentration information needs to be converted to absolute concentration and fractional enrichment (FE) values for metabolic modeling (as described in Eq 2-110 and 2-111). With indirect ^{13}C MRS such as POCE, the calculation FE for resolved metabolites $\frac{^{13}C}{^{13}C+^{12}C}$ is straightforward since EDIT-OFF and EDIT-ON scans contain the required information, and absolute quantification of metabolites is typically obtained with respect to the internal reference concentration of total Creatine, a metabolite known to be stable with age and some diseases (14), and due to being a prominent peak in *in vivo* proton-MRS. Though it must be noted that, any internal concentration reference should be used with caution, especially when used on a disease population. In the case of Creatine, decreased levels have been observed in chronic phases of many pathologies, such as tumors and stroke (15). With direct ^{13}C MRS, absolute quantification and obtaining metabolite FE curves is not straightforward. The absolute concentrations is typically obtained indirectly with a known or assumed reference, such as the natural abundance (1.11%) NAA signals, since creatine is partially overlapping with other metabolites on a direct ^{13}C spectrum (16). The NAA signal would come from either a long >30 min scan before infusion, or by averaging all spectra obtained during a ^{13}C MRS study. In the case of obtaining NAA from acquisitions during a ^{13}C study, it is assumed that NAA does not get ^{13}C labelled. On the other hand, concentrations of NAA is not uniform over the brain, and is known to decrease with disorders related to neuronal loss (15); these anomalies make NAA an undesired internal reference. Another approach would be to have an external reference of a known metabolite with known concentration placed in the vicinity of the coil system, which can be used to estimate concentrations of the metabolites of interest after correcting for coil loading, and relaxation effects (2). However, differences in susceptibility and local magnetic field strength between the sample and external reference further complicate the use of an external reference. FE curves for different metabolites with direct ^{13}C MRS also rely on similar assumptions described above.

Therefore, the combination of direct ^{13}C MRS with indirect ^{1}H-[^{13}C] MRS is expected to provide the benefits of both: High sensitivity, relatively improved absolute concentration estimates, and accurate FE information from indirect MRS, along with improved separation of overlapping resonances, and isotopomer specificity from direct MRS. Together, these methods will provide information that cannot be obtained with either of the two MRS methods in isolation, which we expect will contribute to improved quantitative metabolic modeling at 7T.

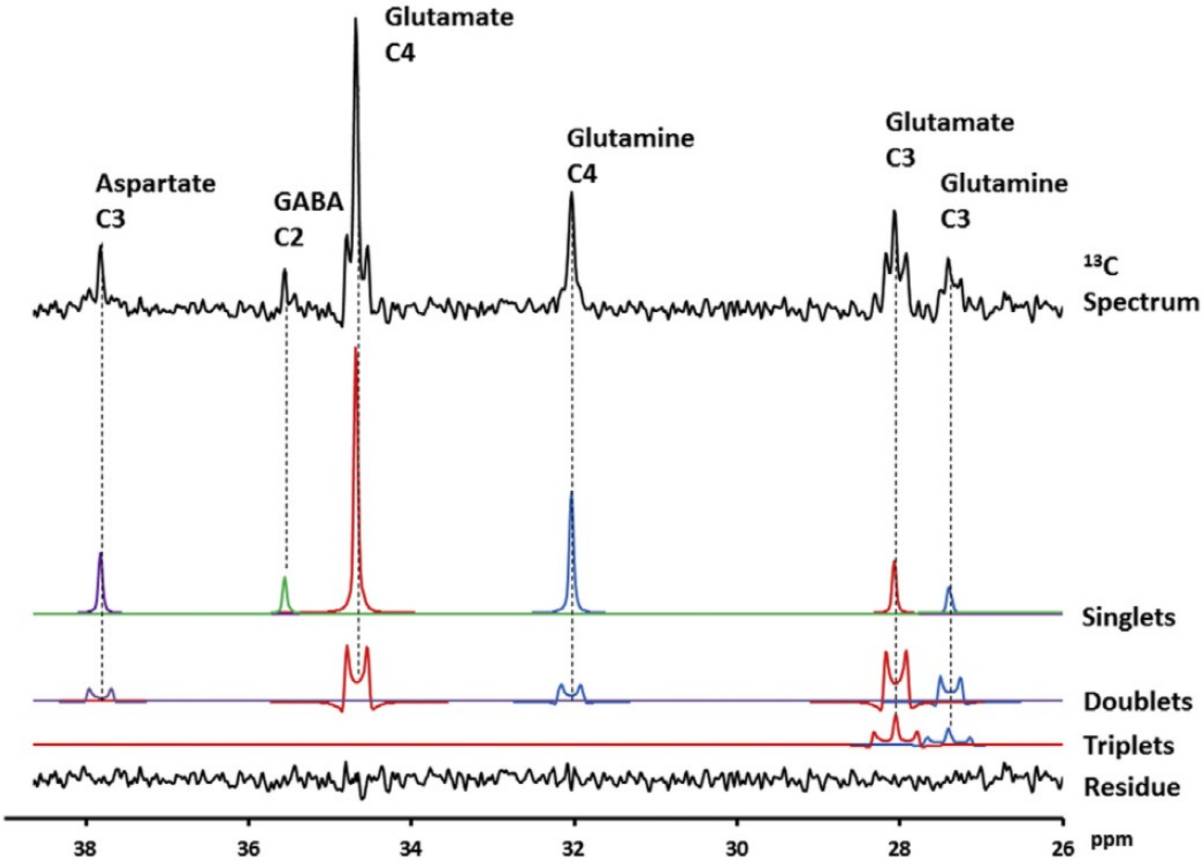

Figure 5-4 *Illustration of* ^{13}C-^{13}C *labeling with direct* ^{13}C *MRS following an infusion of* [1,6-^{13}C$_2$]-Glc *at 11.7T [adopted from (13) with permission [A.3]].*

In this work we report a modified RF chain capable of acquiring both direct and indirect ^{13}C MRS during a dynamic *in vivo* ^{13}C MRS study. The previously described SEAL-PRESS sequence was used to acquire indirect ^{13}C MRS, and a PRESS localized (identical to PRESS localization of SEAL-PRESS) the DEPT, herein referred to as the DEPT-PRESS sequence (as previously reported in 17), was developed such that direct and indirect MRS data can be acquired on the same localized region. We hypothesized that acquisition of both POCE and DEPT MRS in an interleaved fashion would provide sensitivity and FE information benefits of indirect ^{13}C MRS, and spectral dispersion benefits of direct ^{13}C MRS to resolve Glu/Gln-H3 and Glu/Gln-H4.

5.3 Methods

5.3.1 Animal preparation

Experiments were performed on two adult male Long Evans rats (Charles River Laboratories, Montreal, QC, Canada) weighing 380-440g. One rat was used for coil and sequence calibration, the second rat was used for dynamic *in vivo* ^{13}C MRS. The tail vein of the second rat was cannulated for a 1.1M [1,6-^{13}C$_2$]-Glc infusion, after which the animal was placed in the MRI scanner with a ^{1}H-[^{13}C] coil setup consisting of a volumetric ^{1}H transmitter, a ^{1}H Rx-only surface coil, and a quadrature ^{13}C transmit surface coil as described previously (18). Rats were scanned under anesthesia with isoflurane (1-2.5%, free breathing at ~ 30-60 resp/min). Animal preparation and procedures were previously approved by McGill University's animal research ethics committee and are in accordance with guidelines set by the council on animal care.

All scans were performed on a 7T Bruker Biospec 70/30 horizontal bore preclinical scanner (Billerica, MA, USA) with a 12-cm-diameter actively shielded gradient insert (650-mT/m in 150-µs). Data processing and simulations were performed in MATLAB (Natick, MA, USA) using the FID-A toolkit (19). A gradient-echo based multi-slice localizer was used to plan the remainder of experiments. FASTMAP (20) was used for B_0 shimming, which resulted in water line widths of ~24 Hz *in vivo* for 660 µl voxel (5 x 11 x 12 mm^3) in rat brain. Water suppression was achieved with VAPOR (21) utilizing Gaussian pulses (length = 27 ms and 17.1-ms, bandwidth = 200 Hz), and outer volume suppression (OVS) was achieved with AFP hyperbolic secant (HS pulses 22) (length = 2.0 ms, bandwidth = 10,125 Hz).

5.3.2 ^{1}H/^{13}C RF coil setup modifications

The ^{1}H-[^{13}C] coil platform described in Chapter 3 (18) was extended to be capable of direct ^{13}C MRS (Tx/Rx capabilities on the ^{13}C channel). Furthermore, due to limitations on the service-end of the Bruker console (which required the x-nucleus Tx and Rx channels to be delivered from the same line) a quadrature hybrid + quad-hybrid combiner was designed in-house, and built by Helmut Stark (Stark Industries Erlangen, Germany) capable of withstanding ~1kW$_{peak}$, and ~30W$_{rms}$ RF power), to drive the quadrature pair of ^{13}C loops and interface the back-end of the Bruker scanner (Figure 5-5). The quadrature-hybrid combiner circuitry needs to satisfy a few design criteria during transmit (Tx) and receiver (Rx) intervals on the ^{13}C channel. During Tx, the Rx side of the quadrature-hybrid must to be terminated with a high power handling 50Ω resistor to absorb RF power coupled through to the Rx port to for symmetry of the quadrature-hybrid, and to protect the input of the preamplifier. During Rx, the Tx port similarly needs to be terminated with a 50Ω resistor for Rx symmetry. All the above requirements were achieved with strategic placement of PIN diodes (PIN diodes are labeled with open filling in Figure 5-5), where all PIN diodes are forward biased with +5V during the Tx interval, and reverse biased with -34V during the Rx interval on the ^{13}C channel. The use of two quarter wave lines (labeled by λ/4 realized with lumped elements tuned to 75.5MHz) in series (see Figure 5-5) provides isolation (> 35dB @75MHz, >60 dB @ 300MHz when PIN diodes are in +5V state) at both input and output nodes of the preamplifier during Tx, as a low impedance (when parallel PIN diodes to ground are forward biased) after a λ/4 line is transformed to an open circuit (due to a 180° rotation on an impedance smith chart) before the λ/4 line. Insertion losses of the overall quadrature hybrid combiner was minimized by including a Siemens low noise preamplifier modified for 75 MHz (LNA, 30dB gain and noise figure < 0.5dB @ 75.5MHz) as illustrated in Figure 5-5 with insertion losses leading up to the preamplifier > -0.4dB @ 75MHz (PIN diodes OFF, -34V state). A pair of RF switching diodes (labeled with closed filling in Figure 5-5) is placed at the input of the preamplifier as secondary protection to clamp undesired decoupling signals at the ^{1}H frequency or undesired coupling described above.

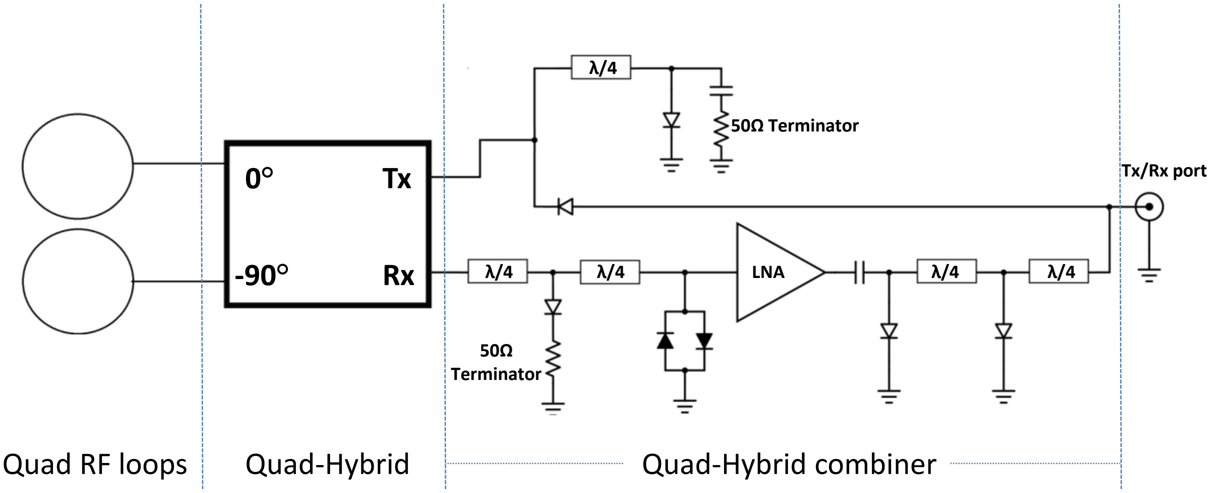

Figure 5-5 *Quadrature hybrid combiner circuitry utilized on the ^{13}C channel.*

5.3.3 Pulse Sequence

The unmodified SEAL-PRESS sequence described in chapter 4 (23) was utilized for indirect ^{13}C MRS with the following parameters (TR = 4000 ms, TE = 8.1 ms, TE_1 = 4.05ms, TE_2 = 4.05 ms, SW = 6.0 kHz, 1502 points, 250-ms acquisition). The reader is referred to chapter 4 for a detailed description of the SEAL-PRESS sequence illustrated in Figure 5-6A.

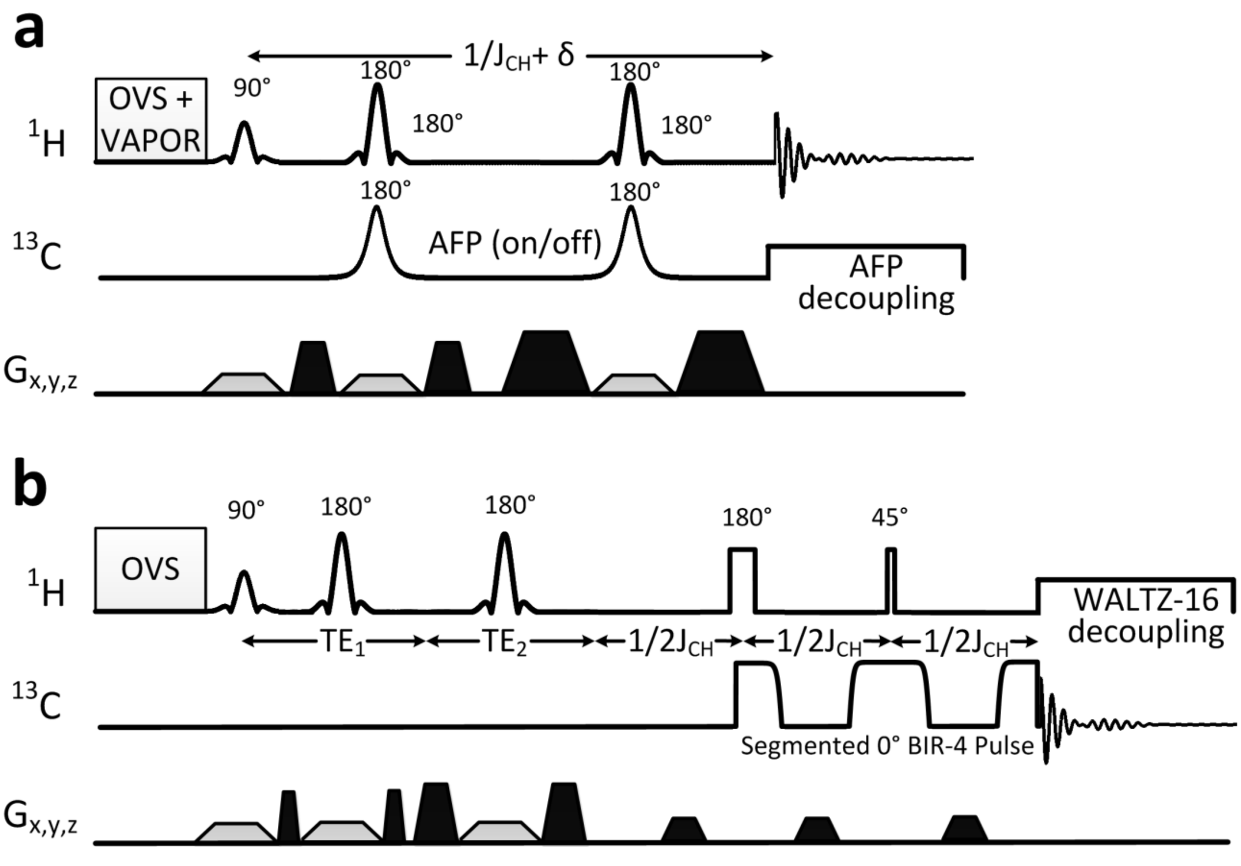

Figure 5-6 *(a) SEAL-PRESS sequence utilized, (b) The developed PRESS localized semi-adiabatic DEPT sequence.*

A semi-adiabatic DEPT sequence previously reported (10) with image selected *in vivo* spectroscopy [ISIS (24)] based localization was modified to be PRESS localized for this work as illustrated in Figure 5-6B; this semi-adiabatic DEPT sequence utilizes a segmented 0° BIR-4 pulse (25) on the ^{13}C channel, which provides improved sensitivity in the presence of an inhomogeneous B_2 field generated by surface coils relative to the use of purely amplitude modulated pulses. The classical DEPT sequence consists of 90° and 180° pulses on the ^{13}C channel; for the segmented BIR-4 pulse, the first and second segments provide constant 90° and 180° rotations, respectively, provided the adiabatic condition is met (26). The final segment of the BIR-4 pulse applied before data acquisition provides a further 90° rotation, and refocuses the nonlinear phase accumulated during the first two segments. The BIR-4 pulse characteristics are as follows (length = 2.0 ms, BW ~ 7 kHz, $B_{2,\ max}$ ~ 5 kHz). Hard pulses were employed for the two 180° and 45° RF pulses on the ^{1}H channel on the DEPT component, with pulse lengths 0.13ms and 0.0325ms, respectively. Spoilers placed between RF pulses (45mT/m, 1ms duration) in the DEPT component and a 32-step phase cycle were employed to eliminate signal from unwanted coherence pathways. The PRESS and OVS modules utilized for the DEPT-PRESS sequence is identical (in terms of excitation and refocusing pulse shapes, pulse lengths and localization gradients) to that of the SEAL-PRESS sequence to achieve identical 3D-localization profiles with both sequences. The spoiler duration of the PRESS component was reduced to 0.25ms during TE_1 and TE_2, such that an overall TE of 4.8ms could be realized (see Figure 5-6B) during PRESS localization, to minimize sensitivity losses of the overall DEPT-PRESS sequence due to T_2 and homo-nuclear J-evolution related losses (17,27).

The WALTZ-16 decoupling scheme (28) was applied on the ^{1}H channel during the DEPT-PRESS acquisition. Each 4 mins of averaged transients (128 averages) were stored separately, and zero-padded to a total of 16,384 data points. The optimized DEPT-PRESS sequence parameters are as follows: TR = 2000ms, TE_1 = 2.8ms, TE_2 = 1.95ms, J_{CH} = 140Hz, SW = 25kHz, 4096 points, 160-ms acquisition).

5.3.4 Phantom experiments and dynamic *in vivo* ^{1}H-[^{13}C] MRS in the rat brain

A requirement of the proposed approach is that the concentrations of Glu and Gln estimated by the two modalities (direct and indirect ^{13}C MRS) need to be in reasonable agreement. One approach to evaluate this is to compare data from multiple water-based phantoms with varying concentrations of ^{13}C labeled Glu and Gln. As such, three 5-ml cylindrical containers were prepared with [3-^{13}C]-Glu and [3-^{13}C]-Gln with Glu/Gln proportions of 0.75:1, 1:1, and 2:1. All phantoms were made with 99% ^{13}C enriched Glu and Gln (Sigma Alrdrich, St. Louis, MO) in distilled water, stored at 4°C until scanned [within three days after preparation to minimize degradation effects of Glutamine in water (29)]. To avoid precipitation of metabolites, Gln concentrations in the first two phantoms were 40mM, and 12.5mM in the third phantom (with Glu concentration determined according to the required ratio).

Estimation of Glu/Gln with indirect ^{13}C MRS was performed only on Glu-H4 and Gln-H4 multiplets of the unedited ^{1}H spectra (since Glx-H4 are attached to ^{12}C nuclei in the described phantoms) with LCModel (30), which are resolved at 7T (see Figure 5-2), using basis sets simulated in FID-A according to the SEAL-PRESS sequence TE. Another alternative to estimating Glu/Gln with LCModel on unedited ^{1}H spectra is to account for the spectral footprint of each metabolite (in the span up to 4ppm shown in Figure 5-2) as typically used for *in vivo* quantification. This approach was not used since decoupling efficiency is set to be >90%, resulting in Glu-H3 and Gln-H3 multiplets to be marginally reduced and would hinder quantification accuracy. Estimation of Glu/Gln with direct ^{13}C MRS was performed on the Glu-C3 and Gln-C3 singlets using the JMRUI software package (31), which are resolved with direct ^{13}C MRS at 7T.

For dynamic *in vivo* ^{13}C MRS, a 1.1 M [1,6-$^{13}C_2$]-Glc (1-^{13}C 99%, 6-^{13}C 97% enriched Cambridge Isotope Laboratories Inc.) solution was prepared in saline and delivered intravenously via tail vein. An initial 124-mg bolus of [1,6-$^{13}C_2$]-Glc was infused over the first 15-seconds, and the rate was tapered off exponentially every 30-seconds to rapidly raise and maintain plasma glucose levels at ~10 mM as previously described (8). The infusion rate was reduced to 6.3-mg/min and maintained 8.25-mins after the infusion onset till the end of the experiment; a total of 1.1g of [1,6-$^{13}C_2$]-Glc was infused.

5.4 Results

5.4.1 Phantom experiments

Direct and indirect ^{13}C MRS was performed with the DEPT-PRESS and SEAL-PRESS sequences, respectively, on the three phantoms with varying ratios of 3- ^{13}C labeled Glu and Gln. Multiple measurements (8 per modality) were made, where each measurement consisted of 128 transients. Due to the higher susceptibility of ^{1}H MRS to shim inhomogeneities (relative to direct ^{13}C MRS), all SEAL-PRESS spectra were obtained on a 256µl (4 x 8 x 8 mm^3) voxel centered within a 1024µl (8 x 16 x 16 mm^3) voxel used for DEPT-PRESS measurements. The smaller 256µl voxel water linewidth was < 8Hz, and the larger voxel water linewidth was < 25 Hz in all phantoms. The 1024µl voxel was beneficial to improve SNR of DEPT-PRESS spectra and improve reproducibility of metabolite quantification, and the smaller voxel for SEAL-PRESS was beneficial to obtain an overall water linewidth < 8Hz to minimize spectral crowding and improve quantification accuracy with LCModel. An example LCModel output of the unedited component from the SEAL-PRESS sequence is shown in Figure 5-7; and an example JMRUI output of a DEPT-PRESS spectrum is shown in Figure 5-8. Both Figure 5-7 and 5-8 are from Phantom 2 with ~1:1 Glu/Gln concentrations. Spectral fitting parameters of LCModel were modified to obtain satisfactory quantification of GluH4 and GlnH4 (as evident in Figure 5-7). However it is also evident that GluH3 and GlnH3 fitting is not optimized, which was not further investigated since Glu/Gln-H3 cannot be resolved at 7T *in vivo*. JMRUI can be used without much user input to obtain required concentration estimates for direct ^{13}C MRS spectra, whereas LCModel thus far has not been extended for the use with direct ^{13}C MRS data [thought could be used with extensive modifications as reported previously (32)]. Quantification accuracy of strongly coupled systems such as Glu/Gln can be improved by accounting for homonuclear J-evolution related losses with respect to TE, and by using simulated basis-sets. This can be easily achieved with LCModel, thus was used to quantify indirect ^{13}C MRS spectra in this work.

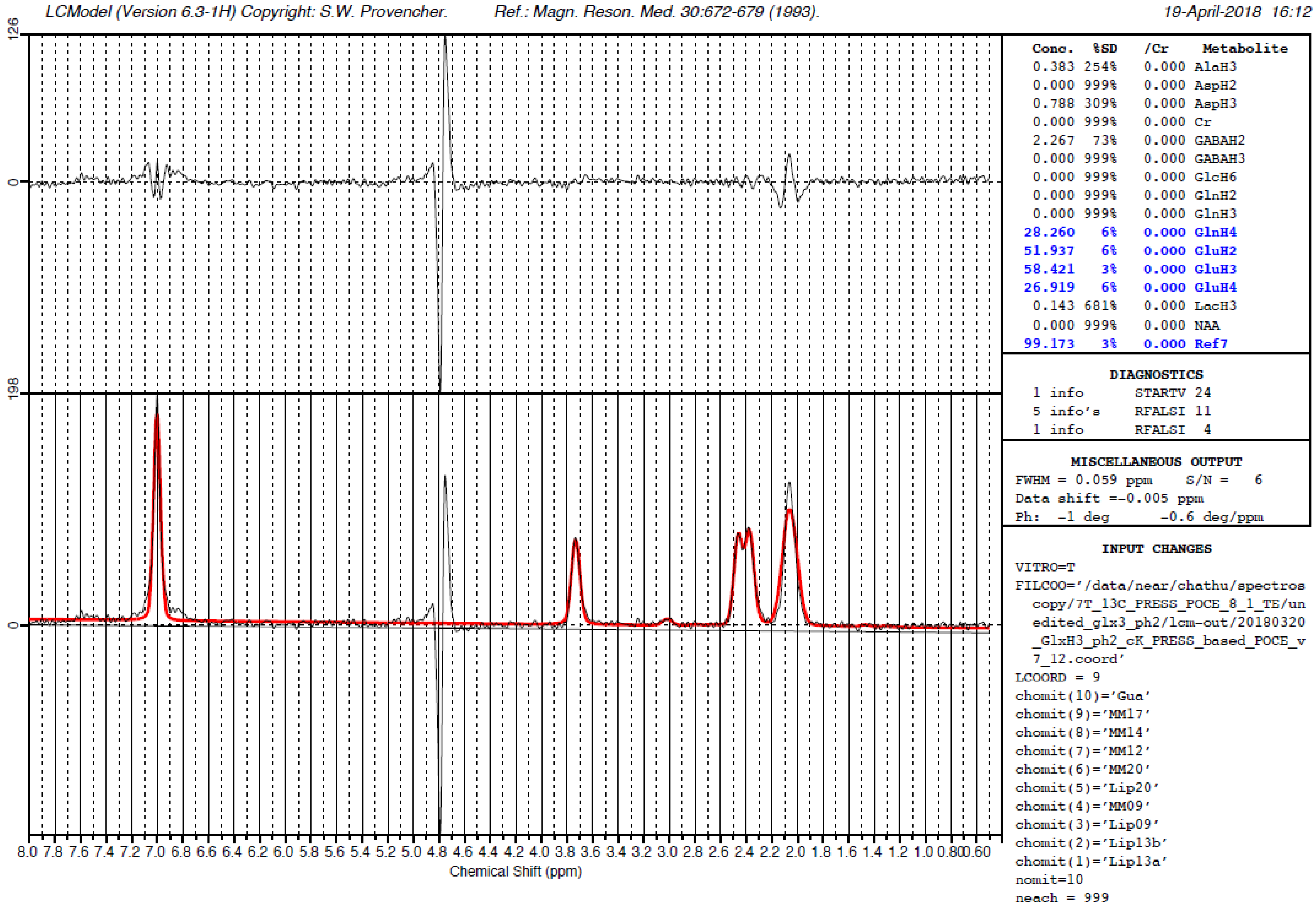

```
LCModel (Version 6.3-1H) Copyright: S.W. Provencher.    Ref.: Magn. Reson. Med. 30:672-679 (1993).    19-April-2018  16:12

  Conc.  %SD    /Cr    Metabolite
  0.383 254%   0.000  AlaH3
  0.000 999%   0.000  AspH2
  0.788 309%   0.000  AspH3
  0.000 999%   0.000  Cr
  2.267  73%   0.000  GABAH2
  0.000 999%   0.000  GABAH3
  0.000 999%   0.000  GlcH6
  0.000 999%   0.000  GlnH2
  0.000 999%   0.000  GlnH3
 28.260   6%   0.000  GlnH4
 51.937   6%   0.000  GluH2
 58.421   3%   0.000  GluH3
 26.919   6%   0.000  GluH4
  0.143 681%   0.000  LacH3
  0.000 999%   0.000  NAA
 99.173   3%   0.000  Ref7

          DIAGNOSTICS
  1 info       STARTV 24
  5 info's     RFALSI 11
  1 info       RFALSI  4

       MISCELLANEOUS OUTPUT
FWHM = 0.059 ppm     S/N =    6
Data shift =-0.005 ppm
Ph:  -1 deg        -0.6 deg/ppm

          INPUT CHANGES
VITRO=T
FILCOO='/data/near/chathu/spectros
  copy/7T_13C_PRESS_POCE_8_1_TE/un
  edited_glx3_ph2/lcm-out/20180320
  _GlxH3_ph2_cK_PRESS_based_POCE_v
  7_12.coord'
LCOORD = 9
chomit(10)='Gua'
chomit(9)='MM17'
chomit(8)='MM14'
chomit(7)='MM12'
chomit(6)='MM20'
chomit(5)='Lip20'
chomit(4)='MM09'
chomit(3)='Lip09'
chomit(2)='Lip13b'
chomit(1)='Lip13a'
nomit=10
neach = 999
```

Figure 5-7 *LCModel output for the unedited component of the SEAL-PRESS sequence acquisition.*

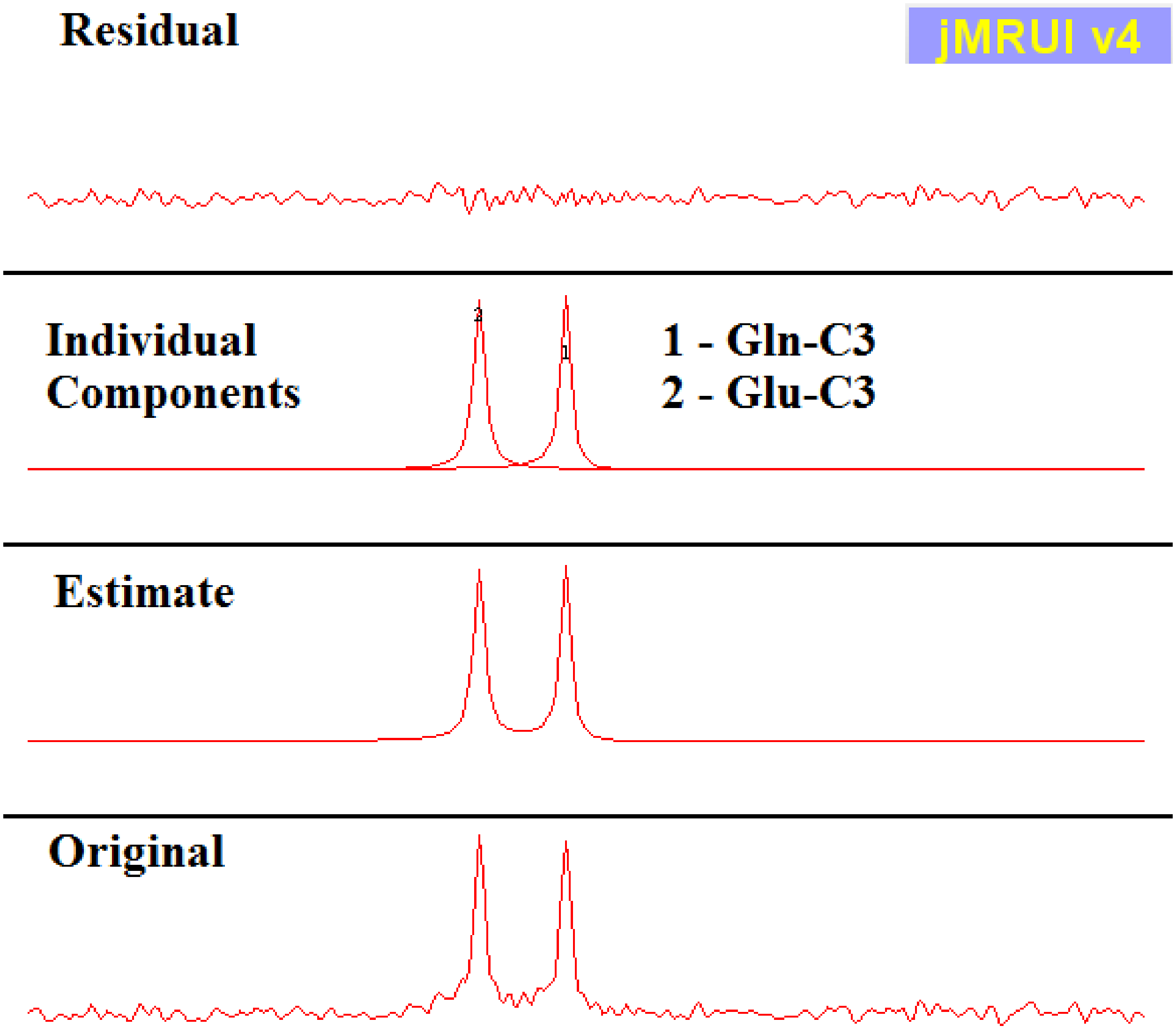

Figure 5-8 *JMRUI output for spectra obtained with the DEPT-PRESS sequence acquisition.*

Table 1 below summarizes the Glu:Gln ratios obtained for the different phantoms with SEAL-PRESS and DEPT-PRESS. To gauge reproducibility of metabolite quantification and uncertainty related to the spectral fit, coefficient of variation (CV) values were calculated and mean Cramer Rao lower bound (CRLB) values provided by LCModel and mean standard deviation Amplitude values (Mean std.Amp) provided by JMRUI are also summarized in Table 1.

Table 5-1 *Glu/Gln concentration estimates obtained with SEAL-PRESS and DEPT-PRESS sequences.*

Phantom # and concentrations (Glu:Gln)	**GluH4:GlnH4 from SEAL-PRESS with LCModel**			**GluC3:GlnC3 from DEPT-PRESS with JMRUI**		
	Mean ± std	CV	Mean %CRLB	Mean ± std	CV	Mean % std. Amp
Phantom 1 (0.75:1)	0.75 ± 0.02	3.3%	4.4%	0.73 ± 0.03	4.1%	0.61%
Phantom 2 (1:1)	0.93 ± 0.08	8.5%	7.8%	1.04 ± 0.06	5.7%	0.95%
Phantom 3 (2:1)	1.92 ± 0.12	6.6%	13.4%	2.33 ± 0.3	12.6%	2.9%

In addition, DEPT-PRESS spectra were obtained without heteronuclear decoupling to calculate weak heteronuclear scalar coupling constant (J_{HC}) for Glu-C3 and Gln-C3. J_{HC} values were found to be in the range of 131-132 Hz, which are in agreement with previous reports (2,8).

5.4.2 Sequential dynamic *in vivo* indirect and direct ^{13}C MRS

A 660-µl voxel (5 x 11 x 12 mm^3 corresponding to A-P, L-R, H-F directions) was placed within the brain anterior biased and dorsally biased (for improved sensitivity with surface coils), as overlaid on an anatomical scan in Figure 5-9. FASTMAP was used to shim a smaller 6 x 6 x 6 mm^3 region centered within the 660-µl voxel, and the larger 660-µl voxel was manual shimming which resulted in a water linewidth of 24 Hz. The larger voxel size used (660-µl relative to 100- µl used in both previous experiments) in theory provides a > 6.6x boost in SNR relative to a 100-µl voxel used in our previous experiments, thus temporal averaging can be reduced by a factor ~ 44x. However the SNR boost factor in practice will be significantly lower primarily due to the spatially varying sensitivity of the ^{1}H surface coil used, and the less optimal shim obtained on a larger region of interest. Temporal averaging of each indirect ^{13}C MRS spectrum was therefore empirically determined to be 2.1mins (32 averages, TR = 4s) with the SEAL-PRESS sequence. Each ~2 min indirect ^{13}C MRS acquisition was interleaved with a 8-

min long direct ^{13}C MRS acquisition using the DEPT-PRESS sequence with the intention of acquiring time-courses with both modalities during a single dynamic *in vivo* ^{13}C MRS experiment.

Figure 5-10 illustrates time-resolved spectra obtained with the SEAL-PRESS sequence, where the temporal midpoint of each scan is labeled relative to the infusion onset. The [1,6-$^{13}C_2$]-Glc infusion protocol was executed following baseline scans with both SEAL-PRESS and DEPT-PRESS sequences.

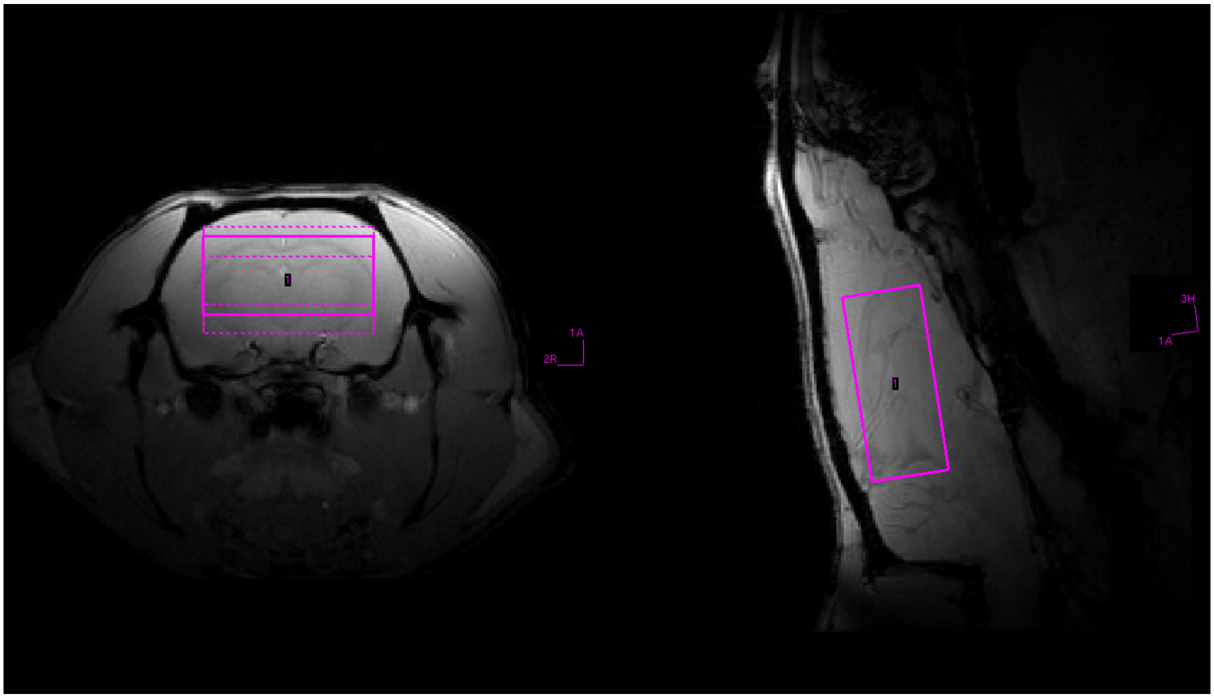

Figure 5-9 *Voxel placement for SEAL-PRESS and DEPT-PRESS sequences.*

It is evident on close inspection of the indirect ^{13}C MRS time-course data, that 2-min acquisitions provide satisfactory SNR, where 11-mins into the experiment ^{13}C labeled Glu-H4 as well as Glc-H6 are visible. Each time-resolved time point was apodized with a 10Hz Lorentz-Gaussian filter). However spectral quality in this experiment rates poorer compared to previous experiments (in chapter 3 and chapter 4) due to the poorer shim attained (~24 Hz relative to ~12

Hz in 100- µl voxels). The top most spectra in Figure 5-10 is an average from the last four time-resolved spectra (unfiltered), illustrating other resolved ^{13}C labeled metabolites observed.

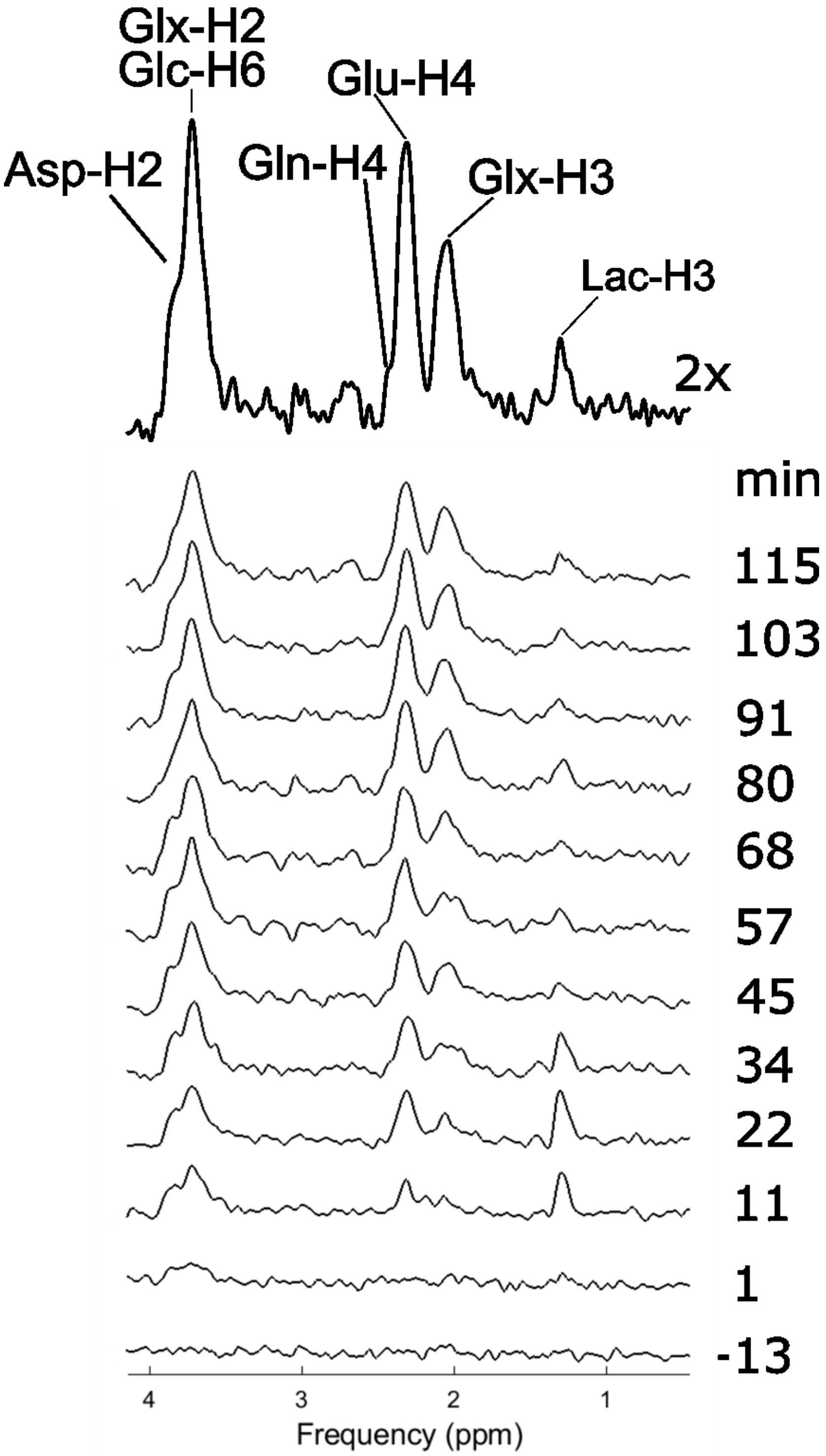

Figure 5-10 *Time resolved indirect* ^{13}*C MRS following the* ^{13}*C labeled glucose infusion.*

Time-resolved 8-min averaged DEPT-PRESS spectra unfortunately had no observable metabolites; and averaging eight such 8-min acquisitions towards the end of the 2-hour experiment surprisingly had no observable features to report either. One aspect we encountered with direct-^{13}C MRS acquisitions in phantom was that there is a noticeable 0th order phase shift between each 8-min averaged block; thus in theory for optimal SNR, individual averages should be separately stored and phase aligned in post-processing prior to averaging. However, even 4-min averaged spectra from *in vivo* DEPT-PRESS spectra were too low to observe meaningful information to perform phase alignment, which may partially account for the sensitivity limitation of the data acquired. The poor shim that was obtained on the large voxel is also another reason that further hampered receive signal sensitivity.

At the end of the infusion study (120 mins into the scan session), additional DEPT-PRESS data was obtained within a larger region (6250μl = 10 x 25 x 25 mm^3) that extended beyond bounds of the brain to validate that the hardware setup was functional. Figure 5-11 illustrates a 16-min average with the sequence within this larger brain region where Glu-C4 and Glc-C6 are observed. It is also noteworthy to highlight that a doublet around the Glu-C4 singlet is visible, which arises from [3, 4- $^{13}C_2$]-Glu, that is synthesized when 4-^{13}C-Glu labeled in the first turn of the TCA cycle enters a second turn of the TCA cycle (9).

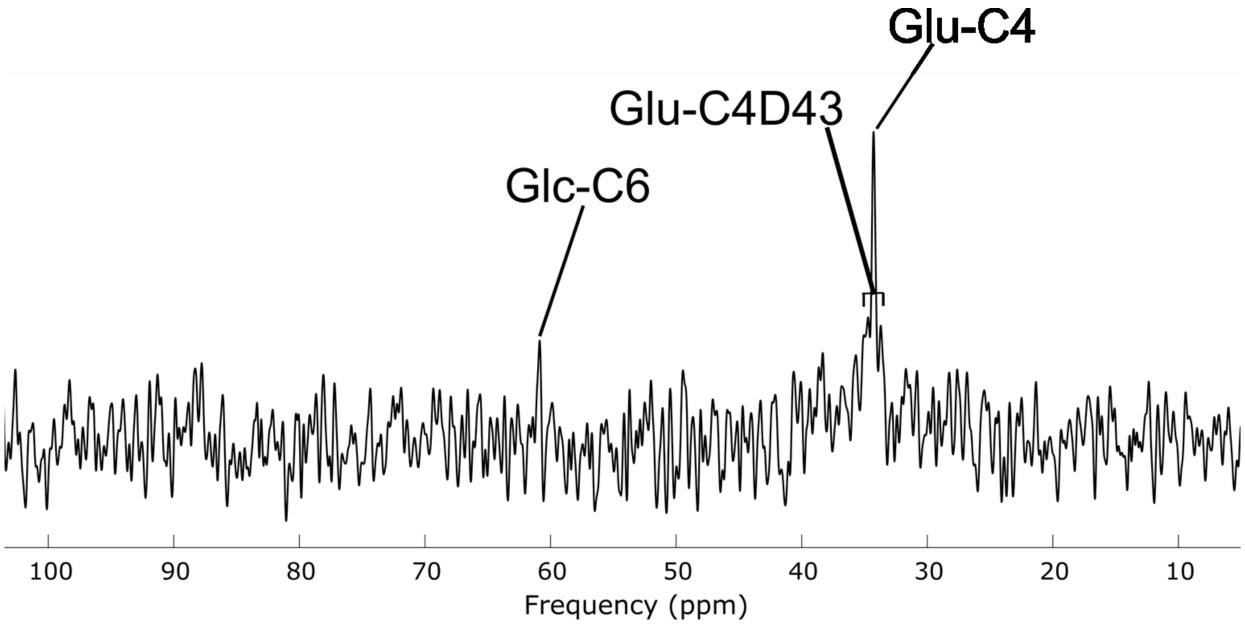

Figure 5-11 *in vivo DEPT-PRESS spectrum.*

5.5 Discussion

In this chapter we report hardware modifications and the design of a PRESS-localized semi-adiabatic DEPT sequence, in combination with a previously described indirect ^{13}C MRS sequence (SEAL-PRESS sequence) with the intention of acquiring indirect and direct ^{13}C MRS data from identical regions during a dynamic *in vivo* ^{13}C MRS study in rat brain.

In the presented set of phantom experiments, differences in T_1, T_2 relaxation rates for Glu and Gln were assumed to be similar; for example area under the curve ratios for Glu/Gln were assumed to directly represent concentration values without accounting for T_1, T_2 effects with both direct and indirect ^{13}C MRS. Rigorous quantification of metabolite concentrations was outside the scope of this work, rather the goal was to validate that the developed hardware and spectroscopy sequences can be used to measure Glu:Gln ratios with reasonable accuracy with localized direct and indirect ^{13}C MRS.

Simulation results for the Glutamate system show that the combined effects of T_2 and homonuclear J-evolution related losses would account for ~10% reduction in polarization for a 5ms TE localization sequence (time between the first excitation pulse on the ^{1}H channel and start of the DEPT sequence), relative to a 0-ms TE localization sequence (such as when ISIS is used). It is therefore conceivable that the TE = 5ms of the PRESS segment on the DEPT-PRESS sequence had an impact on the sensitivity for *in vivo* ^{13}C MRS, compared to the popularly used ISIS localized DEPT sequence (10). In this work, PRESS localized DEPT was primarily utilized to achieve identical localization profiles to the SEAL-PRESS sequence.

The range of CV values and uncertainties associated with metabolite quantification in Table 1 can be attributed to the different concentration levels used for Glu/Gln to avoid precipitation in distilled water when mixed in high concentrations (> 60mM). When comparing data in Table 1, similar or reduced uncertainty levels were expected from Phantom 2 relative to Phantom 1, however the reverse is observed. The marginally increased uncertainty values with Phantom 2 data can likely be attributed to be a result of differences in voxel placement (hence marginally different SNR), and smaller systematic variations such as differences in coil tuning/matching, and shimming.

Time courses with direct ^{13}C-MRS following the infusion of [1, 6-$^{13}C_2$]-Glc in the rat were not detectable due to low SNR with the current platform. The main hindrance is likely non-optimally large quadrature-driven pair of surface coils utilized on the ^{13}C channel, which as a part of the entire coil setup was designed and optimized for indirect ^{13}C MRS in the first study (Chapter 3). The coil loops are ~ 20mm x 40mm in foot print each, which improves the homogeneity of the B_2 field relative to the use of smaller footprint loops, however at the cost of lower sensitivity. Furthermore, to facilitate placement of the ^{1}H Rx-only loop adjacent to the rat head, the quadrature ^{13}C loops had to be placed ~5mm away from the rat head, which resulted in a further loss of sensitivity for direct ^{13}C MRS.

From a hardware perspective, it is unlikely that insertion losses of the quadrature-hybrid combiner are to be blamed for the low sensitivity on the ^{13}C channel since insertion losses leading up to the preamplifier were negligible (> -0.4 dB). The quad-hybrid combiner module was also placed about 2-feet away from the opening of the bore, such that hall-effect induced preamplifier performance degradation would be minimal. There are a few remedies that can be explored to improve receive sensitivity of direct ^{13}C MRS. 1) Develop the ^{13}C/^{1}H surface coil to be optimized for direct ^{13}C MRS, where the ^{13}C loop(s) are fixated proximal to the rat head, and place the proton surface coil above the plane of the ^{13}C loop(s); such a coil configuration will hinder indirect ^{13}C MRS performance, which however will not be as detrimental due to the higher sensitivity of protons than ^{13}C nuclei. 2) Develop a dual quadrature ^{13}C/^{1}H surface coil as previously described by Seres Roig et al. (33) to improve sensitivity on both channels.

FASTMAP was used to shim a 6 x 6 x 6 mm^3 region, and the larger 5 x 11 x 12 mm^3 region was manually shimmed. However, during the time of the experiments, higher order shims on the Bruker system were inoperative due to a technical issue. Unlike small voxels (< 5mm dimensions), where the first order shims would provide a reasonable correction (unless susceptibility artifacts are significant), shimming a larger region (>10mm dimensions) would greatly benefit from higher order shims. We speculate that the higher order shims would have made a significant improvement to the shim in the longer voxel dimensions (L-R and H-F directions), resulting in improved spectral quality of indirect ^{13}C MRS, and ultimately improve SNR of direct ^{13}C MRS for dynamic *in vivo* ^{13}C MRS.

Moving forward, there are benefits to realizing a coil system capable of and sensitive for both direct and indirect ^{13}C MRS acquisitions sequentially during dynamic *in vivo* ^{13}C MRS studies at magnet strengths that cannot resolve Glu/Gln H3 such as 7T. However, obtaining interleaved time-resolved spectra on both indirect and direct ^{13}C channels may be excessive. We can speculate two possible approaches to how both indirect and direct ^{13}C MRS data can be acquired in a useful manner for rodent brain imaging: 1) Predominantly acquire time-resolved indirect ^{13}C spectra, and collect intermittent direct ^{13}C spectra. With this approach, sensitivity and time resolution benefits of indirect ^{13}C MRS will be gained, and the few direct ^{13}C MRS spectra can be used to resolve Glu/Gln-C3 at the ^{13}C MRS time points, which can be provided as input for metabolic modeling. However, further investigating will be required to evaluate the viability of the approach. 2) Acquire direct ^{13}C spectra till nearly the end of an ~120-min experiment, and obtain one indirect ^{13}C spectra towards the end, at which ^{13}C labeling has approached steady state, the indirect ^{13}C spectra in conjunction with the previous direct ^{13}C spectra could be used to quantify, and calculate fractional enrichment curves for all resolvable metabolites, in addition to acquiring time resolved metabolite concentration curves for Glu/Gln C4 and Glu/Gln C3.

Despite the spectral dispersion benefits provided by direct ^{13}C MRS techniques, previous studies report use of > 300µl voxels in rodent brain to compensate for SNR limitations. The development of a dual channel Cryo-probe solution similar in architecture to the room temperature ^{1}H-^{13}C surface RF-coil setup described in chapter 3 is expected to provide ~5-fold improvement in SNR at 7T. The ~5-fold improvement is estimated based on ~4-fold improvements in SNR for mouse brain ^{13}C MRS reported using a Cryo-probe relative to room temperature coils at 9.4T (34), considering the fact that sample noise increases with the square of the Larmor frequency. Such sensitivity Improvements on the ^{13}C channel would pave the way for ~100ul voxel direct ^{13}C spectroscopy with comparable time resolution to indirect ^{13}C MRS.

5.6 Conclusions

We report the development of an RF coil platform and MRS sequences to perform localized direct and direct ^{13}C MRS sequentially during a dynamic *in vivo* ^{13}C MRS study in rat brain. Realization of this platform required custom designed hardware, as well as the design of a PRESS-localized semi-adiabatic DEPT sequence, in combination with a previously described indirect ^{13}C MRS sequence (SEAL-PRESS sequence) with the intention of acquiring indirect and direct ^{13}C MRS data from identically localized regions. The platform was validated in phantom, however the desired level of receive sensitivity was insufficient to obtain meaningful time-resolved spectra with direct ^{13}C MRS *in vivo*. In concluding this work, the most likely limitations were identified, and potential solutions have been suggested for future work.

5.7 References

1. Rothman DL, De Feyter HM, de Graaf RA, Mason GF, Behar KL. 13C MRS studies of neuroenergetics and neurotransmitter cycling in humans. NMR in biomedicine 2011;24(8):943-957.
2. Gruetter R, Adriany G, Choi IY, Henry PG, Lei H, Oz G. Localized in vivo 13C NMR spectroscopy of the brain. NMR in biomedicine 2003;16(6-7):313-338.
3. Morris GA, Freeman R. Enhancement of nuclear magnetic resonance signals by polarization transfer. Journal of the American Chemical Society 1979;101(3):760-762.
4. Doddrell DM, Pegg DT, Bendall MR. Distortionless enhancement of NMR signals by polarization transfer. Journal of Magnetic Resonance (1969) 1982;48(2):323-327.
5. Rothman DL, Behar KL, Hetherington HP, den Hollander JA, Bendall MR, Petroff OA, Shulman RG. 1H-Observe/13C-decouple spectroscopic measurements of lactate and glutamate in the rat brain in vivo. Proceedings of the National Academy of Sciences of the United States of America 1985;82(6):1633-1637.
6. Fitzpatrick SM, Hetherington HP, Behar KL, Shulman RG. The flux from glucose to glutamate in the rat brain in vivo as determined by 1H-observed, 13C-edited NMR spectroscopy. Journal of cerebral blood flow and metabolism : official journal of the International Society of Cerebral Blood Flow and Metabolism 1990;10(2):170-179.
7. Rothman DL, Howseman AM, Graham GD, Petroff OA, Lantos G, Fayad PB, Brass LM, Shulman GI, Shulman RG, Prichard JW. Localized proton NMR observation of [3-13C]lactate in stroke after [1-13C]glucose infusion. Magnetic resonance in medicine 1991;21(2):302-307.

8. Meeus I, Brown MJ, De Graaf DC, Smagghe G. Effects of invasive parasites on bumble bee declines. Conservation biology : the journal of the Society for Conservation Biology 2011;25(4):662-671.
9. de Graaf RA, Mason GF, Patel AB, Behar KL, Rothman DL. In vivo 1H-[13C]-NMR spectroscopy of cerebral metabolism. NMR in biomedicine 2003;16(6-7):339-357.
10. Henry PG, Tkac I, Gruetter R. 1H-localized broadband 13C NMR spectroscopy of the rat brain in vivo at 9.4 T. Magnetic resonance in medicine 2003;50(4):684-692.
11. Shestov AA, Valette J, Ugurbil K, Henry PG. On the reliability of (13)C metabolic modeling with two-compartment neuronal-glial models. Journal of neuroscience research 2007;85(15):3294-3303.
12. Xin L, Mlynarik V, Lanz B, Frenkel H, Gruetter R. 1H-[13C] NMR spectroscopy of the rat brain during infusion of [2-13C] acetate at 14.1 T. Magnetic resonance in medicine 2010;64(2):334-340.
13. Valette J, Tiret B, Boumezbeur F. Experimental strategies for in vivo 13C NMR spectroscopy. Analytical Biochemistry 2017;529:216-228.
14. Saunders Dawn E, Howe Franklyn A, van den Boogaart A, Griffiths John R, Brown Martin M. Aging of the adult human brain: In vivo quantitation of metabolite content with proton magnetic resonance spectroscopy. Journal of Magnetic Resonance Imaging 1999;9(5):711-716.
15. De Graaf RA. In vivo NMR Spectroscopy - 2nd Edition principles and techniques: Wiley; 2007.
16. De Graaf RA. In vivo NMR spectroscopy: Wiley; 2007.

17. Yahya A, Allen PS. Effect of strong homonuclear proton coupling on localized (13)C detection using PRESS. Magnetic resonance in medicine 2005;54(6):1340-1350.

18. Kumaragamage C, Madularu D, Mathieu AP, De Feyter H, Rajah MN, Near J. In vivo proton observed carbon edited (POCE) (13) C magnetic resonance spectroscopy of the rat brain using a volumetric transmitter and receive-only surface coil on the proton channel. Magnetic resonance in medicine 2018;79(2):628-635.

19. Simpson R, Devenyi GA, Jezzard P, Hennessy TJ, Near J. Advanced processing and simulation of MRS data using the FID appliance (FID-A)-An open source, MATLAB-based toolkit. Magnetic resonance in medicine 2015.

20. Gruetter R. Automatic, localized in vivo adjustment of all first- and second-order shim coils. Magnetic resonance in medicine 1993;29(6):804-811.

21. Tkáč I, Starčuk Z, Choi IY, Gruetter R. In vivo 1H NMR spectroscopy of rat brain at 1 ms echo time. Magnetic resonance in medicine 1999;41(4):649-656.

22. Silver MS, Joseph RI, Chen CN, Sank VJ, Hoult DI. Selective population inversion in NMR. Nature 1984;310(5979):681-683.

23. Kumaragamage C, Madularu D, Mathieu AP, Lupinsky D, de Graaf RA, Near J. Minimum echo time PRESS-based proton observed carbon edited (POCE) MRS in rat brain using simultaneous editing and localization pulses. Magnetic resonance in medicine 2018.

24. Ordidge RJ, Connelly A, Lohman JAB. Image-selected in Vivo spectroscopy (ISIS). A new technique for spatially selective nmr spectroscopy. Journal of Magnetic Resonance (1969) 1986;66(2):283-294.

25. Garwood M, Ke Y. Symmetric pulses to induce arbitrary flip angles with compensation for rf inhomogeneity and resonance offsets. Journal of Magnetic Resonance (1969) 1991;94(3):511-525.

26. Garwood M, DelaBarre L. The return of the frequency sweep: designing adiabatic pulses for contemporary NMR. Journal of magnetic resonance 2001;153(2):155-177.

27. Chen X, Boesiger P, Henning A. J-refocused 1H PRESS DEPT for localized 13C MR Spectroscopy. NMR in biomedicine 2013;26(9):1113-1124.

28. Shaka AJ, Keeler J, Freeman R. Evaluation of a new broadband decoupling sequence: WALTZ-16. Journal of Magnetic Resonance (1969) 1983;53(2):313-340.

29. Arii K, Kobayashi H, Kai T, Kokuba Y. Degradation kinetics of l-glutamine in aqueous solution. European Journal of Pharmaceutical Sciences 1999;9(1):75-78.

30. Provencher SW. Estimation of metabolite concentrations from localized in vivo proton NMR spectra. Magnetic resonance in medicine 1993;30(6):672-679.

31. Naressi A, Couturier C, Devos JM, Janssen M, Mangeat C, de Beer R, Graveron-Demilly D. Java-based graphical user interface for the MRUI quantitation package. Magma 2001;12(2-3):141-152.

32. Henry PG, Oz G, Provencher S, Gruetter R. Toward dynamic isotopomer analysis in the rat brain in vivo: automatic quantitation of 13C NMR spectra using LCModel. NMR in biomedicine 2003;16(6-7):400-412.

33. Seres Roig E, Magill AW, Donati G, Meyerspeer M, Xin L, Ipek O, Gruetter R. A double-quadrature radiofrequency coil design for proton-decoupled carbon-13 magnetic resonance spectroscopy in humans at 7T. Magnetic resonance in medicine 2015;73(2):894-900.

34. Sack M, Wetterling F, Sartorius A, Ende G, Weber-Fahr W. Signal-to-noise ratio of a mouse brain (13) C CryoProbe system in comparison with room temperature coils: spectroscopic phantom and in vivo results. NMR in biomedicine 2014;27(6):709-715.

Chapter 6

Summary, Discussion, and Conclusions

6.1 Summary

The overarching goal of this work was to develop novel methods for dynamic *in vivo* carbon-13 MRS of the rat brain. Towards this goal, the main contributions of this thesis were 1) The development of an RF coil platform for POCE-MRS in the rat brain, 2) the development of a pulse sequence with minimal echo-time and thus optimal sensitivity for indirect ^{13}C MRS in rat brain, and 3) the development of hardware and software modifications to enable simultaneous direct and indirect ^{13}C MRS in the rat brain. A brief summary of the findings of these works, as well a discussion of future considerations can be found in the sections below:

6.1.1 Proton Volumetric Resonator Based POCE MRS

Conventionally, localized *in vivo* proton observed carbon edited (POCE) MRS with heteronuclear decoupling (1-6) is performed using surface coils for ^{1}H transmission and reception. With such coil platforms, the use of adiabatic pulses (7) is beneficial to minimize nutation angle errors in the presence of a spatially varying radiofrequency field, and minimize signal losses and artefacts (6). Image selected *in vivo* spectroscopy (ISIS) and LASER, are two classes of localized MRS sequences that have been used to mitigate such B_1^+ inhomogeneities, however with limitations associated with each method. Single-shot localized POCE-MRS techniques mitigate subtraction artefacts associated with ISIS based implementations, and sensitivity of POCE-MRS can be enhanced through the use of short TE sequences due to minimized T_2 and homonuclear J-evolution related losses.

The objective of this work was to develop POCE-MRS with uniform nutation, single-shot localization, combined with a short TE utilizing PRESS. To achieve this, a ^{1}H-[^{13}C] surface coil was paired with a detunable 86 mm volumetric resonator for homogeneous B_1^+. The ^{1}H-[^{13}C] surface coil consists of a ^{1}H Receive (Rx)-only surface coil, and a quadrature driven pair of surface coils on the ^{13}C channel. The ^{1}H Rx-only surface coil provides sensitivity benefits compared to a volume coil approach. Furthermore, the requirement for a T/R switch before the ^{1}H preamplifier is nullified, thus T/R switch related SNR losses are also avoided compared to a surface coil in a transceiver configuration. Using the ^{1}H-[^{13}C] coil setup, a single-shot localized PRESS-based POCE MRS sequence with short conventional pulses was developed, thus enabling uniform nutation combined with a short 12.6-TE; a feat that cannot be achieved with an all-surface coil based approach.

6.1.2 POCE MRS Utilizing Simultaneous Editing And Localization Pulses (SEAL)

Following the development of a 12.6-ms TE PRESS-POCE sequence, the second objective was to design a PRESS localized POCE sequence with TE < 10ms. However, due to instrument limitations (peak B_1 and spoiler gradient strength and stabilization time), conventional methods used for editing and localization would not provide both < 10ms TE and single-shot localization. To that end, Chapter 4 presents a novel single-shot PRESS-localized POCE-MRS sequence that involves the application of simultaneous editing and localization pulses (SEAL-PRESS), allowing the TE to be reduced to a theoretically optimal value of ~ $1/J_{HC}$ (8.1-ms) for within-sequence edited ^{1}H-[^{13}C] spectroscopy. This work involved the design of the sequence with the aid of heteronuclear quantum mechanical density matrix simulations, implementation of the sequence on the Bruker 7-T animal scanner, and validation of the sequence in phantom and *in vivo* rat preparations. Reducing the TE from 12.6-ms (TE of a PRESS-POCE sequence presented in study 1) to 8.1-ms improved signal intensity by >17% for all ^{13}C labeled metabolites primarily due to reduced homonuclear J-evolution and T_2 related losses.

Furthermore as part of this work, we investigated the effects of retarded heteronuclear J-evolution during simultaneous RF pulses on both ^{1}H and ^{13}C channels. The application of simultaneous RF pulses is not a new concept in NMR or for localized MRS sequences reported in the literature; however the phenomenon, to the best of our knowledge, was not well documented. For example, a study by de Graaf et al. (2) reported partial inhibition of heteronuclear J-evolution from a theoretically expected ~7.9ms to 9.4ms for the [2-^{13}C]-acetate spin system during long (>2-ms) simultaneous RF pulses, and was empirically extended to the optimal value. This retardation of heteronuclear J-evolution does not become prominent till relatively broad amplitude modulated pulses are used, which can be attributed to heteronuclear multiple quantum coherence states that arise from heteronuclear anti-phase coherence terms during long inversion/refocusing pulses. Density matrix simulations accurately predict this heteronuclear retardation, considering RF pulse shapes and the spin systems of interest for optimal sequence timings.

6.1.3 Simultaneous Direct and Indirect ^{13}C MRS

The third objective of this work was to investigate methods of improving the metabolic modeling by combining benefits of both indirect and direct ^{13}C MRS. As such, this work describes hardware and pulse sequence developments to extended the ^{13}C RF coil platform developed in chapter 3 to be capable of both direct and indirect ^{13}C MRS sequentially for dynamic *in vivo* rat brain imaging. Both direct ^{13}C MRS and indirect ^{13}C MRS have their inherent benefits and weaknesses. While direct ^{13}C MRS methods provide excellent spectral resolution, sensitivity is poorer due to the lower sensitivity and polarization of ^{13}C nuclei relative to protons. Indirect ^{13}C MRS on the other hand, provides a sensitivity gains over direct ^{13}C methods, however in comparison suffers from spectral crowding as most observable metabolites fall within the 1.2ppm-4ppm range; thus rendering reliable quantification of overlapping metabolites impossible (such as Glu-H3 and Gln-H3 at 7T *in vivo*). Simulation studies (8) show that the reliability of metabolic modeling on a two-compartment model to be improved when at least four time-resolved metabolite curves are used (such as Glu-H4, Gln-H4, Glu-H3, and Gln-H3). Acquisition of both indirect and direct ^{13}C MRS in an interleaved fashion is expected to provide sensitivity benefits and direct fractional enrichment curves from indirect ^{13}C MRS, and spectral dispersion benefits from direct ^{13}C MRS; this is expected to reduce the uncertainty associated with overlapping metabolite peaks, and improve metabolic modeling of Glutamate-Glutamine cycling in the brain *in vivo*.

To acquire both indirect and direct ^{13}C MRS, the previously described SEAL-PRESS sequence and an in-house implemented PRESS localized semi-adiabatic DEPT sequence (both sequences utilizing PRESS localization) were used. Phantom experiments demonstrated the functionality of the hardware and pulse sequences and demonstrated reasonable agreement of metabolite concentration measurements with the two sequences. Though time-resolved spectra were detected as expected with the SEAL-PRESS sequence, meaningful time-resolved spectra were not detected with the DEPT-PRESS sequence. A few factors that may have made a sizable impact on detection sensitivity of direct ^{13}C MRS were identified; one of which can be attributed to the coil architecture which was optimized for POCE MRS. Each of the quadrature driven ^{13}C loops were ~ 20mm x 40mm in foot print each for improved B_2 field homogeneity however ~10mm away from the rat brain, which comes at the cost of reduced sensitivity. In comparison, on a dedicated direct ^{13}C MRS coil platform, for example the ^{13}C MRS coil platform described by Lai et al. (9), a single ^{13}C loop is used with a 15mm diameter and placed proximal to the rat brain for maximal SNR gains. A revised coil design where all surface coils are placed on the same curved plane, with all loop geometries optimized for sensitivity in rat brain imaging, is expected to improve detection with both indirect and direct ^{13}C MRS.

6.2 Overall Discussion

An inherent limitation with a volumetric resonator is its limited peak B_1^+ capabilities relative to localized peak B_1^+ fields attainable with a field-of-view optimized surface coil transmitter. The 86-mm volumetric resonator used has a peak B_1^+ of ~4.1 kHz, thus limiting the use of short, high bandwidth refocusing pulses which would minimize chemical shift displacement errors. Chemical shift displacement errors were < 22% (voxel shift between water and fat) in the developed SEAL-PRESS sequence. It must be noted that the ^{1}H-[^{13}C] surface coil was designed and developed around a readily available detunable 86-mm volumetric resonator, though a smaller inner diameter (~60mm) detunable head-only volumetric resonator would have been equally sufficient, with the benefit of an increased peak B_1^+ field and reduced chemical shift displacement errors.

At higher magnetic field strengths (>9.4T) the implementation of the presented RF coil platform for POCE MRS may require further aspects to be considered; B_1 inhomogeneities may not be easily resolved with a simple volumetric coil setup (when field of view dimensions approach the RF wavelength ~ $\lambda/2$), rather a parallel transmit (pTx) array approach with B_1^+ shimming (10) may be required to attain whole brain B_1^+ homogeneity. In such a situation, considering the complexities associated with the implementation and calibration of pTx, in addition to facilitating compatibility with heteronuclear decoupling for ^{13}C MRS, an all surface coil based approach, with a B_1^+ insensitive localization sequence (such as LASER localized POCE) may turn out to be more practical.

LASER-POCE implementations (3,6,11) reported for *in vivo* studies have >22-ms TE; though the first half of the sequence has five closely spaced inversion pulses and maintains the CPMG character (12,13) for strongly coupled spin systems, the final TE $>1/J_{HC}$ is subject to T_2 and homonuclear J-evolution related losses. A few modifications to LASER-POCE can be suggested to reduce the sequence TE and thus improve sensitivity: 1) The implementation of a BISEP (14) preparation block preceding LASER as reported by Xin et al. for SPECIAL localized BISEP (5), would bring the TE down by ~10-ms on an animal MRI implementation, 2) The implementation of a SEAL-LASER variant, where the TE includes non-selective and selective refocusing to achieve a $1/J_{HC}$ time interval, with simultaneous editing and localization, to realize EDIT OFF and EDIT ON scans.

When it boils down to proton based MRS quantification, in my view (after gaining viewpoints of experts in the field during manuscript revisions), experienced MR spectroscopists fall into two camps; 1) those in favor of short TE MRS with the intention of gaining optimal sensitivity due minimal T_2 and homonuclear J-modulation related losses, and 2) those in favor of longer TE (exact values are magnetic field and application dependent) MRS with reduced macromolecular (MM) signals, at the cost of compromised sensitivity. A long standing criticism for short TE MRS is on the MM contamination and thus the question over reliability of overlapping metabolite quantification. There are two well-known methods to minimizing MM contamination: 1) Obtain a separate MM baseline (metabolite nulled) to be included as a basis set in a linear combination fitting tool (such as LCModel), or 2) if the MM component is mild, allow quantification tools such as LCModel to account for it using its in-built MM baseline. Metabolite nulling can be an effective approach, however due to the preceding inversion recovery component; MM signals are somewhat attenuated and T_1-weighted. To-date, there is no gold standard *in vivo* MRS sequence and the debate over "the best approach to *in vivo* MRS" remains open.

Now returning back to this work, the design of the proton volumetric coil based ^1H-^{13}C coil platform was central to realizing the SEAL-PRESS sequence; which to the best of our knowledge is the first description of a single shot PRESS localized <10 ms-TE sequence with uniform nutation for *in vivo* POCE MRS. Due to the short TE of the SEAL-PRESS sequence, however, effects of MM contamination, and remedies to minimize the effects, are valid concerns to be addressed. It must be noted that MM signals are removed by subtraction on the POCE spectrum, hence is not affected by very short-TE sequences. However, for quantification and calculation of FE components, it is desirable to effectively tease out the MM signals. Since the scope of this work was limited to the development of ^{13}C MRS, such potential concerns that may impact accurate metabolite quantification were not pre-investigated. However, previous ultra-short TE (2.8-ms) POCE MRS reports (5), and recent studies with this sequence (15,16), report the inclusion of a measured MM baseline in the basis-set for improved quantification of fractional enrichment, such an approach is expected to be sufficient to address MM contaminations in this work. Moving forward in studies of brain metabolism in disease, we can suggest the following options to combat macromolecular contamination based on its severity: If macromolecular contamination is low to mild, the pre-loaded macromolecular baseline in LCModel can be used, but if macromolecular contamination is severe, then it would be preferable to obtain a macromolecular baseline to be incorporated in the basis set as reported by Xin et al.

The semi-adiabatic DEPT sequence described in Chapter 5 and previous descriptions of localized DEPT sequences in the literature (17-20) utilize short conventional pulses on the ^{1}H channel during the DEPT component. Thus heteronuclear J-evolution retardation effects during simultaneous RF pulses described in Chapter 4 are expected to be minimal. A localized fully adiabatic DEPT sequence, to the best of our knowledge, has not been reported for *in vivo* MRS; such a sequence with the additional peak B_1^+/B_2^+ constrained RF coil platform (such that inversion/refocusing pulses are required to be in the >1 ms realm) would greatly benefit from density matrix simulations, prior to implementation and calibration of the sequence timings for optimal sensitivity.

Methods presented in this thesis were designed and implemented on a preclinical 7T magnet for rat brain imaging. As described earlier in this thesis, ^{13}C MRS is a powerful technique that can be used to measure cell-specific neuroenergetics and neurotransmission, and thus far remains to be the only noninvasive method capable of this feat noninvasively, *in vivo*. ^{13}C MRS studies described to study disease in rodent models provide unique insights into altered neuronal and glial metabolism which in some instances have been identified in early stages of disease progression. Thus outcomes of ^{13}C MRS studies in rodents provide insights into pathology specific biomarkers that can be extended to be used in the clinic. Techniques developed in this thesis are centered around a volumetric proton transmitter for PRESS localized short TE POCE MRS. Many clinical MRI systems (<= 3T) utilize an in-built volumetric proton transmitter and separate Rx-only head coil for imaging. Modifying such a clinical MRI can be done similar to the RF coil platform developed in chapter 3 for dynamic *in vivo* 13C MRS. SAR constraints associated with heteronuclear decoupling however will need to be addressed for its utility in the clinical setting.

6.3 Conclusions

The described ^{1}H-^{13}C coil platform utilizing a proton volumetric transmitter in Chapter 3, and the SEAL-PRESS sequence described in Chapter 4 in tandem, provides uniform nutation, single-shot PRESS localization, optimal sensitivity and editing efficiency, with a short TE of 8.1-ms; a feat that cannot be achieved with all-surface coil based approaches described in the literature. Single-shot PRESS localization avoids subtraction artifacts associated with multi-shot acquisitions, and the short TE sequence minimizes T_2 and homonuclear J-evolution related losses thus improving sensitivity. Thus the overall POCE MRS platform provides a convenient and sensitive platform from which to study energy metabolism and glutamate neurotransmission in the rat brain *in vivo*.

The RF coil platform was extended to be capable of both direct and indirect ^{13}C MRS sequentially during dynamic *in vivo* ^{13}C MRS experiments. The intention was to harvest the benefits of both detection methods; namely sensitivity gains and direct measurement of fractional enrichment (FE) time courses for resolvable metabolites with indirect detection, larger spectral dispersion, and obtain ^{13}C-^{13}C coupled isotopomer information with direct detection. Together, complementary information with both detection sequences was expected to improve the reliability of ^{13}C metabolic modeling. Though the functionality of the coil platform, and PRESS-localized semi-adiabatic DEPT sequence implemented were validated, due to limited sensitivity of direct ^{13}C detection, time resolved spectra could not be obtained. The most likely causes for the limited direct detection sensitivity were identified, and potential solutions to improve the coil platform for future work were discussed.

6.4 References

1. Chen W, Adriany G, Zhu XH, Gruetter R, Ugurbil K. Detecting natural abundance carbon signal of NAA metabolite within 12-cm3 localized volume of human brain using 1H-[13C] NMR spectroscopy. Magnetic resonance in medicine 1998;40(2):180-184.
2. de Graaf RA, Brown PB, Mason GF, Rothman DL, Behar KL. Detection of [1,6-13C2]-glucose metabolism in rat brain by in vivo 1H-[13C]-NMR spectroscopy. Magnetic resonance in medicine 2003;49(1):37-46.
3. Yang J, Li CQ, Shen J. In vivo detection of cortical GABA turnover from intravenously infused [1-13C]D-glucose. Magnetic resonance in medicine 2005;53(6):1258-1267.
4. Pfeuffer J, Tkac I, Choi IY, Merkle H, Ugurbil K, Garwood M, Gruetter R. Localized in vivo 1H NMR detection of neurotransmitter labeling in rat brain during infusion of [1-13C] D-glucose. Magnetic resonance in medicine 1999;41(6):1077-1083.
5. Xin L, Mlynarik V, Lanz B, Frenkel H, Gruetter R. 1H-[13C] NMR spectroscopy of the rat brain during infusion of [2-13C] acetate at 14.1 T. Magnetic resonance in medicine 2010;64(2):334-340.
6. de Graaf RA, Rothman DL, Behar KL. State of the art direct 13C and indirect 1H-[13C] NMR spectroscopy in vivo. A practical guide. NMR in biomedicine 2011;24(8):958-972.
7. Tannus A, Garwood M. Adiabatic pulses. NMR in biomedicine 1997;10(8):423-434.
8. Shestov AA, Valette J, Ugurbil K, Henry PG. On the reliability of (13)C metabolic modeling with two-compartment neuronal-glial models. Journal of neuroscience research 2007;85(15):3294-3303.

9. Lai M, Gruetter R, Lanz B. Progress towards in vivo brain (13)C-MRS in mice: Metabolic flux analysis in small tissue volumes. Analytical biochemistry 2017;529:229-244.

10. Gilbert KM, Gati JS, Barker K, Everling S, Menon RS. Optimized parallel transmit and receive radiofrequency coil for ultrahigh-field MRI of monkeys. NeuroImage 2016;125:153-161.

11. Jonkers RA, Geraedts TR, van Loon LJ, Nicolay K, Prompers JJ. Multitissue assessment of in vivo postprandial intracellular lipid partitioning in rats using localized 1H-[13C] magnetic resonance spectroscopy. Magnetic resonance in medicine 2012;68(4):997-1006.

12. Carr HY, Purcell EM. Effects of Diffusion on Free Precession in Nuclear Magnetic Resonance Experiments. Physical Review 1954;94(3):630-638.

13. Allerhand A. Analysis of Carr—Purcell Spin-Echo NMR Experiments on Multiple-Spin Systems. I. The Effect of Homonuclear Coupling. The Journal of Chemical Physics 1966;44(1):1-9.

14. Garwood M, Merkle H. Heteronuclear spectral editing with adiabatic pulses. Journal of Magnetic Resonance (1969) 1991;94(1):180-185.

15. Xin L, Lanz B, Lei H, Gruetter R. Assessment of metabolic fluxes in the mouse brain in vivo using 1H-[13C] NMR spectroscopy at 14.1 Tesla. Journal of cerebral blood flow and metabolism : official journal of the International Society of Cerebral Blood Flow and Metabolism 2015;35(5):759-765.

16. Lizarbe B, Lei H, Duarte JMN, Lanz B, Cherix A, Gruetter R. Feasibility of in vivo measurement of glucose metabolism in the mouse hypothalamus by (1) H-[(13) C] MRS at 14.1T. Magnetic resonance in medicine 2018;80(3):874-884.

17. Yahya A, Allen PS. Effect of strong homonuclear proton coupling on localized (13)C detection using PRESS. Magnetic resonance in medicine 2005;54(6):1340-1350.

18. Henry PG, Tkac I, Gruetter R. 1H-localized broadband 13C NMR spectroscopy of the rat brain in vivo at 9.4 T. Magnetic resonance in medicine 2003;50(4):684-692.

19. Chen X, Boesiger P, Henning A. J-refocused 1H PRESS DEPT for localized 13C MR spectroscopy. NMR in biomedicine 2013;26(9):1113-1124.

20. Nabuurs CI, Klomp DW, Veltien A, Kan HE, Heerschap A. Localized sensitivity enhanced in vivo 13C MRS to detect glucose metabolism in the mouse brain. Magnetic resonance in medicine 2008;59(3):626-630.

Appendix A

Copyright Permissions

A.1 Copyright waiver for Figure 2-20

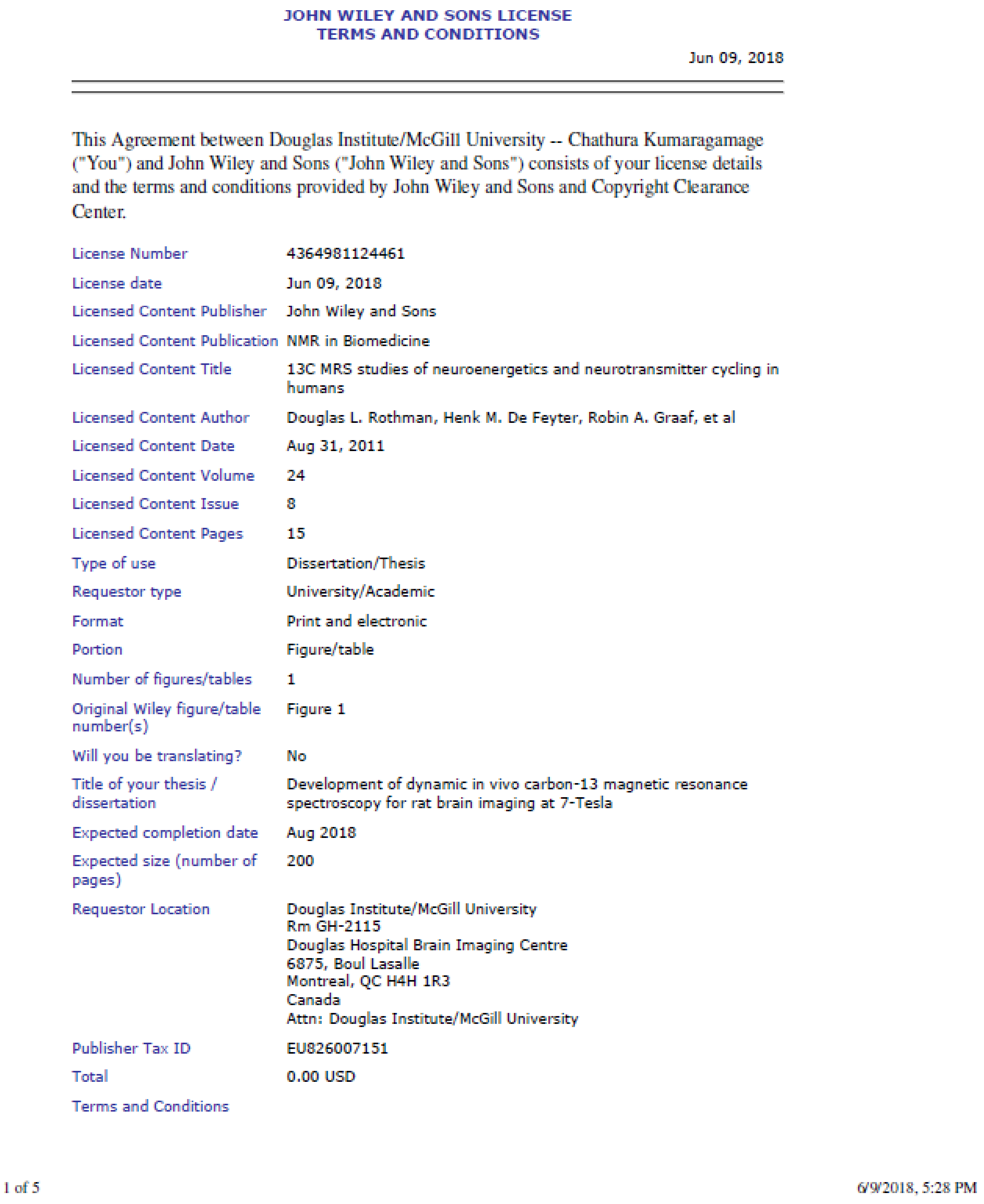

JOHN WILEY AND SONS LICENSE
TERMS AND CONDITIONS

Jun 09, 2018

This Agreement between Douglas Institute/McGill University -- Chathura Kumaragamage ("You") and John Wiley and Sons ("John Wiley and Sons") consists of your license details and the terms and conditions provided by John Wiley and Sons and Copyright Clearance Center.

License Number	4364981124461
License date	Jun 09, 2018
Licensed Content Publisher	John Wiley and Sons
Licensed Content Publication	NMR in Biomedicine
Licensed Content Title	13C MRS studies of neuroenergetics and neurotransmitter cycling in humans
Licensed Content Author	Douglas L. Rothman, Henk M. De Feyter, Robin A. Graaf, et al
Licensed Content Date	Aug 31, 2011
Licensed Content Volume	24
Licensed Content Issue	8
Licensed Content Pages	15
Type of use	Dissertation/Thesis
Requestor type	University/Academic
Format	Print and electronic
Portion	Figure/table
Number of figures/tables	1
Original Wiley figure/table number(s)	Figure 1
Will you be translating?	No
Title of your thesis / dissertation	Development of dynamic in vivo carbon-13 magnetic resonance spectroscopy for rat brain imaging at 7-Tesla
Expected completion date	Aug 2018
Expected size (number of pages)	200
Requestor Location	Douglas Institute/McGill University Rm GH-2115 Douglas Hospital Brain Imaging Centre 6875, Boul Lasalle Montreal, QC H4H 1R3 Canada Attn: Douglas Institute/McGill University
Publisher Tax ID	EU826007151
Total	0.00 USD
Terms and Conditions	

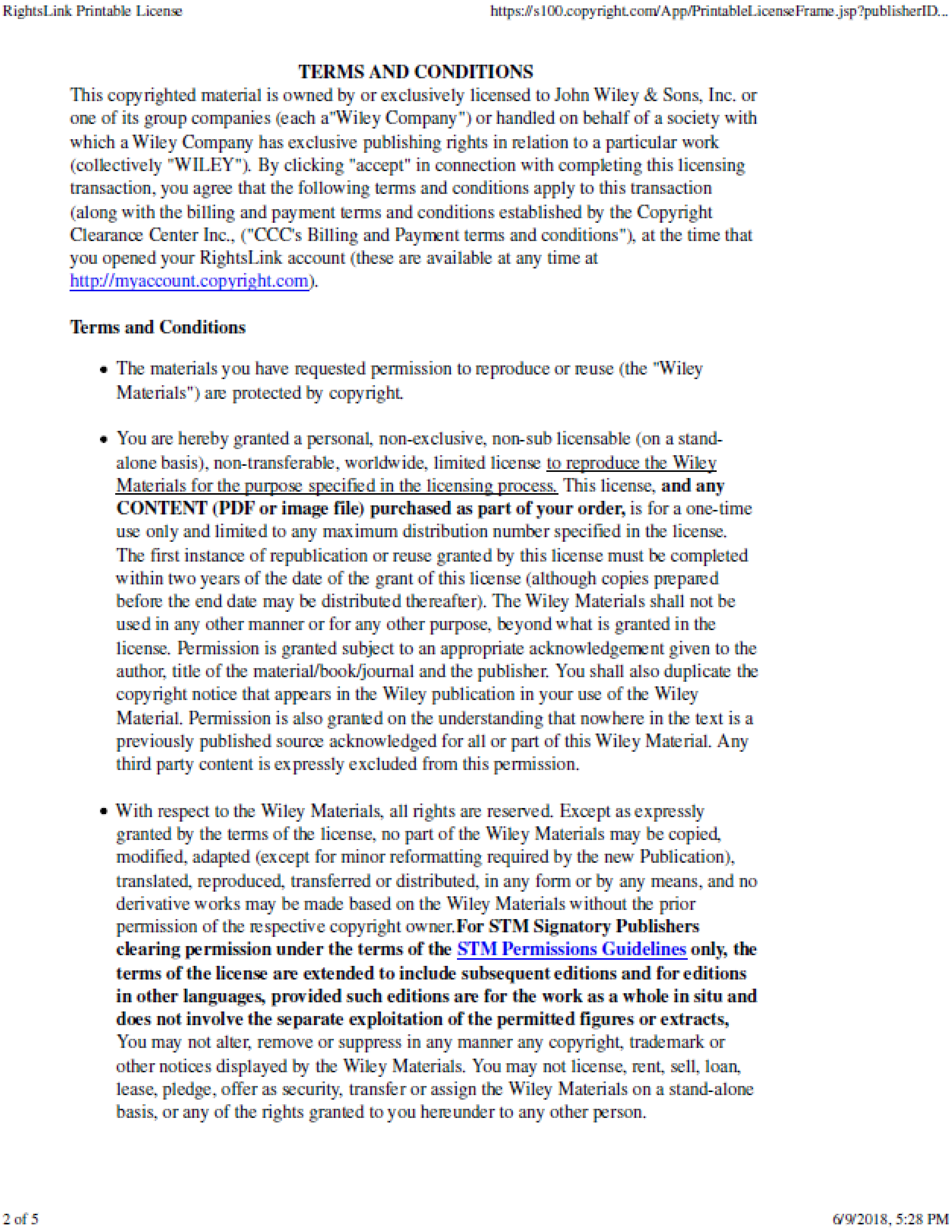

TERMS AND CONDITIONS

This copyrighted material is owned by or exclusively licensed to John Wiley & Sons, Inc. or one of its group companies (each a"Wiley Company") or handled on behalf of a society with which a Wiley Company has exclusive publishing rights in relation to a particular work (collectively "WILEY"). By clicking "accept" in connection with completing this licensing transaction, you agree that the following terms and conditions apply to this transaction (along with the billing and payment terms and conditions established by the Copyright Clearance Center Inc., ("CCC's Billing and Payment terms and conditions"), at the time that you opened your RightsLink account (these are available at any time at http://myaccount.copyright.com).

Terms and Conditions

- The materials you have requested permission to reproduce or reuse (the "Wiley Materials") are protected by copyright.
- You are hereby granted a personal, non-exclusive, non-sub licensable (on a stand-alone basis), non-transferable, worldwide, limited license to reproduce the Wiley Materials for the purpose specified in the licensing process. This license, **and any CONTENT (PDF or image file) purchased as part of your order,** is for a one-time use only and limited to any maximum distribution number specified in the license. The first instance of republication or reuse granted by this license must be completed within two years of the date of the grant of this license (although copies prepared before the end date may be distributed thereafter). The Wiley Materials shall not be used in any other manner or for any other purpose, beyond what is granted in the license. Permission is granted subject to an appropriate acknowledgement given to the author, title of the material/book/journal and the publisher. You shall also duplicate the copyright notice that appears in the Wiley publication in your use of the Wiley Material. Permission is also granted on the understanding that nowhere in the text is a previously published source acknowledged for all or part of this Wiley Material. Any third party content is expressly excluded from this permission.
- With respect to the Wiley Materials, all rights are reserved. Except as expressly granted by the terms of the license, no part of the Wiley Materials may be copied, modified, adapted (except for minor reformatting required by the new Publication), translated, reproduced, transferred or distributed, in any form or by any means, and no derivative works may be made based on the Wiley Materials without the prior permission of the respective copyright owner.**For STM Signatory Publishers clearing permission under the terms of the STM Permissions Guidelines only, the terms of the license are extended to include subsequent editions and for editions in other languages, provided such editions are for the work as a whole in situ and does not involve the separate exploitation of the permitted figures or extracts,** You may not alter, remove or suppress in any manner any copyright, trademark or other notices displayed by the Wiley Materials. You may not license, rent, sell, loan, lease, pledge, offer as security, transfer or assign the Wiley Materials on a stand-alone basis, or any of the rights granted to you hereunder to any other person.

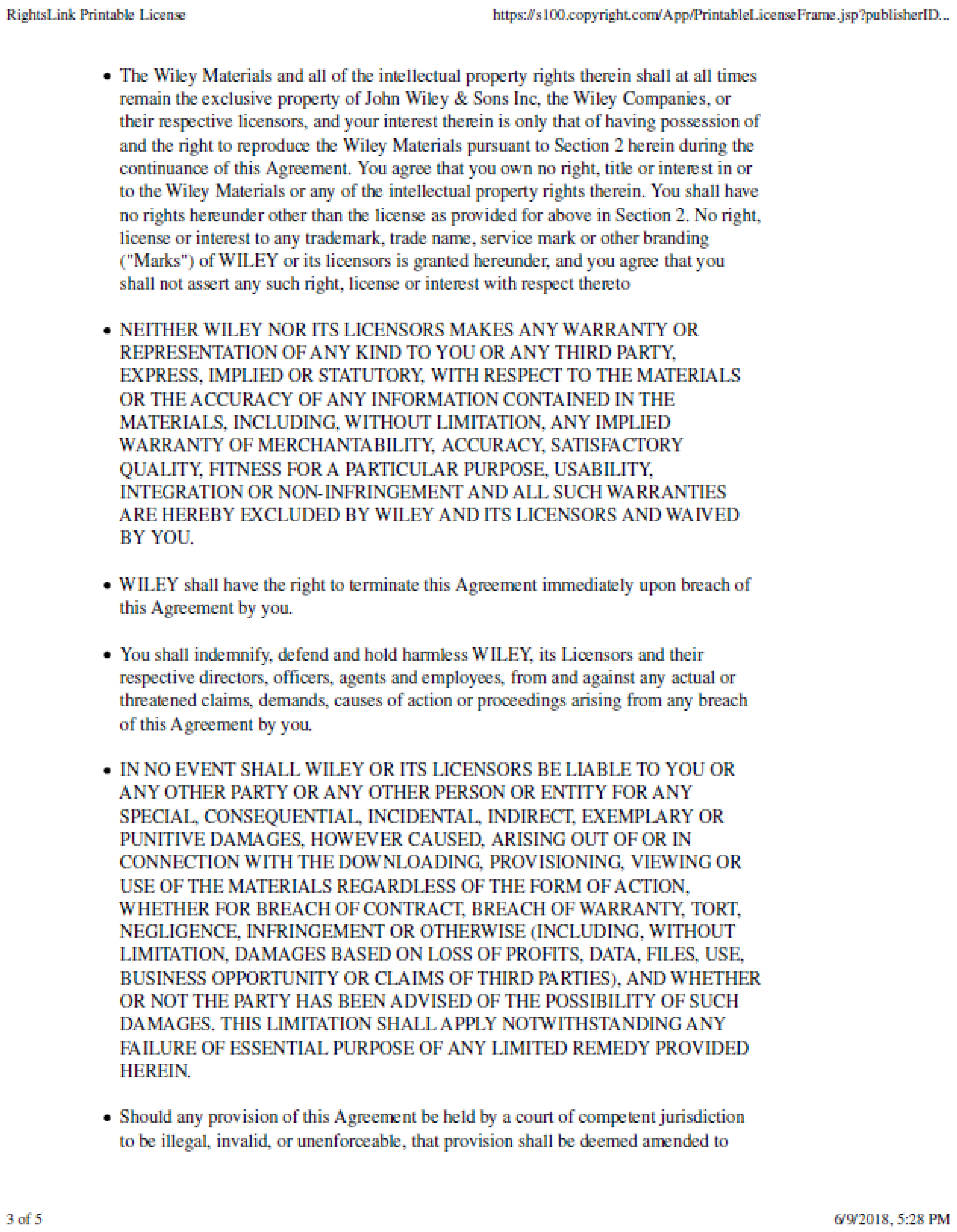

- The Wiley Materials and all of the intellectual property rights therein shall at all times remain the exclusive property of John Wiley & Sons Inc, the Wiley Companies, or their respective licensors, and your interest therein is only that of having possession of and the right to reproduce the Wiley Materials pursuant to Section 2 herein during the continuance of this Agreement. You agree that you own no right, title or interest in or to the Wiley Materials or any of the intellectual property rights therein. You shall have no rights hereunder other than the license as provided for above in Section 2. No right, license or interest to any trademark, trade name, service mark or other branding ("Marks") of WILEY or its licensors is granted hereunder, and you agree that you shall not assert any such right, license or interest with respect thereto

- NEITHER WILEY NOR ITS LICENSORS MAKES ANY WARRANTY OR REPRESENTATION OF ANY KIND TO YOU OR ANY THIRD PARTY, EXPRESS, IMPLIED OR STATUTORY, WITH RESPECT TO THE MATERIALS OR THE ACCURACY OF ANY INFORMATION CONTAINED IN THE MATERIALS, INCLUDING, WITHOUT LIMITATION, ANY IMPLIED WARRANTY OF MERCHANTABILITY, ACCURACY, SATISFACTORY QUALITY, FITNESS FOR A PARTICULAR PURPOSE, USABILITY, INTEGRATION OR NON-INFRINGEMENT AND ALL SUCH WARRANTIES ARE HEREBY EXCLUDED BY WILEY AND ITS LICENSORS AND WAIVED BY YOU.

- WILEY shall have the right to terminate this Agreement immediately upon breach of this Agreement by you.

- You shall indemnify, defend and hold harmless WILEY, its Licensors and their respective directors, officers, agents and employees, from and against any actual or threatened claims, demands, causes of action or proceedings arising from any breach of this Agreement by you.

- IN NO EVENT SHALL WILEY OR ITS LICENSORS BE LIABLE TO YOU OR ANY OTHER PARTY OR ANY OTHER PERSON OR ENTITY FOR ANY SPECIAL, CONSEQUENTIAL, INCIDENTAL, INDIRECT, EXEMPLARY OR PUNITIVE DAMAGES, HOWEVER CAUSED, ARISING OUT OF OR IN CONNECTION WITH THE DOWNLOADING, PROVISIONING, VIEWING OR USE OF THE MATERIALS REGARDLESS OF THE FORM OF ACTION, WHETHER FOR BREACH OF CONTRACT, BREACH OF WARRANTY, TORT, NEGLIGENCE, INFRINGEMENT OR OTHERWISE (INCLUDING, WITHOUT LIMITATION, DAMAGES BASED ON LOSS OF PROFITS, DATA, FILES, USE, BUSINESS OPPORTUNITY OR CLAIMS OF THIRD PARTIES), AND WHETHER OR NOT THE PARTY HAS BEEN ADVISED OF THE POSSIBILITY OF SUCH DAMAGES. THIS LIMITATION SHALL APPLY NOTWITHSTANDING ANY FAILURE OF ESSENTIAL PURPOSE OF ANY LIMITED REMEDY PROVIDED HEREIN.

- Should any provision of this Agreement be held by a court of competent jurisdiction to be illegal, invalid, or unenforceable, that provision shall be deemed amended to

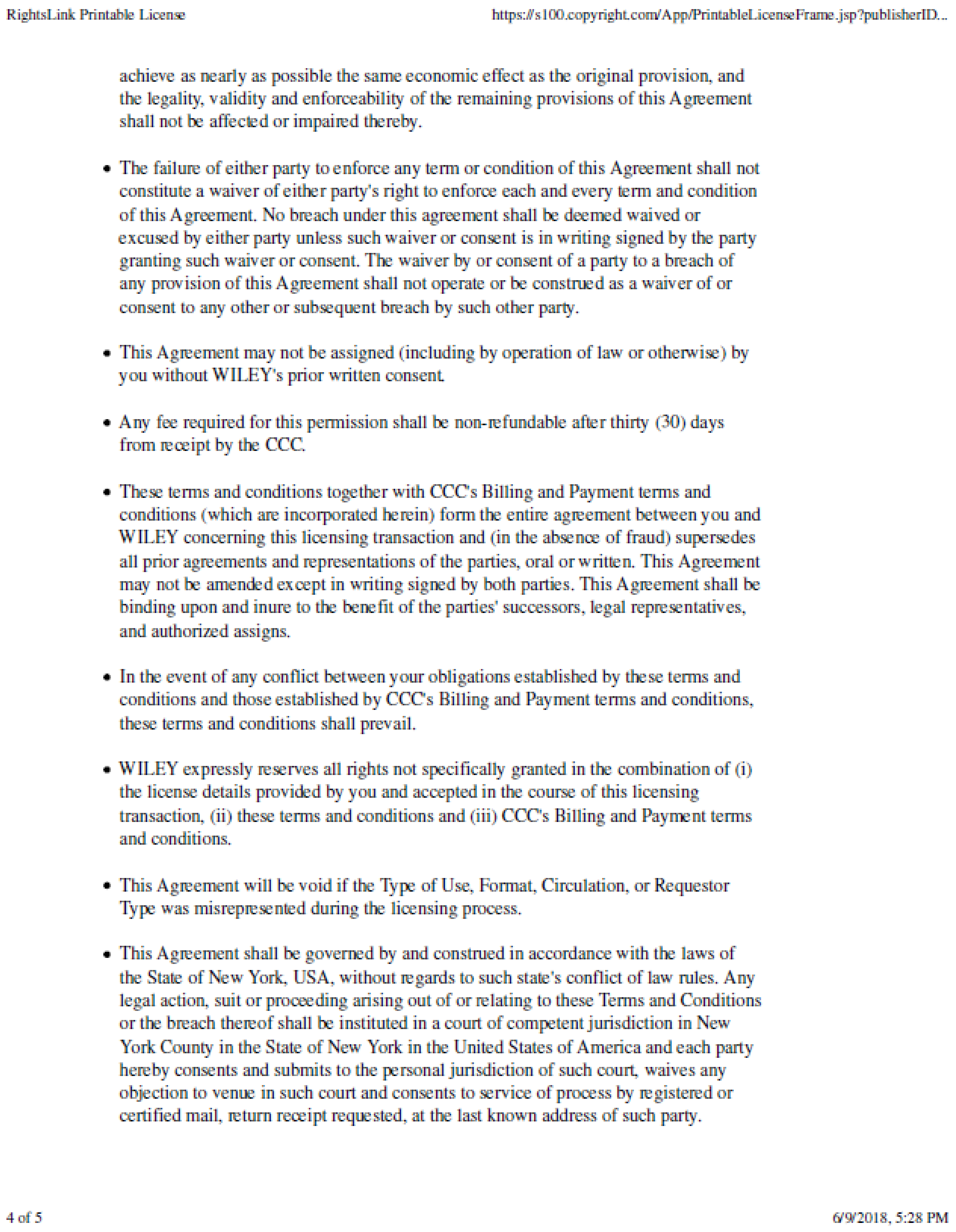

achieve as nearly as possible the same economic effect as the original provision, and the legality, validity and enforceability of the remaining provisions of this Agreement shall not be affected or impaired thereby.

- The failure of either party to enforce any term or condition of this Agreement shall not constitute a waiver of either party's right to enforce each and every term and condition of this Agreement. No breach under this agreement shall be deemed waived or excused by either party unless such waiver or consent is in writing signed by the party granting such waiver or consent. The waiver by or consent of a party to a breach of any provision of this Agreement shall not operate or be construed as a waiver of or consent to any other or subsequent breach by such other party.

- This Agreement may not be assigned (including by operation of law or otherwise) by you without WILEY's prior written consent.

- Any fee required for this permission shall be non-refundable after thirty (30) days from receipt by the CCC.

- These terms and conditions together with CCC's Billing and Payment terms and conditions (which are incorporated herein) form the entire agreement between you and WILEY concerning this licensing transaction and (in the absence of fraud) supersedes all prior agreements and representations of the parties, oral or written. This Agreement may not be amended except in writing signed by both parties. This Agreement shall be binding upon and inure to the benefit of the parties' successors, legal representatives, and authorized assigns.

- In the event of any conflict between your obligations established by these terms and conditions and those established by CCC's Billing and Payment terms and conditions, these terms and conditions shall prevail.

- WILEY expressly reserves all rights not specifically granted in the combination of (i) the license details provided by you and accepted in the course of this licensing transaction, (ii) these terms and conditions and (iii) CCC's Billing and Payment terms and conditions.

- This Agreement will be void if the Type of Use, Format, Circulation, or Requestor Type was misrepresented during the licensing process.

- This Agreement shall be governed by and construed in accordance with the laws of the State of New York, USA, without regards to such state's conflict of law rules. Any legal action, suit or proceeding arising out of or relating to these Terms and Conditions or the breach thereof shall be instituted in a court of competent jurisdiction in New York County in the State of New York in the United States of America and each party hereby consents and submits to the personal jurisdiction of such court, waives any objection to venue in such court and consents to service of process by registered or certified mail, return receipt requested, at the last known address of such party.

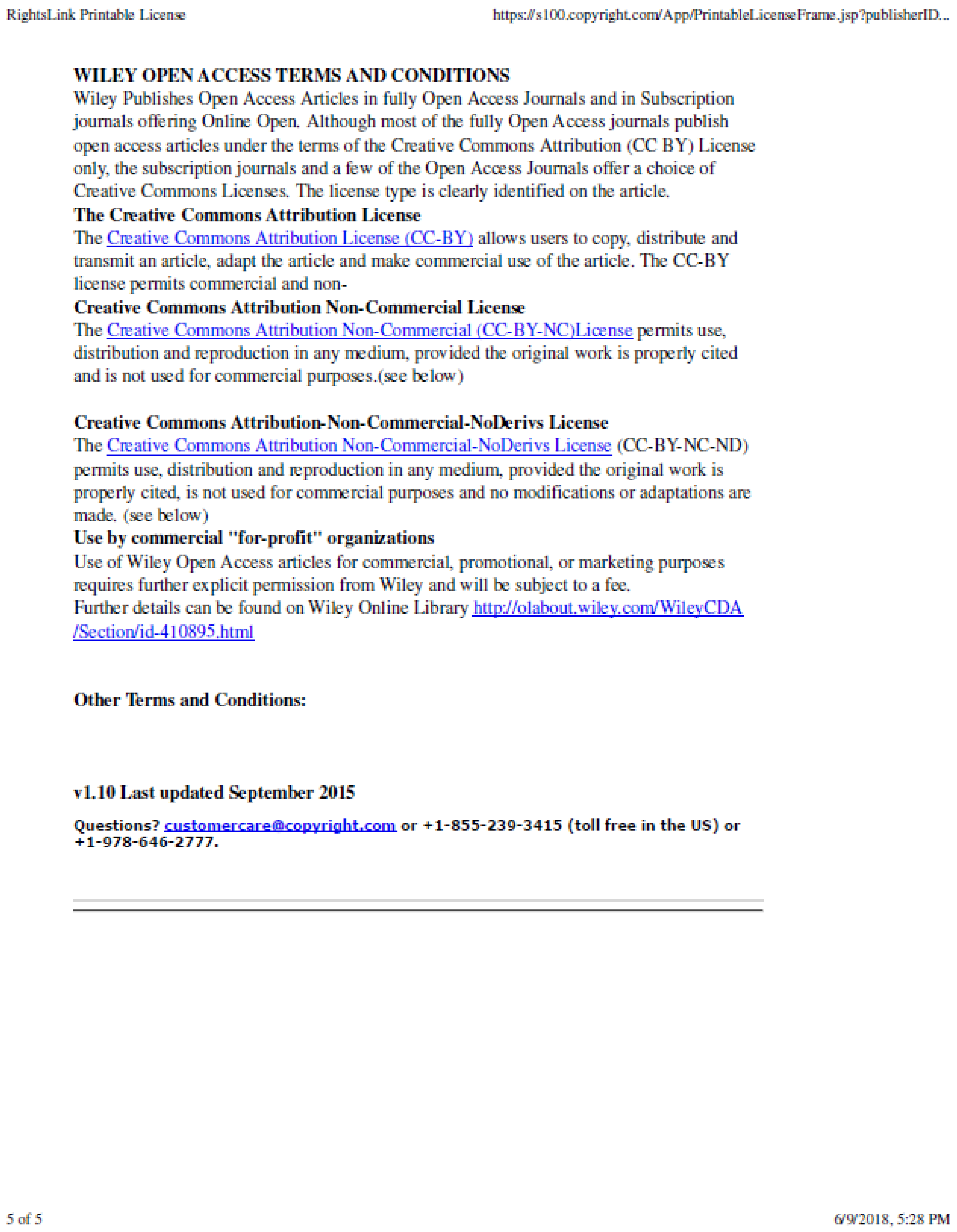

RightsLink Printable License https://s100.copyright.com/App/PrintableLicenseFrame.jsp?publisherID...

WILEY OPEN ACCESS TERMS AND CONDITIONS

Wiley Publishes Open Access Articles in fully Open Access Journals and in Subscription journals offering Online Open. Although most of the fully Open Access journals publish open access articles under the terms of the Creative Commons Attribution (CC BY) License only, the subscription journals and a few of the Open Access Journals offer a choice of Creative Commons Licenses. The license type is clearly identified on the article.

The Creative Commons Attribution License

The Creative Commons Attribution License (CC-BY) allows users to copy, distribute and transmit an article, adapt the article and make commercial use of the article. The CC-BY license permits commercial and non-

Creative Commons Attribution Non-Commercial License

The Creative Commons Attribution Non-Commercial (CC-BY-NC)License permits use, distribution and reproduction in any medium, provided the original work is properly cited and is not used for commercial purposes.(see below)

Creative Commons Attribution-Non-Commercial-NoDerivs License

The Creative Commons Attribution Non-Commercial-NoDerivs License (CC-BY-NC-ND) permits use, distribution and reproduction in any medium, provided the original work is properly cited, is not used for commercial purposes and no modifications or adaptations are made. (see below)

Use by commercial "for-profit" organizations

Use of Wiley Open Access articles for commercial, promotional, or marketing purposes requires further explicit permission from Wiley and will be subject to a fee.

Further details can be found on Wiley Online Library http://olabout.wiley.com/WileyCDA/Section/id-410895.html

Other Terms and Conditions:

v1.10 Last updated September 2015

Questions? customercare@copyright.com or +1-855-239-3415 (toll free in the US) or +1-978-646-2777.

5 of 5 6/9/2018, 5:28 PM

A.2 Copyright waiver for Figure 2-21 & Figure 5-3

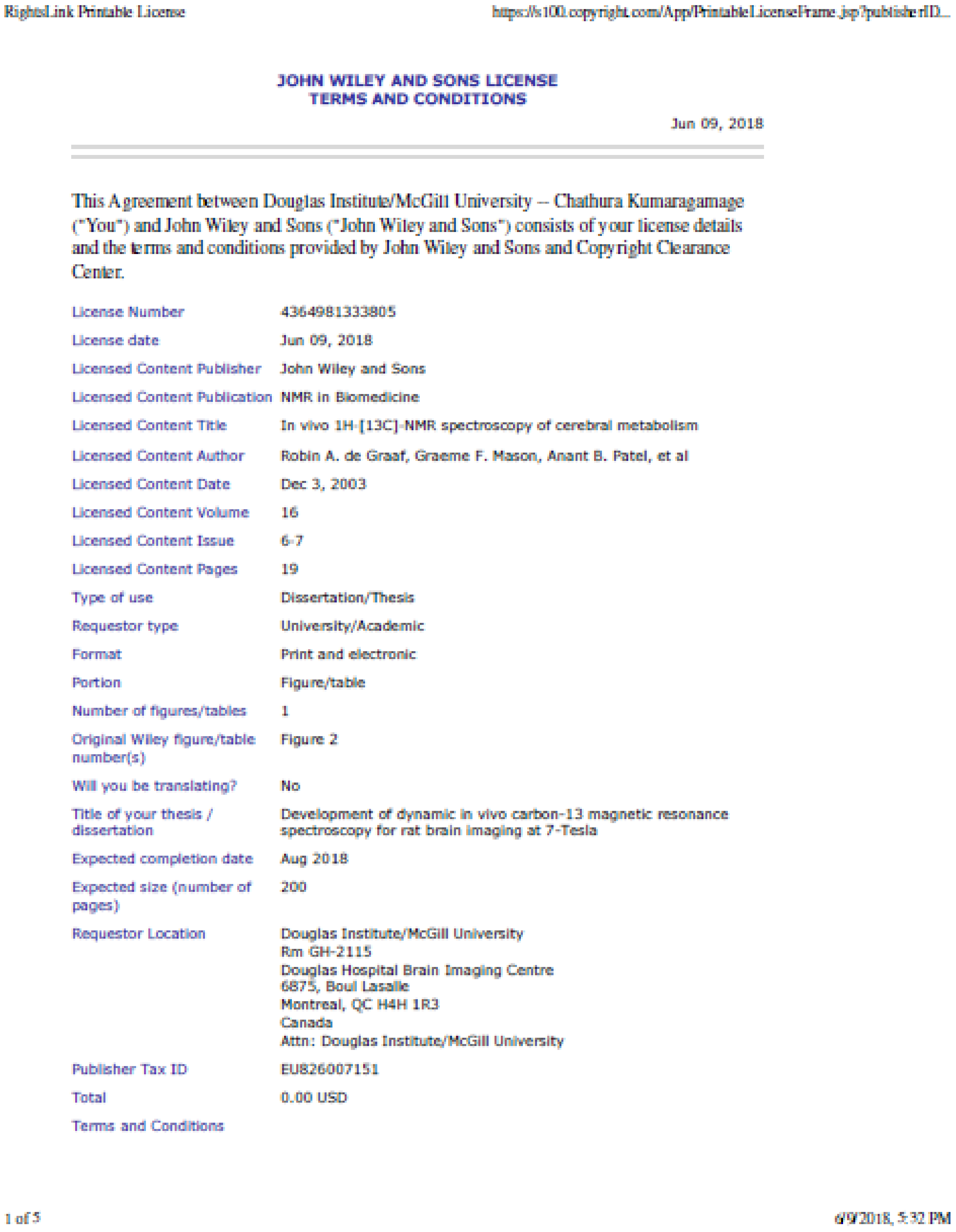

RightsLink Printable License https://s100.copyright.com/App/PrintableLicenseFrame.jsp?publisherID...

JOHN WILEY AND SONS LICENSE
TERMS AND CONDITIONS

Jun 09, 2018

This Agreement between Douglas Institute/McGill University -- Chathura Kumaragamage ("You") and John Wiley and Sons ("John Wiley and Sons") consists of your license details and the terms and conditions provided by John Wiley and Sons and Copyright Clearance Center.

License Number	4364981333805
License date	Jun 09, 2018
Licensed Content Publisher	John Wiley and Sons
Licensed Content Publication	NMR in Biomedicine
Licensed Content Title	In vivo 1H-[13C]-NMR spectroscopy of cerebral metabolism
Licensed Content Author	Robin A. de Graaf, Graeme F. Mason, Anant B. Patel, et al
Licensed Content Date	Dec 3, 2003
Licensed Content Volume	16
Licensed Content Issue	6-7
Licensed Content Pages	19
Type of use	Dissertation/Thesis
Requestor type	University/Academic
Format	Print and electronic
Portion	Figure/table
Number of figures/tables	1
Original Wiley figure/table number(s)	Figure 2
Will you be translating?	No
Title of your thesis / dissertation	Development of dynamic in vivo carbon-13 magnetic resonance spectroscopy for rat brain imaging at 7-Tesla
Expected completion date	Aug 2018
Expected size (number of pages)	200
Requestor Location	Douglas Institute/McGill University Rm GH-2115 Douglas Hospital Brain Imaging Centre 6875, Boul Lasalle Montreal, QC H4H 1R3 Canada Attn: Douglas Institute/McGill University
Publisher Tax ID	EU826007151
Total	0.00 USD
Terms and Conditions	

1 of 5 6/9/2018, 5:32 PM

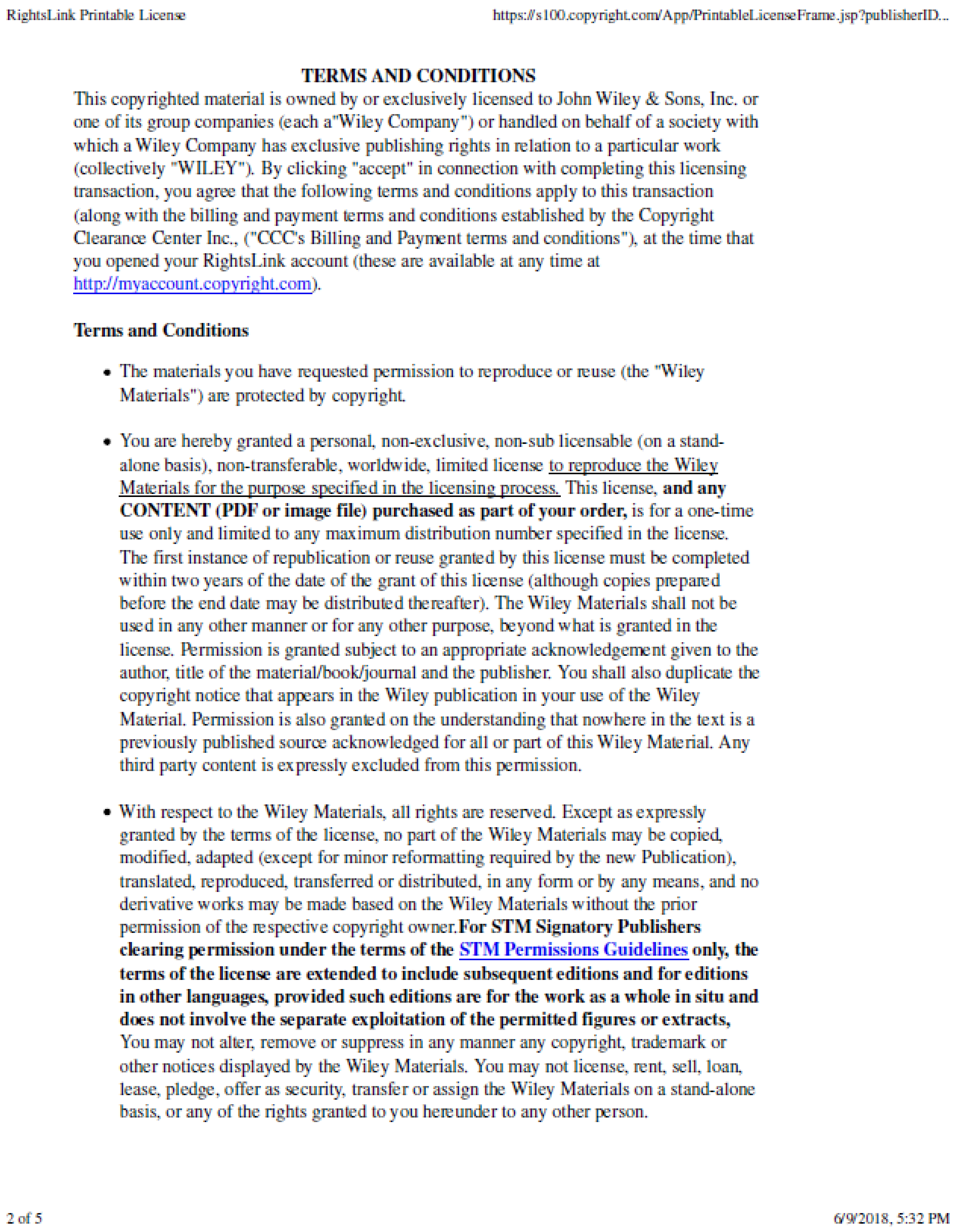

TERMS AND CONDITIONS

This copyrighted material is owned by or exclusively licensed to John Wiley & Sons, Inc. or one of its group companies (each a"Wiley Company") or handled on behalf of a society with which a Wiley Company has exclusive publishing rights in relation to a particular work (collectively "WILEY"). By clicking "accept" in connection with completing this licensing transaction, you agree that the following terms and conditions apply to this transaction (along with the billing and payment terms and conditions established by the Copyright Clearance Center Inc., ("CCC's Billing and Payment terms and conditions"), at the time that you opened your RightsLink account (these are available at any time at http://myaccount.copyright.com).

Terms and Conditions

- The materials you have requested permission to reproduce or reuse (the "Wiley Materials") are protected by copyright.

- You are hereby granted a personal, non-exclusive, non-sub licensable (on a stand-alone basis), non-transferable, worldwide, limited license to reproduce the Wiley Materials for the purpose specified in the licensing process. This license, **and any CONTENT (PDF or image file) purchased as part of your order,** is for a one-time use only and limited to any maximum distribution number specified in the license. The first instance of republication or reuse granted by this license must be completed within two years of the date of the grant of this license (although copies prepared before the end date may be distributed thereafter). The Wiley Materials shall not be used in any other manner or for any other purpose, beyond what is granted in the license. Permission is granted subject to an appropriate acknowledgement given to the author, title of the material/book/journal and the publisher. You shall also duplicate the copyright notice that appears in the Wiley publication in your use of the Wiley Material. Permission is also granted on the understanding that nowhere in the text is a previously published source acknowledged for all or part of this Wiley Material. Any third party content is expressly excluded from this permission.

- With respect to the Wiley Materials, all rights are reserved. Except as expressly granted by the terms of the license, no part of the Wiley Materials may be copied, modified, adapted (except for minor reformatting required by the new Publication), translated, reproduced, transferred or distributed, in any form or by any means, and no derivative works may be made based on the Wiley Materials without the prior permission of the respective copyright owner.**For STM Signatory Publishers clearing permission under the terms of the STM Permissions Guidelines only, the terms of the license are extended to include subsequent editions and for editions in other languages, provided such editions are for the work as a whole in situ and does not involve the separate exploitation of the permitted figures or extracts,** You may not alter, remove or suppress in any manner any copyright, trademark or other notices displayed by the Wiley Materials. You may not license, rent, sell, loan, lease, pledge, offer as security, transfer or assign the Wiley Materials on a stand-alone basis, or any of the rights granted to you hereunder to any other person.

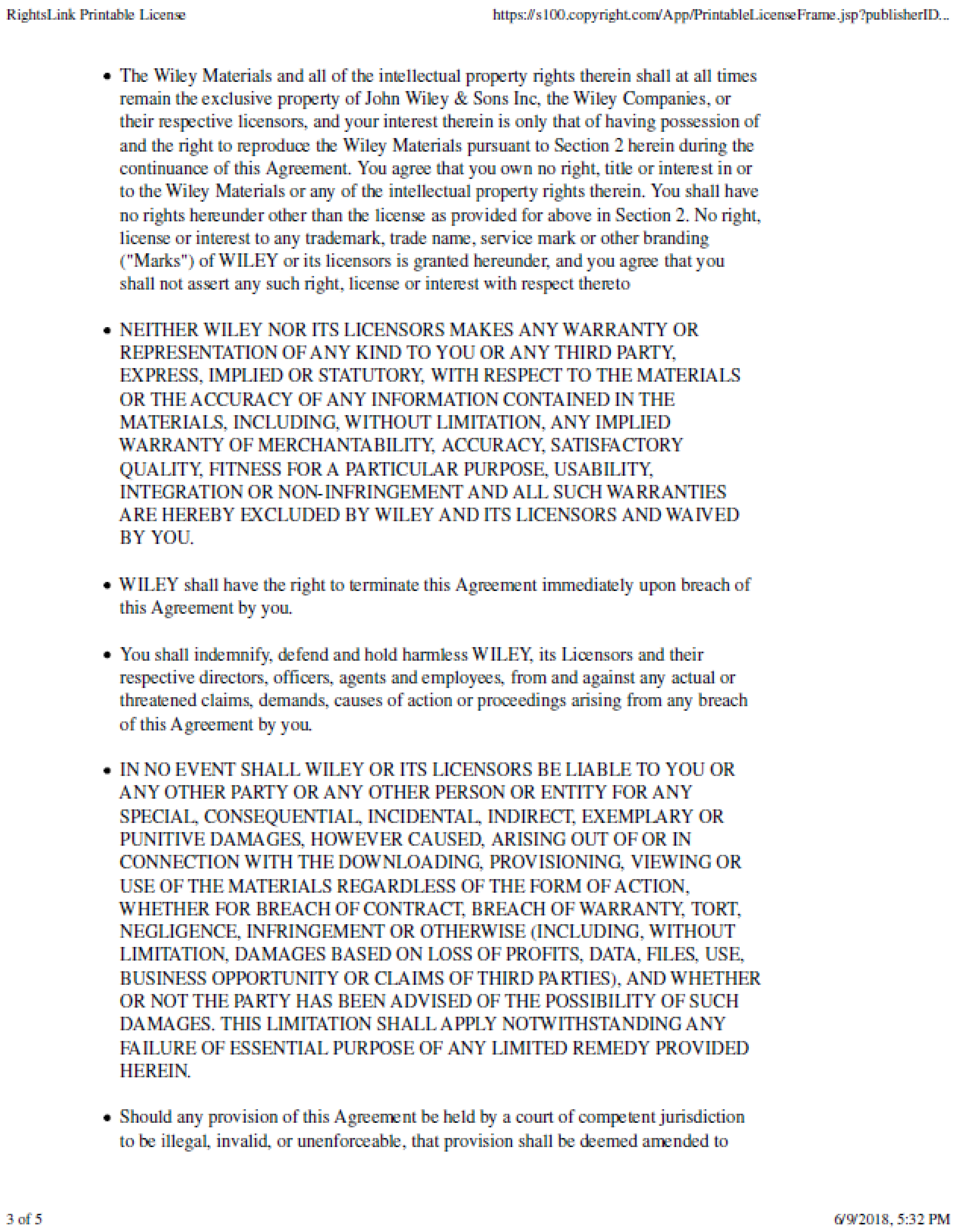

- The Wiley Materials and all of the intellectual property rights therein shall at all times remain the exclusive property of John Wiley & Sons Inc, the Wiley Companies, or their respective licensors, and your interest therein is only that of having possession of and the right to reproduce the Wiley Materials pursuant to Section 2 herein during the continuance of this Agreement. You agree that you own no right, title or interest in or to the Wiley Materials or any of the intellectual property rights therein. You shall have no rights hereunder other than the license as provided for above in Section 2. No right, license or interest to any trademark, trade name, service mark or other branding ("Marks") of WILEY or its licensors is granted hereunder, and you agree that you shall not assert any such right, license or interest with respect thereto

- NEITHER WILEY NOR ITS LICENSORS MAKES ANY WARRANTY OR REPRESENTATION OF ANY KIND TO YOU OR ANY THIRD PARTY, EXPRESS, IMPLIED OR STATUTORY, WITH RESPECT TO THE MATERIALS OR THE ACCURACY OF ANY INFORMATION CONTAINED IN THE MATERIALS, INCLUDING, WITHOUT LIMITATION, ANY IMPLIED WARRANTY OF MERCHANTABILITY, ACCURACY, SATISFACTORY QUALITY, FITNESS FOR A PARTICULAR PURPOSE, USABILITY, INTEGRATION OR NON-INFRINGEMENT AND ALL SUCH WARRANTIES ARE HEREBY EXCLUDED BY WILEY AND ITS LICENSORS AND WAIVED BY YOU.

- WILEY shall have the right to terminate this Agreement immediately upon breach of this Agreement by you.

- You shall indemnify, defend and hold harmless WILEY, its Licensors and their respective directors, officers, agents and employees, from and against any actual or threatened claims, demands, causes of action or proceedings arising from any breach of this Agreement by you.

- IN NO EVENT SHALL WILEY OR ITS LICENSORS BE LIABLE TO YOU OR ANY OTHER PARTY OR ANY OTHER PERSON OR ENTITY FOR ANY SPECIAL, CONSEQUENTIAL, INCIDENTAL, INDIRECT, EXEMPLARY OR PUNITIVE DAMAGES, HOWEVER CAUSED, ARISING OUT OF OR IN CONNECTION WITH THE DOWNLOADING, PROVISIONING, VIEWING OR USE OF THE MATERIALS REGARDLESS OF THE FORM OF ACTION, WHETHER FOR BREACH OF CONTRACT, BREACH OF WARRANTY, TORT, NEGLIGENCE, INFRINGEMENT OR OTHERWISE (INCLUDING, WITHOUT LIMITATION, DAMAGES BASED ON LOSS OF PROFITS, DATA, FILES, USE, BUSINESS OPPORTUNITY OR CLAIMS OF THIRD PARTIES), AND WHETHER OR NOT THE PARTY HAS BEEN ADVISED OF THE POSSIBILITY OF SUCH DAMAGES. THIS LIMITATION SHALL APPLY NOTWITHSTANDING ANY FAILURE OF ESSENTIAL PURPOSE OF ANY LIMITED REMEDY PROVIDED HEREIN.

- Should any provision of this Agreement be held by a court of competent jurisdiction to be illegal, invalid, or unenforceable, that provision shall be deemed amended to

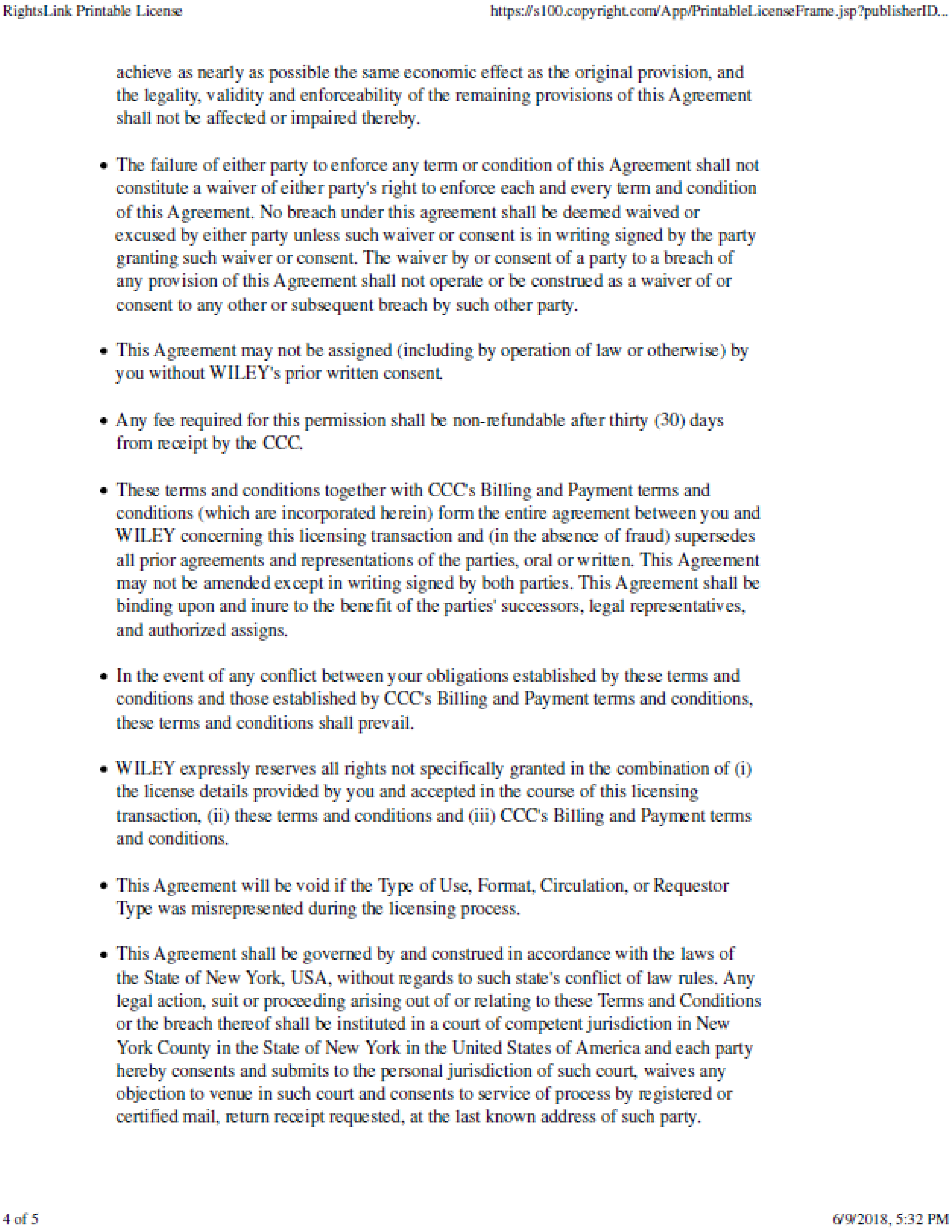

achieve as nearly as possible the same economic effect as the original provision, and the legality, validity and enforceability of the remaining provisions of this Agreement shall not be affected or impaired thereby.

- The failure of either party to enforce any term or condition of this Agreement shall not constitute a waiver of either party's right to enforce each and every term and condition of this Agreement. No breach under this agreement shall be deemed waived or excused by either party unless such waiver or consent is in writing signed by the party granting such waiver or consent. The waiver by or consent of a party to a breach of any provision of this Agreement shall not operate or be construed as a waiver of or consent to any other or subsequent breach by such other party.

- This Agreement may not be assigned (including by operation of law or otherwise) by you without WILEY's prior written consent.

- Any fee required for this permission shall be non-refundable after thirty (30) days from receipt by the CCC.

- These terms and conditions together with CCC's Billing and Payment terms and conditions (which are incorporated herein) form the entire agreement between you and WILEY concerning this licensing transaction and (in the absence of fraud) supersedes all prior agreements and representations of the parties, oral or written. This Agreement may not be amended except in writing signed by both parties. This Agreement shall be binding upon and inure to the benefit of the parties' successors, legal representatives, and authorized assigns.

- In the event of any conflict between your obligations established by these terms and conditions and those established by CCC's Billing and Payment terms and conditions, these terms and conditions shall prevail.

- WILEY expressly reserves all rights not specifically granted in the combination of (i) the license details provided by you and accepted in the course of this licensing transaction, (ii) these terms and conditions and (iii) CCC's Billing and Payment terms and conditions.

- This Agreement will be void if the Type of Use, Format, Circulation, or Requestor Type was misrepresented during the licensing process.

- This Agreement shall be governed by and construed in accordance with the laws of the State of New York, USA, without regards to such state's conflict of law rules. Any legal action, suit or proceeding arising out of or relating to these Terms and Conditions or the breach thereof shall be instituted in a court of competent jurisdiction in New York County in the State of New York in the United States of America and each party hereby consents and submits to the personal jurisdiction of such court, waives any objection to venue in such court and consents to service of process by registered or certified mail, return receipt requested, at the last known address of such party.

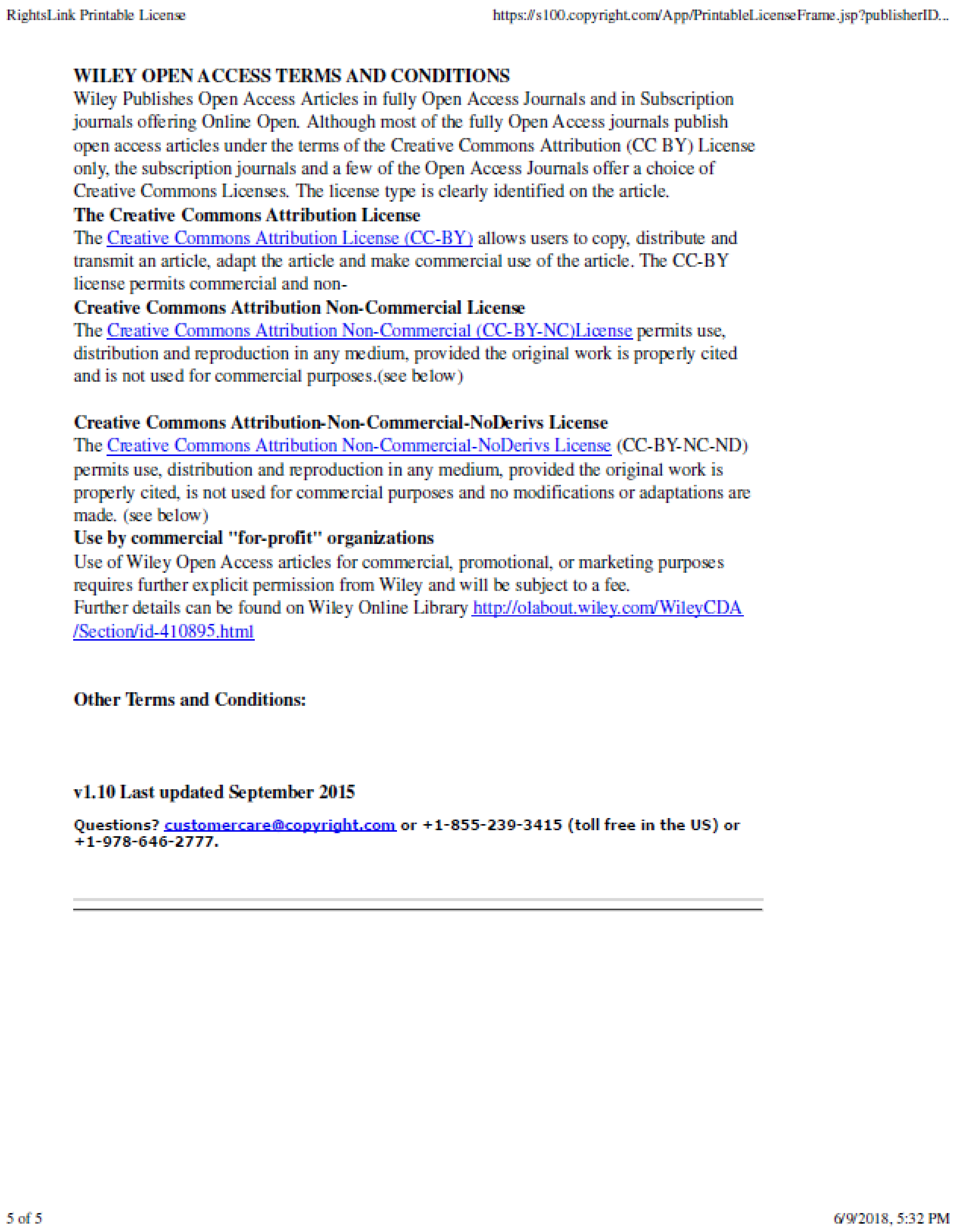

WILEY OPEN ACCESS TERMS AND CONDITIONS

Wiley Publishes Open Access Articles in fully Open Access Journals and in Subscription journals offering Online Open. Although most of the fully Open Access journals publish open access articles under the terms of the Creative Commons Attribution (CC BY) License only, the subscription journals and a few of the Open Access Journals offer a choice of Creative Commons Licenses. The license type is clearly identified on the article.

The Creative Commons Attribution License

The Creative Commons Attribution License (CC-BY) allows users to copy, distribute and transmit an article, adapt the article and make commercial use of the article. The CC-BY license permits commercial and non-

Creative Commons Attribution Non-Commercial License

The Creative Commons Attribution Non-Commercial (CC-BY-NC)License permits use, distribution and reproduction in any medium, provided the original work is properly cited and is not used for commercial purposes.(see below)

Creative Commons Attribution-Non-Commercial-NoDerivs License

The Creative Commons Attribution Non-Commercial-NoDerivs License (CC-BY-NC-ND) permits use, distribution and reproduction in any medium, provided the original work is properly cited, is not used for commercial purposes and no modifications or adaptations are made. (see below)

Use by commercial "for-profit" organizations

Use of Wiley Open Access articles for commercial, promotional, or marketing purposes requires further explicit permission from Wiley and will be subject to a fee.

Further details can be found on Wiley Online Library http://olabout.wiley.com/WileyCDA/Section/id-410895.html

Other Terms and Conditions:

v1.10 Last updated September 2015

Questions? customercare@copyright.com or +1-855-239-3415 (toll free in the US) or +1-978-646-2777.

A.3 Copyright waiver for Figure 5-4

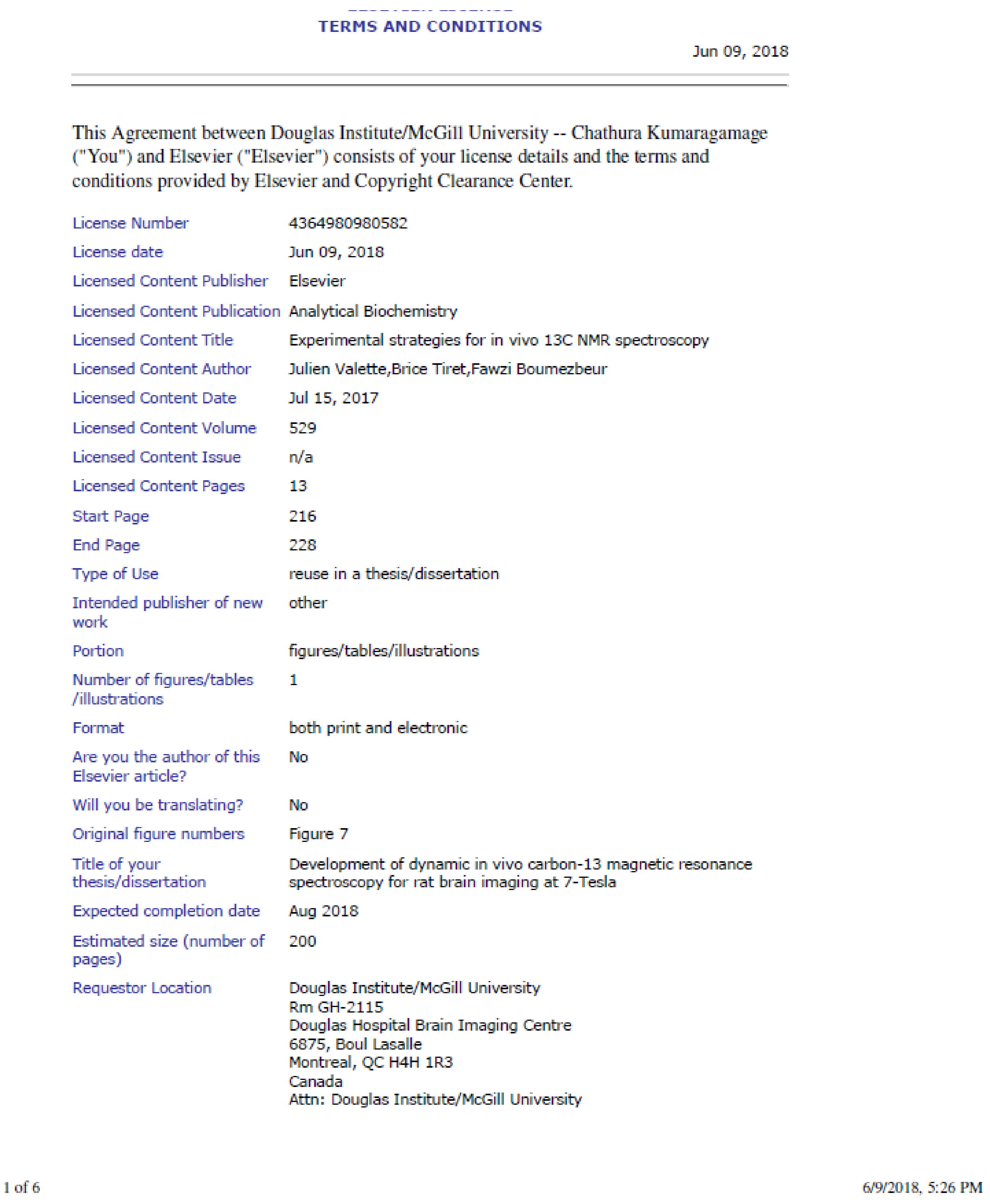

TERMS AND CONDITIONS

Jun 09, 2018

This Agreement between Douglas Institute/McGill University -- Chathura Kumaragamage ("You") and Elsevier ("Elsevier") consists of your license details and the terms and conditions provided by Elsevier and Copyright Clearance Center.

License Number	4364980980582
License date	Jun 09, 2018
Licensed Content Publisher	Elsevier
Licensed Content Publication	Analytical Biochemistry
Licensed Content Title	Experimental strategies for in vivo 13C NMR spectroscopy
Licensed Content Author	Julien Valette,Brice Tiret,Fawzi Boumezbeur
Licensed Content Date	Jul 15, 2017
Licensed Content Volume	529
Licensed Content Issue	n/a
Licensed Content Pages	13
Start Page	216
End Page	228
Type of Use	reuse in a thesis/dissertation
Intended publisher of new work	other
Portion	figures/tables/illustrations
Number of figures/tables /illustrations	1
Format	both print and electronic
Are you the author of this Elsevier article?	No
Will you be translating?	No
Original figure numbers	Figure 7
Title of your thesis/dissertation	Development of dynamic in vivo carbon-13 magnetic resonance spectroscopy for rat brain imaging at 7-Tesla
Expected completion date	Aug 2018
Estimated size (number of pages)	200
Requestor Location	Douglas Institute/McGill University Rm GH-2115 Douglas Hospital Brain Imaging Centre 6875, Boul Lasalle Montreal, QC H4H 1R3 Canada Attn: Douglas Institute/McGill University

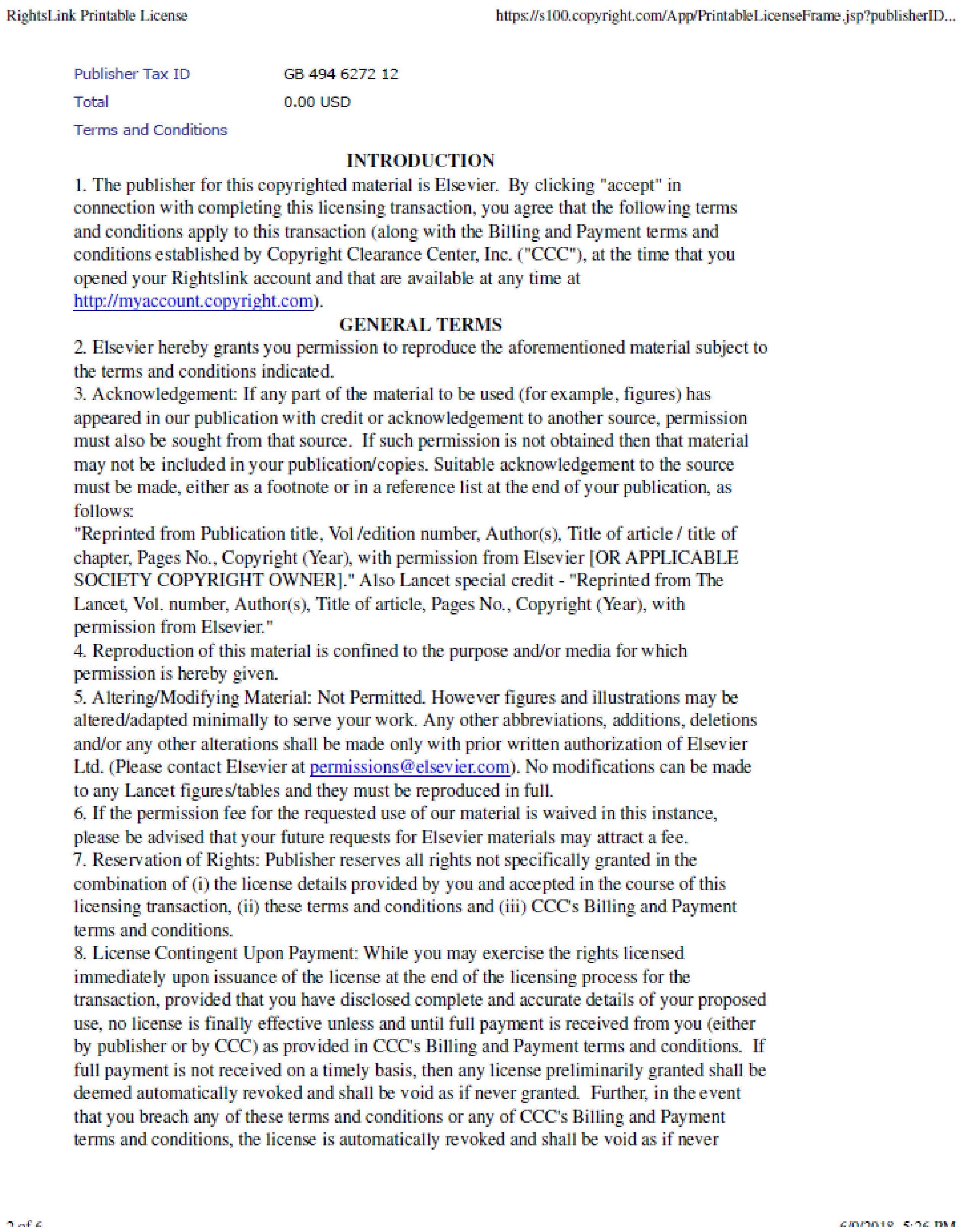

RightsLink Printable License https://s100.copyright.com/App/PrintableLicenseFrame.jsp?publisherID...

Publisher Tax ID	GB 494 6272 12
Total	0.00 USD

Terms and Conditions

INTRODUCTION

1. The publisher for this copyrighted material is Elsevier. By clicking "accept" in connection with completing this licensing transaction, you agree that the following terms and conditions apply to this transaction (along with the Billing and Payment terms and conditions established by Copyright Clearance Center, Inc. ("CCC"), at the time that you opened your Rightslink account and that are available at any time at http://myaccount.copyright.com).

GENERAL TERMS

2. Elsevier hereby grants you permission to reproduce the aforementioned material subject to the terms and conditions indicated.

3. Acknowledgement: If any part of the material to be used (for example, figures) has appeared in our publication with credit or acknowledgement to another source, permission must also be sought from that source. If such permission is not obtained then that material may not be included in your publication/copies. Suitable acknowledgement to the source must be made, either as a footnote or in a reference list at the end of your publication, as follows:

"Reprinted from Publication title, Vol /edition number, Author(s), Title of article / title of chapter, Pages No., Copyright (Year), with permission from Elsevier [OR APPLICABLE SOCIETY COPYRIGHT OWNER]." Also Lancet special credit - "Reprinted from The Lancet, Vol. number, Author(s), Title of article, Pages No., Copyright (Year), with permission from Elsevier."

4. Reproduction of this material is confined to the purpose and/or media for which permission is hereby given.

5. Altering/Modifying Material: Not Permitted. However figures and illustrations may be altered/adapted minimally to serve your work. Any other abbreviations, additions, deletions and/or any other alterations shall be made only with prior written authorization of Elsevier Ltd. (Please contact Elsevier at permissions@elsevier.com). No modifications can be made to any Lancet figures/tables and they must be reproduced in full.

6. If the permission fee for the requested use of our material is waived in this instance, please be advised that your future requests for Elsevier materials may attract a fee.

7. Reservation of Rights: Publisher reserves all rights not specifically granted in the combination of (i) the license details provided by you and accepted in the course of this licensing transaction, (ii) these terms and conditions and (iii) CCC's Billing and Payment terms and conditions.

8. License Contingent Upon Payment: While you may exercise the rights licensed immediately upon issuance of the license at the end of the licensing process for the transaction, provided that you have disclosed complete and accurate details of your proposed use, no license is finally effective unless and until full payment is received from you (either by publisher or by CCC) as provided in CCC's Billing and Payment terms and conditions. If full payment is not received on a timely basis, then any license preliminarily granted shall be deemed automatically revoked and shall be void as if never granted. Further, in the event that you breach any of these terms and conditions or any of CCC's Billing and Payment terms and conditions, the license is automatically revoked and shall be void as if never

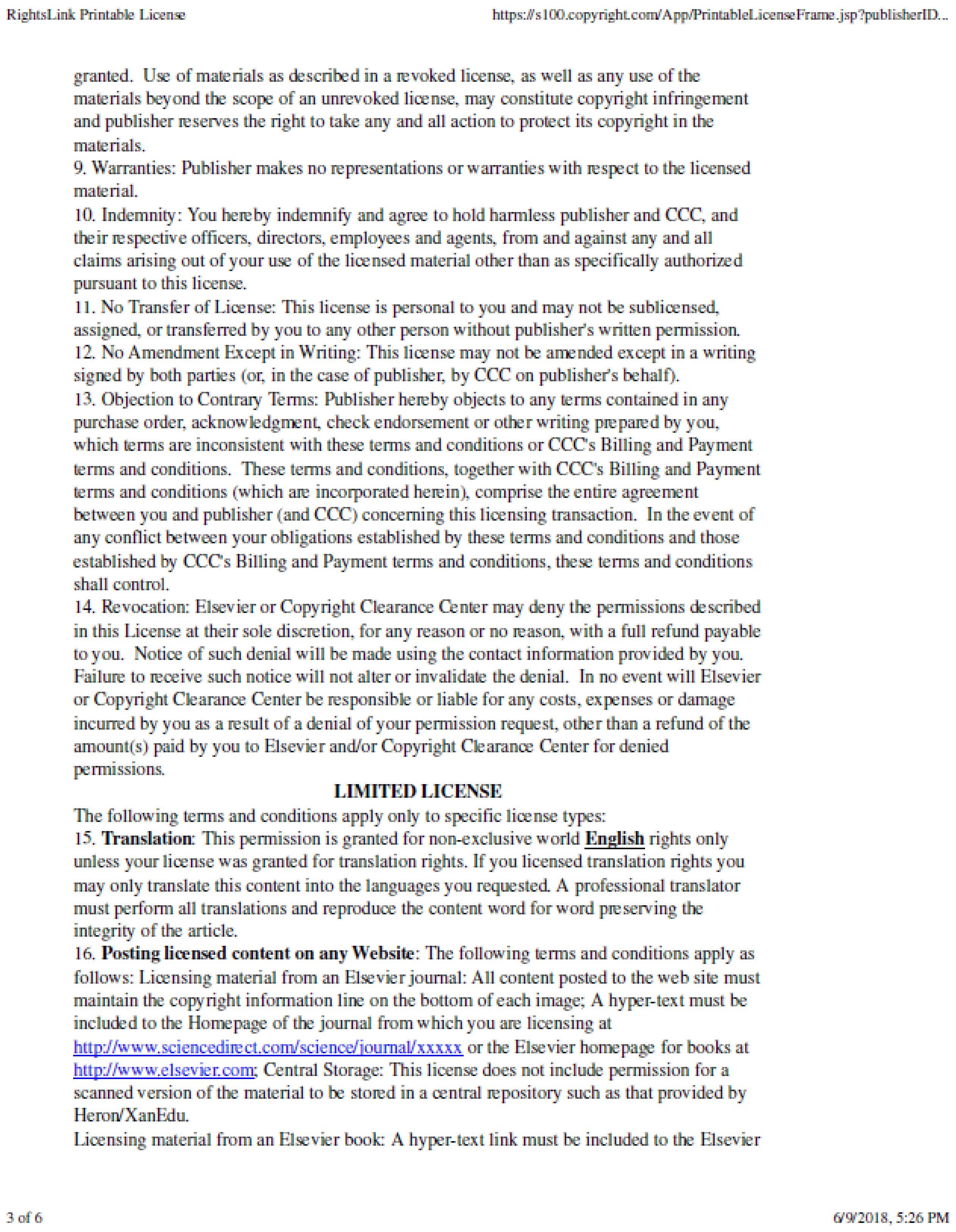

granted. Use of materials as described in a revoked license, as well as any use of the materials beyond the scope of an unrevoked license, may constitute copyright infringement and publisher reserves the right to take any and all action to protect its copyright in the materials.
9. Warranties: Publisher makes no representations or warranties with respect to the licensed material.
10. Indemnity: You hereby indemnify and agree to hold harmless publisher and CCC, and their respective officers, directors, employees and agents, from and against any and all claims arising out of your use of the licensed material other than as specifically authorized pursuant to this license.
11. No Transfer of License: This license is personal to you and may not be sublicensed, assigned, or transferred by you to any other person without publisher's written permission.
12. No Amendment Except in Writing: This license may not be amended except in a writing signed by both parties (or, in the case of publisher, by CCC on publisher's behalf).
13. Objection to Contrary Terms: Publisher hereby objects to any terms contained in any purchase order, acknowledgment, check endorsement or other writing prepared by you, which terms are inconsistent with these terms and conditions or CCC's Billing and Payment terms and conditions. These terms and conditions, together with CCC's Billing and Payment terms and conditions (which are incorporated herein), comprise the entire agreement between you and publisher (and CCC) concerning this licensing transaction. In the event of any conflict between your obligations established by these terms and conditions and those established by CCC's Billing and Payment terms and conditions, these terms and conditions shall control.
14. Revocation: Elsevier or Copyright Clearance Center may deny the permissions described in this License at their sole discretion, for any reason or no reason, with a full refund payable to you. Notice of such denial will be made using the contact information provided by you. Failure to receive such notice will not alter or invalidate the denial. In no event will Elsevier or Copyright Clearance Center be responsible or liable for any costs, expenses or damage incurred by you as a result of a denial of your permission request, other than a refund of the amount(s) paid by you to Elsevier and/or Copyright Clearance Center for denied permissions.

LIMITED LICENSE

The following terms and conditions apply only to specific license types:
15. **Translation**: This permission is granted for non-exclusive world **English** rights only unless your license was granted for translation rights. If you licensed translation rights you may only translate this content into the languages you requested. A professional translator must perform all translations and reproduce the content word for word preserving the integrity of the article.
16. **Posting licensed content on any Website**: The following terms and conditions apply as follows: Licensing material from an Elsevier journal: All content posted to the web site must maintain the copyright information line on the bottom of each image; A hyper-text must be included to the Homepage of the journal from which you are licensing at http://www.sciencedirect.com/science/journal/xxxxx or the Elsevier homepage for books at http://www.elsevier.com; Central Storage: This license does not include permission for a scanned version of the material to be stored in a central repository such as that provided by Heron/XanEdu.
Licensing material from an Elsevier book: A hyper-text link must be included to the Elsevier

homepage at http://www.elsevier.com . All content posted to the web site must maintain the copyright information line on the bottom of each image.

Posting licensed content on Electronic reserve: In addition to the above the following clauses are applicable: The web site must be password-protected and made available only to bona fide students registered on a relevant course. This permission is granted for 1 year only. You may obtain a new license for future website posting.
17. **For journal authors:** the following clauses are applicable in addition to the above:
Preprints:
A preprint is an author's own write-up of research results and analysis, it has not been peer-reviewed, nor has it had any other value added to it by a publisher (such as formatting, copyright, technical enhancement etc.).
Authors can share their preprints anywhere at any time. Preprints should not be added to or enhanced in any way in order to appear more like, or to substitute for, the final versions of articles however authors can update their preprints on arXiv or RePEc with their Accepted Author Manuscript (see below).
If accepted for publication, we encourage authors to link from the preprint to their formal publication via its DOI. Millions of researchers have access to the formal publications on ScienceDirect, and so links will help users to find, access, cite and use the best available version. Please note that Cell Press, The Lancet and some society-owned have different preprint policies. Information on these policies is available on the journal homepage.
Accepted Author Manuscripts: An accepted author manuscript is the manuscript of an article that has been accepted for publication and which typically includes author-incorporated changes suggested during submission, peer review and editor-author communications.
Authors can share their accepted author manuscript:

- immediately
  - via their non-commercial person homepage or blog
  - by updating a preprint in arXiv or RePEc with the accepted manuscript
  - via their research institute or institutional repository for internal institutional uses or as part of an invitation-only research collaboration work-group
  - directly by providing copies to their students or to research collaborators for their personal use
  - for private scholarly sharing as part of an invitation-only work group on commercial sites with which Elsevier has an agreement
- After the embargo period
  - via non-commercial hosting platforms such as their institutional repository
  - via commercial sites with which Elsevier has an agreement

In all cases accepted manuscripts should:

- link to the formal publication via its DOI
- bear a CC-BY-NC-ND license - this is easy to do
- if aggregated with other manuscripts, for example in a repository or other site, be shared in alignment with our hosting policy not be added to or enhanced in any way to appear more like, or to substitute for, the published journal article.

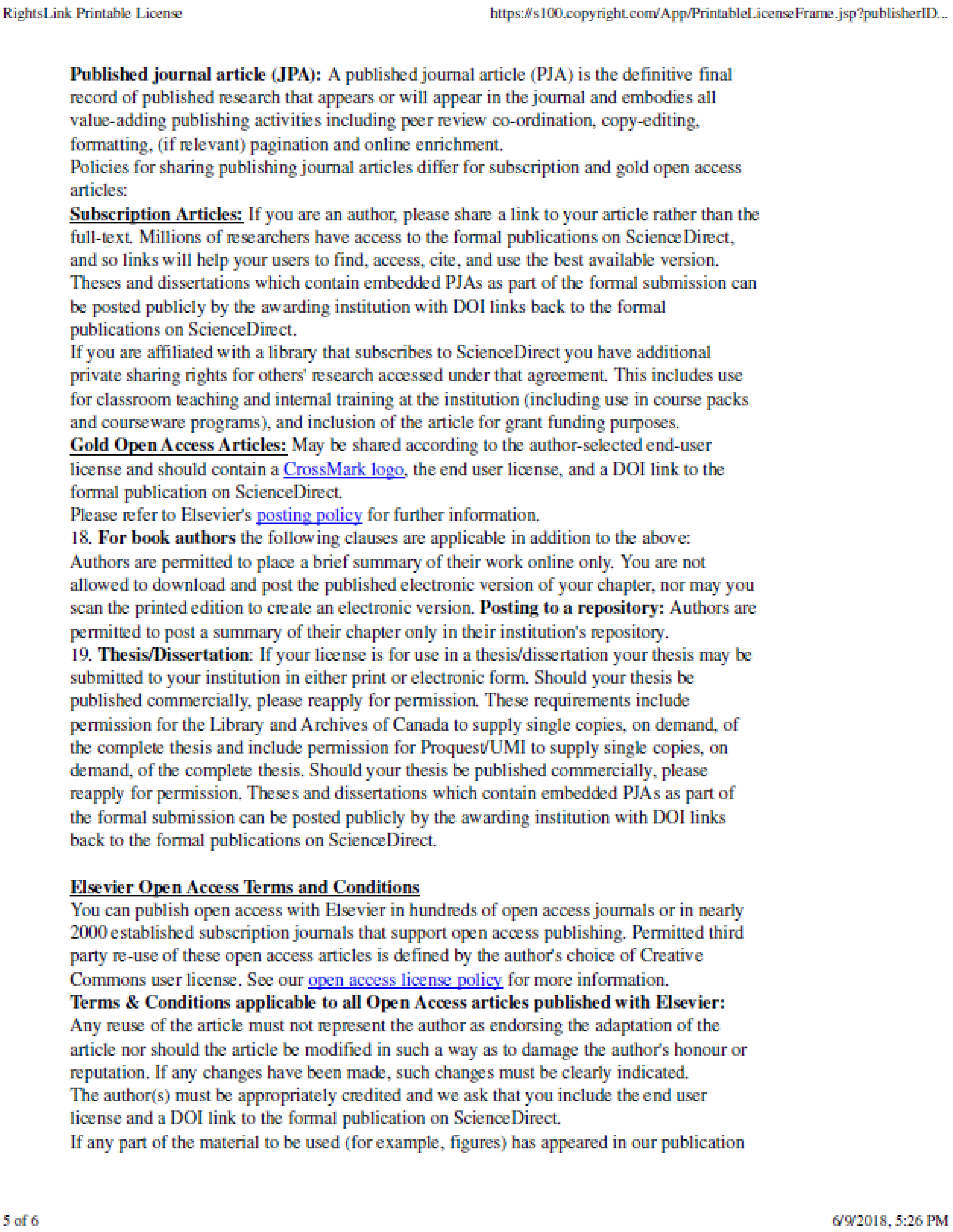

Published journal article (JPA): A published journal article (PJA) is the definitive final record of published research that appears or will appear in the journal and embodies all value-adding publishing activities including peer review co-ordination, copy-editing, formatting, (if relevant) pagination and online enrichment.

Policies for sharing publishing journal articles differ for subscription and gold open access articles:

Subscription Articles: If you are an author, please share a link to your article rather than the full-text. Millions of researchers have access to the formal publications on ScienceDirect, and so links will help your users to find, access, cite, and use the best available version.

Theses and dissertations which contain embedded PJAs as part of the formal submission can be posted publicly by the awarding institution with DOI links back to the formal publications on ScienceDirect.

If you are affiliated with a library that subscribes to ScienceDirect you have additional private sharing rights for others' research accessed under that agreement. This includes use for classroom teaching and internal training at the institution (including use in course packs and courseware programs), and inclusion of the article for grant funding purposes.

Gold Open Access Articles: May be shared according to the author-selected end-user license and should contain a CrossMark logo, the end user license, and a DOI link to the formal publication on ScienceDirect.

Please refer to Elsevier's posting policy for further information.

18. **For book authors** the following clauses are applicable in addition to the above: Authors are permitted to place a brief summary of their work online only. You are not allowed to download and post the published electronic version of your chapter, nor may you scan the printed edition to create an electronic version. **Posting to a repository:** Authors are permitted to post a summary of their chapter only in their institution's repository.

19. **Thesis/Dissertation**: If your license is for use in a thesis/dissertation your thesis may be submitted to your institution in either print or electronic form. Should your thesis be published commercially, please reapply for permission. These requirements include permission for the Library and Archives of Canada to supply single copies, on demand, of the complete thesis and include permission for Proquest/UMI to supply single copies, on demand, of the complete thesis. Should your thesis be published commercially, please reapply for permission. Theses and dissertations which contain embedded PJAs as part of the formal submission can be posted publicly by the awarding institution with DOI links back to the formal publications on ScienceDirect.

Elsevier Open Access Terms and Conditions

You can publish open access with Elsevier in hundreds of open access journals or in nearly 2000 established subscription journals that support open access publishing. Permitted third party re-use of these open access articles is defined by the author's choice of Creative Commons user license. See our open access license policy for more information.

Terms & Conditions applicable to all Open Access articles published with Elsevier:

Any reuse of the article must not represent the author as endorsing the adaptation of the article nor should the article be modified in such a way as to damage the author's honour or reputation. If any changes have been made, such changes must be clearly indicated.

The author(s) must be appropriately credited and we ask that you include the end user license and a DOI link to the formal publication on ScienceDirect.

If any part of the material to be used (for example, figures) has appeared in our publication

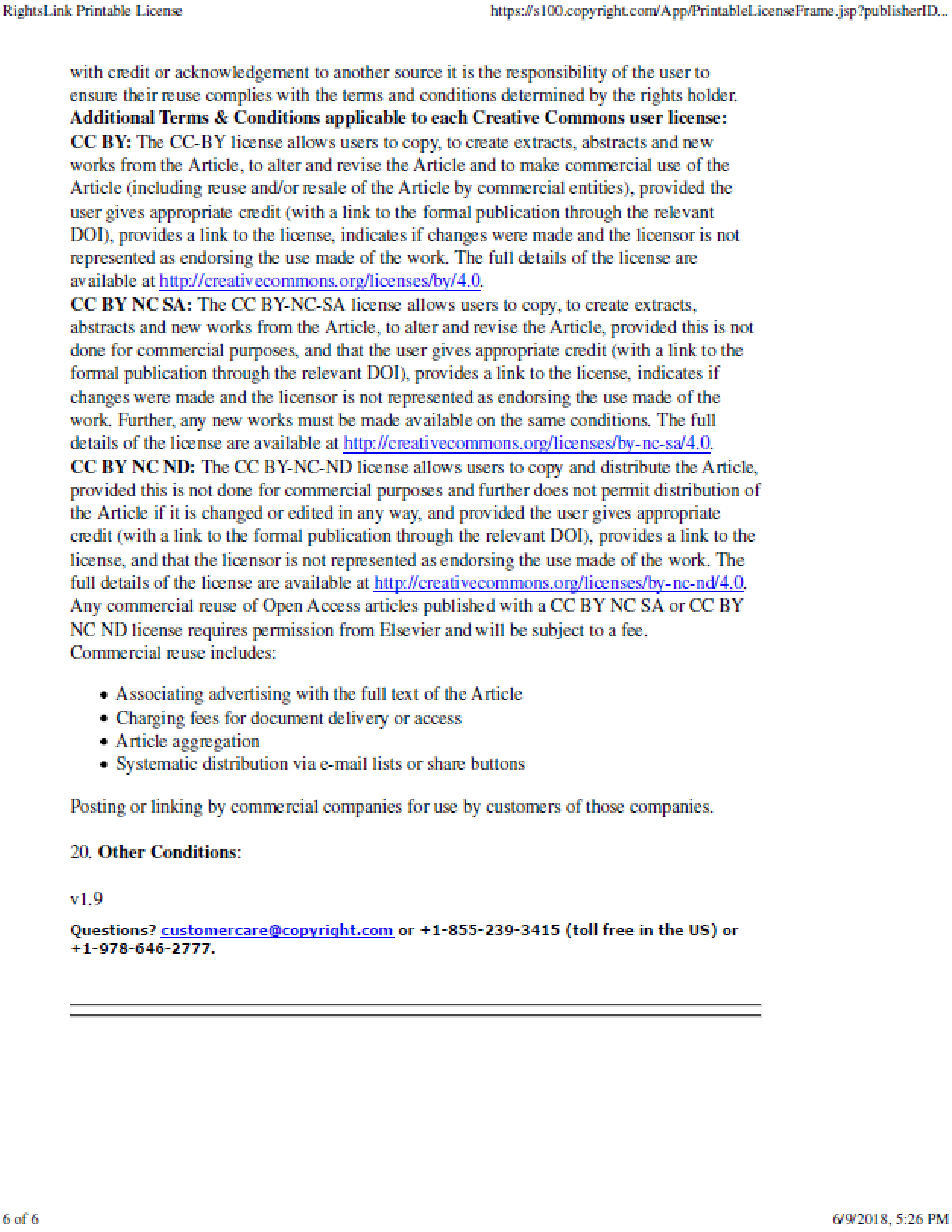

with credit or acknowledgement to another source it is the responsibility of the user to ensure their reuse complies with the terms and conditions determined by the rights holder.

Additional Terms & Conditions applicable to each Creative Commons user license:

CC BY: The CC-BY license allows users to copy, to create extracts, abstracts and new works from the Article, to alter and revise the Article and to make commercial use of the Article (including reuse and/or resale of the Article by commercial entities), provided the user gives appropriate credit (with a link to the formal publication through the relevant DOI), provides a link to the license, indicates if changes were made and the licensor is not represented as endorsing the use made of the work. The full details of the license are available at http://creativecommons.org/licenses/by/4.0.

CC BY NC SA: The CC BY-NC-SA license allows users to copy, to create extracts, abstracts and new works from the Article, to alter and revise the Article, provided this is not done for commercial purposes, and that the user gives appropriate credit (with a link to the formal publication through the relevant DOI), provides a link to the license, indicates if changes were made and the licensor is not represented as endorsing the use made of the work. Further, any new works must be made available on the same conditions. The full details of the license are available at http://creativecommons.org/licenses/by-nc-sa/4.0.

CC BY NC ND: The CC BY-NC-ND license allows users to copy and distribute the Article, provided this is not done for commercial purposes and further does not permit distribution of the Article if it is changed or edited in any way, and provided the user gives appropriate credit (with a link to the formal publication through the relevant DOI), provides a link to the license, and that the licensor is not represented as endorsing the use made of the work. The full details of the license are available at http://creativecommons.org/licenses/by-nc-nd/4.0. Any commercial reuse of Open Access articles published with a CC BY NC SA or CC BY NC ND license requires permission from Elsevier and will be subject to a fee.

Commercial reuse includes:

- Associating advertising with the full text of the Article
- Charging fees for document delivery or access
- Article aggregation
- Systematic distribution via e-mail lists or share buttons

Posting or linking by commercial companies for use by customers of those companies.

20. **Other Conditions**:

v1.9

Questions? customercare@copyright.com or +1-855-239-3415 (toll free in the US) or +1-978-646-2777.